To the Graduate Council:
I am submitting herewith a dissertation written by David Fieser entitled "Laser Precision Manufacturing: Microstructure, Surface, and Property Control." I have examined the final paper copy of this dissertation for form and content and recommend that it be accepted in partial fulfillment of the requirements for the degree of Doctor of Philosophy, with a major in Mechanical Engineering.

_____

Anming Hu, Major Professor

We have read this dissertation
and recommend its acceptance:

_____

Zhili Feng

_____

Seungha Shin

_____

Peter Liaw

Accepted for the Council:

_____

Marieke Van Puymbroeck

Vice Provost and Dean of the Graduate School

To the Graduate Council:
I am submitting herewith a dissertation written by David Fieser entitled "Laser Precision Manufacturing: Microstructure, Surface, and Property Control." I have examined the final electronic copy of this dissertation for form and content and recommend that it be accepted in partial fulfillment of the requirements for the degree of Doctor of Philosophy, with a major in Mechanical Engineering.

Anming Hu, Major Professor

We have read this dissertation
and recommend its acceptance:

Zhili Feng

Seungha Shin

Peter Liaw

Accepted for the Council:

Marieke Van Puymbroeck

Vice Provost and Dean of the Graduate School

(Original signatures are on file with official student records.)

Laser Precision Manufacturing: Microstructure, Surface, and Property Control

A Dissertation Presented for the

Doctor of Philosophy

Degree

The University of Tennessee, Knoxville

David Fieser

May 2026

© by David Fieser, 2026
All Rights Reserved.

Acknowledgements

First, I would like to express my deepest gratitude to my advisor, Dr. Anming Hu, for his guidance, support, and patience throughout my PhD. His mentorship has shaped how I think about research and engineering, and his confidence in me has been crucial at every stage of this work. I am especially grateful for his willingness to give me both direction and independence, and for always pushing me to aim higher in the quality and impact of my work.

I would also like to sincerely thank Dr. Suresh Babu for his guidance, insight, and encouragement. His perspective on both the scientific details and the broader significance of this research has been invaluable.

I am deeply grateful to Dr. Peter K. Liaw for his guidance, discussions, and for providing access to key resources. His support has had a substantial impact on the direction and depth of this work.

I would like to sincerely thank my dissertation committee members: Dr. Zhili Feng, Dr. Seungha Shin, and Dr. Peter Liaw for their time, invaluable feedback, and dedicated service. Their guidance and insights have been instrumental in shaping the quality and direction of this research. I am also grateful to the faculty and staff of the Department of Mechanical Engineering and the University of Tennessee, Knoxville, for providing an environment and resources that made this work possible. I would also like to thank Dr. Doug Aaron and Dr. Brett G. Compton, who served on my qualifying committee and provided valuable feedback and access to important resources early in my PhD.

I am grateful to Drs. Yanfei Gao, Seungha Shin, and Wenda Tan for their collaboration and support through the National Science Foundation (NSF) under Award No. CMMI-2412544, "Collaborative Research: Additive Manufacturing

of Crack-Free Tungsten Using Ultrashort Pulsed Lasers" (PI: Dr. Anming Hu, NSF Program: AM-Advanced Manufacturing, Division of Civil, Mechanical, & Manufacturing Innovation).

I gratefully acknowledge support from the UTK 100 Talented PhD Scholarship. Portions of the Atom Probe Tomography and photoluminescence spectroscopy research presented in this dissertation were conducted as part of a user project at the Center for Nanophase Materials Sciences (CNMS), a U.S. Department of Energy, Office of Science User Facility at Oak Ridge National Laboratory, under CNMS Proposal ID: CNMS2025-R-03093. I also wish to acknowledge Prof. Philip Rack, Leonard G. Penland Chair and Director of the Center for Materials Processing, as well as the State of Tennessee and the Tennessee Higher Education Commission, for their support of the Center for Materials Processing and the broader materials research community at UTK. I am especially grateful to Dr. Neil Evans at the Electron Microscopy Center at UTK's Institute for Advanced Materials & Manufacturing for his training and guidance on SEM and other characterization techniques that made this work possible. I am likewise grateful to Dr. Michael Koehler at the Diffraction Facility at UTK's Institute for Advanced Materials & Manufacturing for his training and guidance on XRD and related measurements. I would also like to thank Kaijun Yin and Dr. Jian-Min Zuo for their assistance with high-resolution transmission electron microscopy.

Finally, I am thankful to my colleagues, lab mates, and collaborators for their help, conversations, and support over the years. Their willingness to share ideas, experience, and the occasional troubleshooting session made this work more productive and far more enjoyable. In particular, I would like to thank Unmanaa Dewanjee, Lingyue Zhang, Hugh Shortt, Denzel Bridges, Yucheng Lan, Antonino Gulino, Giuseppe Compagnini, Matthew Mench, Matthew Yao, Baldur Steingrimsson, Ilia N. Ivanov, James Burns, Michael Lawton, Sumit Bahl, Amirkoushyar Ziabari, Tomas Grejtak, Janet M. Meier, Mason Smith, Alex Plotkowski, and Elaine McDonald for their support and collaboration.

"If you want the rainbow, you gotta put up with the rain."

– Dolly Parton

Abstract

Laser precision manufacturing enables targeted control of microstructure, surface state, and functional properties by coupling laser energy delivery with environmental and spatial boundary conditions. This dissertation investigates that coupling across three length scales: nanoscale synthesis, mesoscale powder bed fusion, and microscale surface processing.

At the nanoscale, femtosecond laser ablation in liquids is used to synthesize high-purity $CuCoMn_{1.75}NiFe_{0.25}$ high-entropy alloy nanoparticles. A scalable ablation platform with continuous filtration is demonstrated, and the resulting nanoparticles retain a single-phase face-centered cubic structure with promising electrocatalytic activity for oxygen reduction, oxygen evolution, and hydrogen evolution reactions. Extending this work, a systematic comparison of ablation in ethanol and liquid nitrogen reveals that solvent choice governs particle size distribution, crystallographic defect density, elemental homogeneity, and surface oxide chemistry. Liquid nitrogen quenching preserves compositional fidelity and produces structurally continuous nanoparticles, whereas ethanol ablation yields nanocrystalline aggregates with higher mixing enthalpy and reduced thermodynamic stability. Cooling simulations and thermodynamic descriptor analysis connect these differences to solvent-dependent heat extraction rates and to the balance between enthalpy and entropy contributions.

At the mesoscale, laser powder bed fusion of a near-eutectic Al–Ce–Ni–Mn–Zr alloy designed for elevated-temperature service is optimized through a 60-build design of experiments that maps laser power, scan speed, and hatch spacing to porosity and hardness responses. A Rosenthal-based cooling rate metric captures more than half the variation in both responses, yielding a defined processing window (350–370 W, 1400–1800 mm/s, 0.14–0.18 mm hatch) that produces porosity below 0.01 vol%

and as-built hardness up to 160 HV at cooling rates of 3.0–3.6 $\times$ 10^6 K/s. At the microscale, a hybrid two-temperature model is developed for multi-pulse femtosecond laser processing of tungsten. The method solves the full coupled electron–lattice system during each pulse on a fine grid and hands off the equilibrated profile to Crank–Nicolson diffusion on a coarser grid through the inter-pulse gap, running roughly two orders of magnitude faster than monolithic integration. Validation against a scanning experiment at 40 MHz shows that the predicted melt zone diameter of 25.0 μm matches the measured central zone exactly, with no fitted parameters.

Across all scales, the results show that jointly controlling energy delivery, processing environment, and thermal boundary conditions provides repeatable pathways from process inputs to microstructure to properties.

Table of Contents

1 Introduction **1**

1.1 Laser Precision Manufacturing Fundamentals 1

1.2 Laser Ablation in Liquid and Nanojoining: Physics at a Nanoscale . . 6

1.2.1 Size-Dependent Properties of Nanoparticles 6

1.2.2 Ultrafast Laser Ablation Mechanisms 9

1.2.3 Laser Induced Nanojoining 14

1.3 Microscale Laser Joining of Metallic Systems 17

1.3.1 Mechanisms of Microscale Laser Joining 17

1.3.2 Joint Zones: Fusion Zone, HAZ, and Base Material 19

1.3.3 Metallurgical Phenomena in Dissimilar Laser Joints 21

1.3.4 Solidification Behavior and Joint Integrity 23

1.3.5 Joint Characterization Descriptors 25

1.4 Laser Powder Bed Fusion: Macroscopic Laser-Materials Interaction . 28

1.4.1 Process Description and Geometric Controls 29

1.4.2 Energy Input Metrics and Normalized Process Maps 31

1.4.3 Melt Pool Physics and Rapid Solidification 33

1.4.4 Microstructure and Property Descriptors for Laser Powder Bed Fusion 35

1.5 Materials Background 38

1.5.1 High-entropy alloys 38

1.5.2 High-entropy alloy laser ablation in liquid 40

1.5.3 Al–Ce–Ni–Mn–Zr Near-Eutectic (DuAlumin-3D-type) High-Temperature Aluminum Alloys 42

1.5.4 Laser Processing of Refractory Metals: Physics, Mechanisms, and Defect Formation in Tungsten 48

2 Scalable Femtosecond-Laser Ablation Synthesis of High-Purity $CuCoMn_{1.75}NiFe_{0.25}$ HEA Nanoparticles 52

2.1 Motivation and Background 54

2.2 Materials and Methods 57

2.2.1 Material Synthesis 57

2.2.2 Microstructure, Phase, and Electrochemical Characterization . 59

2.3 Results and Discussion 61

2.3.1 Morphology, Phase, and Composition 61

2.3.2 Nanoparticle Composition 61

2.3.3 Laser Ablation and Joining Mechanisms 69

2.3.4 Electrochemical Performance of HEA Nanoparticles 73

2.4 Conclusions 75

3 Solvent-Controlled Surface Nanostructure and Thermodynamic Stability of $CuCoMn_{1.75}NiFe_{0.25}$ HEA Nanoparticles 77

3.1 Disclosure 78

3.2 Motivation and Background 79

3.3 Experimental 84

3.3.1 Material Synthesis 84

3.3.2 Characterization Techniques 85

3.3.3 Simulations and Quantitative Calculations 87

3.4 Results and Discussion 92

3.4.1 Bulk Material Baseline Composition 92

3.4.2 Nanoparticle Microstructure 93

3.4.3 Particle Morphology 96

3.4.4 Elemental Composition and Distribution 98

3.4.5 Thermodynamic Stability 104

3.4.6 Solvent-Controlled Cooling Dynamics and Defect Evolution . . 109
3.4.7 Oxide Shell Analysis and Optical Behavior 112
3.4.8 Conclusions 117

4 Process Optimization in LPBF of Al-Ce-Ni-Mn-Zr 120
4.1 Disclosure 121
4.2 Motivation and Background 122
4.3 Materials and Methods 125
4.3.1 Materials 125
4.3.2 Laser Powder Bed Fusion 125
4.3.3 Experimental Design and Statistical Methods 126
4.3.4 Hardness and Characterization 130
4.4 Results 133
4.4.1 Pore Defects 133
4.4.2 X-ray Computed Tomography 134
4.4.3 Microstructure Characterization 139
4.4.4 Hardness 140
4.4.5 Roughness 142
4.5 Discussion 144
4.6 Conclusions 149

5 Laser Processing of Tungsten: A Computationally Efficient Hybrid Two-Temperature Model for Multi-Pulse Femtosecond Laser Heat Accumulation 151
5.1 Disclosure 152
5.2 Motivation and Background 153
5.3 Methods 157
5.3.1 Femtosecond Laser Irradiation 157
5.3.2 Surface Characterization 157
5.3.3 Governing Equations 157

5.3.4 Material Properties . . . 159
5.3.5 Boundary and Initial Conditions . . . 160
5.3.6 Hybrid Two-Phase Solution Strategy . . . 160
5.3.7 Phase 1: Stiff ODE Integration on the Fine Grid . . . 161
5.3.8 Phase 2: Crank–Nicolson Inter-Pulse Diffusion . . . 163
5.3.9 Grid Mapping Between Phase 1 and Phase 2 . . . 165
5.3.10 Fluence and Radial Profile Reconstruction . . . 165
5.3.11 Computational Cost . . . 166
5.4 Results and Discussion . . . 167
5.4.1 Verification and Convergence . . . 168
5.4.2 Single-Pulse Electron–Lattice Dynamics . . . 169
5.4.3 Multi-Pulse Heat Accumulation . . . 172
5.4.4 Radial and Cross-Sectional Temperature Fields . . . 176
5.4.5 Computational Performance . . . 177
5.4.6 Experimental Validation . . . 179
5.5 Conclusions . . . 184

6 Conclusions and Outlook **185**
6.1 Summary of Contributions . . . 185
6.2 Conclusions . . . 187
6.3 Future Work and Outlook . . . 189

Bibliography **191**

Appendices **240**

A Experimental Results **241**
A.1 LPBF Processing Parameters and Results for ACNMZ . . . 241

B Publications **244**

Vita **246**

List of Tables

3.1 Nanoparticle and solver parameters common to both the ethanol and liquid-nitrogen simulations. 89

3.2 Ethanol simulation parameters (convective heat-flux boundary condition model). 89

3.3 Liquid-nitrogen simulation parameters (conduction through NP/gas-shell/LN_2 stack). The far-field LN_2 boundary is held at 77 K throughout the simulation. 90

3.4 Elemental composition (wt%) of fs-ablated nanoparticles compared with theoretical and bulk values. 98

3.5 Atomic composition from XPS (at%). 101

3.6 Complete XPS fitting results. Binding energy and FWHM are given for each fitted peak component, and atomic percentages sum to the element totals in Table 3.5. 104

3.7 Thermodynamic quantitative parameters for experimental materials. . 105

4.1 Key processing parameters for LPBF. 128

4.2 Response surface model coefficients for log-porosity [$\log(\varphi)$], Eq. 4.1, listed in order of ascending p-value. $F(df_1, df_2)$ is the overall F-statistic on df_1 and df_2 degrees of freedom; p_F is the corresponding overall model p-value; $\hat{\sigma}$ is the residual standard error. 139

4.3 Response surface model coefficients for Vickers hardness (HV), Eq. 4.2, listed in order of ascending p-value. $F(df_1, df_2)$ is the overall F-statistic on df_1 and df_2 degrees of freedom; p_F is the corresponding overall model p-value; $\hat{\sigma}$ is the residual standard error. 142

5.1 Material properties for tungsten. 159
5.2 Tabulated total thermal conductivity $k_{\mathrm{hyb}}(T)$ for tungsten, used for both Drude k_{e0} modulation and Phase 2 diffusion. 160
5.3 Default simulation parameters. 167
5.4 Wall-clock times for multi-pulse simulations at default conditions (W, 40 W, 18 MHz, $w_0 = 100\,\mu\mathrm{m}$, $\tau_p = 500\,\mathrm{fs}$). 178
5.5 Experimental conditions and measured damage zone widths for tungsten samples processed at $f_{\mathrm{rep}} = 40\,\mathrm{MHz}$, $\tau_p = 500\,\mathrm{fs}$, $w_0 \approx 100\,\mu\mathrm{m}$. 180

A.1 Complete LPBF processing parameters and results for ACNMZ. Void% and hardness (HV) are averages. E_a is the areal energy density ($\mathrm{J/mm^2}$). 241

List of Figures

1.1 Schematic illustration of laser–surface optical interactions showing (a) the definition of the incident angle θ_i between the incoming beam and the surface normal, (b) light trapping within an oxidized surface layer due to internal reflections, and (c) enhanced absorption on a rough surface arising from multiple scattering and repeated internal reflections within surface asperities. 3

1.2 Two-temperature model schematic and representative electron and lattice temperature evolution after laser excitation. 5

1.3 Nanoscale surface-to-volume scaling from Eq. (1.1) and illustrative size-dependent melting temperature trend from Eq. (1.3) for spherical Au nanoparticles versus particle diameter d. 8

1.4 Contour plot of electron (top) and lattice temperatures (bottom) for copper, irradiated with a laser pulse of a fluence slightly above ablation threshold (140 mJ cm^{-2}). The solid line in the top figure represents the Gaussian intensity profile of the laser pulse of 100 fs duration. The solid line in the bottom part shows the ablation temperature. 11

1.5 Laser ablation and optical breakdown thresholds as a function of pulse duration for fused silica, highlighting how the threshold separation defines the usable processing window and ablation quality from femtosecond to picosecond irradiation. 13

1.6 Laser-induced joining of Ag nanowires by different types of lasers. (a,b) Focused CW laser, nanowelding of silver nanowire networks for transparent conductive electrodes. (c–f) Focused CW laser, crystalline nanojoining of silver nanowire percolated networks. (g–j) ns laser joining of silver nanowires. (k–m) fs laser single-point nanowelding of silver nanowires. 18
1.7 The illustration of the welded joint showing the base material, HAZ, and fusion zone (weld metal) regions 20
1.8 The schematic illustration of the typical welding defects of laser beam keyhole welded butt joints. 23
1.9 Solidification cracking susceptibility analysis: (a) schematic of the dendritic growth within the mushy zone; (b) T-$(fAl)^{1/2}$ curves of AA7075 + 7055 weld; (c) T-$(fAl)^{1/2}$ curves of AA7075 + 7150 weld. . 24
1.10 Hardness profile of weld, compared to actual weld macrographic image. 27
1.11 Schematic of the LPBF process. 29
1.12 Effect of temperature gradient G and growth rate R on the morphology and size of solidification microstructure. 35
1.13 AlSi10Mg deposited by LPBF with laser beam diameter = 0.3 mm, velocity 2250 mm/s resulting in a deposit pore density of 0.4% (left) and laser beam diameter = 1 mm, velocity 250 mm/s resulting in a deposit pore density of 9.2% (right). 37
1.14 Illustrations showing the lattice structure of (a) FCC, (b) BCC, and (c) hexagonal close-packed HEAs. Each color represents a different element. 39

1.15 Qualitative representation of the laser-based synthesis of high-entropy alloy nanoparticles. The synthesis method consisted of the following stages: ultrashort-pulsed laser irradiation of the bulk HEA (a), the atomization/ionization of the bulk causing the formation of a plume, and subsequent nucleation and condensation of the ablated matter in the vapor phase of the liquid (b) and the colloidal high-entropy alloy nanoparticles electrostatically stabilized in ethanol (c). 41
1.16 Microstructure of as-fabricated (a-b) Al-Ce-Ni-Mn and (d-e) Al-Ce-Ni-Mn-Zr alloys. Backscattered-electron scanning electron microscopy (BSE-SEM) images at (a) lower magnification with a higher magnification inset showing Mn-rich, rosette-shaped intermetallic particles (marked with yellow arrows, confirmed by the energy-dispersive X-ray spectroscopy (EDS) map in Figure S1) and (b) shows a crack in the alloy (lower magnification image in the inset) formed after removal from the build plate which is associated with Mn-rich rosettes. (c) Inverse pole figure (IPF) map of the stress-relived (HT450) Al-Ce-Ni-Mn alloy, showing columnar grain structure in the alloy. BSE-SEM images at (d) lower magnification and (e) higher magnification (at the melt pool center) show the eutectic structure and (f) IPF map shows equiaxed grain structure in the as-fabricated Al-Ce-Ni-Mn-Zr alloy. The inset in (e) is a high-angle annular dark-field (HAADF)-STEM image of the eutectic solidification microstructure. The curved dotted lines in (a), (c), (d) and (f) mark the melt pool boundaries. BD indicates the build direction. 44
1.17 (a) Liquidus projection of the Al-Ce-Ni alloy system. (b) Liquidus projection of the Al-Ce-Mn alloy system. 45

1.18 In situ neutron creep data showing the load transfer behavior between the intermetallic second phase and the Al matrix: (a-c) plots of lattice stress for each phase vs. creep macrostrain for (a, b) HT350 and (c) HT450 during stress-jump creep tests at 300 °C (a, c) and 350 °C (b). (d, e) plots of lattice stress for each phase vs. macrostrain for HT350 during tensile tests at (d) R.T. and (e) 300 °C. IM stands for the $Al_{27}Ni_6Ce_3$ intermetallic second phase. For creep tests (a-c), applied macroscopic stress is given as a fraction of yield stress (%YS) and macroscopic creep strain rates (s^{-1}) are shown for each stress level. The error bars represent standard error of the mean. 47

2.1 Phase diagram for $Fe_xCo_{20}Ni_{20}Mn_yCu_{20}$ system calculated by Thermo-Calc using the HEA 1.0 database. 55

2.2 Schematic of the HEA ablation system. 58

2.3 (a) XRD analysis of femtosecond-ablated high-entropy alloy nanoparticles in diverse media, including bulk composition. (b) High-entropy alloy nanoparticles ablated in water exhibiting a core–shell structure. 62

2.4 XPS analysis of $CuCoMn_{1.75}NiFe_{0.25}$ nanoparticles ablated in water. (a) Survey scan, with O-1s subplot. (b) Cu-2p. (c) Co-2p. (d) Mn-2p. (e) Ni-2p. (f) Fe-2p. (g) C-1s. (h) O-1s deconvolution. 64

2.5 (a) High-entropy alloy nanoparticles ablated in ethanol with an organic shell encasing a metallic core. (b) Raman shift spectra of HEA nanoparticles ablated in different media, displaying carbon D and G bands. (c) EDS of ceramic shell nanoparticles showing all five elements. 66

2.6 Size analysis of HEA nanoparticles. 67

2.7 (a) SEM image of HEA nanoparticles at low laser power and fluence. (b) SEM image of HEA nanoparticle chains after ablation at high laser fluence. (c) TEM image of high laser fluence chains after washing away organic material. 68

2.8 (a) UV-NIR spectra of nanoparticle solutions after fs irradiation. (b) TEM image of ethanol-ablated HEA nanoparticles. (c) TEM image of the same nanoparticle solution after fs irradiation. 69
2.9 (a) Illustration of the laser ablation process for the formation of nanoparticles. (b) Depiction of surface nanojoining process. 71
2.10 Hydrodynamic diameter of HEA nanoparticle solution. 72
2.11 (a) LSV plots demonstrating multi-function catalysis of HEA nanoparticles, featuring hydrogen evolution, oxygen reduction, and oxygen evolution. (b) LSV curves for aluminum–air battery showing output current density. (c) LSV curves for aluminum–air battery showing output power density. 74

3.1 Reconstruction of the bulk $CuCoMn_{1.75}NiFe_{0.25}$ alloy from atom probe tomography. The tip length is 500 nm. 92
3.2 High-resolution TEM images of nanoparticles ablated in LN_2 (a–c) and ethanol (d–f). In (a), the orange box marks the region enlarged in (b,c), showing lattice fringes and stacking faults/nanotwins near the particle edge. In (d), the green and blue boxes indicate areas enlarged in (e,f), highlighting crystallinity and defect structures. Stacking faults/nanotwins are visible near the nanoparticles' grain boundary or edge. Insets in (b,e,f) are FFT patterns. 93

3.3 Structural analysis of nanoparticles ablated in ethanol. (a) Bright-field TEM image showing a representative agglomeration of spherical nanoparticles. (b) Low-magnification image highlighting the region selected for 4D-STEM analysis (yellow box). (c) High-resolution STEM image with an inset diffraction pattern confirming a nanocrystalline FCC structure. (d) Averaged diffraction pattern from the scanned region, with indexed (111) and (220) rings indicating an FCC symmetry. (e) RGB composite of virtual dark-field images constructed from the (111) and (220) diffraction rings, illustrating spatial variation in nanocrystalline domain orientations. (f–h) Localized diffraction patterns corresponding to positions marked in (e), showing distinct diffraction spot arrangements consistent with variations in the local crystal orientation and grain structure. 95

3.4 Particle size distributions and low-magnification TEM images of nanoparticles produced by femtosecond laser ablation. (a–c) Nanoparticles ablated in ethanol: (a,b) TEM images, (c) size distribution. (d–f) Nanoparticles ablated in liquid nitrogen: (d,e) TEM images, (f) size distribution. 97

3.5 EDS mapping on the femtosecond-laser ablated nanoparticles in LN_2 (a) and ethanol (b). 99

3.6 STEM bright-field images and corresponding Mn-based elemental ratios for nanoparticles ablated in (A) liquid nitrogen and (B) ethanol. 100

3.7 XPS scans showing (a) Mn 2p orbital, (b) O 1s orbital, (c) Survey scans. 102

3.8 Full XPS core-level spectra of $CuCoMn_{1.75}NiFe_{0.25}$ nanoparticles ablated in ethanol and LN_2: (a) Mn 2p, (b) Fe 2p, (c) Co 2p, (d) Ni 2p, (e) Cu 2p, (f) O 1s, (g) survey. All binding energies are calibrated to the adventitious C 1s peak at 284.8 eV. The spectra supplement Table 3.6 by displaying each fitted multiplet component for direct visual comparison between the two ablation environments. 103

3.9 Thermodynamic map in Ω–ΔH_{mix} space. 106
3.10 Thermodynamic stability maps for theoretical, bulk, and laser-ablated $CuCoMn_{1.75}NiFe_{0.25}$ compositions. (a) δ–ΔH_{mix} phase formation map with labeled phase regions. Inset magnifies the nanoparticle compositions. (b) Three-dimensional δ–ΔH_{mix}–ΔS_{mix} view of the same data. 108
3.11 (a) COMSOL simulation of nanoparticle surface cooling in liquid media. (b) Geometry of LN_2 nanoparticle showing gas shell. 111
3.12 UV–Vis absorbance (a), Tauc plots (b), PL excitation–emission maps for LN_2 (c) and ethanol (d), and emission spectra at 300 nm excitation (e) of LN_2- and ethanol-ablated nanoparticles. Dashed lines show the linear fit regions whose intercepts give the optical band gap. 114

4.1 Build geometry. (A) Build locations. (B) Rendering of build plate. (C) Detail of completed builds with a zoomed version of a color-separated version of the computer-aided design model. Each region is identified in this model. The design of the sample and geometric features along with high-throughput characterization allows for study of geometric dependence of process parameter design. 126
4.2 Distribution of the 60 LPBF build parameter sets in the laser power–scan speed–hatch spacing design space. 128
4.3 SEM images of defects observed in ACNMZ samples. (A–C) Spherical gas pores from parameter set 23 at increasing magnifications. (D–F) Irregular lack-of-fusion defects from parameter set 27 at increasing magnifications. 133
4.4 Representative XCT reconstruction data with associated SEM-BSE images illustrating defect distributions across processing conditions. Results for XCT and hardness are summarized for all parameter sets in Appendix A.1. 135

4.5 Relationship between LPBF processing conditions and porosity formation. (A) BSE image showing keyhole gas pore at low scan speed. (B) BSE image showing lack-of-fusion porosity at high scan speed. (C) Porosity as a function of laser power at three hatch distances. (D) Porosity as a function of scan speed at three hatch distances. 136
4.6 Pore size and shape characteristics. (A) Histogram of volume-equivalent diameters measured from XCT. (B) Average sphericity plotted against scan speed for all XCT-analyzed samples. 138
4.7 Backscatter electron micrographs of three representative coupons produced with Parameter Sets 10, 16, and 40, corresponding to low, intermediate, and high energy inputs, respectively. 140
4.8 Influence of processing parameters on Vickers hardness. (A) Hardness as a function of laser power. (B) Hardness as a function of scanning speed. Shaded regions represent 95% confidence intervals. 141
4.9 Surface roughness characterization. (A) Optical image of a representative sample (parameter set 10). (B) Corresponding 3D surface topography. (C) Areal arithmetic mean height (S_a) for selected samples. 143
4.10 Relationships between areal energy density, cooling rate, hardness, and porosity. (A) Hardness versus areal energy density. (B) Porosity versus areal energy density. (C) Hardness versus cooling rate. (D) Porosity versus cooling rate. Parameter sets 10, 16, and 40 are highlighted. . . 145
4.11 Surface roughness comparison. (A) Roughness values for ACNMZ compared with other metal systems across a range of scan speeds. (B) Surface roughness as a function of areal energy density. 147

5.1 Depth-resolved electron temperature $T_e(z)$ (red) and lattice temperature $T_l(z)$ (blue) profiles in tungsten at selected delays after the pulse center. The shaded amber region indicates where $T_l > T_e$ (temperature inversion). Laser conditions: $\tau_p = 500\,\mathrm{fs}$, $F = 0.014\,\mathrm{J/cm^2}$, $A = 0.55$. . 170

5.2 (a) Surface electron and lattice temperature evolution for a single 500 fs pulse in tungsten (log-scale ordinate). (b) Zoomed view of the inversion region where $T_l > T_e$, with the peak inversion magnitude annotated. (c) Comparison of surface dynamics across tungsten, copper, and aluminum under identical irradiation conditions (solid lines: T_e, dashed lines: T_l). 172

5.3 Heat accumulation for case C1 (W, 40 W, 18 MHz, $w_0 = 100\,\mu\mathrm{m}$). (a) Per-pulse post-equilibration temperature T_{eq} and pre-pulse residual temperature T_{resid} versus pulse number. The shaded region represents the per-pulse temperature excursion. (b) Lattice temperature profiles $T_l(z)$ at selected pulse counts (1, 10, 100, 500, 1000, and 1800), showing progressive thermal penetration into the bulk. 174

5.4 Surface electron temperature T_e (blue) and lattice temperature T_l (red) during the first six pulses (P1 through P6) for case C1. Each pulse produces a sub-picosecond T_e spike followed by rapid electron–lattice equilibration. The dashed green line traces the rising inter-pulse baseline temperature. 174

5.5 Peak surface temperature inversion $(T_l - T_e)$ versus pulse number over 1800 pulses (case C1). The thin line shows pulse-by-pulse data and the thick line is a 50-pulse moving average. 176

5.6 (a) Radial residual temperature profiles after 1800 pulses (case C1) at several depths below the irradiated surface. The beam $1/e^2$ radius is $w_0 = 100\,\mu\mathrm{m}$. (b) Residual surface temperature versus pulse number at five radial positions for case C1. The on-axis position $r = 0$ accumulates heat most rapidly. 177

5.7 Two-dimensional cross-sectional temperature map $T(r, z)$ after 1800 pulses for case C1. The vertical axis is depth, increasing downward, and the horizontal axis is radial distance from the beam center. . . . 178

5.8 Wall-clock time versus number of pulses, demonstrating linear computational scaling. The dashed line shows a linear fit with a slope of 85 ms/pulse. 179

5.9 Optical micrographs of all ten tungsten samples. Top row: power series S1–S5 at 60 mm/min. Bottom row: speed series S6–S10 at 80 W. Annotations show measured HAZ widths and morphological classification. 181

5.10 Raman spectroscopy of sample S4 (80 W, 60 mm/min). (a) Optical micrograph with Raman measurement locations indicated by crosshairs. (b) Spectrum from the debris zone showing strong monoclinic γ-WO_3 peaks. (c) Spectrum from the light oxidation zone with the same WO_3 peak positions at reduced intensity. Labeled peaks correspond to δ(O–W–O) bending modes at 134, 273, and 327 cm^{-1}, ν(W–W) at 187 cm^{-1}, ν(O–W–O) at 715 cm^{-1}, and ν(W–O) at 808 cm^{-1}. 181

5.11 Simulation results for sample S8 (80 W, 300 mm/min, 40 MHz) after 2832 pulses. (a) Reconstructed radial surface temperature profile. The shaded region marks the predicted melt zone ($T > T_{\text{melt}}$, diameter 25.0 µm). Dashed lines indicate the experimentally measured central zone boundary (Ø25 µm). (b) Two-dimensional surface temperature field obtained by revolving the radial profile. The dashed circle marks the predicted melt boundary. 183

Nomenclature

κ_e	Electron thermal conductivity
τ_p	Pulse duration
C_e	Electron heat capacity
C_l	Lattice heat capacity
F	Laser fluence
f_{rep}	Laser repetition rate
G	Electron–phonon coupling constant
S	Laser source term
T_e	Electron temperature
T_l	Lattice temperature
T_m	Melting temperature
w_0	Laser spot radius ($1/e^2$)
4D-STEM	Four-Dimensional Scanning Transmission Electron Microscopy
ACNMZ	Al–Ce–Ni–Mn–Zr (DuAlumin-3D alloy designation)
AIC	Akaike Information Criterion
APT	Atom Probe Tomography
BCC	Body-Centered Cubic

BDF	Backward Differentiation Formula
BSE	Backscatter Electron
BSE-SEM	Backscatter Electron Scanning Electron Microscopy
CW	Continuous Wave
DBTT	Ductile-to-Brittle Transition Temperature
DOE	Design of Experiments
EDS	Energy-Dispersive X-ray Spectroscopy
FCC	Face-Centered Cubic
FWHM	Full Width at Half Maximum
FZ	Fusion Zone
HAADF	High-Angle Annular Dark-Field
HAZ	Heat-Affected Zone
HEA	High-Entropy Alloy
HER	Hydrogen Evolution Reaction
HRTEM	High-Resolution Transmission Electron Microscopy
HV	Vickers Hardness
IPF	Inverse Pole Figure
LPBF	Laser Powder Bed Fusion
LSV	Linear Sweep Voltammetry
ODE	Ordinary Differential Equation

OER	Oxygen Evolution Reaction
ORR	Oxygen Reduction Reaction
OV	Oxygen Vacancy
PL	Photoluminescence
SEM	Scanning Electron Microscopy
STEM	Scanning Transmission Electron Microscopy
TEM	Transmission Electron Microscopy
TTM	Two-Temperature Model
USP	Ultrashort Pulse
VDF	Virtual Dark-Field
XCT	X-ray Computed Tomography
XPS	X-ray Photoelectron Spectroscopy
XRD	X-ray Diffraction

Chapter 1

Introduction

1.1 Laser Precision Manufacturing Fundamentals

Laser precision manufacturing refers to laser based processing in which the spatial distribution and temporal delivery of laser energy are deliberately controlled, together with the local processing environment, to produce repeatable and localized material modification. In engineering terms, the laser is treated as a programmable energy source whose intensity, interaction time, and path are selected to deposit energy and momentum with high locality. In this dissertation, that definition is extended to emphasize that the processing environment is not merely a boundary condition. It is a controllable input that can be tuned to influence energy coupling, heat removal, fluid and plume dynamics, and surface chemistry during processing. Environmental conditions such as the surrounding medium or atmosphere, gas chemistry and pressure, shielding and flow, and thermal management at interfaces can therefore be used to steer the mechanisms that ultimately set microstructure, surface state, and functional properties.

The central hypothesis of this work is that predictable and transferable material outcomes are achieved by jointly controlling laser energy delivery, environmental conditions, and spatial constraints, and that these coupled controls can be tuned to intentionally tailor distinct microstructures, surface states, and functional properties. A comprehensive treatment of foundational laser processing concepts and their practical manifestations across major

process classes is developed in *Laser Material Processing* by Steen and Mazumder, which is used here as a baseline reference for terminology and core concepts [1].

To address laser precision manufacturing across its full scope requires drawing on several bodies of knowledge. This chapter reviews these foundations at three scales: nanoscale processing for nanoparticle synthesis, microscale processing for localized microstructure control, and macroscale processing for powder bed fusion. While the applications differ, this work will employ a consistent organizing framework that connects what is controlled in the process to what is produced in the material, while accounting for environmental factors that strongly influence coupling and surface evolution. A high level overview of laser processing categories and their engineering context is available in Majumdar and Manna's review, which frames laser processing around major manufacturing functions and provides a useful bridge between fundamentals and application specific chapters [2].

The defining feature of laser precision manufacturing is controllability of energy input in both space and time. Spatial control is achieved through beam delivery and motion, including spot size, focus position, intensity distribution, incidence angle, and scan strategy. Temporal control is achieved through continuous wave power modulation or pulsed operation, including pulse duration, repetition rate, duty cycle, burst structure, and dwell time. Environmental and boundary conditions include the surrounding medium or atmosphere, gas composition and pressure, shielding and flow conditions, and thermal management such as preheating, substrate heat sinking, and insulation. These factors act alongside laser settings to determine energy coupling, melt or plume stability, cooling conditions, and the surface chemistry pathways that govern microstructural evolution and surface state. Comprehensive reviews of laser–matter interaction and industrial laser processing can be further found in [2, 3].

The laser material interaction begins with optical coupling at the surface and, for powders or semitransparent media, within a near surface volume. Absorption and reflectivity govern how much incident laser power is converted to internal energy, and this conversion depends on wavelength, angle of incidence, polarization,

surface condition, and temperature, as well as environmental factors that modify the surface during processing such as oxidation, adsorption, and reaction with the surrounding medium. For metals, these dependencies are not a secondary detail as they can dominate process stability and efficiency because reflectivity is often high and absorptivity can change substantially as the surface transitions from solid to melt and as surface chemistry evolves. A conceptual depiction of some of these phenomena can be found in Figure 1.1.

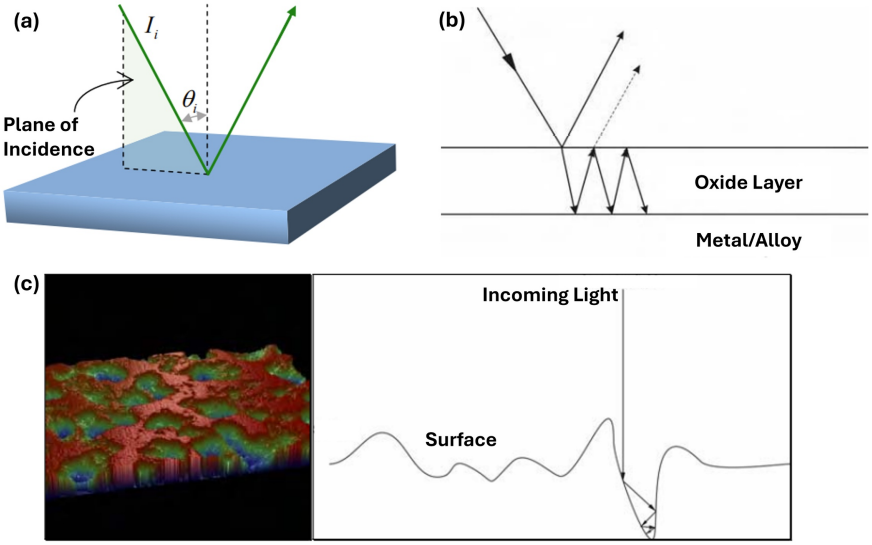


Figure 1.1: Schematic illustration of laser–surface optical interactions showing (a) the definition of the incident angle θ_i between the incoming beam and the surface normal, (b) light trapping within an oxidized surface layer due to internal reflections, and (c) enhanced absorption on a rough surface arising from multiple scattering and repeated internal reflections within surface asperities.

Note. Adapted from [4].

Once energy is absorbed, the governing physics shifts to transport and phase change under geometry and environmental boundary conditions. Heat flow, constrained by part geometry and interface heat sinking, determines melt pool dimensions, thermal gradients, and the spatial extent of the heat-affected zone, while phase change determines whether the process operates in a conduction dominated regime, transitions to keyhole behavior, or produces vaporization and ablation.

Environmental factors such as shielding gas composition and flow, ambient pressure, and reactive media influence melt pool stability and surface reactions, which can shift coupling behavior and affect defect formation. In joining and track based melting processes, melt pool formation and resolidification impose rapid solidification conditions that control microstructural scale selection, segregation behavior, and defect formation [3, 5, 6].

Because this work spans continuous wave (CW) and femtosecond regimes, it is necessary to introduce the time scale dependence of modeling assumptions. For CW and longer pulse durations, the material response is commonly captured with single temperature heat conduction models coupled to melting and solidification, because energy exchange between electrons and the lattice is fast relative to the energy deposition time. For ultrashort pulses, energy is deposited into the electronic subsystem on time scales comparable to or shorter than electron–phonon equilibration, and the electron temperature and lattice temperature can be meaningfully different during the early stages of excitation [7, 8]. This time scale framing also clarifies why ultrafast lasers are often associated with high precision ablation and reduced collateral thermal damage relative to longer pulse machining. In Figure 1.2, the laser pulse deposits energy into the electron subsystem first, producing a rapid increase in T_e, while the lattice temperature T_l initially lags due to slower coupling. Electron–phonon coupling then transfers energy from electrons to the lattice on the picosecond timescale, raising T_l and driving both subsystems toward thermal equilibration as the temperatures relax [9].

This work is organized by scale, but it is unified by the same process inputs to structure and surface state to properties logic. At the nanoscale, the primary process family is pulsed laser ablation in liquids for nanoparticle synthesis. In this route, a solid target is ablated while immersed in a liquid, and the transient plume produce rapid quenching and chemical environments that can yield colloidal nanoparticles with high purity and minimal contamination [11, 12]. At the microscale, this work focuses on laser joining and localized modification of bulk components. In

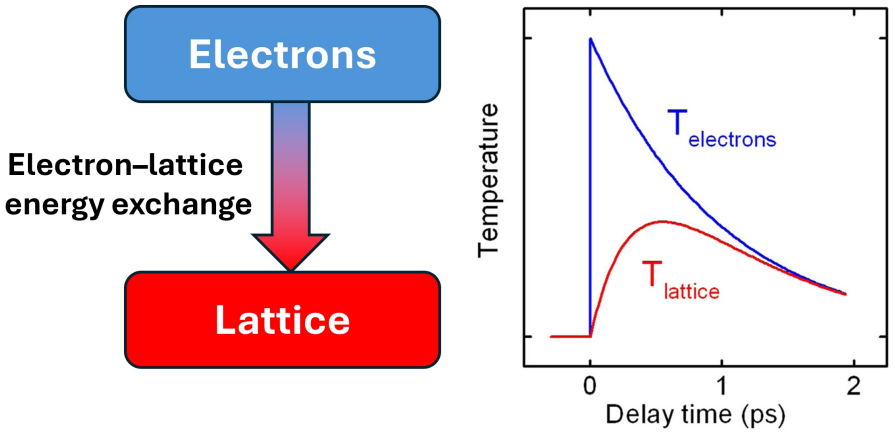


Figure 1.2: Two-temperature model schematic and representative electron and lattice temperature evolution after laser excitation.

Note. Adapted from [10].

joining, the laser acts as a localized heat source capable of producing fusion joints with small interaction volumes, enabling fine control of weld geometry, dilution, and heat-affected zone dimensions relative to many conventional joining methods. Beam size, pulse shaping, and scan strategy influence interfacial reactions and defect formation, particularly in dissimilar material systems that are central to modern electrification and microelectronics [13]. Localized modification at the microscale includes surface engineering and cladding, where the objective is to tailor surface state and near surface structure to achieve targeted properties such as wear resistance, corrosion resistance, or functional response while leaving bulk properties largely unchanged [14]. At the macroscale, we discuss laser powder bed fusion and related track-based processing topics. Laser powder bed fusion consolidates material layer by layer through repeated scanning of melt tracks, producing complex thermal cycling that couples strongly to residual stress evolution, microstructure development, and defect formation [3].

Across all three families, we will return to the same guiding question: how do controlled process inputs shape the thermal history, how does that thermal history impose structure and surface state, and how do those states govern properties that matter for performance. The remainder of the introduction will use this section's

definitions and modeling regimes to establish the conceptual continuity required to move from ultrafast nanoscale synthesis to microscale joining and modification and finally to macroscale track based manufacturing.

1.2 Laser Ablation in Liquid and Nanojoining: Physics at a Nanoscale

Understanding how materials behave at the nanoscale is necessary for both nanoparticle synthesis and nanostructure assembly. In this regime, the high surface-to-volume ratio of nanoparticles leads to properties that differ from bulk matter [15]. These nanoscale phenomena are central not only to the generation of nanoparticles by laser ablation in liquids, but also to the assembly of nanostructures via nanojoining processes. In nanojoining, nanosized building blocks (e.g., nanoparticles or nanowires) are permanently bonded to create integrated devices, often using laser-based techniques [16]. Laser-induced nanojoining offers a non-contact, high-precision means to weld or sinter nanomaterials together while preserving their properties through localized energy delivery [17]. An understanding of nanoscale material behavior is therefore required to appreciate both the production of nanoparticles in liquid-phase laser ablation and their subsequent integration into larger functional structures.

1.2.1 Size-Dependent Properties of Nanoparticles

Nanoparticles are typically defined as particles with at least one dimension below $\sim$100 nm, though many of the strongest size-dependent effects emerge below $\sim$10 nm, where a significant fraction of atoms reside at the surface [18]. Such particles exhibit pronounced size-dependent behavior owing to their high surface area relative to

volume. For a spherical particle of diameter d and volume V, naturally:

$$\frac{A}{V} = \frac{6}{d}. \tag{1.1}$$

As particle size diminishes, an increasing proportion of atoms have unsatisfied bonds at the surface, raising the surface free energy. A compact way to express the growing thermodynamic weight of the surface is

$$G(d) \approx G_{\text{bulk}} + \gamma A, \tag{1.2}$$

where $G(d)$ is the Gibbs free energy of a particle of diameter d, G_{bulk} is the bulk contribution to the free energy, γ is the surface or interfacial energy, and A is the surface area [15]. Consequently, surface effects dominate many physical and chemical properties of nanoparticles. For example, characteristics like melting point, solubility, and chemical reactivity can all shift with particle size, often markedly different from bulk values. A commonly used curvature form for melting point depression is

$$T_m(d) \approx T_{m,\infty}\left(1 - \frac{4\sigma_{sl}}{\rho_s H_f d}\right), \tag{1.3}$$

where $T_m(d)$ is the melting temperature of a particle of diameter d, $T_{m,\infty}$ is the bulk melting temperature, σ_{sl} is the solid to liquid interfacial energy, ρ_s is the solid density, and H_f is the enthalpy of fusion per unit mass [19]. These A/V and melting temperature trends for spherical Au nanoparticles are illustrated in Figure 1.3. A widely used curvature relation for increased equilibrium solubility is

$$\ln\left(\frac{S(r)}{S_\infty}\right) = \frac{2\gamma V_m}{rRT}, \tag{1.4}$$

where $S(r)$ is the solubility for particles of radius r, S_∞ is the bulk solubility, γ is the particle to solvent interfacial energy, V_m is the molar volume of the solid, R is the gas constant, and T is absolute temperature [20]. A well-known example is seen in noble

metal nanoparticles: gold in bulk is inert and yellow, but 20 nm gold particles appear red and exhibit a strong surface plasmon resonance [21, 22]. Similarly, the catalytic activity of a material can increase substantially at the nanoscale due to the increased surface area [23].

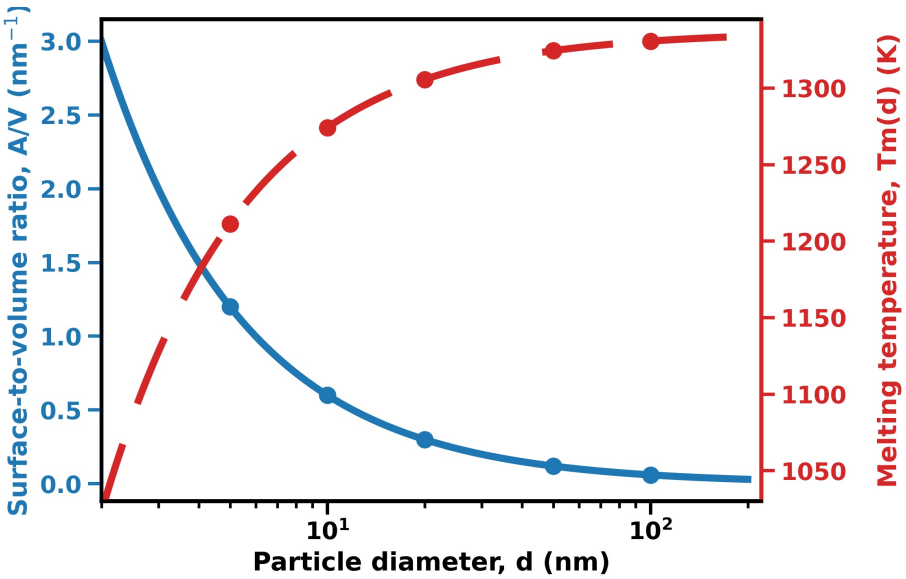


Figure 1.3: Nanoscale surface-to-volume scaling from Eq. (1.1) and illustrative size-dependent melting temperature trend from Eq. (1.3) for spherical Au nanoparticles versus particle diameter d.

Because surface atoms dominate the free energy, nanoparticle stability and functional response in a liquid are set primarily by the chemistry of the outermost atomic layers [15]. In dispersion, bare nanoparticles reduce interfacial free energy by decreasing total surface area through aggregation and, for metallic systems, by coalescence into larger bodies. Colloidal stability is improved by adding molecules that coat the particle surfaces, reduce their tendency to stick together, and create repulsive forces that keep them dispersed, most commonly through electrostatic double layer repulsion from charged surface groups or steric repulsion from an adsorbed polymer layer [24]. In citrate reduction syntheses of gold nanoparticles, adsorbed citrate provides negative surface charge that stabilizes the dispersion when electrostatic repulsion is not screened by high ionic strength, while polymer caps such

as poly(vinylpyrrolidone) provide steric stabilization through an adsorbed layer that resists particle contact [25].

1.2.2 Ultrafast Laser Ablation Mechanisms

On femtosecond to few-picosecond timescales, laser energy is deposited primarily into the electronic subsystem within the optical absorption depth, while the lattice remains comparatively cold. This separation of timescales motivates the two-temperature model (TTM), which treats electrons and lattice as coupled subsystems characterized by an electron temperature $T_e(\mathbf{x}, t)$ and a lattice temperature $T_l(\mathbf{x}, t)$ [26, 27].

In its standard diffusive form for metals, the coupled energy balances are

$$C_e(T_e)\,\frac{\partial T_e}{\partial t} = \nabla \cdot \big(k_e(T_e, T_l)\,\nabla T_e\big) - G(T_e, T_l)\,\big(T_e - T_l\big) + S(\mathbf{x}, t), \tag{1.5}$$

$$C_l(T_l)\,\frac{\partial T_l}{\partial t} = \nabla \cdot \big(k_l(T_l)\,\nabla T_l\big) + G(T_e, T_l)\,\big(T_e - T_l\big), \tag{1.6}$$

where $C_e(T_e)$ is the electron volumetric heat capacity, $C_l(T_l)$ is the lattice volumetric heat capacity, $k_e(T_e, T_l)$ and $k_l(T_l)$ are the electron and lattice thermal conductivities, $G(T_e, T_l)$ is the electron–phonon coupling factor, and $S(\mathbf{x}, t)$ is the volumetric laser energy deposition rate.

A useful diagnostic timescale for electron–phonon equilibration is

$$\tau_{e\text{–}ph} \approx \frac{C_e}{G}, \tag{1.7}$$

which sets how long hot electrons can redistribute energy before the lattice heats appreciably [26].

For a normally incident pulse and a one-dimensional depth coordinate z into the target, a common source term uses Beer Lambert absorption

$$S(z, t) = (1 - R)\,\alpha\, I(t)\, e^{-\alpha z}, \tag{1.8}$$

where R is the surface reflectivity, α is the absorption coefficient, and $I(t)$ is the incident surface intensity. The optical absorption depth is $\delta = 1/\alpha$.

For a Gaussian temporal profile normalized by fluence F,

$$I(t) = \frac{2F}{\sqrt{\pi}\,\tau} \exp\left[-\left(\frac{t}{\tau}\right)^2\right], \tag{1.9}$$

where τ is a pulse-width parameter and

$$F = \int_{-\infty}^{\infty} I(t)\, dt \tag{1.10}$$

is the incident energy per unit area.

In typical ultrashort-pulse excitation of metals, T_e rises rapidly during the pulse and can substantially exceed T_l (Figure 1.4), then relaxes toward T_l on the electron–phonon coupling timescale while electron heat conduction redistributes energy into the near surface region. The resulting spatiotemporal evolution of T_l sets initial conditions for melting, superheating, and subsequent material removal pathways [26, 28].

If the deposited energy is sufficiently high, the laser-heated surface melt can be driven into a deeply superheated, metastable state and relax by *phase explosion* (explosive boiling).[30, 31] In this limit, the lattice temperature exceeds the equilibrium boiling temperature faster than hydrodynamic expansion can relieve pressure, pushing the melt toward the liquid–vapor spinodal where the nucleation barrier collapses.[30, 31] Vapor embryos then form throughout the melt volume by homogeneous nucleation rather than at the surface, and their rapid growth fragments the molten layer into a two-phase ejecta composed of vapor plus liquid droplets.[30, 32] Atomistic simulations show that this fragmentation is not a slow "boiling" process but a collective breakup of a superheated layer on sub-nanosecond to nanosecond timescales once the stability limit is crossed, producing a dense mixture of gas, clusters, and droplets that seeds later nanoparticle populations.[32]

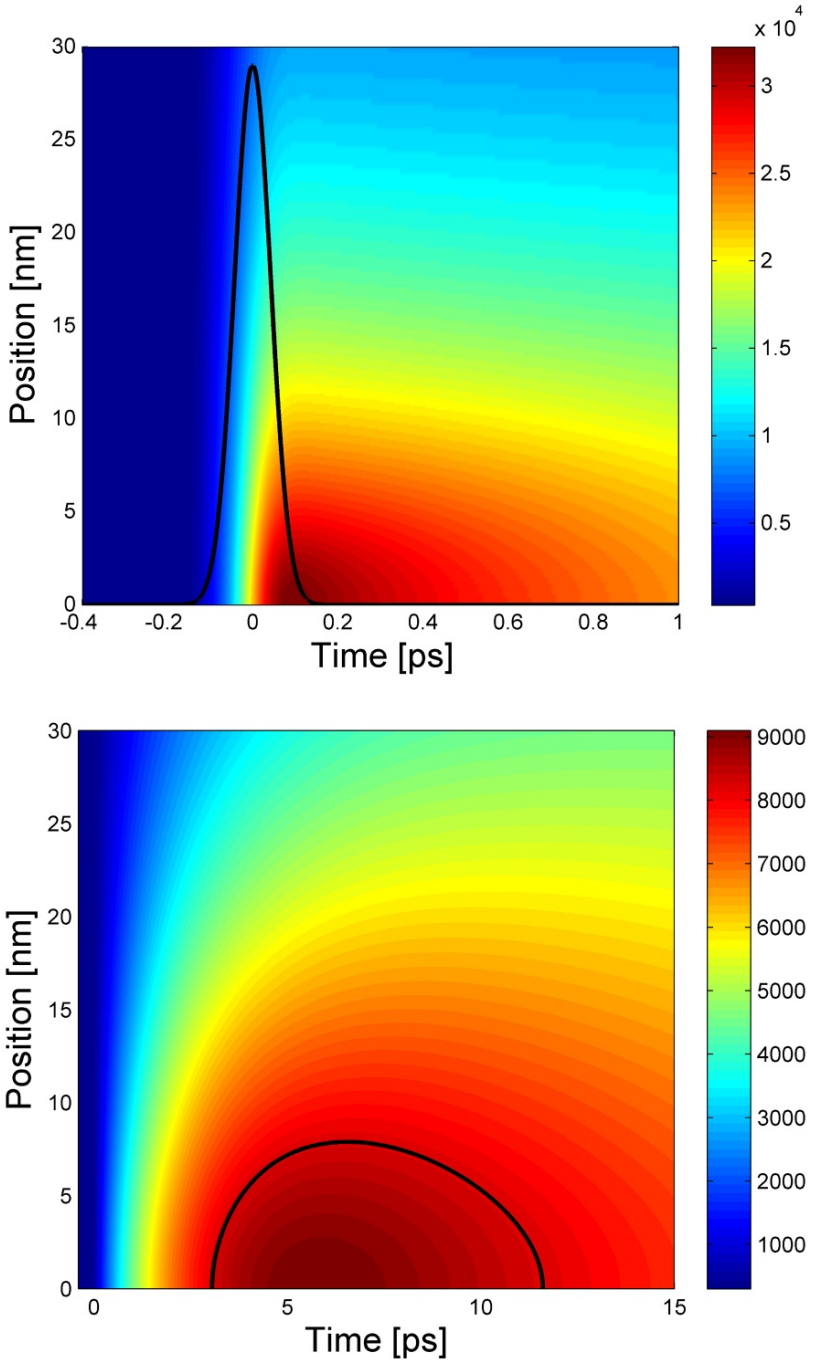


Figure 1.4: Contour plot of electron (top) and lattice temperatures (bottom) for copper, irradiated with a laser pulse of a fluence slightly above ablation threshold (140 mJ cm^{-2}). The solid line in the top figure represents the Gaussian intensity profile of the laser pulse of 100 fs duration. The solid line in the bottom part shows the ablation temperature.

Note. Adapted from [29, 26].

Phase explosion is distinguished experimentally by an abrupt change in the material-removal regime with fluence.[31] Below threshold, mass loss is consistent with surface evaporation and melt ejection, while above threshold the ablated mass and plume optical signature increase sharply in a manner consistent with volumetric vapor nucleation in the superheated melt.[31] For nanosecond excitation of metals this transition commonly occurs at fluences on the order of a few J/cm^2, reflecting the need to superheat a finite melt thickness into the metastable region.[31]

In liquids, the surrounding fluid strongly modifies the fate of this two-phase ejecta through confinement and heat extraction.[33] The rapid expansion of vapor and hot fragments launches a pressure wave and inflates a cavitation bubble that temporarily encloses the ablated material.[33, 34] Within the bubble, the ejecta experiences steep temperature gradients and rapid cooling as it mixes with vaporized solvent and transfers heat across the bubble boundary.[34] As the vapor fraction cools and condenses, supersaturation rises and drives nucleation of clusters, while pre-existing droplets and clusters can grow by condensation and coalescence.[34, 35] Time-resolved scattering experiments resolve the emergence of nanoparticle populations on the bubble timescale and show that particles can exist both inside the bubble volume and in the surrounding liquid after ejection from the bubble interface during expansion and collapse.[34, 35] The resulting colloid therefore reflects two coupled steps: an initial, high-density two-phase ejection produced by phase explosion, followed by confinement-mediated cooling, condensation, and aggregation processes governed by cavitation-bubble dynamics.[34, 35]

Under sufficiently extreme conditions, especially for femtosecond excitation at very high peak intensity, *Coulomb explosion* can contribute to material ejection as a distinct early-time, nonthermal pathway.[36, 37] In this mechanism, the optical field produces rapid near-surface ionization and electron depletion through strong-field processes (multiphoton ionization and tunneling), and the rate of electron removal can temporarily exceed the rate at which charge is replenished by carrier transport.[36, 38]

The irradiated region therefore accumulates a transient net positive charge on sub-picosecond timescales, establishing an outward electrostatic field whose magnitude is set by the evolving charge separation.[38] The resulting Coulomb stress can exceed the material's cohesive strength before significant lattice heating or hydrodynamic expansion occurs, leading to an impulsive disruption of bonding and direct ejection of atomic and ionic fragments from the surface.[39, 40]

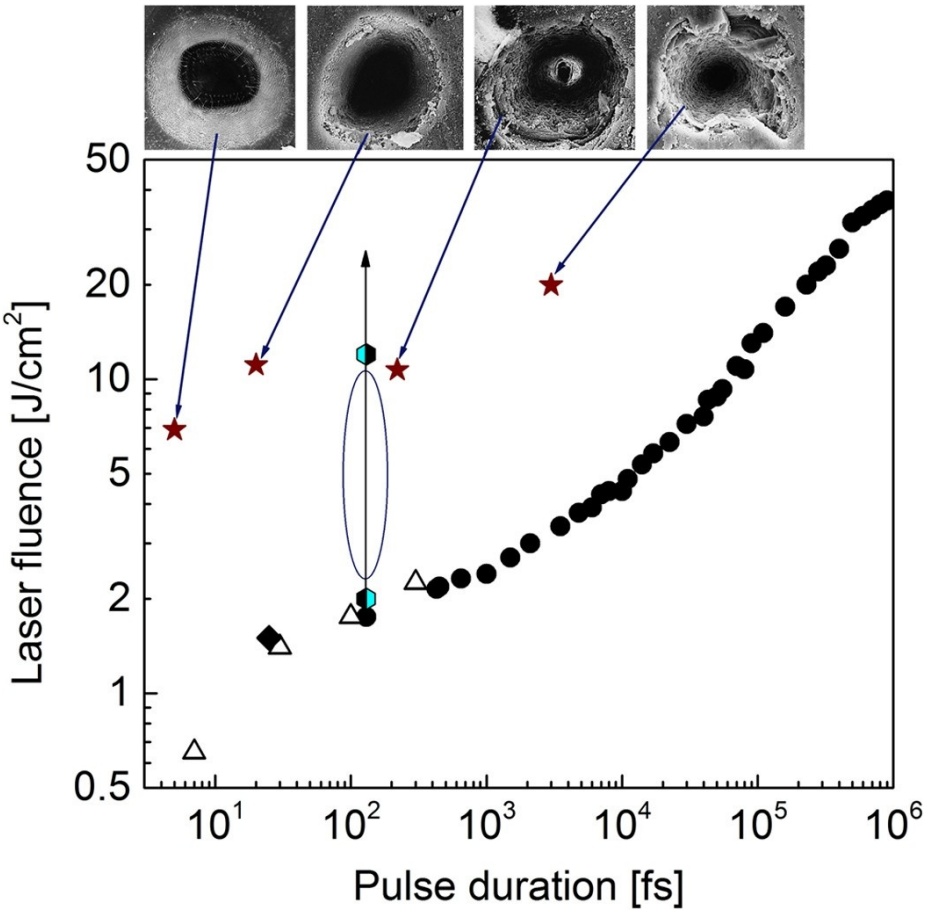


Figure 1.5: Laser ablation and optical breakdown thresholds as a function of pulse duration for fused silica, highlighting how the threshold separation defines the usable processing window and ablation quality from femtosecond to picosecond irradiation.

Note. Figure adapted from [41]. Threshold data compiled from [36, 42, 43, 44].

Because the driving force is electrostatic rather than thermodynamic, Coulomb explosion does not require the lattice to reach melting or boiling conditions and

can operate during the earliest stage of ultrafast irradiation, producing much cleaner ablation since low thermal energy is deposited and the thermal shockwave is minimal (Figure 1.5).[39, 40] It is most pronounced in dielectrics and wide-bandgap materials, where limited carrier density and mobility reduce screening and slow neutralization, allowing large transient fields to develop.[36, 39] In metals, mobile electrons screen charge separation over very short lengths and times, which generally suppresses sustained Coulomb stresses and shifts the dominant removal pathway toward thermally mediated ablation at comparable fluence.[45, 37] Nevertheless, Coulomb-driven ion ejection can still appear in metals in regimes where strong electron emission and nonequilibrium carrier dynamics briefly outpace screening, such as when emitted electrons remain near the surface and reinforce the local field during the pulse.[45, 38] Experimentally, this interpretation is consistent with reports of prompt energetic ion emission and field-driven ejection signatures under femtosecond irradiation conditions.[38, 39]

1.2.3 Laser Induced Nanojoining

Laser induced nanojoining refers to processes that permanently bond nanoscale building blocks, such as particles, wires, and thin films, into larger functional assemblies by converting weak physical contacts into joints with primary chemical bonding. This distinction matters because many nanostructured devices, including transparent conductive networks and nanoscale interconnects, are ultimately limited not by the material properties of the building blocks themselves but by the resistance and mechanical fragility of the contact points between them [46, 16]. Joining those contacts into low-resistance, load-bearing interconnects significantly improves both electrical and mechanical performance while retaining the geometric advantages of a nanoscale architecture [16].

The physical challenge is one of spatial selectivity. The laser must raise the junction temperature high enough to activate mass transport while limiting heat

spread so that the surrounding wires, particles, or films remain unaffected. This balance is governed by the thermal diffusion length during the interaction time τ,

$$\ell_d \approx \sqrt{\chi\,\tau} = \sqrt{\frac{k}{\rho c}\,\tau}, \tag{1.11}$$

which sets how far heat can travel from the absorption site before the pulse ends. To understand why the junction heats preferentially, it helps to write the absorbed volumetric heating rate in terms of a local field enhancement factor $\eta(\mathbf{x})$ that captures geometric concentration of optical energy at asperities, nanogaps, and wire crossings,

$$q'''(\mathbf{x},t) = \eta(\mathbf{x})\,(1-R)\,\alpha\,I(t)\,e^{-\alpha z}. \tag{1.12}$$

The thermal response of the network is then governed by energy conservation under strong geometric confinement,

$$\rho c\,\frac{\partial T}{\partial t} = \nabla\cdot(k\nabla T) + q'''(\mathbf{x},t). \tag{1.13}$$

When ℓ_d is comparable to or smaller than the characteristic junction size, the heated volume stays localized and the heat-affected region does not propagate far along the wire. This is the central reason that short-pulse irradiation can weld nanowire crossings while leaving the rest of the network intact [47]. In ultrafast regimes, the earliest energy deposition can involve electron–lattice nonequilibrium, but the outcome that governs joining is the lattice temperature field that drives melting and diffusion at the interface [16].

Once the junction reaches sufficient temperature, bonding proceeds by either localized melting and resolidification or solid-state sintering through diffusion-driven neck growth. Both pathways share the same thermodynamic driving force: the reduction in total surface free energy as two curved surfaces merge into a lower-curvature neck. The Laplace pressure that drives viscous flow or melt redistribution

scales as

$$\Delta p \sim \gamma \left(\frac{1}{R_1} + \frac{1}{R_2} \right) \sim \frac{\gamma}{x}, \tag{1.14}$$

for a neck of characteristic radius x between features of radius r, and this pressure becomes very large at nanoscale radii. In the solid state, the same capillarity argument governs diffusion, and classical initial-stage sintering kinetics relate neck size to time through a power law,

$$\left(\frac{x}{r} \right)^n = K(T)\, t, \tag{1.15}$$

where the exponent n depends on the dominant transport path and $K(T)$ contains the relevant diffusivity [48, 49]. Because $K(T)$ scales with an Arrhenius diffusivity $D = D_0 \exp(-Q/k_B T)$, even modest increases in junction temperature can accelerate neck growth by orders of magnitude, and surface and interface diffusion are often rate-controlling at nanoscale contacts where surface atom fractions are high [49].

An additional feature that broadens the nanojoining process window is the depression of effective melting and softening temperatures at the junction. The neck region is highly curved and surface-dominated, so in Gibbs-Thomson type descriptions, the solid-liquid equilibrium shifts as surface and interfacial energy become thermodynamically significant at small radii [50]. In practice, this means that local melting and rapid resolidification can occur at lower average energy input than would be needed for a bulk geometry: the process can operate either through a thin interfacial melt layer that freezes into a fused bridge, or through diffusion-driven sintering that forms a crystalline neck without gross melting of the entire building block [16, 49]. The outcome depends on laser fluence and repetition rate, which set the peak junction temperature, and on the cooling rate, which determines how long diffusion and defect annihilation can proceed before the junction freezes.

Experimental demonstrations across several material systems confirm this picture. In silver nanowire networks used as transparent conductive electrodes, Ha and co-workers showed that femtosecond irradiation preferentially welds wire crossings through localized heating near the junction, producing fused contacts while preserving

overall wire morphology and crystallinity, with improved sheet resistance at high optical transmittance [47]. Nanojoining is not limited to improving random overlaps: Lin and co-workers demonstrated in situ joining of spatially separated silver nanowires into designed Y- and T-type junctions using femtosecond pulses, where the joint geometry depended on beam polarization direction and gap size [51]. The approach extends to dissimilar materials as well. Zheng and co-workers reported that nanosecond Nd:YAG irradiation can join silver nanowires to TiO_2 and CuO nanowires by localized photothermal heating combined with photoexcited carrier and plasmon-related effects, forming functional metal-semiconductor heterojunctions [52]. These results show that with appropriate choices of pulse duration, wavelength, polarization, and focusing, laser nanojoining can create a mechanically strong, low-resistance interconnect at a targeted nanoscale contact while leaving the surrounding nanostructure largely unchanged [16]. Representative examples of laser-induced joining of Ag nanowires using these different laser regimes are shown in Figure 1.6.

The diffusion length and neck growth relations together define a straightforward processing criterion. Joining selectivity requires ℓ_d to stay below the characteristic feature size of the network, while successful bonding requires $K(T)\,t$ to be large enough to reach a neck-to-particle ratio that provides the desired electrical and mechanical continuity. Pulsed irradiation satisfies both conditions simultaneously because it can raise the junction to a high peak temperature for a short time while confining heat spread, then rely on rapid cooling to freeze the joint and preserve the rest of the structure.

1.3 Microscale Laser Joining of Metallic Systems

1.3.1 Mechanisms of Microscale Laser Joining

Microscale laser joining uses intense localized heating to melt a very small volume and then rapidly solidify it, forming a metallurgical bond while leaving most of the part

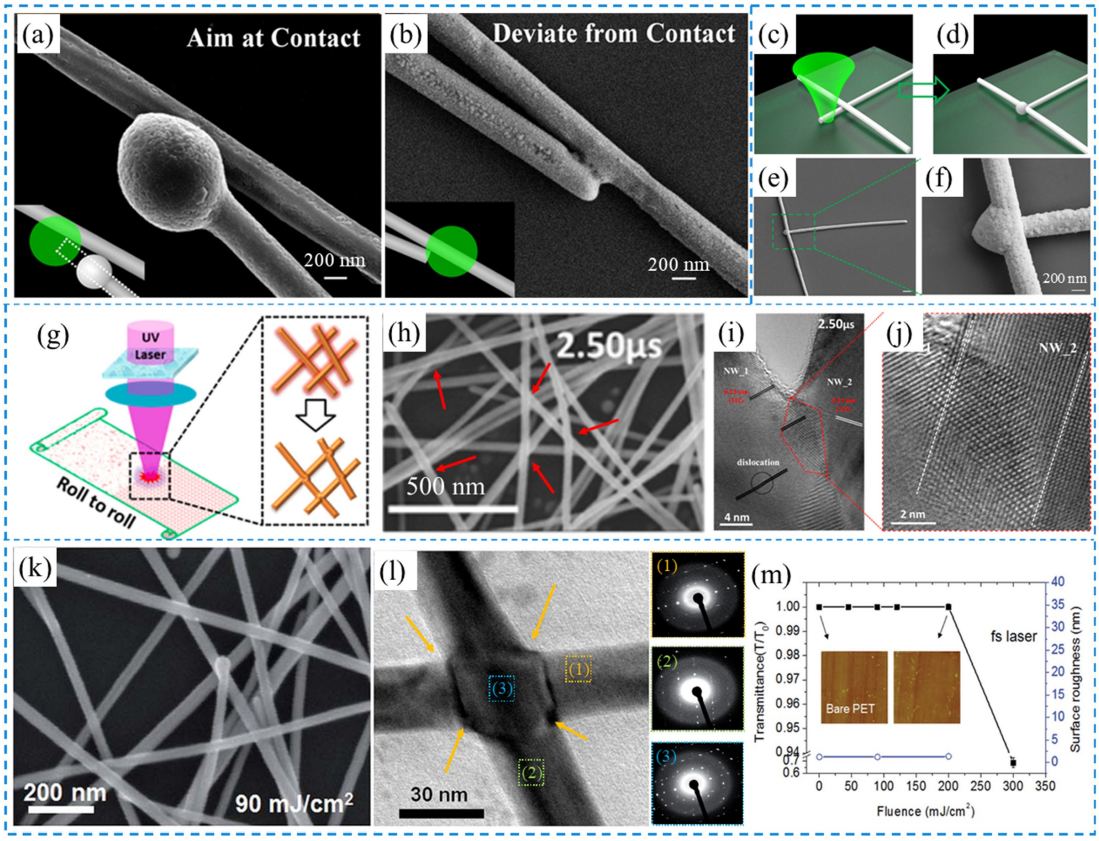


Figure 1.6: Laser-induced joining of Ag nanowires by different types of lasers. (a,b) Focused CW laser, nanowelding of silver nanowire networks for transparent conductive electrodes. (c–f) Focused CW laser, crystalline nanojoining of silver nanowire percolated networks. (g–j) ns laser joining of silver nanowires. (k–m) fs laser single-point nanowelding of silver nanowires.

Note. Adapted from [16]. Panels (a,b) from [47]; panels (c–f) from [53]; panels (g–j) from [54]; panels (k–m) from [17].

relatively cool. A tightly focused beam creates a small melt pool that fuses the mating surfaces with minimal bulk heating. Joint quality is governed by a few core process settings that control melt pool size, shape, and penetration depth. Laser power sets the overall energy delivered and strongly influences how much material melts. Welding speed controls how long the beam interacts with each location. Slower speeds increase local energy input and typically produce deeper penetration and a wider melt pool, while faster speeds reduce energy input and can lead to shallow tracks or incomplete bonding if absorption is insufficient. Spot size controls energy density. A smaller spot concentrates energy and tends to produce deeper, narrower fusion zones, while a larger spot spreads energy and favors wider, shallower melting. These variables work together to determine the operating mode. Lower energy density commonly produces a conduction dominated weld with shallow penetration, while higher energy density can produce keyhole behavior with deeper, narrower penetration.[55] If power is too low or speed is too high, lack of fusion becomes likely. If energy density is excessive, instability, spatter, or porosity can increase. The shielding environment also matters because the melt pool is highly reactive at these temperatures. Inert shielding gas is typically used to limit oxidation and contamination, which otherwise promotes defects and weakens the joint.[56]

1.3.2 Joint Zones: Fusion Zone, HAZ, and Base Material

Laser welds are usually described using three metallurgical regions: the fusion zone (FZ), the heat-affected zone (HAZ), and the base material. The FZ is the material that melts and then resolidifies. It often solidifies with grains that grow outward from the fusion boundary, frequently starting with epitaxial growth from partially melted grains and then developing columnar grains controlled by the local thermal gradient [57, 58]. Next to the FZ is the HAZ. This region does not melt, but the thermal cycle can still change phases, dissolve precipitates, or temper existing microstructures. A

schematic illustration of these three zones and their spatial relationships in a welded joint is shown in Figure 1.7.

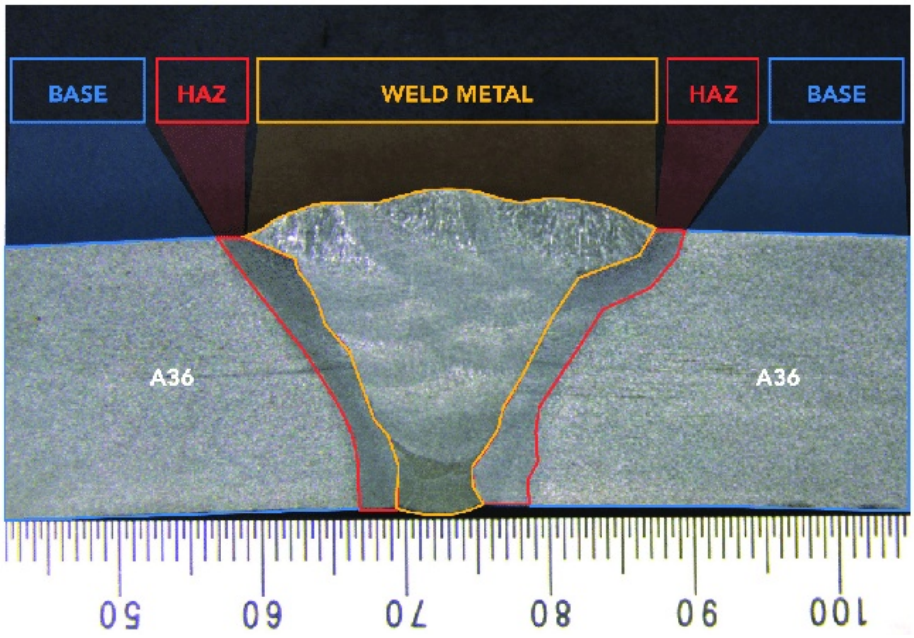


Figure 1.7: The illustration of the welded joint showing the base material, HAZ, and fusion zone (weld metal) regions

Note. Adapted from [59].

In steels, the region closest to the fusion boundary can be heated high enough to fully austenitize and then transform on cooling into hard martensite, while regions farther away may only partially transform or may mainly temper pre existing martensite [60, 61]. This is why welding metallurgy often separates the HAZ into upper critical, intercritical, and subcritical regions, and it is also common to split the upper critical region into coarse grained and fine grained subzones [60]. These microstructural gradients produce mechanical gradients. In many high strength steels, martensite formation in the FZ can produce the highest hardness, while a softer band can appear in the HAZ when prior martensite is tempered or decomposed [61, 62]. In precipitation strengthened aluminum alloys, softening in the FZ and HAZ is often linked to precipitate dissolution, transformation, and coarsening during the weld thermal cycle [63]. Because the laser heat source is highly concentrated, microscale

laser welding can produce a very narrow HAZ along the fusion line, sometimes on the order of tens to a few hundred micrometers depending on thickness and parameters [64, 58].

1.3.3 Metallurgical Phenomena in Dissimilar Laser Joints

Laser joining of dissimilar metals adds challenges because the molten region contains material from both sides of the joint. Mixing produces dilution and a composition transition zone near the fusion boundary, so the local chemistry varies across the weld and the phases that form on solidification can differ from either base metal.[65] In many dissimilar combinations, limited mutual solubility promotes the formation of intermetallic compounds at the interface or within the fusion zone.[66] In aluminum and steel joints, Fe Al intermetallics such as Fe_2Al_5 commonly appear and are very hard and brittle.[67] A continuous intermetallic layer along the interface is usually the most damaging case because it concentrates strain and provides an easy crack path, which strongly reduces ductility and toughness.[66, 68] If intermetallics are discontinuous and finely dispersed, the mechanical penalty can be smaller than for a continuous layer.[66] The usual strategy is to limit intermetallic thickness by minimizing time at high temperature and by controlling where melting occurs. The concentrated heat source and short interaction time in laser welding can help by raising cooling rates and reducing interdiffusion, which tends to suppress intermetallic growth.[66, 69] Practical controls include beam offset toward one side, tailored pulsed energy delivery, and the use of filler or interlayers to shift the local composition away from intermetallic rich ranges.[66, 69]

Despite tight process control, microscale laser welds can still develop porosity, hot cracking, incomplete fusion, and underfill, and the balance between laser settings and alloy behavior largely determines which defect dominates. Porosity forms when gas becomes trapped during solidification. In deep penetration welding, instability or rapid collapse of the keyhole can trap vapor or shielding gas in the melt pool and

freeze it in as pores[70, 71]. Rapid cooling also reduces the time available for dissolved gases to escape, and in aluminum systems hydrogen can dissolve during heating and then be trapped during solidification as gas porosity[72]. These trends get worse with poor surface condition or inadequate shielding because additional contaminants and reaction products increase gas generation and make the melt pool less stable.

Hot cracking, also called solidification cracking, occurs as the weld metal passes through its weak semi-solid range. Shrinkage and thermal contraction impose tensile strain while thin liquid films remain along boundaries in the mushy region, allowing intergranular separation when feeding is insufficient[73]. Risk increases when alloy chemistry produces a wide solidification range or promotes low melting boundary liquid, and when the weld pool shape and solidification pattern reduce liquid backfilling. Parameter choices that increase strain demand or reduce feeding time can therefore promote cracking even in fast cooling laser welds.

Incomplete fusion is a geometric and thermal failure to melt and join the intended interface. It is most often driven by insufficient delivered energy density at the joint or by beam placement errors that miss part of the faying surface. At high travel speeds, the molten region narrows and penetration drops, and the process can transition into lack of fusion or lack of penetration because the parent material does not have time to melt[74]. This sensitivity is amplified in highly conductive alloys such as aluminum and copper because heat is removed quickly, which demands either higher power density, slower travel, or improved coupling. Figure 1.8 illustrates the typical welding defects that can occur in laser beam keyhole welded butt joints, showing how melt pool dynamics and keyhole stability control the formation of these critical flaws.

Underfill reflects a deficit of metal in the final bead profile and is commonly linked to melt loss or melt flow that withdraws material from the crown before freezing. In full penetration keyhole welding, recoil driven flow and keyhole dynamics can drive downward melt flow and direct melt loss that produces underfill and related edge defects[75]. Excessive power density can also increase evaporation and spatter, while poor fit up can create a volume deficit that cannot be replenished without filler.

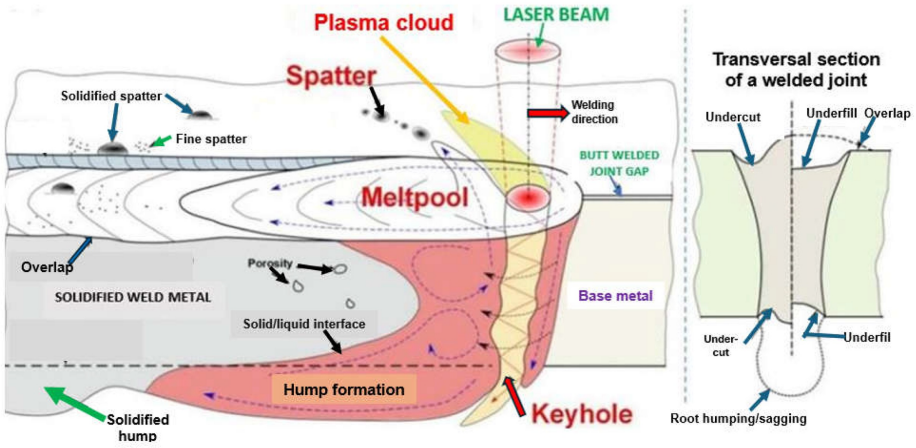


Figure 1.8: The schematic illustration of the typical welding defects of laser beam keyhole welded butt joints.

Note. Adapted from [74].

In practice, defect mitigation is a trade space. Increasing energy density can remove incomplete fusion but may destabilize the keyhole and raise porosity or underfill, while alloys that are crack sensitive often require both parameter control and composition control to keep the semi-solid region resistant to separation.

1.3.4 Solidification Behavior and Joint Integrity

Solidification behavior strongly controls weld soundness and joint performance. One of the most important factors is the freezing range of the fusion zone composition, which can be written as $\Delta T_f = T_L - T_S$ where T_L is the liquidus temperature and T_S is the solidus temperature. Alloys that solidify across a wide temperature interval tend to be more susceptible to solidification cracking because a semi-solid region persists longer during cooling [76, 73]. In this interval, dendrites form and solute partitions into the remaining liquid, so the final liquid becomes enriched and is pushed into thin films along interdendritic and grain boundary regions [76]. These thin liquid films have poor resistance to tensile strain, so weld contraction can open intergranular cracks when feeding is inadequate [76]. In contrast, alloys with a narrow freezing range, or compositions that solidify close to isothermally, reduce the duration and extent of

this vulnerable semi-solid interval and therefore reduce cracking tendency [76]. Figure 1.9 illustrates the solidification cracking susceptibility analysis framework, showing the dendritic growth mechanism in the mushy zone and the T-$(fAl)^{1/2}$ curves that quantify cracking susceptibility across different aluminum alloy compositions.

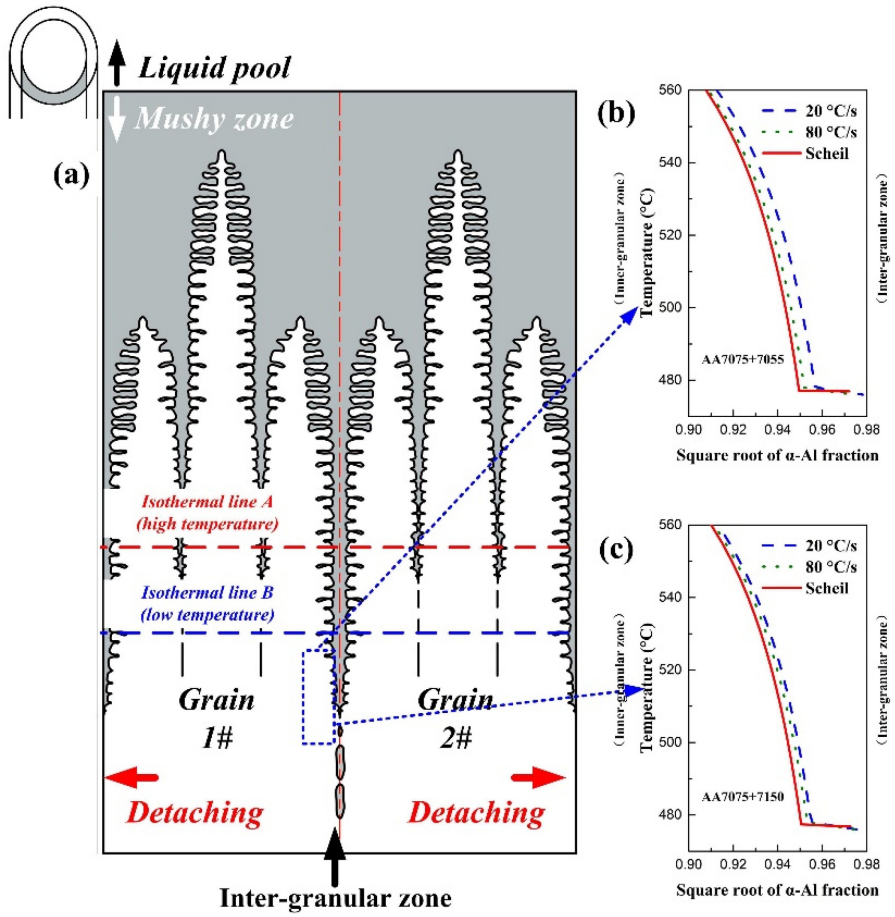


Figure 1.9: Solidification cracking susceptibility analysis: (a) schematic of the dendritic growth within the mushy zone; (b) T-$(fAl)^{1/2}$ curves of AA7075 + 7055 weld; (c) T-$(fAl)^{1/2}$ curves of AA7075 + 7150 weld.

Note. Adapted from [77].

What happens at the end of solidification also matters. The last liquid can solidify into a eutectic or other low melting constituent along boundaries. If this terminal liquid remains sufficiently fluid and well connected, it can feed shrinkage and help close microvoids. If it instead forms a brittle, continuous boundary network, it

can provide an easy crack path even if the phase is hard [76]. This is one reason why composition control is so effective in practice. Near eutectic aluminum silicon compositions, including silicon bearing filler strategies, reduce crack susceptibility by narrowing the freezing range and promoting a terminal eutectic that improves feeding [78, 79].

Joint integrity is not only about cracks and voids. Many structural alloys rely on precipitates or transformation products for strength, and welding thermal cycles can dissolve, coarsen, or transform those strengthening features. In steels with martensitic or multiphase microstructures, subcritical heat-affected zone exposure can temper martensite and produce a local soft zone that may govern failure [80]. In precipitation hardened aluminum alloys, the fusion zone solidifies without the original precipitate state, and the heat-affected zone often experiences precipitate dissolution or overaging, which reduces hardness unless a suitable post weld aging treatment is applied [63, 81]. Rapid solidification can sometimes produce very fine cellular structures and supersaturated solid solutions that raise strength locally, but this benefit is only reliable when the resulting phases remain finely distributed and do not form continuous brittle films. In short, the best joints combine a solidification path that resists cracking with a heat-affected zone response that preserves, or can be restored to, the desired strengthening state through filler selection, parameter control, and post weld heat treatment.

1.3.5 Joint Characterization Descriptors

Microscale laser weld quality is usually reported using a small set of descriptors that connect what formed in the joint to how it carries load. A standard set includes interface morphology, phase constitution, hardness distribution, defect population, and fracture location. These descriptors are complementary. Together they explain what the weld produced, where property gradients exist, and which region controls failure.

Interface morphology describes the geometry and continuity of the bond region and the fusion boundary. In similar material welds it is often reported as the smoothness of the fusion line and whether grains extend across the fusion boundary, which indicates how the melt pool interacted with the surrounding solid. In dissimilar joints, morphology reporting focuses on whether the interface is a sharp chemical boundary or a graded transition and whether any reaction layer is continuous, intermittent, or broken up. A continuous intermetallic reaction layer at a dissimilar interface is widely treated as a critical feature because it is associated with brittle behavior and crack sensitive fracture paths [68]. Cross section microscopy paired with composition mapping is typically used to measure layer thickness, continuity, and local shape features that correlate with fracture initiation.

Phase constitution records which phases exist in each region of the weldment and where they appear. This is typically established using etched metallography combined with diffraction based methods such as X ray diffraction, electron backscatter diffraction, or transmission electron microscopy when phases are fine. Because microscale welds cool quickly, the fusion zone can contain transformation products that differ from the base material. For Ti-6Al-4V laser welds, the as welded fusion zone is commonly reported as predominantly α' martensite due to rapid cooling [82]. In dissimilar welds, phase constitution also includes identifying reaction products at the interface, since these phases can dominate local hardness and fracture mode.

Hardness distribution is commonly reported as a microhardness traverse across the joint from base material through the heat-affected zone into the fusion zone. The profile provides a direct map of mechanical heterogeneity that often mirrors phase and microstructure changes. In laser welded advanced steels such as DP600, hardness commonly peaks in the fusion zone while a local dip can appear in the heat-affected zone due to tempering or microstructural modification [83]. In dissimilar joints, hardness can show a sharp spike at an interfacial reaction layer and then drop into the softer base material, which helps identify the likely weak link before full mechanical testing. Figure 1.10 shows a representative hardness profile overlaid with

the corresponding weld cross section, illustrating how measured hardness variation maps to metallurgical features across the joint.

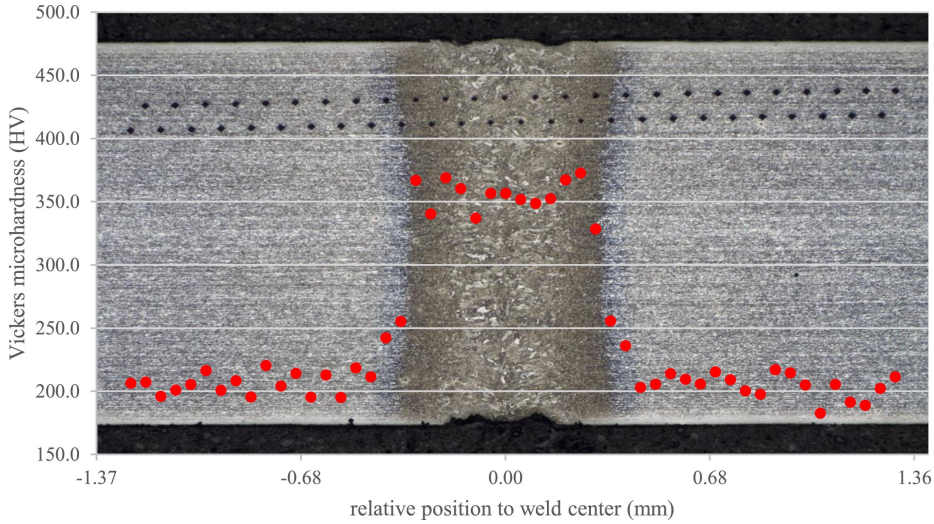


Figure 1.10: Hardness profile of weld, compared to actual weld macrographic image.

Note. Adapted from [83].

Defect population describes the type, size scale, and spatial distribution of internal flaws such as porosity and microcracks. For microscale welds, small pores can be performance limiting because the joint cross section is small, so studies often report pore size distributions and defect density rather than only qualitative observations. X ray micro computed tomography is frequently used to quantify three dimensional pore populations and to report pore size and morphology metrics in laser welds [84]. These defect descriptors are then correlated with parameter changes to distinguish stable processing windows from conditions that generate internal flaws.

Fracture location links the metallurgical state of the joint to performance by reporting where failure occurs during tensile shear, pull, peel, or fatigue testing. If the weld region is not the limiting feature, fracture may move into the base material, while fracture along the interface or within a softened heat-affected zone indicates the controlling weakness. In dissimilar steel aluminum laser welding brazing, shifting the laser spot position can change interfacial microstructure and shift fracture from the interface into the aluminum base material [85]. Reporting fracture location alongside

fractography provides a practical validation that the chosen processing conditions produced a joint whose weakest region is understood and, when possible, moved away from brittle interfacial features.

1.4 Laser Powder Bed Fusion: Macroscopic Laser-Materials Interaction

Laser powder bed fusion (LPBF) is a track based manufacturing process that builds a fully dense metal part by repeatedly melting thin layers of powder with a scanned laser beam. While the nanoscale and microscale topics in this dissertation emphasize localized interactions, laser powder bed fusion highlights how repeated melt tracks and repeated thermal cycles accumulate across a large part. At this scale, the key challenge is that small changes in energy delivery and local boundary conditions can shift the melt pool regime, change defect formation pathways, and alter solidification conditions in ways that strongly affect microstructure and properties. Comprehensive reviews describe laser powder bed fusion as a coupled problem in laser energy coupling, melt pool fluid flow, vapor driven ejection, and rapid solidification, all operating within a powder bed whose thermal and optical properties differ from a solid surface [86, 3].

This section is organized around four connected ideas. First, the process is described in terms of the layer cycle and the geometric controls that set how tracks overlap. Second, parameter sets are reduced to energy metrics and then to normalized process maps that support comparison across materials and machines. Third, melt pool behavior is summarized using the balance between absorbed energy input and heat losses, with emphasis on regime transitions that govern porosity and spatter. Finally, common microstructure and property descriptors are defined in a way that supports later chapters that analyze track based manufacturing data and link it to outcomes.

1.4.1 Process Description and Geometric Controls

In laser powder bed fusion, a thin powder layer is spread across a build plate by a recoater blade or roller. A laser then scans a programmed path across selected regions of the layer, locally melting powder and often partially remelting the previously solidified layer beneath. After solidification, the build platform steps downward by one layer thickness and the sequence repeats until the part is complete [86, 3]. Processing is typically conducted in an inert environment, often argon or nitrogen, to limit oxidation and to reduce the risk of powder ignition. Many systems also use a heated build plate, which reduces thermal gradients and helps stabilize processing for alloys that are crack sensitive [3]. A schematic of the LPBF process is shown in Figure 1.11.

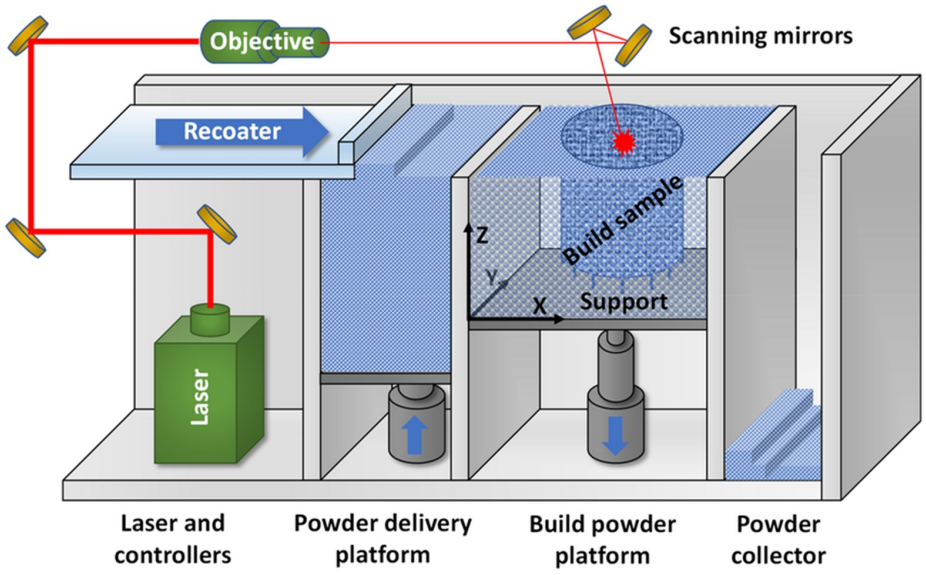


Figure 1.11: Schematic of the LPBF process.

Note. Adapted from [87].

The basic building block of the process is the melt track, sometimes called a scan track or bead. A single pass of the laser forms a melt pool that moves with the beam, solidifies rapidly, and leaves behind a track whose width and depth depend on absorbed power, scan speed, beam size, and the surrounding thermal boundary

conditions [86, 88]. Parts are filled by placing many tracks next to each other within a layer, then repeating for many layers. Because of this repeated overlap, geometric descriptors are essential for connecting process settings to build outcomes.

Within a layer, the key geometric parameters are track width, hatch spacing, and hatch overlap. Track width is the lateral size of a solidified melt track at the top surface. Hatch spacing is the center to center distance between adjacent scan vectors. If hatch spacing is too large relative to track width, unmolten regions remain between tracks, which promotes lack of fusion porosity. If hatch spacing is very small, overlap becomes large and repeated remelting increases local heat accumulation, which can increase distortion and can also increase evaporation and spatter in high power regimes [89, 86]. An intuitive overlap descriptor is an overlap ratio defined by one minus the hatch spacing divided by the track width. This ratio captures how aggressively the process remelts neighboring tracks and is often a strong driver of density and surface finish trends in parameter studies.

Layer thickness sets the vertical step size and controls how much powder must be melted to form a continuous layer. Thicker layers increase build rate, but they also increase the energy needed to fully melt through the powder and to fuse into the prior layer. If layer thickness is increased without adjusting power, speed, or scan strategy, the process can shift toward incomplete melting and lack of fusion defects. Conversely, very thin layers promote better fusion and smoother surfaces, but at the cost of longer build times and more total thermal cycles for a given part height [3]. Systematic studies show that layer thickness interacts strongly with power and speed, which motivates the use of combined metrics rather than any single parameter in isolation [3].

Scan strategy describes how scan vectors are ordered and oriented across the part. Common strategies include long raster scans with rotation between layers, stripe based filling, island based filling, and separate contour scans that define the outer boundary. Scan strategy matters because it sets the local heat accumulation pattern and the direction of solidification relative to the part geometry. Rotating scan

direction between layers can reduce anisotropy in residual stress accumulation, while islands can reduce long scan vectors that otherwise concentrate heat into continuous bands. Recent reviews emphasize that scan strategy is not an auxiliary setting. It can meaningfully change thermal history, residual stress, and defect propensity even at fixed power and speed [90].

1.4.2 Energy Input Metrics and Normalized Process Maps

Laser powder bed fusion is often described using a small set of machine parameters including laser power, scan speed, hatch spacing, layer thickness, and beam size. These parameters are useful for machine operation, but they are not ideal for comparing results across systems because materials differ in absorptivity and thermophysical properties, and machines differ in beam profiles and spot size. For this reason, many studies use energy input metrics that combine parameters into effective measures of how much energy is delivered per unit length, area, or volume [86, 3].

A common starting point is line energy, defined as laser power divided by scan speed. Line energy is a convenient proxy for how much energy is available to form a track, and it often correlates with track width and penetration in a fixed material and machine setting. Extending this idea, an areal energy metric divides power by the product of scan speed and hatch spacing, which is the energy delivered per unit area of a layer. A volumetric energy density divides power by scan speed, hatch spacing, and layer thickness, which is the energy delivered per unit volume of the built material. These metrics are often used to produce simple process maps that classify regimes of low density, high density, and instability [3].

Energy metrics are helpful, but they also have important limitations. Volumetric energy density assumes that energy deposition scales only with the nominal input variables and that all delivered energy is effectively absorbed and used to melt a target volume. In practice, absorptivity changes with temperature, surface state, and melt pool regime. Beam size and beam profile change the spatial distribution

of intensity. Scan strategy changes local heat accumulation and remelting. Powder properties such as packing density and particle size distribution change both optical absorption and thermal conduction. A careful analysis by Scipioni Bertoli and co workers showed that volumetric energy density can collapse some trends but can also obscure regime changes and can mislead parameter transfer when beam size or absorptivity differs [91].

To improve transferability, several authors have developed normalized process maps that are based on heat transfer scaling and that use dimensionless groups. These maps aim to separate regimes such as lack of fusion, stable conduction melting, and keyhole melting using variables that incorporate both process settings and material properties. An advantage is that two experiments with different spot sizes or different materials can still be compared within the same normalized framework if the relevant properties are known [92, 93].

One widely used approach starts from an analytical heat conduction solution for a moving Gaussian heat source and defines a normalized power and a normalized velocity. In this framework, the normalized velocity v^* is defined as the scan speed multiplied by beam radius and divided by two times the thermal diffusivity. The normalized power q^* is defined as absorptivity times laser power divided by 2π times thermal conductivity times melting temperature times beam radius [92]. These definitions embed key material properties and explicitly include beam size, so the resulting map is less sensitive to differences in optics and conductivity than a raw volumetric energy density. Normalised processing diagrams constructed in q^* and v^* space have been used to predict melt pool dimensions and to define boundaries between stable melting and defect prone regimes [92, 93].

Recent work extends this idea by combining normalized heat transfer with defect criteria that are grounded in melt pool geometry. For example, predictive process diagrams use analytical estimates of melt pool width and depth to assess whether adjacent tracks will overlap sufficiently, whether the melt pool will penetrate into the prior layer, and whether conditions approach keyhole formation [94]. These maps are

especially useful in early parameter selection because they allow an initial estimate of processing windows before extensive trial builds. In this dissertation, normalized maps provide a consistent way to discuss track based process regimes alongside nanoscale and microscale topics that also rely on energy delivery and boundary condition control.

1.4.3 Melt Pool Physics and Rapid Solidification

The melt pool in laser powder bed fusion forms when absorbed laser energy raises the local temperature above the melting point and supplies enough latent heat to sustain a liquid region that moves with the beam. Melt pool geometry and stability follow from a balance between absorbed power input and heat losses, with the dominant losses being conduction into the underlying solid and into the surrounding powder, plus smaller contributions from convection and radiation at the free surface [86, 3]. Because the powder bed has lower effective thermal conductivity than a dense solid, heat is more confined near the surface and melt pools can become deeper for the same nominal settings when compared with scanning on a solid plate [86].

As power density increases or scan speed decreases, the melt pool can transition from conduction melting to keyhole melting. In conduction melting, the free surface remains relatively flat and absorption is dominated by surface absorptivity. In keyhole melting, intense local heating produces significant vaporization and recoil pressure, which depresses the free surface and forms a vapor cavity. Multiple reflections inside this cavity increase effective absorption and can create deeper penetration at the cost of greater instability [86, 95]. High speed imaging and synchrotron studies show that keyhole dynamics are a primary driver of pore formation through collapse of the vapor cavity, which can trap gas and produce nearly spherical pores [88, 96].

Powder bed fusion adds additional complexity because vapor driven flow can entrain and eject powder. Metal vapor can form a jet that drives a local gas flow above the melt pool. This flow can strip powder away from regions around the

scan track, creating a denuded zone that changes local powder availability and alters energy coupling in subsequent passes [92]. Spatter and powder ejection can also land elsewhere in the bed, creating local surface roughness and increasing the chance of lack of fusion in later layers [92, 86]. These mechanisms connect melt pool physics to both near term track quality and longer term build reliability.

Melt pool fluid flow further shapes track geometry and surface state. Surface tension gradients drive Marangoni flow, which redistributes liquid metal within the pool. Recoil pressure from evaporation pushes liquid outward from the hottest region and can deepen the pool in keyhole regimes. These flows interact with capillary forces at the rim of the pool and can lead to instabilities such as balling when conditions produce a thin unstable track. Balling is often associated with high scan speed, low wetting, or insufficient track width relative to the capillary stability length, and it can degrade both density and surface finish [3].

Once the laser passes, the melt pool solidifies under high thermal gradients and high solidification velocities. Rapid solidification is often described using two local descriptors. The thermal gradient describes how quickly temperature changes with distance ahead of the solidification front. The solidification rate describes how quickly the solid liquid interface advances. The product of these terms is the cooling rate, which strongly influences microstructural scale. High cooling rates produce fine cellular or dendritic structures and can trap solute in supersaturated solid solutions, while lower cooling rates allow coarser features and stronger segregation [3]. The effect of temperature gradient G and growth rate R on the morphology and size of solidification microstructure is shown in Figure 1.12.

These solidification conditions often produce strong texture and anisotropy because grains can grow epitaxially from the underlying solid and align with the direction of maximum heat flow. In many alloys, grains grow upward through multiple layers because the melt pool partially remelts the top of the prior layer, providing a favorable template for epitaxial growth. Classic studies of titanium alloy parts produced by selective laser melting show columnar prior beta grains aligned with the

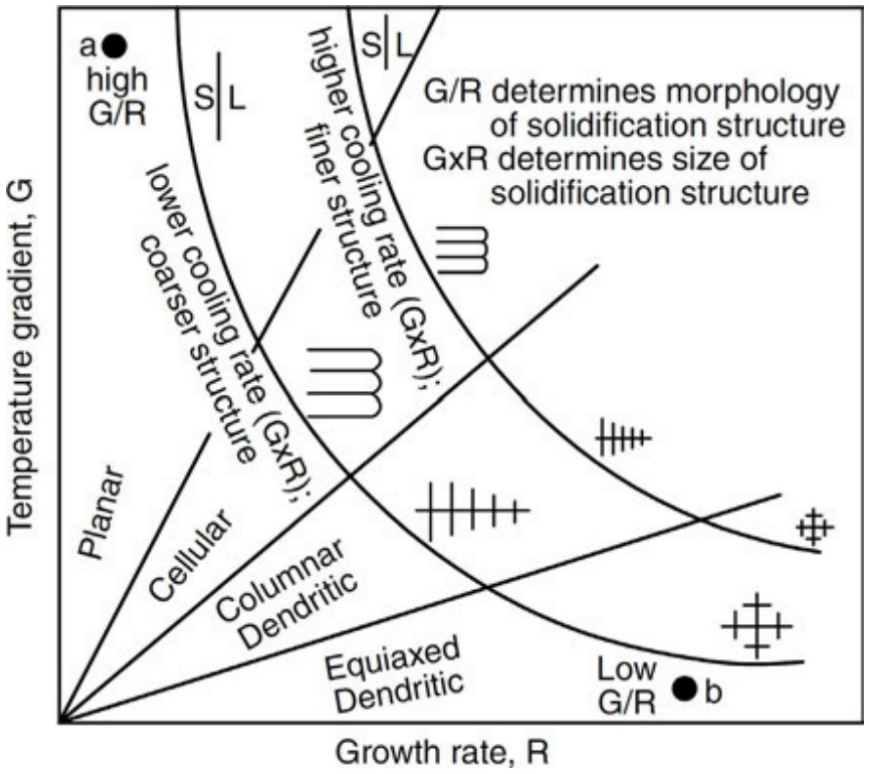


Figure 1.12: Effect of temperature gradient G and growth rate R on the morphology and size of solidification microstructure.

Note. Adapted from [97, 3].

build direction and a fine transformed microstructure within these grains, reflecting the combination of steep gradients and repeated thermal cycling [98]. Heat treatment studies show that post build thermal exposure can coarsen or transform these features, which provides a pathway to tailor microstructure after fabrication when needed [99].

1.4.4 Microstructure and Property Descriptors for Laser Powder Bed Fusion

Macro scale laser powder bed fusion studies typically report a set of descriptors that connect process conditions to part quality. These descriptors are selected because they are measurable across many alloys and because they capture the main failure modes

of the process. In this dissertation, the most important categories are microstructure descriptors that describe what solidified, defect descriptors that describe what did not consolidate, and property metrics that describe performance relevant outcomes.

Grain morphology and texture are primary microstructure descriptors. Grain morphology includes the fraction of columnar versus equiaxed grains and the characteristic grain size. Texture describes the preferred crystallographic orientation that develops during directional solidification. Both are governed by the local thermal gradient and the solidification rate, so they are sensitive to scan strategy, part geometry, and build plate preheat in addition to power and speed [3]. Phase constitution is also critical for alloys that undergo solid state transformations. For titanium alloys, rapid cooling can produce martensitic α' while slower cooling or subsequent thermal cycling can decompose this martensite into $\alpha + \beta$. For precipitation hardened alloys, the thermal history can alter precipitate state even if the primary solidification structure is similar [98, 100, 3].

Defect population is often summarized by relative density and by defect type. Relative density is the fraction of the part volume that is solid rather than pore. It can be measured by Archimedes methods, by polished cross section image analysis, or by three dimensional X ray micro computed tomography. Micro computed tomography is particularly valuable because it can quantify pore size distributions and spatial clustering without destroying the part, which supports correlation between defect populations and local process conditions [84].

Defect type matters because different pores form by different mechanisms and have different implications for processing and performance. Lack of fusion pores are often irregular and are associated with insufficient overlap between tracks or insufficient penetration into the prior layer. Keyhole pores are often more rounded and are associated with unstable vapor cavity collapse during high power density melting [96, 88]. Gas pores can also be present due to entrapped gas in the powder or due to dissolved gas in the melt that is trapped during rapid solidification. Cracking is another defect class that can arise from high thermal stress, from solidification

cracking in susceptible alloys, or from liquation along grain boundaries during thermal cycling [3].

An example of pore population sensitivity to process conditions is shown in Figure 1.13, where different beam diameters and scan speeds lead to large shifts in pore density for AlSi10Mg.

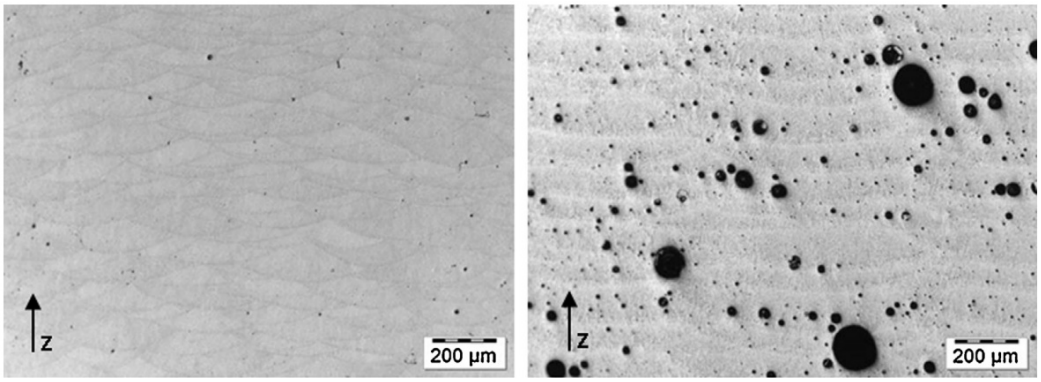


Figure 1.13: AlSi10Mg deposited by LPBF with laser beam diameter = 0.3 mm, velocity 2250 mm/s resulting in a deposit pore density of 0.4% (left) and laser beam diameter = 1 mm, velocity 250 mm/s resulting in a deposit pore density of 9.2% (right).

Note. Adapted from [101, 3].

Two property metrics are commonly used as first order indicators of part performance. Density is a property metric because it strongly correlates with fatigue life and tensile ductility and because porosity is a dominant processing limitation in many alloys [3]. Hardness is a second widely reported metric because it is sensitive to microstructural scale and phase constitution and can be mapped spatially across a build. Hardness trends often reflect changes in cooling rate and phase transformation state and can therefore provide indirect evidence of local thermal history. Parameter studies frequently report hardness alongside density because an optimal window often requires both high density and a microstructure state that supports the desired strength and toughness balance [3].

The process descriptors and outcome metrics in this section support the same guiding logic that connects the other scales in this dissertation. Process inputs

define energy delivery in space and time. That energy delivery, combined with boundary conditions, sets melt pool regime and thermal history. The thermal history sets microstructure, surface state, and defect populations. Those outcomes set performance relevant properties. This framework will be revisited in later chapters that analyze track based data and relate it to microstructure and property control.

1.5 Materials Background

This section introduces two recurring materials topics that are used throughout later chapters. The first is the fundamentals of high-entropy alloys as a design space and as a phase selection problem. The second is how laser ablation in liquids can transform a bulk high-entropy alloy into nanoparticle populations while imposing strong nonequilibrium chemistry at the particle surface.

1.5.1 High-entropy alloys

High-entropy alloys (HEAs) are metallic alloys intentionally built from several major elements rather than one base element. Each element is present at a substantial fraction, so the alloy is not a dilute solid solution. This design approach opens a very large composition space and enables combinations of strength, toughness, corrosion resistance, and thermal stability that are difficult to reach by traditional alloy development that starts from a single dominant element [102, 103, 104]. Early work established that multi-element, near-equiatomic compositions can form relatively simple crystal structures rather than always forming many brittle compounds [102, 103]. Most HEAs still have typical metal structures, shown in Figure 1.14.

High-entropy alloys are often introduced through four commonly cited characteristics. First, the *high-entropy effect* suggests that the large configurational entropy of multi-principal-element mixtures can favor chemically disordered solid solutions over ordered intermetallic compounds at elevated temperature. Second,

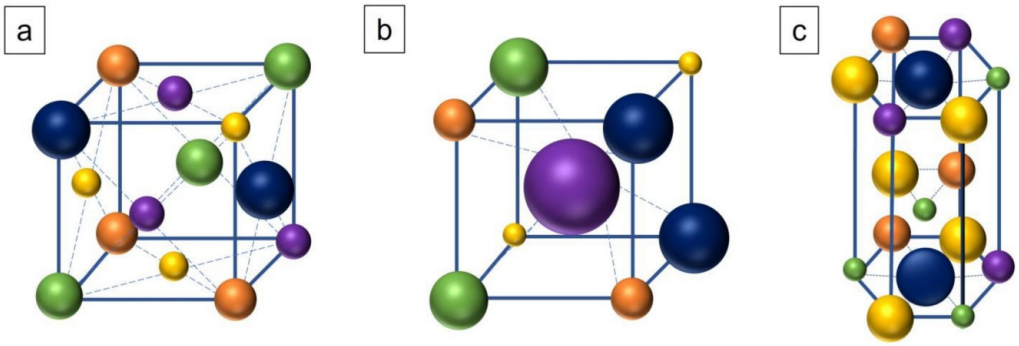


Figure 1.14: Illustrations showing the lattice structure of (a) FCC, (b) BCC, and (c) hexagonal close-packed HEAs. Each color represents a different element.

Note. Adapted from [105].

severe lattice distortion arises because atoms with different sizes and bonding environments share the same crystal lattice, producing local strain fields that can strengthen the alloy by resisting dislocation motion. Third, *sluggish diffusion* is the idea that chemical complexity can reduce average diffusion rates, which can slow coarsening and phase separation during thermal exposure. Fourth, the *cocktail effect* describes how combining several elements can yield properties that are not a simple rule of mixtures, enabling unexpected combinations such as high strength with good toughness or corrosion resistance. These ideas are helpful as an organizing framework, but they are not universal laws, and the observed phases and properties still depend strongly on composition and processing history [106, 107, 104].

A key idea in HEAs is that chemical complexity can sometimes promote the formation of disordered solid solutions such as face-centered cubic (FCC) or body-centered cubic (BCC) phases [108, 106, 107]. The physical picture is a competition between the enthalpy that favors chemical ordering or compound formation and the entropy that favors disorder, together with kinetics that may prevent equilibrium partitioning during cooling [107, 108]. Because the balance depends on composition and processing route, the so-called core effects of HEAs should be treated as tendencies rather than universal rules [106, 107, 104].

For practical design, phase selection is often screened with simple descriptors derived from the constituent elements. Common examples include atomic size mismatch and the related δ metric, mixing enthalpy and mixing entropy combined in the Ω metric, and valence electron concentration, which correlates with whether face-centered cubic or body-centered cubic solid solutions are favored [109, 110, 108]. These metrics are useful for narrowing candidates, but they do not replace experimental validation because short-range order, segregation, and process-dependent nonequilibrium effects can shift phase stability and properties [107, 108, 104].

Mechanically, HEAs can be strong because local chemical variations distort the lattice and impede dislocation motion, which is a generalized form of solid solution strengthening [111]. In some compositions, high strength can coexist with high ductility and toughness due to sustained strain hardening mechanisms such as stacking fault formation and deformation twinning [112, 104]. These features make HEAs a useful platform for laser-based processing studies where rapid heating and rapid cooling can stabilize metastable structures and refine microstructure [108, 107].

1.5.2 High-entropy alloy laser ablation in liquid

Laser ablation in liquid, often implemented as pulsed laser ablation in liquids, is a synthesis route where a focused laser pulse strikes a solid target immersed in a liquid and ejects material that rapidly cools to form a colloid of nanoparticles [113, 114, 11]. The process is commonly described in three coupled steps: energy deposition creates a hot, dense plume at the target surface; the plume expands into the surrounding liquid and drives a cavitation bubble; then rapid quenching inside and around the bubble produces nuclei that grow into nanoparticles, with additional growth and reshaping possible during subsequent pulses [114, 11, 115]. A qualitative schematic of this sequence is shown in Figure 1.15.

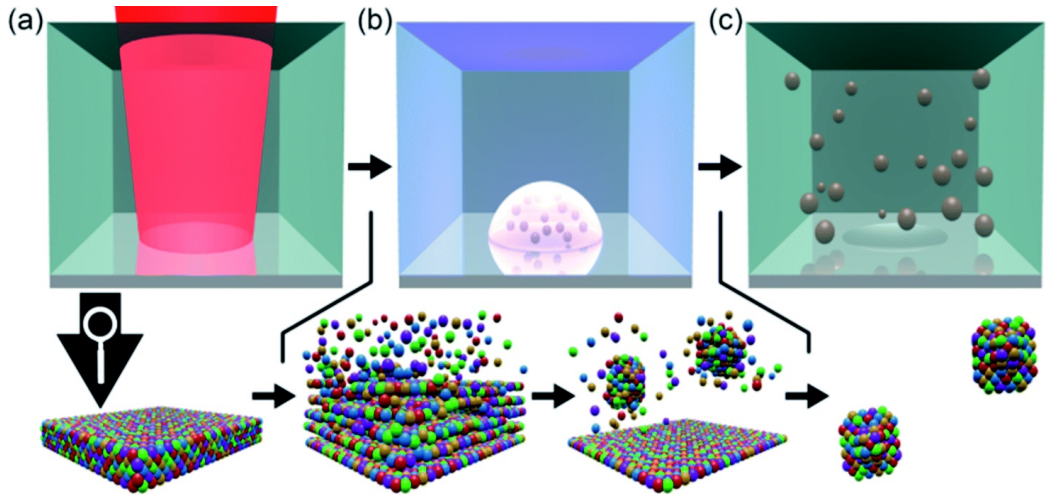


Figure 1.15: Qualitative representation of the laser-based synthesis of high-entropy alloy nanoparticles. The synthesis method consisted of the following stages: ultrashort-pulsed laser irradiation of the bulk HEA (a), the atomization/ionization of the bulk causing the formation of a plume, and subsequent nucleation and condensation of the ablated matter in the vapor phase of the liquid (b) and the colloidal high-entropy alloy nanoparticles electrostatically stabilized in ethanol (c).

Note. Adapted from [116].

Compared with many wet chemical syntheses, laser ablation in liquid can generate nanoparticles without added reducing agents or stabilizers, which is attractive when clean surfaces are needed for surface-sensitive spectroscopy or catalytic studies [11]. The liquid is not a passive coolant. It controls heat removal, bubble dynamics, and interfacial reactions that set particle size, size distribution, and surface chemistry [114, 11]. For example, water and oxygen-containing environments often promote oxide shell formation, while organic solvents can introduce carbon-containing surface species and alter reduction conditions, which can change optical response, colloidal stability, and apparent composition in surface-sensitive measurements [114, 11].

Applying this method to HEA targets provides a route to high-entropy alloy nanoparticles under extreme thermal gradients and quench rates that are difficult to reach in bulk processing [116, 117, 118]. The central challenge is compositional fidelity. Even if the bulk target is equiatomic, preferential ablation, preferential evaporation, and selective oxidation can bias the nanoparticle composition, especially for elements

with very different vapor pressures or oxygen affinity [114, 116, 118]. Recent studies show that both the laser conditions and the target preparation can strongly influence stoichiometry and productivity, highlighting that HEA nanoparticle synthesis is not only a materials problem but also a process control problem [116, 118, 119]. In addition, the surrounding liquid can affect phase outcome and the degree of surface oxidation in HEA nanoparticles synthesized by ultrashort-pulse ablation [117].

For this dissertation, HEA laser ablation in liquid is a useful materials module because it combines multi-element phase selection with rapid solidification and a tunable local chemical environment. It offers an experimentally accessible way to study how laser-driven thermal histories and surrounding media influence phase formation, segregation, and surface chemistry in complex alloys [107, 120, 116].

1.5.3 Al–Ce–Ni–Mn–Zr Near-Eutectic (DuAlumin-3D-type) High-Temperature Aluminum Alloys

Designing aluminum alloys that retain strength and dimensional stability at 300–400 °C is intrinsically difficult, and the constraints are significantly amplified in laser powder bed fusion. Most commercial high-strength Al alloys rely on metastable, coherent precipitates formed by solid-state aging, such as θ' (Al-Cu) or η' (Al-Zn-Mg). Above ∼200–250 °C, these precipitate populations coarsen rapidly or dissolve, producing a steep loss in strength and a corresponding rise in creep rate. This limitation persists even when LPBF refines grains, as grain-boundary-mediated deformation becomes increasingly competitive at elevated homologous temperatures. The LPBF thermal history also introduces microstructural heterogeneity across melt pools and layers, characterized by spatially varying cooling rates, remelting, and cyclic reheating, that produces nonuniform phase fractions and solute segregation. These coupled challenges motivate alloy concepts that are not primarily precipitation-hardened, but instead possess stable strengthening architectures formed during solidification and retained during service [121, 122].

The Al–Ce Eutectic Strategy and Early Progression

Al–Ce eutectic and intermetallic architectures offer a practical route to elevated-temperature stability because Ce has negligible solid solubility (< 0.05 wt.%) and slow diffusivity in α-Al. This enables the formation of intermetallic phases that are comparatively resistant to coarsening at temperatures where conventional precipitates rapidly degrade. In near-eutectic Al–Ce alloys, strengthening arises from a significant volume fraction of intermetallic, classically $Al_{11}Ce_3$ in binary compositions, distributed as a eutectic constituent rather than a low-volume-fraction precipitate population. The conceptual advantage is twofold: the reinforcing phase fraction is set by the liquid-state solubility rather than solid-state solubility limits, and LPBF provides rapid solidification that refines eutectic length scales to sub-100 nm interphase spacings. Early work on cast Al–Ce systems established that these alloys can retain properties after prolonged thermal exposure, a characteristic described as "ageless" behavior, positioning Al–Ce as a high-temperature platform rather than a conventional age-hardening system [123, 124, 125].

Translating this concept to additive manufacturing required demonstrating that the eutectic-strengthened microstructure could survive the LPBF thermal cycle. Binary Al–Ce alloys proved processable, but they provide only a modest intermetallic volume fraction ($\sim$10 vol.% for Al–10Ce), which limits the maximum attainable yield strength. This motivated the progression to multicomponent systems. The introduction of Manganese (Mn) in Al–10Ce–8Mn alloys highlighted a design tension: increasing the intermetallic fraction and complexity can enhance high-temperature strength but often reduces room-temperature ductility and increases cracking susceptibility [126].

The transition to Al–Ce–Ni–Mn compositions represented a more targeted eutectic design. Ni-containing Al eutectics are known for high-temperature constituents, and in Al–Ce-based systems, Ni additions shift the eutectic point to substantially higher reinforcing phase fractions ($\sim$35 vol.%). While these alloys exhibited high creep

resistance at 300–400 °C, they revealed an LPBF-specific limitation: the solute-rich design required an aggressive stress-relief heat treatment (e.g., 450 °C for 2 h) to prevent solid-state cracking upon removal from the build plate. This treatment, however, coarsened the as-fabricated solidification microstructure, degrading the nanoscale length scales that enable peak creep resistance [127, 122].

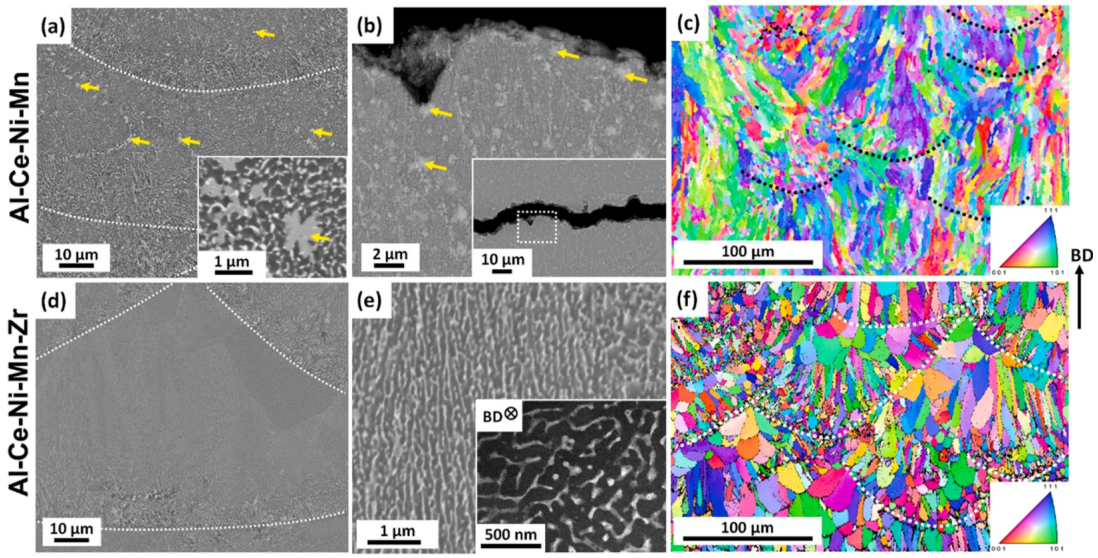


Figure 1.16: Microstructure of as-fabricated (a-b) Al-Ce-Ni-Mn and (d-e) Al-Ce-Ni-Mn-Zr alloys. Backscattered-electron scanning electron microscopy (BSE-SEM) images at (a) lower magnification with a higher magnification inset showing Mn-rich, rosette-shaped intermetallic particles (marked with yellow arrows, confirmed by the energy-dispersive X-ray spectroscopy (EDS) map in Figure S1) and (b) shows a crack in the alloy (lower magnification image in the inset) formed after removal from the build plate which is associated with Mn-rich rosettes. (c) Inverse pole figure (IPF) map of the stress-relived (HT450) Al-Ce-Ni-Mn alloy, showing columnar grain structure in the alloy. BSE-SEM images at (d) lower magnification and (e) higher magnification (at the melt pool center) show the eutectic structure and (f) IPF map shows equiaxed grain structure in the as-fabricated Al-Ce-Ni-Mn-Zr alloy. The inset in (e) is a high-angle annular dark-field (HAADF)-STEM image of the eutectic solidification microstructure. The curved dotted lines in (a), (c), (d) and (f) mark the melt pool boundaries. BD indicates the build direction.

Note. Adapted from [122].

The Near-Eutectic Al–Ce–Ni–Mn–Zr (DuAlumin-3D) Lineage

Addressing the trade-off between printability and microstructural refinement required mechanistic clarity on phase selection, particularly the role of Mn. Dedicated phase-equilibria studies showed that small levels of Mn substituting for Ni shift the Al-rich corner of the liquidus projection, suppressing eutectic Al_3Ni in favor of more coarsening-resistant phases like $Al_{23}Ni_6(Ce,Mn)_4$ and $Al_{20}Mn_2Ce$ [128]. This provided the thermodynamic basis for using Mn to steer phase constitution without necessarily increasing the brittle phase fraction to the point of cracking.

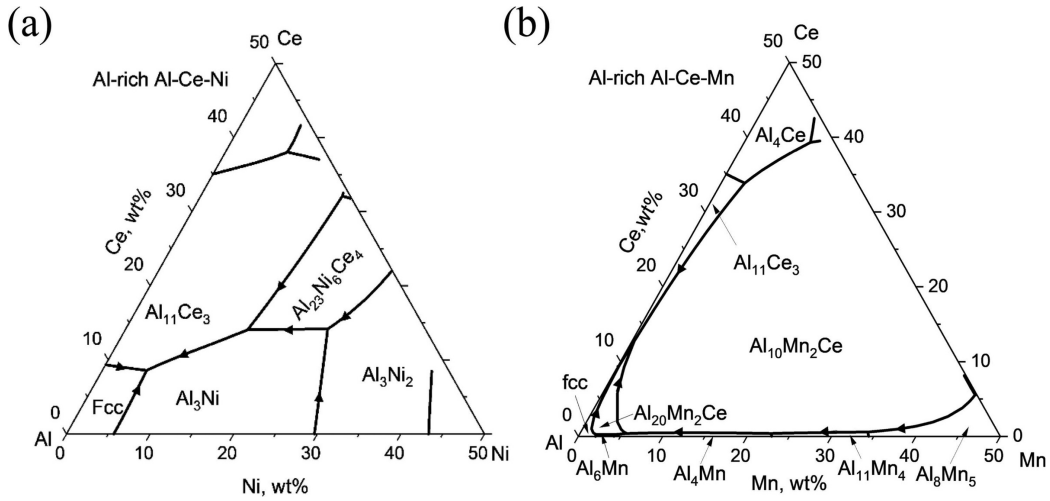


Figure 1.17: (a) Liquidus projection of the Al-Ce-Ni alloy system. (b) Liquidus projection of the Al-Ce-Mn alloy system.

Note. Data from [128].

The near-eutectic Al–Ce–Ni–Mn–Zr (DuAlumin-3D-type) alloys represent the current state-of-the-art in this lineage. By adjusting the Ce/Ni ratios and adding Zirconium (Zr), researchers achieved crack-free LPBF processing without the need for high-temperature stress relief. Zr serves a dual purpose: it improves processability through grain refinement and hot-tearing resistance, and it introduces a secondary strengthening channel via nanoscale $L1_2$-Al_3Zr precipitation. This hierarchical microstructure, consisting of fine α-Al grains decorated by a rigid, sub-100 nm

eutectic network and internally strengthened by coherent nanoprecipitates, retains the ultrafine length scales required for maximum performance [122].

Mechanistically, the strongest evidence for creep resistance in this family points to dislocation obstruction by the eutectic-derived second phase. In-situ neutron diffraction during creep has provided direct evidence of load transfer from the soft Al matrix to the rigid intermetallic skeleton. However, recent work suggests a microstructure-dependent mechanism map: at 300–400 °C, the rate-limiting mechanism is proposed to be Orowan looping when a continuous second-phase network is present, and dislocation climb when the second phase fragments into fine dispersoids. This distinction matters because it ties the creep rate not only to phase stability but also to the connectivity of the reinforcing phase, a feature directly controlled by LPBF parameters and post-processing [122, 127].

Limitations remain in ductility and reliability. Solute-rich eutectic microstructures are less damage-tolerant than conventional Al alloys. In the Al–Ce–Ni–Mn system, elevated-temperature fatigue studies show that once pore populations are refined, oxide inclusions become the dominant crack initiation sites, indicating that powder handling and atmosphere control are as critical as alloy chemistry [129]. Creep ductility is also governed by cavitation. Recent investigations into Al–Ce–Ni–Mn–Zr alloys identified constrained diffusional cavity growth with continuous cavity nucleation as the primary failure mode. This makes the creep ductility highly sensitive to local microstructural rate variations and melt-pool-scale heterogeneities [130]. Consequently, the research gap has shifted from basic phase stability toward managing defect-driven failures and understanding how the hierarchical architecture can be toughened without sacrificing its high-temperature strength.

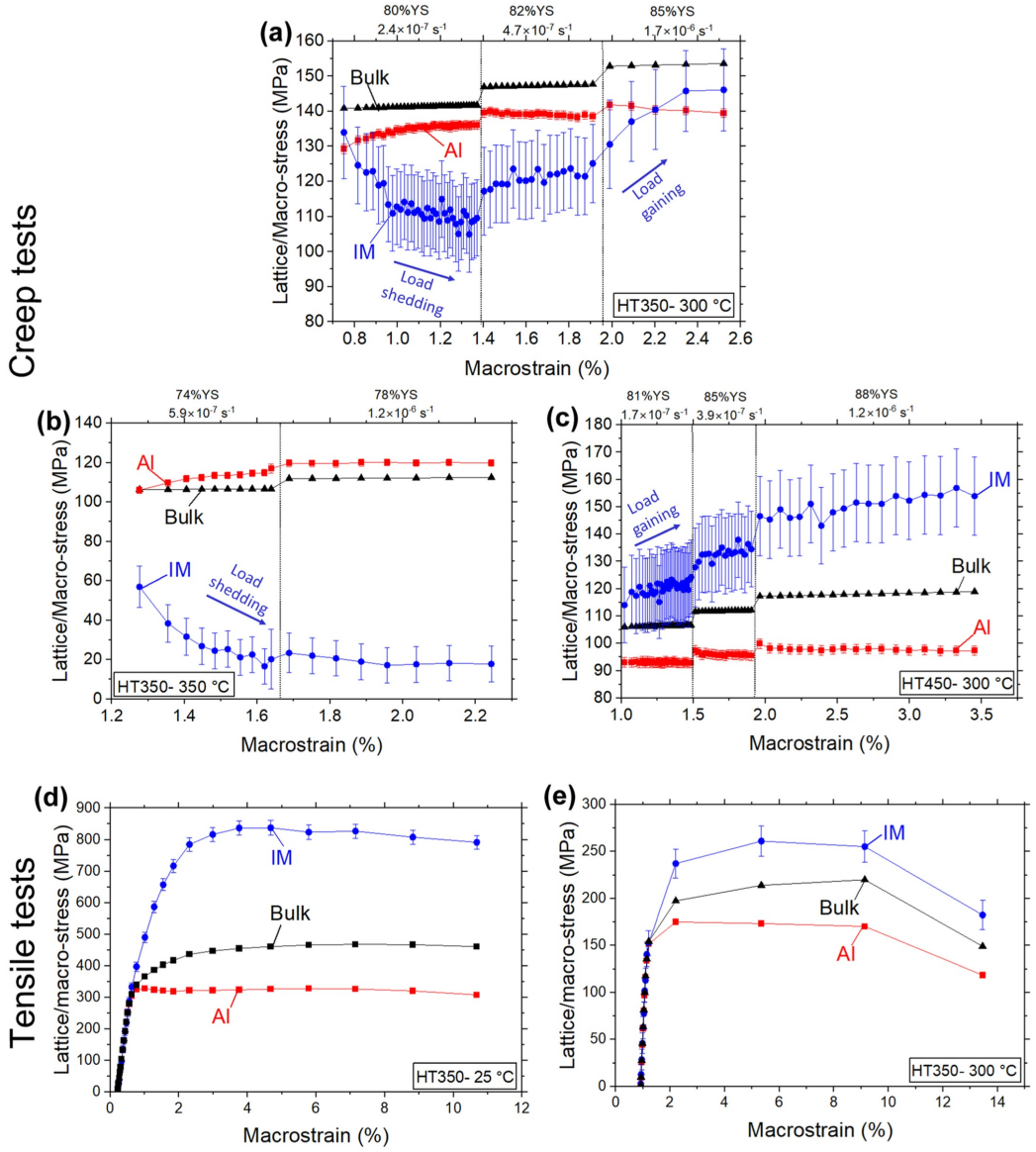


Figure 1.18: In situ neutron creep data showing the load transfer behavior between the intermetallic second phase and the Al matrix: (a-c) plots of lattice stress for each phase vs. creep macrostrain for (a, b) HT350 and (c) HT450 during stress-jump creep tests at 300 °C (a, c) and 350 °C (b). (d, e) plots of lattice stress for each phase vs. macrostrain for HT350 during tensile tests at (d) R.T. and (e) 300 °C. IM stands for the $Al_{27}Ni_6Ce_3$ intermetallic second phase. For creep tests (a-c), applied macroscopic stress is given as a fraction of yield stress (%YS) and macroscopic creep strain rates (s^{-1}) are shown for each stress level. The error bars represent standard error of the mean.

Note. Adapted from [122].

1.5.4 Laser Processing of Refractory Metals: Physics, Mechanisms, and Defect Formation in Tungsten

The laser processing of refractory metals, specifically tungsten (W), presents a distinct set of challenges that diverge sharply from the processing of structural alloys like steels or aluminum. Although the underlying photon–electron–phonon coupling sequence and the pulse duration dependent regimes described in Sections 1.1 and 1.2.2 still apply, tungsten's extreme thermophysical properties compress the viable processing window and amplify the consequences of thermal fluctuation. This subsection therefore focuses on the material-specific factors that make tungsten uniquely difficult to process and on the defect mitigation strategies that follow from those constraints.

Thermophysical Constraints and Energy Coupling

Tungsten is characterized by the highest melting point of all metals ($T_m \approx 3422$°C), high density ($\rho \approx 19.25$ g/cm^3), and significant thermal conductivity ($k \approx 173$ W/m·K at room temperature). These properties fundamentally alter the energy balance during laser irradiation. The high melting and boiling points necessitate extreme energy densities to initiate phase change, while the high thermal conductivity drives rapid heat dissipation away from the interaction zone [131]. This competition typically results in steep thermal gradients ($> 10^6$ K/m), which are particularly detrimental due to tungsten's ductile-to-brittle transition temperature (DBTT). Unlike FCC metals that remain ductile at low temperatures, BCC tungsten exhibits a DBTT typically between 200 °C and 400 °C, causing the material to fracture in a brittle manner under the residual stresses induced by rapid cooling [132].

Energy coupling is further complicated by optical reflectivity. At standard solid-state laser wavelengths ($\lambda \approx 1\,\mu$m), solid tungsten reflects approximately 60%–80% of incident radiation depending on surface roughness [133]. However, absorptivity is highly non-linear with temperature. As the material heats, phonon populations increase, enhancing electron–phonon scattering and raising absorptivity. This positive

feedback loop can lead to runaway heating once a threshold temperature is exceeded. At elevated temperatures in non-inert atmospheres, tungsten also rapidly oxidizes to form volatile oxides (e.g., WO_3), which can alter surface emissivity and lead to mass loss or toxic fume generation, requiring strict atmosphere control [134].

Tungsten-Specific Interaction Behavior Across Pulse Regimes

The general framework for pulse duration dependent laser–matter interaction, including the transition from thermally equilibrated CW and nanosecond processing to the electron–lattice nonequilibrium regime described by the two-temperature model (Equations 1.5–1.6), was established in Sections 1.1 and 1.2.2. In tungsten, however, several material-specific properties shift the practical implications of these regimes.

In the long-pulse and CW regime, the combination of high thermal conductivity and high melting point means that the heat diffusion length $l_T \approx \sqrt{D\tau_p}$ is large and the energy required to reach the melting threshold is substantial. The result is a wide heat-affected zone relative to the melt volume and a strong tendency toward recast layers, microcracks, and collateral thermal damage [135]. These consequences are more severe in tungsten than in most engineering metals because the material passes through its DBTT during cooldown, so even modest thermal damage zones can nucleate cracks.

In the ultrashort pulse regime, tungsten's relatively strong electron–phonon coupling constant g_{ep} accelerates lattice heating after electronic excitation, which narrows the window of electron–lattice nonequilibrium compared with noble metals such as gold or copper. Despite this, femtosecond pulses still deposit energy faster than significant lattice expansion can occur, so ablation proceeds through phase explosion or spallation before a deep thermal wave develops, minimizing the HAZ and suppressing melt formation [136, 137]. A practical complication specific to tungsten is the prominence of incubation effects: repeated pulse exposure progressively lowers the ablation threshold through defect accumulation and surface roughening, which must be accounted for in multi-pulse process planning [138].

Defect Mechanisms: Cracking and Porosity

Despite the precision of ultrashort-pulse (USP) lasers, structural integrity remains the primary bottleneck for volumetric processing such as laser powder bed fusion. Two dominant defect classes persist in tungsten processing.

The most critical failure mode is cracking, driven by the mismatch between tungsten's high elastic modulus ($E \approx 411$ GPa) and its low fracture toughness at room temperature. During the rapid cooling characteristic of laser processing (10^3–10^6 K/s), thermal contraction generates tensile residual stresses. Since the material cools below the DBTT while still under significant stress, it cannot accommodate strain plastically, leading to intergranular and transgranular cracking [139, 140]. In additive manufacturing, these cracks often align parallel to the build direction along grain boundaries or manifest as delamination between layers.

The second major defect class is porosity and balling. In fusion-based processing, tungsten's high surface tension ($\gamma \approx 2.5$ N/m) and viscosity in the molten state impede melt flow and wettability. This leads to the balling phenomenon, where the melt pool breaks into discontinuous spheres to minimize surface energy, causing lack-of-fusion voids and rough surfaces [141]. Any residual oxygen in the powder or chamber can also form volatile oxides that become trapped as gas porosity upon rapid solidification.

Processing Strategies and Mitigation

Overcoming these limitations requires a coordinated strategy that addresses thermal management, atmosphere control, and parameter optimization together.

The most effective approach for mitigating cracking in tungsten is maintaining the material above its DBTT throughout the process. High-temperature preheating, typically above 400 °C and ideally above 800 °C, reduces the thermal gradient (∇T) and keeps the material in a ductile state during the solidification stress transient [142]. Field-assisted sintering technology and substrate heating have shown success in

producing crack-free tungsten components, although practical implementation in laser systems is complex.

Alongside thermal management, strict oxygen control below 100 ppm is mandatory to prevent oxide-induced embrittlement. In terms of laser parameters, a volumetric energy density approach is often used to map the process window. However, for tungsten, simply increasing power is insufficient. The scan strategy, such as checkerboard patterning or remelting passes, must be optimized to manage residual stress accumulation. For microstructuring, operating in the gentle ablation regime at fluences slightly above threshold using femtosecond pulses minimizes the formation of recast layers and laser-induced periodic surface structures, which can degrade surface quality [143].

Open questions remain. Predictive models that couple the electron–lattice nonequilibrium framework introduced in Section 1.2.2 with macroscopic residual stress evolution are still maturing. There is also a lack of sufficient in-situ monitoring data linking specific thermal signatures to the onset of micro-cracking in refractory metals. Closing these gaps through process–structure modeling validated by experimental manufacturing is necessary for advancing laser precision manufacturing of tungsten components.

Chapter 2

Scalable Femtosecond-Laser Ablation Synthesis of High-Purity $CuCoMn_{1.75}NiFe_{0.25}$ HEA Nanoparticles

Source disclosure. The content of this chapter draws from our Nanomaterials article authored by David Fieser, Yucheng Lan, Antonino Gulino, Giuseppe Compagnini, Doug Aaron, Matthew Mench, Denzel Bridges, Hugh Shortt, Peter Liaw, and Anming Hu: *Synthesis and Unique Behaviors of High-Purity HEA Nanoparticles Using Femtosecond Laser Ablation*, *Nanomaterials* **14**(6), 554 (2024), doi: 10.3390/nano14060554 [144]. The article is cited here with permission.

Support and contributions disclosure. P.L. discloses support from the National Science Foundation (DMR-1611180, DMR-1809640, and DMR-2226508), including program directors J. Madison, J. Yang, G. Shiflet, and D. Farkas; the US Army Research Office (W911NF-13-1-0438 and W911NF-19-2-0049), including program managers A.D. Brown, M.P. Bakas, S.N. Mathaudhu, and D.M. Stepp; and the Center for Materials Processing at the University of Tennessee, with C. Rawn and P. Rack as center directors. A.G. and G.C. disclose support from the PON project Bionanotech Research and Innovation Tower, financed by the Italian Ministry for Education, University and Research.

2.1 Motivation and Background

Chapter 1 established the central hypothesis of this dissertation: that predictable and transferable material outcomes are achieved by jointly controlling laser energy delivery, environmental conditions, and spatial constraints, and that these coupled controls can be tuned to intentionally tailor distinct microstructures, surface states, and functional properties. It also developed the physical framework for pulsed laser ablation in liquids, including the ultrafast electron–lattice coupling described by the two-temperature model, the phase explosion and Coulomb explosion pathways that govern material ejection, and the cavitation-mediated cooling and nucleation sequence that produces colloidal nanoparticles from a solid target. This chapter applies that framework at the nanoscale by using femtosecond laser ablation in liquid to synthesize high-entropy alloy nanoparticles from a bulk $CuCoMn_{1.75}NiFe_{0.25}$ target. The central question is whether the coupled process inputs of laser energy delivery and liquid medium chemistry can be tuned to produce single-phase, compositionally faithful HEA nanoparticles at a practically useful production rate.

The $CuCoMn_{1.75}NiFe_{0.25}$ composition was selected for several reasons. Copper, cobalt, and nickel are well-established catalytic elements, and the deliberate enrichment of manganese was motivated by its known activity toward the oxygen reduction reaction (ORR) [145, 146]. This combination of transition metals also has demonstrated effectiveness in brazing and welding applications and a high probability of forming a single-phase FCC solid solution based on published phase stability criteria [147, 148, 149, 150, 151, 152]. The iron content was kept low to minimize the formation of BCC secondary phases while maintaining compositional complexity. As shown in Figure 2.1, the Thermo-Calc phase diagram for the $Fe_xCo_{20}Ni_{20}Mn_yCu_{20}$ system confirms that the selected chemistry sits comfortably within the single-phase FCC region, providing confidence that the bulk target material and, by extension, the ablated nanoparticles should retain a disordered solid solution structure. By targeting a composition that is both catalytically relevant and thermodynamically predicted to

be single phase, the study provides a direct test of whether femtosecond laser ablation can preserve multi-element compositional fidelity during the rapid quenching and nucleation that occur in the liquid environment.

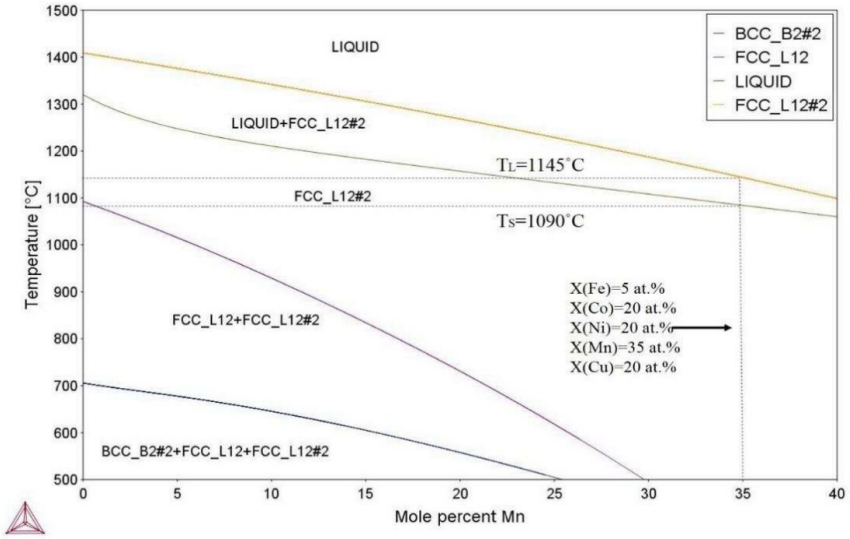


Figure 2.1: Phase diagram for $Fe_xCo_{20}Ni_{20}Mn_yCu_{20}$ system calculated by Thermo-Calc using the HEA 1.0 database.

Note. Adapted from [147].

Despite growing interest in HEA-based nanomaterials, existing synthesis routes each carry limitations that constrain scalability, purity, or both [105]. Carbothermal shock produces nanoparticles anchored to carbon substrates, which can introduce unwanted substrate reactions in applications such as hydrogen evolution, CO_2 reduction, and N_2 reduction where high surface coverage is required [153]. Mechanical alloying is time-intensive and carries contamination risk from milling media [149, 154]. Microwave heating effectiveness varies strongly with material dielectric properties, and wet chemistry methods face challenges in nanoparticle size control and environmental safety [155, 156, 157, 158]. Laser ablation synthesis is attractive for its precision and minimal contamination risk, but prior implementations have struggled with inconsistent particle sizes and high energy requirements, which have limited practical throughput [159]. These limitations establish the need for a synthesis

approach that simultaneously addresses purity, compositional fidelity, and production rate.

Recent work in laser-based HEA nanoparticle synthesis has made progress toward addressing some of these gaps. Redka et al. [160] investigated single-pulse, sub-picosecond ablation of CrMnFeCoNi and AISI304, showing that the HEA target had a slightly lower ablation threshold and produced larger crater diameters, indicating efficient processability with ultrashort-pulse lasers. Waag et al. [116] demonstrated kinetically controlled laser ablation in liquid to synthesize CoCrFeMnNi nanoparticles with equimolar stoichiometry and diameters below 5 nm, with potential utility in heterogeneous catalysis for oxygen evolution reactions. Rawat et al. [161] explored the formation of Cu-Ni-enriched phases in nonequiatomic AlSiCrMnFeNiCu HEA nanoparticles through laser processing, providing insight into how laser treatment can manipulate nanoparticle composition and phase constitution. Jahangiri et al. [117] studied the synthesis of HfNbTaTiZr refractory HEA nanoparticles using femtosecond laser ablation, examining the effects of different solvents and laser fluence on nanoparticle structure with emphasis on photothermal therapy applications. Singh et al. [119] surveyed laser-based fabrication methods and applications of HEA nanoparticles reported to date. Collectively, these studies demonstrate that ultrashort-pulse laser ablation in liquid is a viable route to HEA nanoparticles, but none have achieved the combination of compositional fidelity, single-phase purity, and high production rate that would make the method practical for functional applications at scale.

In this chapter, we address these gaps by developing and testing a femtosecond laser ablation synthesis method in liquid that is designed for high-throughput production of single-phase HEA nanoparticles. The approach uses a 500 fs laser to ablate a rotating bulk HEA target immersed in a liquid medium, with continuous filtration to maintain optical transparency and sustain ablation efficiency. We systematically investigate the role of the liquid environment as a controllable process input by comparing ablation in deionized water, liquid nitrogen, ethanol, and

hydrocarbon solvents. We report characterization of morphology, phase, composition, and surface chemistry to establish how the liquid medium influences phase purity and surface state. We also report the discovery of a nanoparticle chaining phenomenon driven by laser-induced nanojoining at elevated pulse energies [162, 163], and we evaluate the electrocatalytic performance of the synthesized nanoparticles in oxygen reduction, oxygen evolution, hydrogen evolution, and aluminum-air battery applications. The results are interpreted within the process–structure–property framework established in Chapter 1.

2.2 Materials and Methods

2.2.1 Material Synthesis

Bulk Material of HEA

A cylindrical $CuCoMn_{1.75}NiFe_{0.25}$ high-entropy alloy with a diameter of 9 mm and length of 40 mm was produced using a 10 g titanium-gettered arc melter (MRF, Materials Research Furnaces Inc., Allenstown, NH, USA) at 600 amperes. This process employed a quarter-inch diameter lanthanated tungsten tip to ensure effective mixing. The arc melter's vacuum chamber underwent oxygen purging for one hour, reaching a vacuum pressure of 50 mTorr with the aid of a roughing pump. It was then backfilled to 0.5 atmosphere using high-purity argon (99.999% by volume) with a 5 s fill time before each melting cycle, which lasted a minimum of 20 s in a copper mold. The process included 5 min water cooling intervals after each of the seven flips to achieve a homogenous mix. The HEA's constituent elements, namely, Co (99.95% metals basis), Cu (99.9% metals basis), Mn (99.95% metals basis), Ni (99.98% metals basis), and Fe (99.95% metals basis), were measured with 1 mg accuracy.

HEA Nanoparticle Synthesis through Laser Ablation

In our synthesis method for HEA nanoparticles, a femtosecond laser was directed onto the surface of a cylindrical bulk HEA, which was fully immersed in a liquid medium. To ensure consistent ablation, the sample was rotated at a tunable speed up to nearly 9000 rotations per minute. As a result, the nanoparticles produced were immediately submerged in the surrounding liquid medium. This medium, along with the nanoparticles, was then extracted and collected using Whatman 1001-0155 cellulose filter paper (McMaster-Carr, Santa Fe Springs, CA, USA). The filter paper, characterized by its 180 μm thickness, 55 mm diameter, and 11 μm pore size, proved effective in capturing the nanoparticles despite its relatively large pores. An additional parameter influencing ablation performance was the mixing of the ablated material within the liquid medium over time. As nanoparticles accumulated, transparency decreased, attenuating laser propagation and slowing down ablation. Within this work, we used continuous filtration to remove nanoparticles, improving optical penetration. The device is detailed in Figure 2.2.

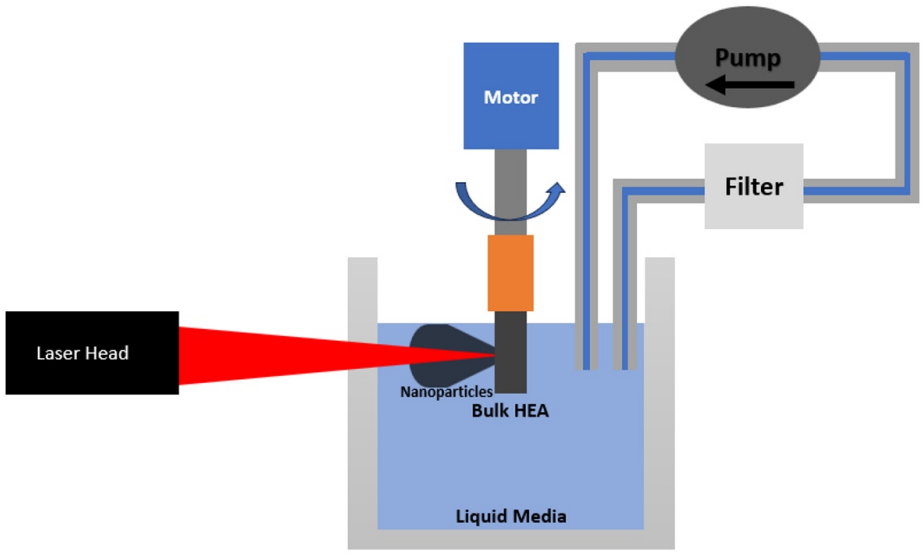


Figure 2.2: Schematic of the HEA ablation system.

Laser ablation in this study was conducted using a unique femtosecond laser system (100 W 500 fs Amplitude Tangor 100®, Amplitude Laser Inc., Milpitas, CA, USA) under a range of average power levels and frequencies, with a consistent pulse width of 500 fs and a laser focal diameter fixed at 50 μm. The average laser power settings varied from 0.2 W to 50 W, while the frequency range was maintained between 50 kHz and 100 kHz.

2.2.2 Microstructure, Phase, and Electrochemical Characterization

Scanning electron microscopy (SEM) was conducted with a ThermoFisher Scientific Helios 5 Dual-Beam system (Thermo Fisher Scientific, Waltham, MA, USA). Transmission electron microscopy (TEM) was performed with a Zeiss Libra200 (Zeiss Group, Oberkochen, Germany). The phase compositions of the welds were analyzed by X-ray diffraction using a Malvern Panalytical Empyrean diffractometer with Cu-Kα radiation (Malvern Panalytical Ltd., Malvern, United Kingdom). X-ray photoelectron spectroscopy (XPS) was performed with a PHI 5000 VersaProbe II. Particle size analysis was performed with ImageJ software V 1.8.0.

The catalytic performance of HEA nanoparticles was characterized using a rotating disk electrode with a diameter of 5 mm made of glassy carbon. Catalyst ink was made by mixing HEA nanoparticles and Ketjen Black in ethanol, maintaining a weight ratio of 2:1. Prior to the dispersion of the nanoparticles, 10 μL of Nafion solution was incorporated into the ethanol solvent to enhance the stability of the catalyst layer. A total of 150 μg of the catalyst, with a concentration of 3 μg/μL, was applied to the electrode in increments of 10 μL, applied dropwise onto the desired surface in five separate drops for uniform coverage. After application, the electrode was left to dry for two hours. Electrochemical tests were conducted for both the ORR and the oxygen evolution reaction (OER), as well as for the hydrogen evolution reaction (HER). These tests were performed at a consistent rotational speed

of 1600 RPM. ORR tests took place in an oxygen-saturated environment, using a 0.1 M KOH electrolyte. In contrast, OER and HER tests required the electrolyte to be degassed with nitrogen, with OER tests also using 0.1 M KOH, while HER tests were conducted in 0.5 M $KHCO_3$. We employed linear sweep voltammetry (LSV) with a Biologic-SP200 potentiostat to evaluate the electrochemical performance of our system. Tests were performed over a wide voltage range to separate the chemical reactions. ORR tests were conducted at 1.5 V down to 0 V, HER testing was conducted starting at 0.25 V and swept down to -1 V, and OER started at 1 V and swept to 2 V. To accurately reference the electrochemical potentials during our experiments, a Hg/HgO reference electrode was employed, set at a potential of +1.44 V, according to the Nernst equation.

Additional electrochemical characterizations were performed using an in-house constructed aluminum–air (Al–air) battery flow battery system, measured with battery testing apparatus [145]. This system featured an anode made from an Al 7075 anode and a cathode comprised of carbon fiber paper (model TGP-H-060, Fuel Cell Earth LLC, Woburn, MA, USA) onto which our synthesized HEA nanoparticle catalyst ink was deposited. The electrolyte used was an alkaline aqueous solution of 6 M KOH. Prior to assembly, the carbon fiber papers serving as the cathode were cleaned using ultrasonic agitation in ethanol, followed by drying. The catalyst ink layer was prepared by creating an ink composed of HEA nanoparticles, Ketjen Black, and carbon Super-P at a weight ratio of 3:3:1. This mixture was then dispersed in pure ethanol to achieve a concentration of 1 mg/mL. A total of 1 mL of the ink was carefully applied to the carbon fiber paper in a controlled, dropwise manner. For the anode, a commercially available Al 7075 plate measuring 2 cm by 2 cm by 6 mm was used. To evaluate the electrochemical performance of the HEA nanoparticles in this Al–air battery system, linear sweep voltammetry was performed with a Biologic-SP200 potentiostat (BioLogic USA, Knoxville, TN, USA). The tests began with an initial voltage close to the open-circuit voltage, approximately 1.5 V, and progressed down to 0 V. We performed these measurements at a consistent scan

rate of 10 mV/s. This methodical approach allowed for a detailed analysis of the electrochemical characteristics of our setup under controlled conditions.

2.3 Results and Discussion

2.3.1 Morphology, Phase, and Composition

The nanoparticles obtained from the experiments were subjected to X-ray diffraction (XRD) analysis along with the original FCC bulk HEA [$a = 3.6476$ Å], the results of which are depicted in Figure 2.3a. The initial ablation experiments were conducted in deionized water. XRD analysis reveals a multi-phase composition identifiable as a metal phase [FCC, $a = 3.5360$ Å] and a metal oxide phase [FCC, $a = 4.3700$ Å]. Further structural insights were gained through TEM, shown in Figure 2.3b, which uncovered a core–shell configuration of the nanoparticles. Accordingly, this core–shell structure is characterized by a solid metal core surrounded by a metal oxide shell, with the indexed peaks presented in Figure 2.3a. Laser-induced periodic surface structures with characteristic ripples form on the HEA surface during ablation. Morphological changes at the target–liquid interface can influence plasma ejection dynamics. In turn, this provides potential routes to intentionally tailor nanoparticle size distributions or composition. However, the underlying physics of the relationship between the surface ripple and the morphology of the ablated nanoparticles is worth further investigation [164, 165, 166].

2.3.2 Nanoparticle Composition

To examine both the surface states and internal composition of the nanoparticles, XPS analysis was conducted. The findings from this analysis are presented in Figure 2.4. The XPS peaks corresponding to the metals are evident in parts (b–f) of Figure 2.4. Analysis of these curves reveals the normalized ratio of the metals present in the nanoparticles as 1:0.89:1.97:0.93:0.37. This observed ratio also aligns with

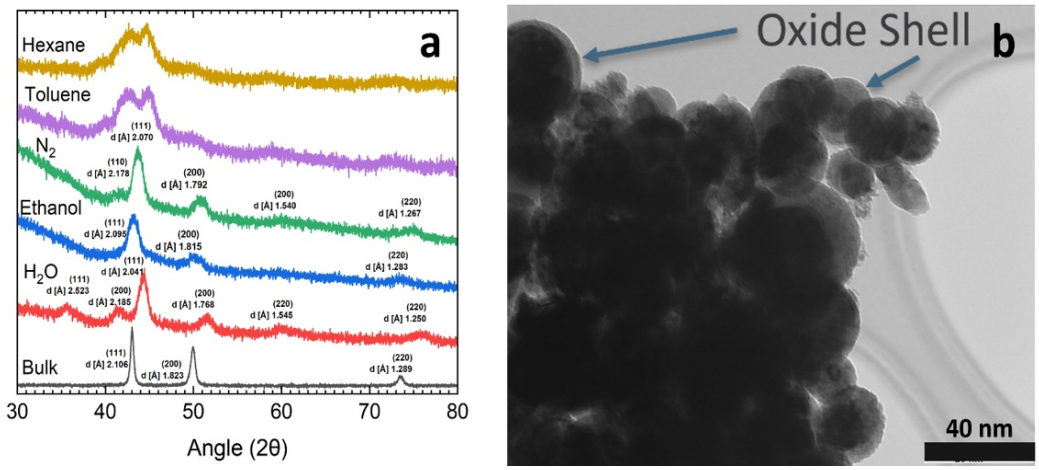


Figure 2.3: (a) XRD analysis of femtosecond-ablated high-entropy alloy nanoparticles in diverse media, including bulk composition. (b) High-entropy alloy nanoparticles ablated in water exhibiting a core–shell structure.

the intended stoichiometric composition of CuCoMnNiFe, which is 1:1:1.75:1:0.25, indicating a high degree of accuracy in nanoparticle synthesis. The oxygen orbital scans can be identified in Figure 2.4h. Two deconvoluted peaks are observed. The presence of two distinct peaks in the XPS scan provides valuable insights into the chemical structure. The first peak, observed at around 530.5 eV, is indicative of the standard bonding environment of oxygen in the alloy oxide. This peak represents the oxygen atoms that are fully integrated into the lattice structure of the oxide phase, reflecting a stable, typical oxide composition. The second peak, appearing at 532.2 eV, is particularly interesting as it signifies the presence of oxygen vacancies within the oxide structure. In the physical sense, oxygen vacancies are essentially spots in the oxide lattice where oxygen atoms would be expected but are absent. The ratio of the intensities of these two peaks (at 530.5 eV and 532.2 eV) can be used as a quantitative measure of the oxygen vacancy ratio in the oxide phase [167]. A higher intensity of the peak at 532.2 eV, relative to the peak at 530.5 eV, suggests a greater proportion of oxygen vacancies. These vacancies can alter the material's properties, such as its ability to conduct electricity, its magnetic behavior, and its catalytic activity in speeding up chemical reactions [168, 169, 170, 171]. In this case,

the ratio of oxygen vacancies to lattice oxygen is 0.78, indicating a substantial presence of oxygen vacancies in the material. The XPS results corroborate the presence of all constituent elements in the bulk high-entropy alloy. As depicted in Figure 2.4, the emergence of peaks corresponding to each element in the bulk material validates the successful synthesis of proper HEA nanoparticles. Peaks for copper, cobalt, manganese, nickel, and iron are visible. Since our composition has high amounts of manganese and low amounts of iron, the evidence of high fidelity is demonstrated by the strength and clarity of the peaks associated with manganese, and the weak peaks associated with iron. EDS measurements on TEM do not identify remarkable compositional differences among these nanoparticles. The presence of carbon can be attributed to possible surface contamination during sample transportation. Raman spectroscopy analyses were conducted on this nanoparticle composition immediately after synthesis, with the results presented in Figure 2.5b. These findings reveal an absence of significant carbon signals, reinforcing the assertion that the carbon detected in the XPS analysis likely originates from later surface adsorption rather than being an integral component of the nanoparticles.

The investigation into water media-ablated nanoparticles produced useful results, yet the resulting nanoparticles were not purely metallic. Exploration was extended to other liquid media, encompassing liquid nitrogen, ethanol, and various hydrocarbon liquids. Although initially a promising concept, especially due to its oxygen-free nature, the nanoparticles produced in liquid nitrogen underwent phase separation. This separation manifested as distinct pure metal and nitride phases [FCC, a = 4.7241 Å]. This phenomenon is clear in Figure 2.3a, providing confirmation of the impurity phase. When samples were ablated in toluene and hexane, the resulting nanoparticles exhibited significant carbide content, along with the presence of unbound organic materials interspersed among them. These compositions are also represented in Figure 2.3a. A distinct phase separation is observable in these lines, further highlighted by the emergence of a clearly defined amorphous region. This latter feature is particularly evident in the lower angle region, spanning from 30° to

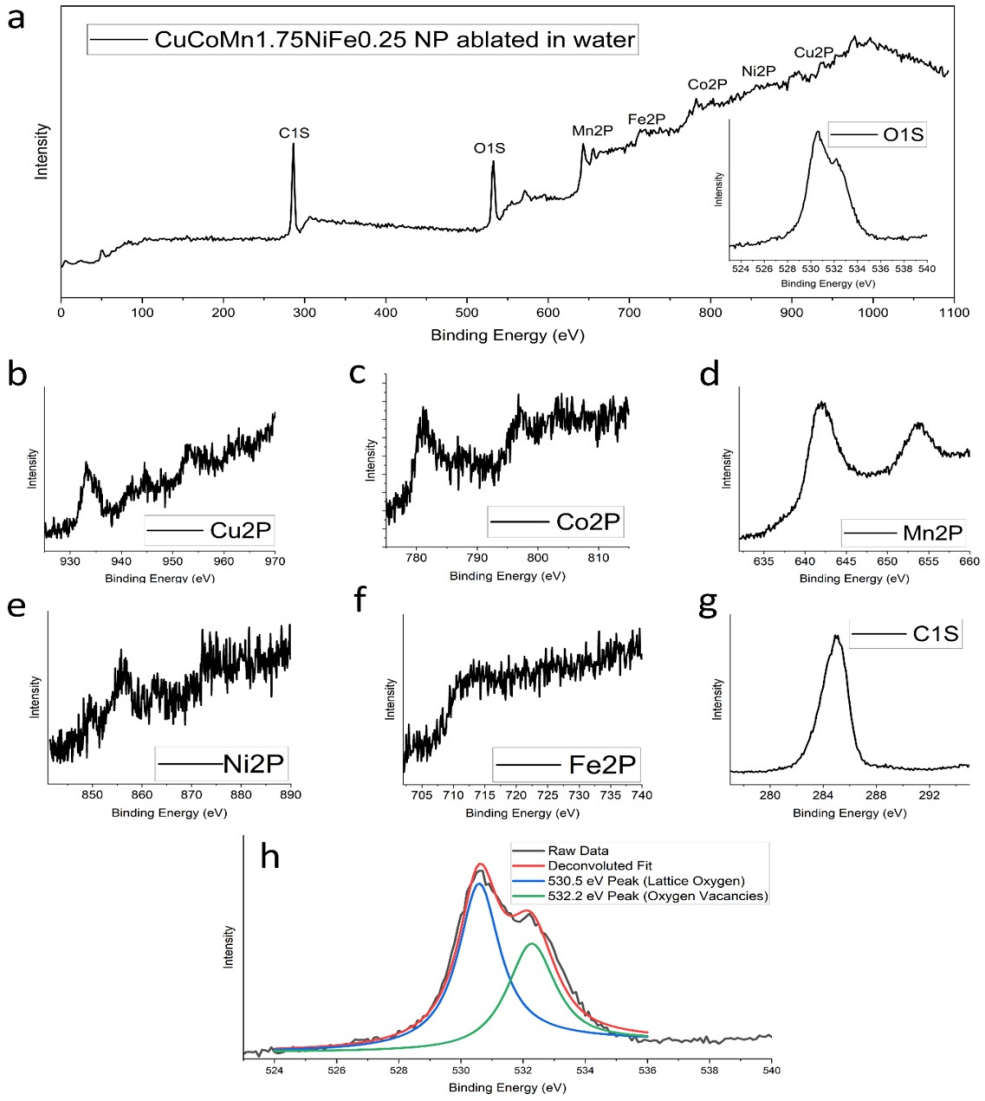


Figure 2.4: XPS analysis of $CuCoMn_{1.75}NiFe_{0.25}$ nanoparticles ablated in water. (a) Survey scan, with O-1s subplot. (b) Cu-2p. (c) Co-2p. (d) Mn-2p. (e) Ni-2p. (f) Fe-2p. (g) C-1s. (h) O-1s deconvolution.

40°, where there is increased scattering. Samples ablated in ethanol had the most promising results, with a clear single-phase metal composition [FCC, $a = 3.630$ Å]. An amorphous region is still visible in the blue line in Figure 2.3a. This trend was theorized to be an organic shell present around a metal core. The investigation of the nanoparticle morphology was conducted using TEM, as depicted in Figure 2.5a. This image reveals a distinct thin shell encircling the nanoparticle's core. To look deeper into these findings, Raman spectroscopy was employed on nanoparticles extracted from various media. The spectrum shown in Figure 2.5b for ethanol corresponds to unwashed nanoparticles ablated in ethanol, where a pronounced presence of carbon D and G bands is evident. The detection of the D and G bands in the Raman spectrum is a compelling indication of the presence of organic material. The D band, which typically appears around 1350 cm^{-1}, is characteristic of disordered or amorphous carbon structures and indicates organic compounds that have not attained a fully crystalline graphite structure [172, 173]. Conversely, the G band, located near 1580 cm^{-1}, represents the graphitic or more ordered carbon structures. This band is associated with the vibrations of sp^2-bonded carbon atoms in a two-dimensional hexagonal lattice, which is a hallmark of graphitic carbon, commonly present in organic materials [172, 173]. This result is different from femtosecond laser ablation of Fe nanoparticles, where a hexagonal diamond shell is reported [174]. The difference may be attributed to various laser pulse widths and pulse energies since the carbon phase is dependent on the Coulomb explosion of organic molecules [173]. The concurrent presence of both the D and G bands suggests a composite carbonaceous nature of the nanoparticles, encompassing both ordered and disordered carbon forms.

In conjunction with this study, EDS was also employed on TEM as a complementary technique to verify the presence of all anticipated elements within the sample, as illustrated in Figure 2.5c. This figure specifically emphasizes the Kα orbital transitions of the elements under investigation. The EDS experiment shows the clear presence of copper, cobalt, manganese, nickel, and iron. The peak associated with copper stands out because it is strengthened by the presence of copper in the

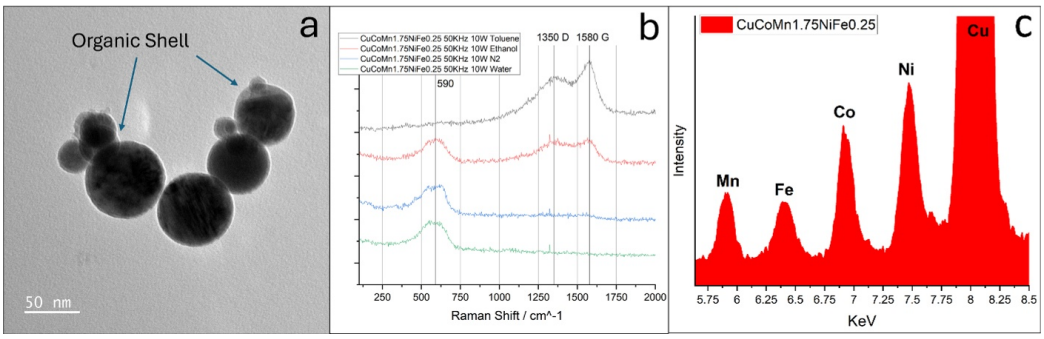


Figure 2.5: (a) High-entropy alloy nanoparticles ablated in ethanol with an organic shell encasing a metallic core. (b) Raman shift spectra of HEA nanoparticles ablated in different media, displaying carbon D and G bands. (c) EDS of ceramic shell nanoparticles showing all five elements.

TEM grids. The preliminary EDS spectrum, as highlighted, reveals distinct peaks corresponding to these Kα transitions, providing clear evidence for the existence of each element within the sample. The quantitative analysis is still under way.

Given that the nanoparticles exhibited a single-phase metal structure, ethanol was chosen as the preferred medium for ablation. The particle size analysis was initially conducted using SEM, with the results presented in Figure 2.6. Analysis of the SEM images reveals that while there is some variation in the size of the nanoparticles, they predominantly cluster within one standard deviation of the average size, approximately 60 nm. The slight decrease in mean size at higher laser fluences may be a result of laser-induced breakdown or an unusual welding phenomenon which will be discussed later in this chapter. For the statistical study shown in Figure 2.6, the chain particles were not calculated. For an optimized yield rate, the system's production rate was tested at 5 W, which produced 10 mg per minute. Since the maximum power of the laser is 100 W, in principle, a linear scaling of 200 mg per minute rate can be feasible by multi-beam parallel processing. Therefore, the current method is scalable for a much higher production rate.

An unexpected phenomenon emerged during the size analysis, as illustrated in Figure 2.7. At pulse energies above 250 mJ, the nanoparticles exhibited a tendency to form elongated chains, extending up to microns in length. Figure 2.7a

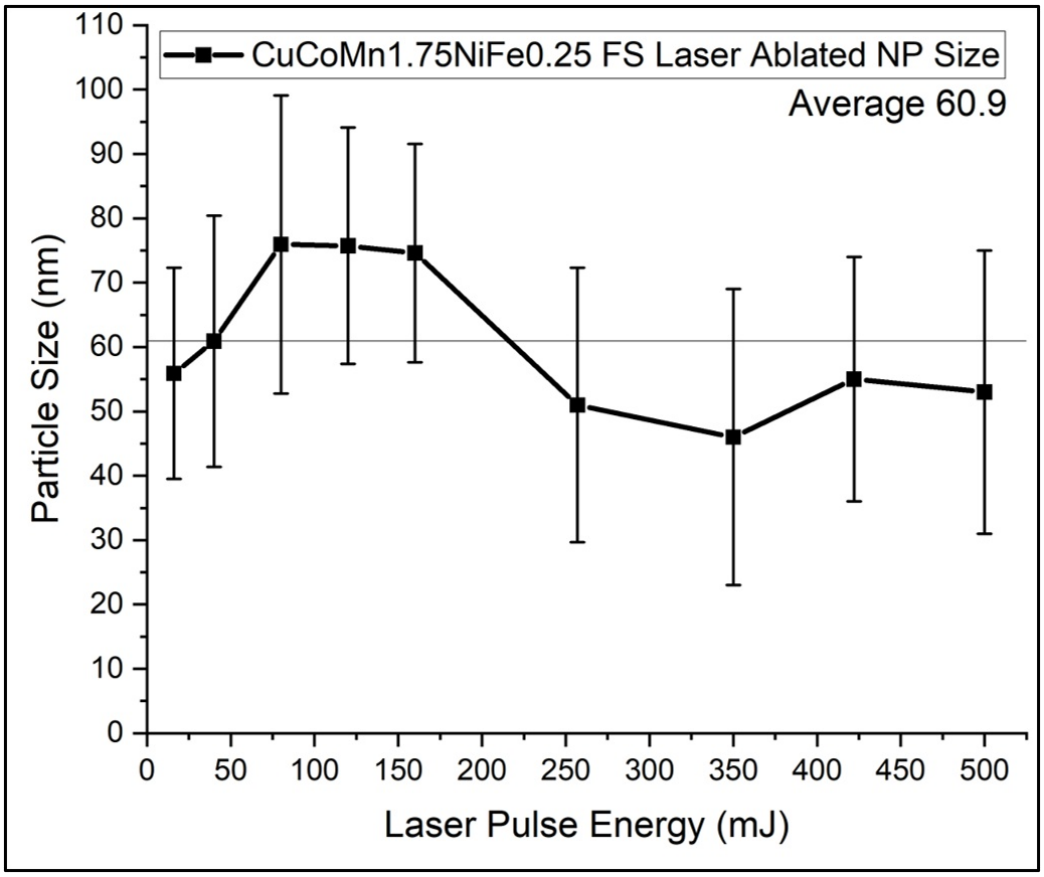


Figure 2.6: Size analysis of HEA nanoparticles.

displays the common clustering of nanoparticles at lower laser fluences, aligning with typical expectations in nanoparticle analysis [175]. In contrast, Figure 2.7b reveals the formation of these extensive chains under higher laser powers. Initially, the hypothesis was that organic strands could be the cause of this clustering. This led to thorough and vigorous washing of the samples with deionized water to remove any potential organic residues. Despite this, subsequent TEM observations confirmed the persistence of the chaining phenomenon.

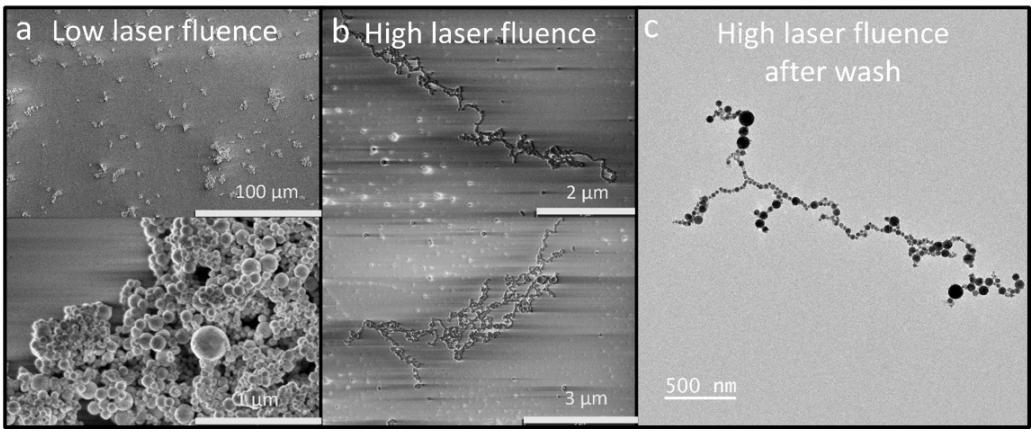


Figure 2.7: (a) SEM image of HEA nanoparticles at low laser power and fluence. (b) SEM image of HEA nanoparticle chains after ablation at high laser fluence. (c) TEM image of high laser fluence chains after washing away organic material.

To explore this phenomenon more thoroughly, an experiment was designed in which a laser was directed through a solution of nanoparticles while stirring continuously. Initially, the nanoparticles were ablated using low laser fluence, as depicted in Figure 2.7a and Figure 2.8b. This feature resulted in a random distribution of nanoparticles, a typical characteristic of nanoparticle agglomeration. Subsequently, the laser's power was set to 50 W at 100 Hz, providing intense photon irradiation at a low density to the solution. The nanoparticles underwent irradiation at various time intervals, and after a period of 20 min, their characteristics were analyzed using UV-NIR spectroscopy, shown in Figure 2.8a. Following this process, TEM was employed to examine the particles synthesized in the solution, revealing the formation of nanoparticle chains akin to those observed in high fluence

ablation, as demonstrated in Figure 2.8c. This experiment successfully confirmed that femtosecond laser irradiation can promote the growth of nanoparticle chains. Such a process might offer advantageous properties, e.g., enhancing electrocatalytic effects by reducing resistance in the HEA catalyst. However, further research is required to establish these potential benefits conclusively. The notable high absorption observed in the UV region (∼200 nm) of Figure 2.8a for the irradiated nanoparticle solutions requires further study to fully discern the underlying causes. Increased optical density at shorter wavelengths is indicative of light-scattering effects and plasma resonance absorption, both consistent with the formation of nanoparticle chains and aggregates. Additionally, residual organic compounds from ablation processing, as well as potential surface reconstruction of metal nanoparticles, can introduce electronic state transitions that absorb intensely at higher photon energies in the UV.

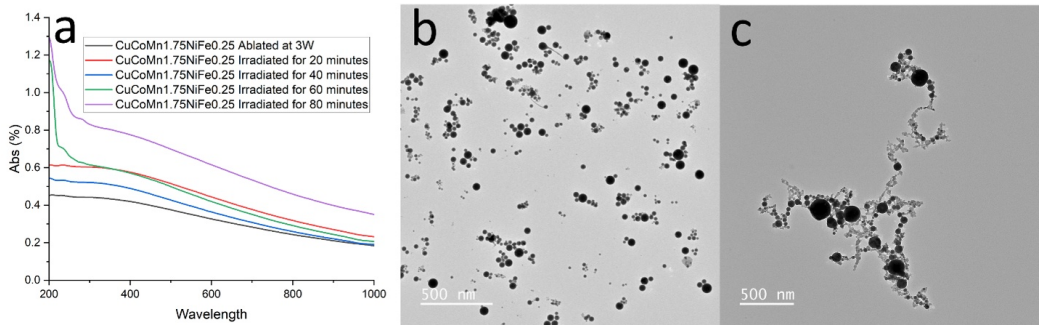


Figure 2.8: (a) UV-NIR spectra of nanoparticle solutions after fs irradiation. (b) TEM image of ethanol-ablated HEA nanoparticles. (c) TEM image of the same nanoparticle solution after fs irradiation.

2.3.3 Laser Ablation and Joining Mechanisms

Nonthermal ablation, important in femtosecond laser-induced joining of nanoparticles, involves ultrafast interactions where femtosecond laser pulses primarily affect the material's electrons. This rapid interaction leads to intense electron excitation and ionization, affecting the material's structure without notable lattice heating, while still

increasing the energy [176, 177]. This sudden energy boost causes some electrons to be ejected from the atom [178]. As a result [177], there is a significant imbalance between the positively charged protons and negatively charged electrons, leading to a Coulomb explosion. The Coulomb explosion refers to the phenomenon where positively charged ions repel each other due to the lack of sufficient electrons to balance the charge. This repulsion causes a rapid expansion and ejection of material from the surface, which is the key aspect of nonthermal ablation under femtosecond laser irradiation [179]. The process of electron ejection and subsequent Coulomb explosion, induced by femtosecond lasers, determines how these lasers modify a material's structures at the nanoscale. Figure 2.9a depicts this laser ablation method followed by the formation of nanoparticles. The process unfolds in distinct stages. Initially, the target material absorbs energy from femtosecond laser pulses, leading to the excitation of electrons and the creation of a dense electron cloud near the surface. This electron cloud constitutes the initial stage of plasma formation, setting the stage for the subsequent Coulomb explosion. As the electron cloud gains energy, further ionization occurs, leading to the generation of plasma, a mixture of free electrons and ions. During the Coulomb explosion, the intense repulsive forces between the positively charged ions in the plasma lead to the rapid expansion and ejection of material from the target surface. This explosive release propels the atoms into the surrounding space. Following their expulsion into a liquid medium, these atoms undergo collision, cooling, slowing down, and nucleation, the process by which they combine and solidify, resulting in the formation of discrete solid particles. The fate of these particles varies. Some remain within the laser beam, undergoing further fragmentation by the laser pulses and thereby reduction in size, while others exit the beam and maintain their larger dimensions. These are evident in the bimodal hydrodynamic diameter distribution scan using an Anton Paar Light Sizer, shown in Figure 2.10. Two maxima of the population are found at 40 nm and 270 nm. At higher repetition rates, increased laser pulses overlapping on trapped particles may enable secondary fragmentation, reducing sizes below the initial distribution.

Factors such as repetition rate and target rotation speed alter pulse counts across ablation areas, likely influencing nanoparticle dimensions, composition uniformity, and microstructure through cumulative energy deposition effects.

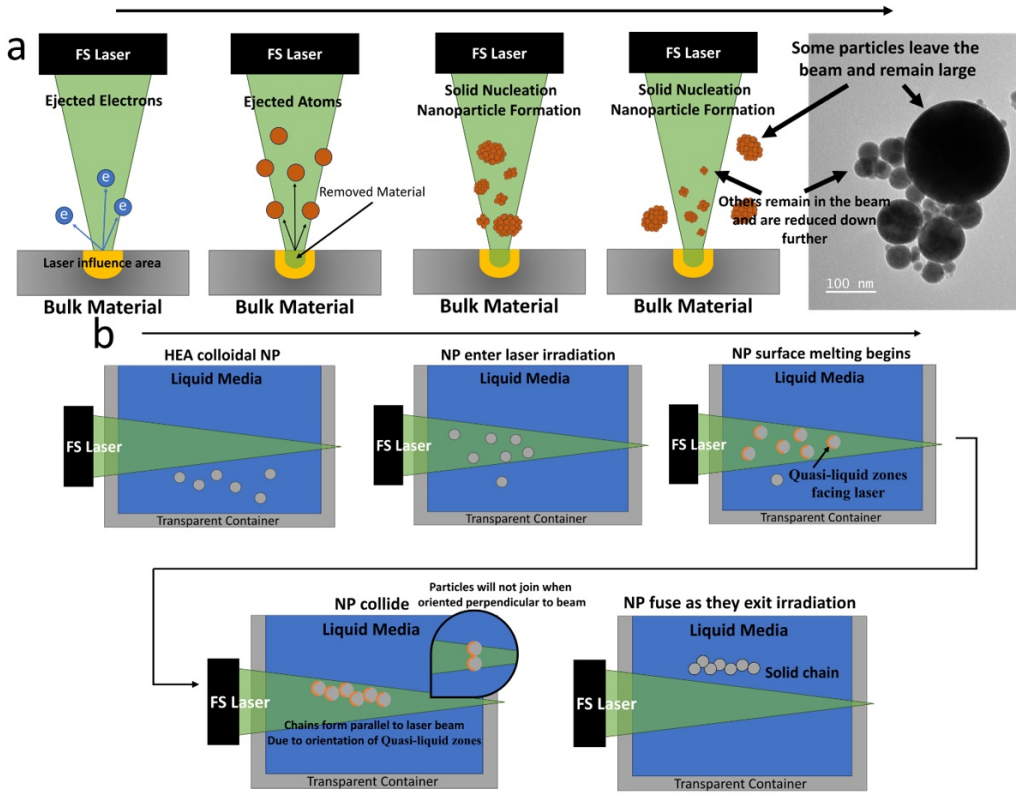


Figure 2.9: (a) Illustration of the laser ablation process for the formation of nanoparticles. (b) Depiction of surface nanojoining process.

Nonthermal melting, a phase transition induced by low femtosecond laser fluence, is the mechanism responsible for nanoparticle joining. The nonlinear adsorption induced by the femtosecond laser causes a shift in electron density, leading to a slight imbalance that does not reach the threshold of Coulomb explosion or electron ejection [178]. Instead, this imbalance also weakens the interatomic bonds, creating a quasi-liquid state at the irradiated spots. As a result, nanoparticles can merge or fuse at these quasi-liquid zones while maintaining their individual structural integrity and properties [178]. This transition occurs without a corresponding rise in the lattice's thermal energy, so the nanoparticles' structural integrity is preserved. Understanding

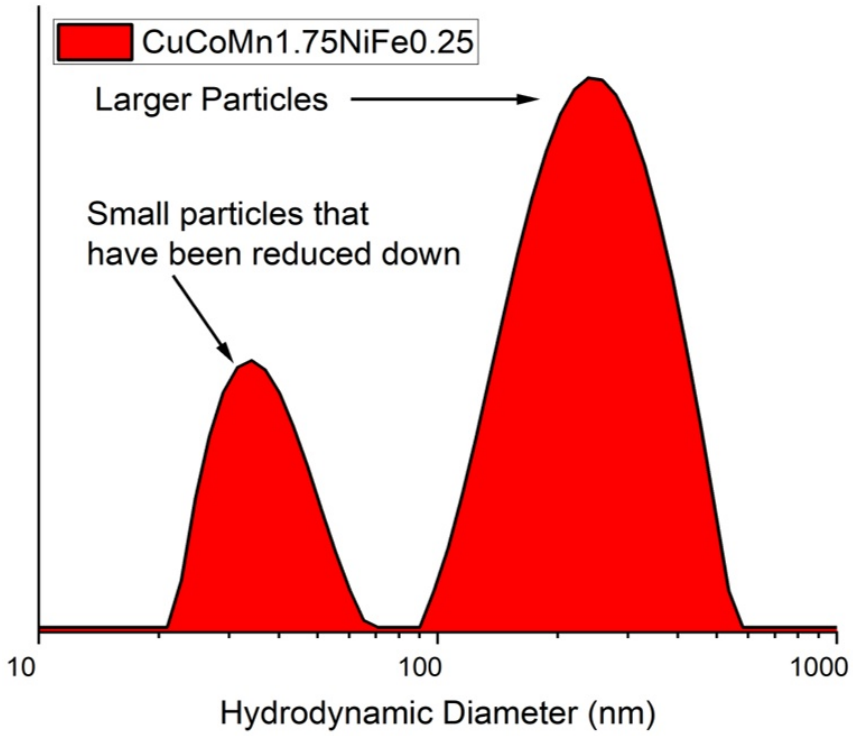


Figure 2.10: Hydrodynamic diameter of HEA nanoparticle solution.

this phenomenon can explain why our nanoparticles join when placed under relatively low laser fluence. The direct mechanism for our nanoparticle fusion is detailed in Figure 2.9b. In the process described, HEA nanoparticles are introduced into a zone of direct laser irradiation, where the density of the laser is intentionally kept low to avoid the aforementioned Coulomb explosions. Instead, the focus is on inducing surface melting of these nanoparticles. As the nanoparticles traverse this irradiated zone, the outermost layer undergoes a phase transformation into a quasi-liquid state due to the laser's thermal influence. As the nanoparticles, now with molten surfaces, move within the laser field, they encounter and collide with each other. The surface liquid layers enable the nanoparticles to fuse with each other. Upon exiting the area of laser influence, the nanoparticles begin to cool down. This cooling results in the solidification of the quasi-liquid layers, effectively welding the nanoparticles together to form the long chains shown in Figure 2.7c and Figure 2.8c. These

chains cannot de-weld due to surface melting not penetrating all the way through the fused zones. This fusion forms a consolidated mass. The formation of chains or aggregates depends on the orientation of the liquid zones relative to the beam and on the beam diameter. The orientation of these quasi-liquid zones is such that it is less possible to support perpendicular alignment relative to the laser beam. This directional limitation is further reinforced by the beam's spatial constraints, which may restrict the chain length of joined particles. The light excitation of high-entropy nanoparticles may clarify the formation mechanism of fused particles. Also, the thermal accumulation effect due to high repetition may also contribute to laser-induced nanojoining [180, 181].

2.3.4 Electrochemical Performance of HEA Nanoparticles

HEA nanoparticles have attracted interest as electrocatalysts for energy conversion and storage [105]. Figure 2.11a presents LSV plots for the synthesized nanoparticles. The curves show activity toward three reactions: HER, ORR, and OER. This triple functionality makes the nanoparticles candidates for fuel cells, electrolyzers, and metal–air batteries.

The unique multi-elemental nature of HEAs contributes to a versatile electronic structure, which is beneficial for catalyzing oxygen reduction reactions in alkaline aluminum–air batteries [182]. This adaptability allows for the fine-tuning of electronic properties, which benefits ORR performance. Introducing HEA nanoparticles as a catalyst in aluminum–air batteries uses these properties for improved electrochemical performance. Following the characterization of aluminum–air batteries, we implemented these particles within our previously characterized batteries. This test evaluated the catalytic performance of the synthesized nanoparticles. LSV measurements with a two-electrode configuration, as presented in Figure 2.11b, showed improved battery performance with the introduction of our nanoparticles. In this case, Al was the anode and HEA was deposited on carbon fiber paper

as the cathode. Specifically, the LSV curves indicate a baseline performance of under 250 mA/cm^2 without a catalyst (only Ketjen Black and carbon Super-P). The integration of our HEA nanoparticles as the sole variable adjustment propelled the performance to approach 325 mA/cm^2. A similar increase in the power density can be seen in Figure 2.11c. The maximum power density increased from 70 mW/cm^2 at a discharge current of 125 mA/cm^2 to 90 mW/cm^2 at a current density of 160 mA/cm^2. This increase confirms the catalytic activity of the nanoparticles.

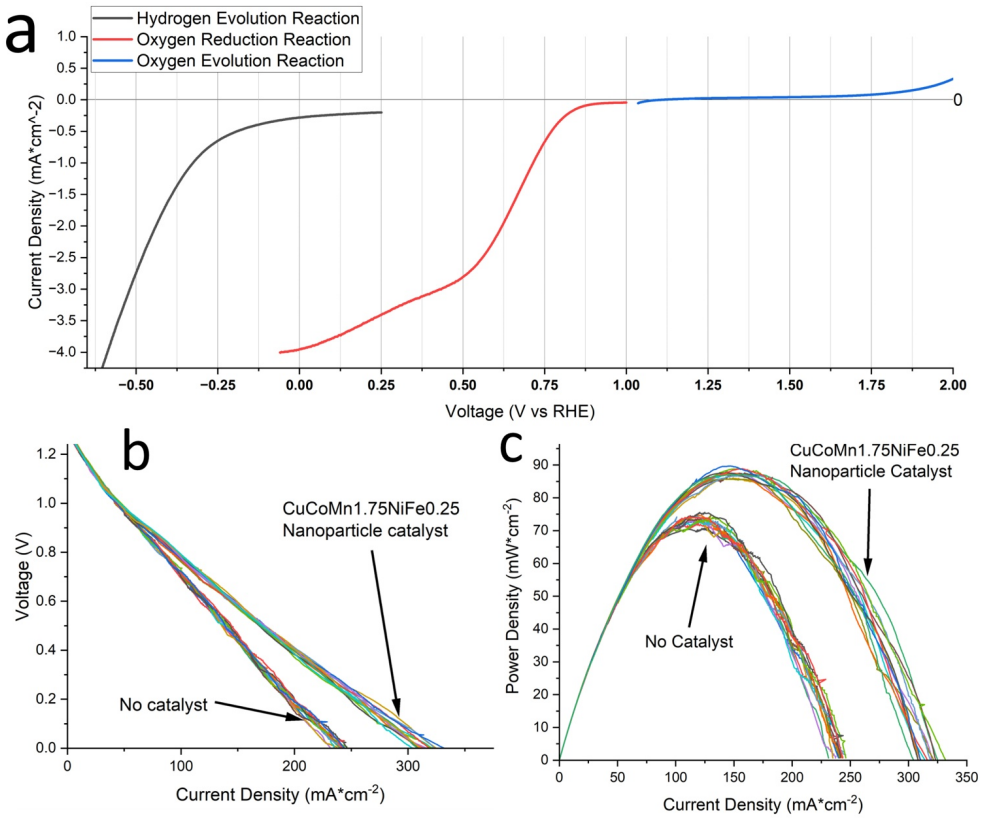


Figure 2.11: (a) LSV plots demonstrating multi-function catalysis of HEA nanoparticles, featuring hydrogen evolution, oxygen reduction, and oxygen evolution. (b) LSV curves for aluminum–air battery showing output current density. (c) LSV curves for aluminum–air battery showing output power density.

2.4 Conclusions

The central hypothesis of this dissertation states that predictable and transferable material outcomes are achieved by jointly controlling laser energy delivery, environmental conditions, and spatial constraints, and that these coupled controls can be tuned to intentionally tailor distinct microstructures, surface states, and functional properties. The results of this chapter provide direct evidence for that hypothesis at the nanoscale.

The strongest test of environmental control came from the systematic variation of the liquid medium while holding laser parameters constant. Water, liquid nitrogen, ethanol, and hydrocarbon solvents each produced a different phase outcome from the same bulk HEA target: oxide-shell core-shell particles in water, phase-separated metal and nitride in liquid nitrogen, carbide-contaminated particles with amorphous organic residues in hydrocarbons, and single-phase FCC metallic nanoparticles in ethanol. The phase constitution and surface chemistry of the nanoparticles were therefore set not by the laser alone, but by the combination of laser energy delivery and the reactive environment at the ablation site. This is the defining claim of the hypothesis: the processing environment is a controllable input that determines microstructure and surface state, not a passive boundary condition.

Laser energy delivery provided a second independent control axis. At moderate fluence, the process produced discrete nanoparticles with a mean size of approximately 60 nm. At elevated pulse energies above 250 mJ, the same laser system accessed a nonthermal surface melting regime that fused nanoparticles into micron-length chains through laser-induced nanojoining. No change in target material or liquid medium was required to shift between these two outcomes. The ability to switch from isolated particle synthesis to directed chain assembly by adjusting a single energy delivery parameter demonstrates that laser energy and environmental conditions act as independent, tunable knobs that jointly determine the nanostructure architecture, exactly as the hypothesis predicts.

Compositional fidelity provides evidence for the predictability component of the hypothesis. XPS analysis confirmed that the nanoparticles retained the designed $CuCoMn_{1.75}NiFe_{0.25}$ stoichiometry with a measured elemental ratio of 1:0.89:1.97:0.93:0.37, closely matching the intended 1:1:1.75:1:0.25. This result was achieved under extreme thermal gradients and rapid quenching in the liquid environment, conditions that could easily bias composition through preferential ablation or selective oxidation. The fact that stoichiometry was preserved indicates that the process is not stochastic under these conditions but produces a repeatable and predictable compositional outcome when the laser and environmental parameters are properly selected.

The functional property measurements close the process–structure–property loop that the hypothesis requires. The single-phase, compositionally faithful nanoparticles synthesized in ethanol exhibited electrocatalytic activity toward ORR, OER, and HER. When integrated as the cathode catalyst in an aluminum-air battery, they increased the limiting current density from under 250 mA/cm^2 to approximately 325 mA/cm^2 and raised peak power density from 70 mW/cm^2 to 90 mW/cm^2. These measurable performance gains trace directly back to the phase purity and surface state established by the choice of liquid medium, which in turn was set by the environmental control input. The chain from process input to microstructure to surface state to functional property is unbroken, and each link was governed by a deliberate control decision rather than by chance.

Ongoing work seeks to extend this control framework by studying how pulse number, repetition rate, and target rotation speed influence particle size distribution and chain architecture, with the goal of establishing quantitative process maps that connect laser delivery parameters to nanoparticle population characteristics.

Chapter 3

Solvent-Controlled Surface Nanostructure and Thermodynamic Stability of $CuCoMn_{1.75}NiFe_{0.25}$ HEA Nanoparticles

3.1 Disclosure

Source disclosure. The content of this chapter draws from our published Langmuir article, authored by David Fieser, Kaijun Yin, Hugh Shortt, Unmanaa Dewanjee, Baldur Steingrimsson, Ilia N. Ivanov, James Burns, Peter K. Liaw, Jian-Min Zuo, and Anming Hu: *Surface Nanostructure Control and Thermodynamic Stability Analysis of Femtosecond Laser-Ablated* $CuCoMn_{1.75}NiFe_{0.25}$ *Nanoparticles*, *Langmuir* **41**(23), 14727–14742 (2025), doi: 10.1021/acs.langmuir.5c05617 [183]. The article is cited here with permission.

Support and contributions disclosure. The work reported in this chapter was supported by the University of Tennessee, Knoxville, through a hiring package. D.F. discloses support from the UTK 100 Talented PhD Scholarship. Atom Probe Tomography and Photoluminescence Spectroscopy activities were conducted as part of a user project at the Center for Nanophase Materials Sciences, a US Department of Energy, Office of Science User Facility at Oak Ridge National Laboratory (Proposal ID: CNMS2025-R-03093). Support for the Center for Material Processing from the State of Tennessee and the Tennessee Higher Education Commission is also disclosed. P.K.L. discloses support from the National Science Foundation (DMR-2226508). The authors also disclose contributions from Richard Haasch (University of Illinois Urbana-Champaign) related to data acquisition.

3.2 Motivation and Background

Chapter 1 established the central hypothesis of this dissertation: that predictable and transferable material outcomes are achieved by jointly controlling laser energy delivery, environmental conditions, and spatial constraints, and that these coupled controls can be tuned to intentionally tailor distinct microstructures, surface states, and functional properties. Chapter 2 provided the first direct test of that hypothesis at the nanoscale, demonstrating that femtosecond laser ablation in liquid synthesizes single-phase, compositionally faithful $CuCoMn_{1.75}NiFe_{0.25}$ high-entropy alloy nanoparticles from a bulk target, and that the choice of liquid medium determines whether the product is a pure metallic phase, an oxide core–shell structure, or a phase-separated mixture. Critically, that study identified the ablation environment as a controllable input that governs phase constitution, but it did not resolve how the solvent controls the internal defect structure, atomic-scale surface state, or thermodynamic stability of the nanoparticles once a single-phase product is achieved. This chapter addresses that gap by examining the same $CuCoMn_{1.75}NiFe_{0.25}$ composition under controlled variation of the ablation medium, with the specific aim of determining whether the environmental control axis can be tuned to predictably set nanoparticle surface nanostructure and thermodynamic stability independent of laser energy delivery.

Surface state and thermodynamic stability are the two attributes that ultimately determine whether the compositional promise of HEA nanoparticles translates into functional performance [184, 185]. As established in Chapter 1, the high configurational entropy of multi-principal-element alloys stabilizes single-phase solid solutions that would otherwise decompose into brittle intermetallic compounds [103, 102, 186, 187], enabling combinations of strength, ductility, and thermal stability that are difficult to achieve in conventional single-principal-element alloys [188, 189]. At the nanoscale, however, the competition between entropy-driven stabilization and enthalpy-driven decomposition intensifies because compositional fluctuations can

span a significant fraction of the particle volume, making it necessary to test bulk thermodynamic criteria against nanoparticles produced under far-from-equilibrium conditions.

To quantify this competition for the compositions studied here, we employ the thermodynamic and geometric descriptors that capture the competing roles of entropy, enthalpy, and lattice distortion in multicomponent alloys. One of the most widely applied is the Ω parameter, which balances the configurational entropy against the enthalpy of mixing and is expressed as

$$\Omega = \frac{T_m \, \Delta S_{\mathrm{mix}}}{|\Delta H_{\mathrm{mix}}|}, \tag{3.1}$$

where T_m is the alloy melting temperature, ΔS_{mix} is the configurational entropy of mixing, and ΔH_{mix} is the enthalpy of mixing. Because Ω decreases as ΔH_{mix} rises, alloys with high positive enthalpies of mixing tend to destabilize into multiphase mixtures. A second important descriptor is the atomic size difference, δr, which quantifies lattice distortion in an n-component alloy:

$$\delta r = \sqrt{\sum_{i=1}^{n} c_i \left(1 - \frac{r_i}{\bar{r}}\right)^2}, \qquad \bar{r} = \sum_{i=1}^{n} c_i r_i, \tag{3.2}$$

where c_i is the atomic fraction of the ith element, r_i its atomic radius, and $\bar{r}$ is the average atomic radius. Together, Ω and δr provide semi-quantitative guidelines for phase formation: according to Yang and Zhang [109], the condition $\Omega > 1$ with $\delta r < 7$ favors solid solutions, $1 < \Omega < 10$ with $4 < \delta r < 10$ often yields a mixture of solid solutions and intermetallics, and $1 < \Omega < 3$ with $7 < \delta r < 15$ typically results in intermetallic compounds. These relationships emphasize that enthalpy, entropy, and size effects must be jointly considered when designing HEAs, particularly at the nanoscale where compositional fluctuations can strongly alter phase stability. The thermodynamic calculations presented in Section 3.4.5 apply these descriptors to the nanoparticle compositions measured by EDS, providing a quantitative test of

whether bulk phase-stability criteria hold under the far-from-equilibrium conditions of femtosecond laser ablation.

Chapter 2 demonstrated that femtosecond-laser-ablated $CuCoMn_{1.75}NiFe_{0.25}$ nanoparticles synthesized in ethanol exhibited electrocatalytic activity toward oxygen reduction, oxygen evolution, and hydrogen evolution, and meaningfully improved aluminum–air battery performance, establishing a direct connection between the controlled synthesis environment and downstream functional properties [144]. However, exploiting these catalytic properties at scale requires understanding not only how to produce a single-phase nanoparticle, but also how the ablation medium shapes the surface chemistry, oxide passivation, and compositional uniformity that govern active-site density and catalytic stability [190, 158]. The integration of HEA compositions into functional nanomaterials remains challenging precisely because synthesizing multi-element nanoparticles while maintaining a homogeneous single-phase structure requires advanced fabrication techniques that preserve uniform compositions at the nanoscale. Multiphase mixtures otherwise complicate structural stability and functional control [191, 192, 193].

The advantages of ultrafast energy delivery established in Chapter 2 are highlighted by comparing against trials with longer laser pulses, which have generally not succeeded in synthesizing single-phase high-entropy nanomaterials. Ninomiya et al. [194] prepared sub-micron CrMnFeCoNi HEA particles using nanosecond-pulsed Nd:YAG laser ablation in water. The particles exhibited polycrystalline structures with Cr–Mn- and Co–Ni-rich regions and slight elemental variations due to oxidation. Tahir et al. [118] demonstrated that CoCrFeMnNi HEA nanoparticles produced by pulsed laser ablation from powder-pressed targets were more homogeneous and productive than those from ball-milled or single-crystal targets. Although powder-pressed targets formed solid-solution FCC particles, the others formed core–shell structures because of segregation effects. Jahangiri et al. [117] showed how solvent choice leads to compositional deviations and varying oxidation states for HfNbTaTiZr nanoparticles. Although a uniform single phase was not achieved, their study

illustrates how synthesis parameters create nanoparticles with different compositional and structural properties by adjusting solvent and laser conditions.

Chapter 2 demonstrated that femtosecond laser ablation in liquid overcomes many of these limitations, producing high-purity, single-phase FCC nanoparticles in ethanol with compositional fidelity closely matching the bulk target [144, 160]. The exceptional precision of femtosecond lasers enables ultrafast energy deposition with minimal thermal damage, precise control over target modifications, and the ability to process a wide range of materials [195, 196, 197, 113, 179]. Although Chapter 2 confirmed that ethanol yielded single-phase nanoparticles while water, liquid nitrogen, and hydrocarbon solvents did not, it did not systematically characterize the structural origin of this solvent sensitivity or how the ablation medium governs nanoparticle defect structures, surface chemistry, and thermodynamic stability within the single-phase regime [105, 192].

Recent efforts in this area include Li et al.'s [198] high-entropy oxide ceramic work, which revealed size-dependent segregation in $RE_2(Ce_{0.2}Zr_{0.2}Hf_{0.2}Sn_{0.2}Ti_{0.2})_2O_7$ nanoparticles synthesized by femtosecond laser ablation. Small particles showed segregation, whereas larger particles were homogeneously mixed, highlighting complex thermodynamic behavior under ultrafast ablation conditions. Rawat et al. [199] studied solvent effects in pulsed laser ablation in liquids of AlCrCuFeNi HEAs, showing that ethanol favored homogeneous solid-solution nanoparticles while water produced larger core–shell particles with oxidized Al-rich shells. Maksimovic et al. [200] alloyed Si and Cr films using femtosecond pulses to form nano-disks and sub-100 nm structures with spatially controlled composition, demonstrating how ultrafast patterning can inform nanoscale HEA design. Waag et al. [116] introduced a kinetically controlled laser ablation method to prepare equimolar CoCrFeMnNi HEA nanoparticles under 5 nm diameter, yielding stable, ligand-free colloids with high production rates and strong redox activity for oxygen evolution catalysis. Redka et al. [201] examined femtosecond laser ablation dynamics of CrMnFeCoNi HEAs via pump–probe microscopy and transfer-matrix modeling, finding higher

ablation efficiency, thinner spallation layers, and reduced plume absorption relative to stainless steel. Liu et al. [202] developed a laser solid-phase technique to synthesize CrMnFeCoNi HEA nanoparticles encapsulated in graphene shells on porous graphene supports, achieving uniform compositions and high production rates without post-processing while delivering excellent oxygen-evolution activity and stability. Zhang et al. [203] demonstrated femtosecond laser sintering of NbMoTaWZr refractory HEA nanoparticles into uniform single-phase BCC grains, using localized plasmon resonance to drive fast mixing and eliminate segregation. Singh et al. [119] surveyed laser-based fabrication methods and applications of HEA nanoparticles reported to date. A gap remains in understanding how these nanoparticles' atomic structures, defect features, and chemical composition evolve under ultrafast, far-from-equilibrium synthesis conditions, and specifically how the choice of ablation medium controls these attributes when the laser energy delivery parameters are held constant.

In this chapter, we build on the synthesis platform developed in Chapter 2 by closely examining the structural and chemical attributes of $CuCoMn_{1.75}NiFe_{0.25}$ nanoparticles generated under controlled variation of the ablation environment. Whereas Chapter 2 compared four solvents to identify which medium produces a single-phase product, this study focuses on the two most promising media, ethanol and liquid nitrogen, and applies advanced characterization including atom probe tomography, 4D-STEM, and photoluminescence spectroscopy to resolve how each environment shapes crystallographic features, defect populations, surface chemistry, and thermodynamic stability. The results are interpreted within the process–structure–property framework established in Chapter 1, with emphasis on whether the environmental control axis provides predictable and transferable tuning of nanoparticle attributes as the dissertation hypothesis requires.

3.3 Experimental

3.3.1 Material Synthesis

Bulk HEA

We employed a $CuCoMn_{1.75}NiFe_{0.25}$ high-entropy alloy rod, produced via a standard arc-melting procedure under inert conditions, as the starting material for this study. In brief, elemental Cu, Co, Mn, Ni, and Fe were combined in atomic proportions to match our target composition and cast into a homogenous alloy with minimal contamination. The final rod measured 9 mm in diameter and 40 mm in length and was subsequently sectioned into smaller cylindrical targets for femtosecond laser ablation. Additional fabrication details, such as flipping intervals, water-cooling cycles, and vacuum parameters, are described in a previous publication [144].

HEA Nanoparticle Synthesis through Laser Ablation

Nanoparticles were synthesized by ablating the $CuCoMn_{1.75}NiFe_{0.25}$ target with a femtosecond laser (Amplitude Tangor 100, Amplitude Laser Inc., Milpitas, CA, USA) that delivers 500 fs pulses at a wavelength of 1,030 nm. The laser frequency used in this study was maintained at 50 kHz, and the average power was maintained at 5 W. The beam was focused to a spot of about 50 micrometers on the target surface, which was rotated at speeds up to 7,000 rpm to expose fresh material. Particle fabrication is controlled at typical room temperatures or stable cryogenic temperatures to simulate the most common scalable fabrication parameters.

We performed ablation in two different liquids: ethanol at ambient conditions and liquid nitrogen in a cryogenic setting. We have previously explored numerous solvents in the past including water and acetone. These two media have given us the most interesting results for industrial applications and thus have motivated this study. The ablated particles dispersed directly into the liquid, thereby minimizing contamination.

More information about the laser ablation system, including a device schematic, can be found in the previous study [144]. After ablation, we stored the resulting colloidal solutions in sealed containers. The collected nanoparticles were gathered and isolated by centrifugations, then rinsed with deionized water to remove residual media. The final nanoparticle dispersions were dried and then used for subsequent analyses.

Although the present experiments were performed on a laboratory scale, the laser ablation and collection geometry were chosen with scalability in mind. The use of a 9 mm diameter, 40 mm long $CuCoMn_{1.75}NiFe_{0.25}$ cylinder fully immersed in liquid and rotated at speeds up to ∼7000 rpm ensures that fresh HEA surface is continuously presented to the femtosecond beam and that the process can, in principle, be extended simply by increasing target length or laser power. With this method, we estimate a 200 mg per minute fabrication rate. At the same time, continuous withdrawal of the nanoparticle suspension through cellulose filter paper maintains optical transparency in the ablation cell, allows uninterrupted ablation, and relies only on low-cost, disposable consumables. Combined with the standard arc-melting route used to produce the feedstock cylinders, these features indicate that the synthesis strategy is not intrinsically limited to small batch sizes, even though detailed cost and throughput analyses are beyond the scope of the present work.

3.3.2 Characterization Techniques

Nanoparticle Imaging

TEM was performed using a Talos (Thermo Fisher Scientific, USA) operating at 200 kV. Nanoparticle suspensions were drop-cast onto lacey carbon-coated copper grids and air-dried at in vacuum. High-resolution TEM (HRTEM) was used to visualize defect structures, while selected area electron diffraction patterns provided crystallographic information. For the quantitative size analysis, over 200 nanoparticles were measured to determine the size distribution.

Four-dimensional scanning transmission electron microscopy (4D-STEM) datasets were acquired over selected regions using an electron probe with a 0.46 mrad convergence angle and a 1.7 nm full width at half maximum (FWHM). Diffraction patterns were recorded using an electron microscopy pixelated area detector (Thermo Fisher Scientific, USA) at a frame rate of 1,000 frames per second). The nanometer-scale probe was formed using a 50 μm condenser aperture in an μProbe mode.

Elemental Composition

Atom Probe Tomography (APT) samples were prepared using a Thermo Fisher Helios DualBeam focused ion beam–scanning electron microscope. Bulk alloy specimens were site-specifically lifted out and sharpened into needle-shaped tips. The needles have a radius less than 170 nm with a tip less than 20 nm. Four independent needles were fabricated to provide redundancy, and measurements were performed until consistent datasets were obtained. Atom probe tomography was then conducted on a Cameca LEAP 4000X HR.

EDS on the same Talos microscope equipped with an integrated four-crystal Super-X EDS detector (FEI), operated at 200 kV. Elemental maps were acquired to confirm the presence and spatial distribution of Cu, Co, Mn, Ni, Fe, and additional elements, such as oxygen.

XPS measurements were performed on a Kratos AXIS Supra+ using an Al Kα source (photon energy = 1486.6 eV). Survey scans were acquired over 0–1200 eV, followed by high-resolution scans with a pass energy of 20 eV. Charge compensation was employed when necessary, and binding energies were calibrated to the C 1s peak at 284.8 eV.

Optical Spectroscopy

Optical absorption measurements were conducted using a SCI-UV1000 spectrophotometer manufactured by Scilogex USA. The instrument is equipped with a deuterium

lamp as the ultraviolet source and a tungsten lamp as the visible to near infrared source, providing a wavelength range of 200 to 1000 nanometers. Quartz cuvettes with a 3.5 milliliter volume and a 10-millimeter path length were used for all measurements. Spectra were recorded in standard absorbance mode across the full wavelength range with automatic lamp switching, and baseline correction was performed using a solvent reference prior to sample analysis.

Photoluminescence (PL) spectroscopy was performed at ORNL CNMS on a HORIBA Fluorolog 3T. Excitation was stepped from 250 to 500 nm in increments of 1 nm, and for each excitation step the emission spectrum was recorded from 250 to 500 nm. Excitation and emission monochromator slits were both set to 8 nm.

3.3.3 Simulations and Quantitative Calculations

We simulated post-ablation cooling of a single high-entropy-alloy nanoparticle in COMSOL Multiphysics version 6.3 [204]. For the ethanol case, the computational domain was a single three-dimensional sphere of radius 40 nm (the particle). The Heat Transfer in Solids interface was used with an initial particle temperature of 1200 °C ($\approx 1.47\times10^{3}$ K). Heat loss to the surrounding ethanol was applied as a convective heat-flux boundary on the particle surface with external temperature 298 K [205]. For the liquid-nitrogen case, the domain comprised three concentric spheres: a 40 nm particle, a 10 nm nitrogen-gas shell, and an outer LN_2 region. The outer boundary of the LN_2 region was held at 77 K, and heat flowed by conduction across the solid–gas–liquid stack, and the gas shell and LN_2 were initialized at the bath temperature. The solid was assigned density 8000 kg m^{-3}, heat capacity 450 J kg^{-1} K^{-1}, and thermal conductivity 20 W m^{-1} K^{-1}, values consistent with reports for equiatomic CoCrFeMnNi and closely related single-phase fcc concentrated solid-solution alloys [206]. A literature solidus–liquidus interval of ∼1290–1340 °C for CrMnFeCoNi was plotted on the cooling curves as a reference [207]. For ethanol, the effective boundary conductance followed a conduction-limited estimate with Nusselt number = 2, giving

$h = k_e/R_{\mathrm{np}} \approx 4.3\times10^{6}$ W m^{-2} K^{-1} for $k_e = 0.17$ W m^{-1} K^{-1} and $R_{\mathrm{np}} = 40$ nm. This is lower than the 10^{8}–10^{9} W m^{-2} K^{-1} interfacial conductances reported for metal–water systems but is appropriate for an isolated nanoparticle where transport in the stagnant layer is conduction-limited [208, 209, 210]. Time-dependent studies ran from 0 to 1 μs, and output was recorded every 1 ns for ethanol and every 10 ps for LN_2 (to provide 100$\times$ higher temporal resolution).

Simulation geometry and meshing. For the ethanol case the domain was a single sphere meshed with a free tetrahedral grid using one Size node: maximum element size 10 nm, minimum element size 2 nm, element growth rate 1.3, curvature resolution 0.3, no boundary layer or swept mesh. This produced approximately 1–2×10^{4} elements and was verified to be converged with respect to the reported surface-temperature output. For liquid nitrogen, two Size nodes were used: (i) a surface-refinement node on the nanoparticle boundary (maximum 3 nm, minimum 1 nm) and (ii) a domain refinement node for the gas shell (maximum $t_{\mathrm{gas}}/5 = 2$ nm, minimum $t_{\mathrm{gas}}/20 = 0.5$ nm). The LN_2 far-field domain used the initial global size from the first build step. This configuration produced a few $\times10^{4}$ elements and was likewise converged for the surface-temperature output. No boundary layer or swept meshes were used in either case.

Solver configuration. Both models used a Time Dependent study with the default backward differentiation formula (BDF) time integrator, a relative tolerance of 1×10^{-5}, a fully coupled nonlinear formulation with automatic nonlinear stepping, and the default PARDISO direct linear solver. Surface temperature was monitored by a single point probe located at coordinates $(R_{\mathrm{np}}, 0, 0)$ on the nanoparticle surface. No events, additional heat sources, or supplementary physics interfaces were included. Time and temperature data were exported from the probe table as plain text and all cooling curves were plotted from those files. The complete material property values and study controls used in both simulations are summarized in Tables 3.1–3.3.

Table 3.1: Nanoparticle and solver parameters common to both the ethanol and liquid-nitrogen simulations.

Parameter	Value	Unit	Note
NP radius, R_{np}	40	nm	Nanoparticle radius
NP initial temperature, T_{init}	1200	°C	$\approx 1.47 \times 10^3$ K
Solid density, ρ_s	8000	$\mathrm{kg \cdot m^{-3}}$	HEA effective
Solid heat capacity, $c_{p,s}$	450	$\mathrm{J \cdot kg^{-1} \cdot K^{-1}}$	
Solid thermal conductivity, k_s	20	$\mathrm{W \cdot m^{-1} \cdot K^{-1}}$	
Time integrator	BDF	–	default
Relative tolerance	1×10^{-5}	–	
Linear solver	PARDISO	–	

Table 3.2: Ethanol simulation parameters (convective heat-flux boundary condition model).

Parameter	Value	Unit	Note
Bath temperature, T_{bath}	298	K	[205]
Ethanol thermal conductivity, k_e	0.17	$\mathrm{W \cdot m^{-1} \cdot K^{-1}}$	at ∼25 °C
Nusselt number, Nu	2	–	conduction-limited
Convective coefficient, $h = k_e/R_{\mathrm{np}}$	4.25×10^6	$\mathrm{W \cdot m^{-2} \cdot K^{-1}}$	applied on NP surface
Time window	$0–1.0 \times 10^{-6}$	s	
Output step	1×10^{-9}	s	1 ns
Mesh Size node	max 10; min 2; growth 1.3; curvature 0.3	nm	single node; no BL

Table 3.3: Liquid-nitrogen simulation parameters (conduction through NP/gas-shell/LN_2 stack). The far-field LN_2 boundary is held at 77 K throughout the simulation.

Parameter	Value	Unit	Note
Gas-shell thickness, t_{gas}	10	nm	
LN_2 far-field radius, R_{out}	1000	nm	
Bath/far-field temperature	77	K	[205]
Gas thermal conductivity, k_g	0.026	$\mathrm{W{\cdot}m^{-1}{\cdot}K^{-1}}$	N_2 gas
Gas heat capacity, $c_{p,g}$	1040	$\mathrm{J{\cdot}kg^{-1}{\cdot}K^{-1}}$	
Gas density, ρ_g	1.2	$\mathrm{kg{\cdot}m^{-3}}$	
LN_2 thermal conductivity, k_l	0.15	$\mathrm{W{\cdot}m^{-1}{\cdot}K^{-1}}$	at ∼77 K
LN_2 heat capacity, $c_{p,l}$	2040	$\mathrm{J{\cdot}kg^{-1}{\cdot}K^{-1}}$	
LN_2 density, ρ_l	800	$\mathrm{kg{\cdot}m^{-3}}$	
Time window	$0–1.0 \times 10^{-6}$	s	same as ethanol
Output step	1×10^{-11}	s	10 ps; 100× denser
Mesh (NP boundary)	max 3; min 1	nm	first Size node
Mesh (gas shell)	max 2; min 0.5	nm	second Size node; no BL

The enthalpy of mixing for the alloy compositions considered, ΔH_{mix}, also referred to as the enthalpy of formation, is given by [199, 211]. We assume the enthalpy of mixing is mainly used to describe thermodynamic properties of solution, whereas the enthalpy of formation is often used for some intermetallic compounds [212].

$$\Delta H_{\mathrm{mix}} = \sum_{i=1, i\neq j}^{n} \Omega_{ij} c_i c_j = 4 \sum_{i=1, i\neq j}^{n} \Delta H_{ij}^{\mathrm{mix}} c_i c_j. \tag{3.3}$$

Here, c_i and c_j refer to the atomic percentages corresponding to the i-th and j-th alloy component, respectively. The term n represents the number of alloy components, whereas

$$\Omega_{ij} = 4\,\Delta H_{ij}^{\mathrm{mix}}. \tag{3.4}$$

is an interaction parameter between the i-th and j-th alloy components. Miedema's model provides a simple approach for calculating the binary mixing pair combinations, $\Delta H_{ij}^{\mathrm{mix}}$ [213]. Based on notions of atomic volume and solvation energy, and originally intended for application to liquids, the semi-empirical Miedema's model defines pairwise interactions of atomic species without regard to the actual crystal structure,

producing [214]

$$\Delta H_{ij}^{\text{mix}} = f(c_i, c_j)\left(c_i\,\Delta H_{\alpha\,\text{in}\,\beta}^{\text{sol}} + c_j\,\Delta H_{\beta\,\text{in}\,\alpha}^{\text{sol}}\right). \tag{3.5}$$

where

$$f(c_i, c_j) = c_i\,c_j\,(1 + \delta c_i c_j). \tag{3.6}$$

represents the surface contact area of species i and j. Tabulated values for these parameters are available for many elements. The formulas for the enthalpy of mixing according to Miedema's model contain two additional terms, when applied to solid alloys [215, 214]. The first term, H_{elastic}, accounts for the elastic strain of solid solutions. The second term, H_{struct}, discriminates between FCC, hexagonal-close-packed and BCC structures of transition metals and depends on their valence electron counts [214]. Although Miedema's model was originally introduced for binary compounds, the model has been generalized to ternary compounds and beyond [216, 217, 218, 214]. This has enabled the screening of a large number of compounds. Miedema's model has been employed for predicting the formation of high-entropy glasses as well as HEAs [214, 211]. In this work, the binary mixing pair combinations, $\Delta H_{ij}^{\text{mix}}$, were estimated using an online Miedema Calculator [219, 220] with the estimates verified separately using a Python script developed by the Wolverton Research Group at Northwestern University [221]. Thermodynamic parameters assume ideal mixing.

3.4 Results and Discussion

3.4.1 Bulk Material Baseline Composition

Owing to its atomic-scale spatial resolution and quantitative detection efficiency, APT provides elemental ratios with the lowest statistical error among the techniques applied in this study. The measured composition (Co 26.45 at.%, Mn 25.33 at.%, Ni 23.70 at.%, Cu 17.85 at.%, Fe 6.68 at.%) is therefore taken as the most reliable baseline for assessing the true bulk stoichiometry. This benchmark is particularly important because subsequent compositional analyses of the nanoparticles rely on EDS. While EDS is less precise for bulk quantification, it offers the ability to probe both the bulk and the nanoscale particles under identical experimental conditions. For consistency in comparative thermodynamic calculations presented later in the manuscript, EDS values are used for both the starting alloy and the nanoparticles, with the APT dataset serving as the reference validation for bulk accuracy.

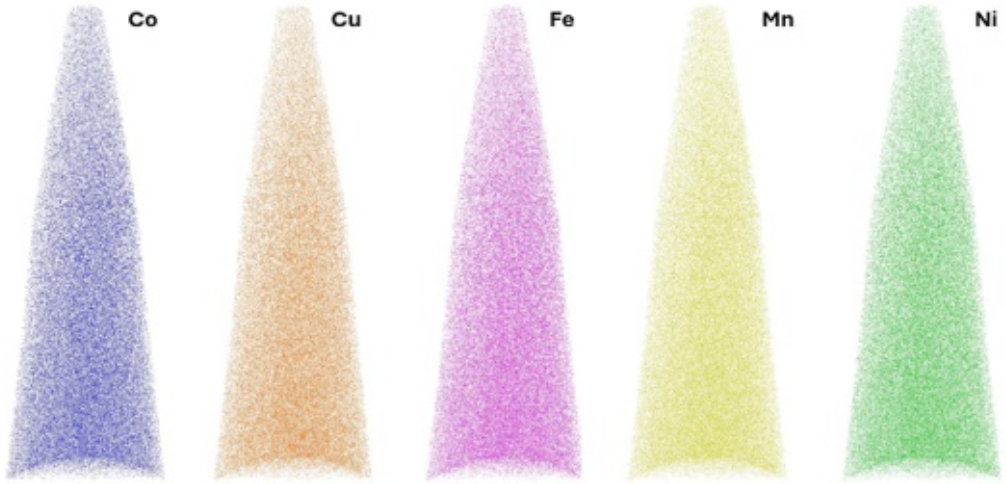


Figure 3.1: Reconstruction of the bulk $CuCoMn_{1.75}NiFe_{0.25}$ alloy from atom probe tomography. The tip length is 500 nm.

Figure 3.1 shows the APT reconstruction of the bulk material. The spatially homogeneous distributions of Co, Mn, Ni, Cu, and Fe indicate no detectable elemental

segregation at the nanoscale, supporting the use of this dataset as the baseline composition for downstream comparisons.

3.4.2 Nanoparticle Microstructure

Figure 3.2 presents a series of high-resolution TEM images illustrating the morphology and defect structures of nanoparticles produced via femtosecond laser ablation in liquid nitrogen and ethanol. Figure 3.2a shows a representative spherical nanoparticle with an inset selected area electron diffraction pattern confirming an FCC crystal structure. Closer examination of the lattice fringes in Figure 3.2c reveals pronounced stacking faults and nanotwins near the particle edge, possibly originating from the rapid solidification conditions inherent to laser ablation.

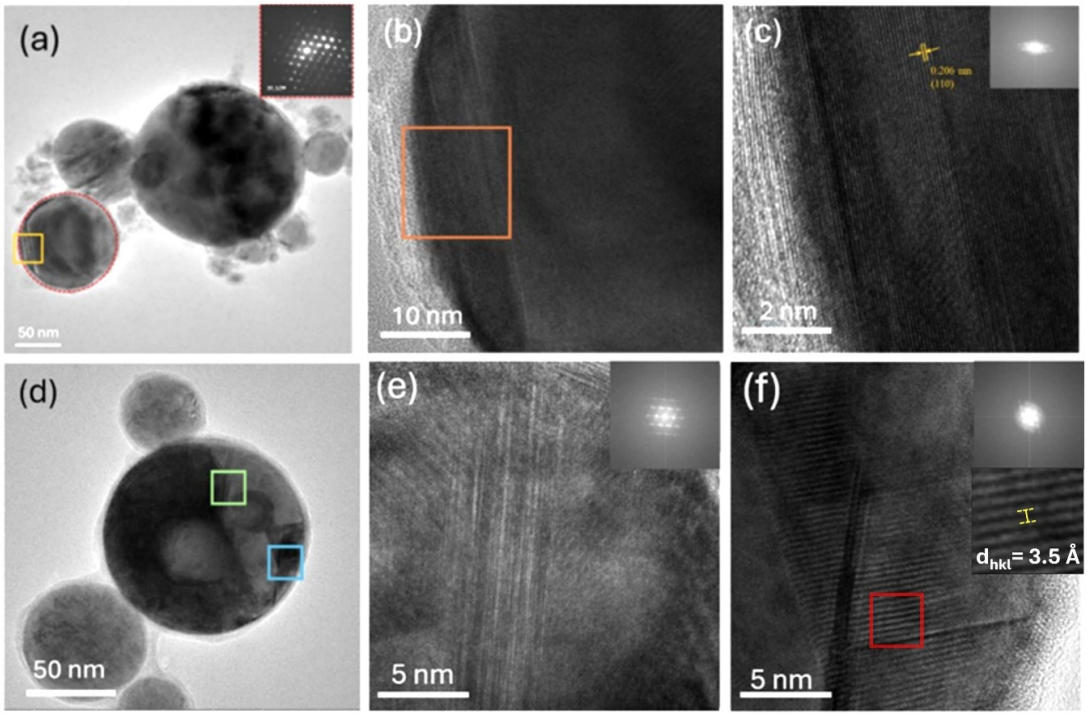


Figure 3.2: High-resolution TEM images of nanoparticles ablated in LN_2 (a–c) and ethanol (d–f). In (a), the orange box marks the region enlarged in (b,c), showing lattice fringes and stacking faults/nanotwins near the particle edge. In (d), the green and blue boxes indicate areas enlarged in (e,f), highlighting crystallinity and defect structures. Stacking faults/nanotwins are visible near the nanoparticles' grain boundary or edge. Insets in (b,e,f) are FFT patterns.

Figure 3.2d–f display HRTEM images of nanoparticles generated in ethanol. The particles are generally spherical with no plastic deformation and exhibit a uniform, thin, low-contrast outer layer, suggesting the presence of an organic coating due to solvent interactions during ablation. Some areas of the particles show continuous lattice fringes across their volume, indicating single-crystalline character with minimal grain boundaries, while others contain multiple crystalline domains separated by darker contrast regions, consistent with polycrystalline structures formed by rapid quenching or coalescence. Lattice-fringe measurements yield an interplanar spacing of ∼0.20 nm, consistent with the FCC symmetry. Additionally, linear-fringe deviations and disruptions are observed, indicative of stacking faults or twin boundaries. In some of the larger particles examined, subtle contrast variations near the core suggest localized strain or elemental heterogeneity.

Figure 3.3 presents a detailed crystallographic analysis of nanoparticles ablated in ethanol using virtual dark-field (VDF) imaging and localized diffraction-pattern mapping. The averaged diffraction pattern from the entire particle, shown in Figure 3.3d, reveals multiple concentric rings (2–3 rings), characteristic of a polycrystalline structure composed of randomly oriented nanocrystalline domains. Typically, polycrystals are indexed as shown, even though they may display some individual diffraction spots.

These concentric rings were used to generate VDF images corresponding to specific lattice spacings, subsequently combined into an RGB composite image (Figure 3.3e). In the VDF images, numerous discrete bright spots appear throughout the field of view, each representing a localized nanocrystalline domain contributing to specific diffraction rings. The high density and clear spatial separation of these bright spots confirm the polycrystalline nature of the particles. The RGB composite image distinctly highlights regions corresponding to dominant diffraction characteristics, such as the (111), (220), or nanocrystalline-type orientations. The multicolored domains visible in the composite image correspond to crystallites differing in orientation and lattice spacing, with sizes approximately 2–4 nm. This observation

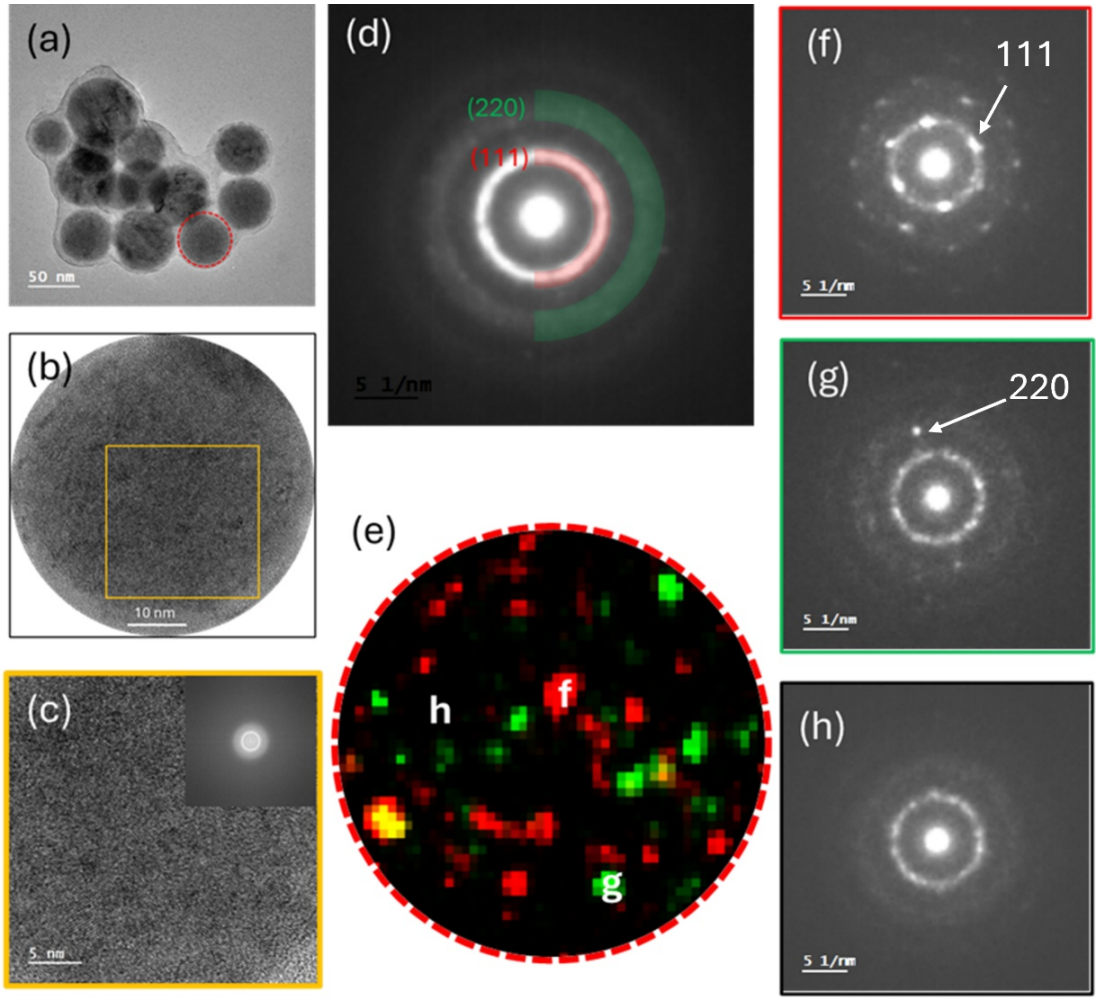


Figure 3.3: Structural analysis of nanoparticles ablated in ethanol. (a) Bright-field TEM image showing a representative agglomeration of spherical nanoparticles. (b) Low-magnification image highlighting the region selected for 4D-STEM analysis (yellow box). (c) High-resolution STEM image with an inset diffraction pattern confirming a nanocrystalline FCC structure. (d) Averaged diffraction pattern from the scanned region, with indexed (111) and (220) rings indicating an FCC symmetry. (e) RGB composite of virtual dark-field images constructed from the (111) and (220) diffraction rings, illustrating spatial variation in nanocrystalline domain orientations. (f–h) Localized diffraction patterns corresponding to positions marked in (e), showing distinct diffraction spot arrangements consistent with variations in the local crystal orientation and grain structure.

aligns with the TEM findings in Figures 3.2b–c, where irregular contrast, lattice discontinuities, and localized defect structures such as stacking faults and twin boundaries indicate multiple internal nanocrystalline domains.

Selected area diffraction patterns from specific regions within the particle are presented in Figures 3.3f–h, each illustrating distinct crystalline orders and orientations. Panel (f), representing a region dominated by (111) orientation, exhibits sharp ring segments accompanied by distinct, strong individual diffraction spots corresponding to the (111) lattice planes. Panel (g) corresponds to a region dominated by the (220) orientation, showing clear individual diffraction spots over faint rings, indicating locally more ordered nanocrystalline structure. In contrast, panel (h) represents a region typifying a highly disordered nanocrystalline structure, displaying broad, diffuse diffraction rings without clear individual spots, reflective of smaller crystallite sizes and random orientations.

The considerable variability in diffraction patterns over short spatial distances further confirms that each particle comprises numerous nanocrystals with varying orientations and structural coherence. Many ethanol-ablated nanoparticles thus appear as compact aggregates of nanocrystalline grains rather than single crystals or large polycrystals, consistently supported by high-resolution TEM images (Figure 3.2c–e) and localized diffraction analysis.

3.4.3 Particle Morphology

Figure 3.4 shows the particle-size distributions obtained from the TEM analysis of nanoparticles synthesized by femtosecond laser ablation in liquid nitrogen and ethanol. For the sample produced in liquid nitrogen, the histogram reveals a relatively broader distribution of particle sizes, with most particles exhibiting radii between 10 and 60 nm. The calculated mean particle radius is 44.82 nm, accompanied by a standard deviation of 20.30 nm, indicating substantial variability in particle size. The histogram features a pronounced peak in the 30–40 nm range, yet a significant

fraction of particles exhibits radii extending beyond 80 nm, reflecting a long-tailed distribution toward larger sizes. The corresponding low-magnification TEM images show clusters of well-dispersed particles with predominantly spherical morphologies and limited aggregation. While the majority of particles appear moderately uniform, the broader size spread is visually supported by the presence of both smaller and much larger particles within the same field of view, consistent with the histogram trend.

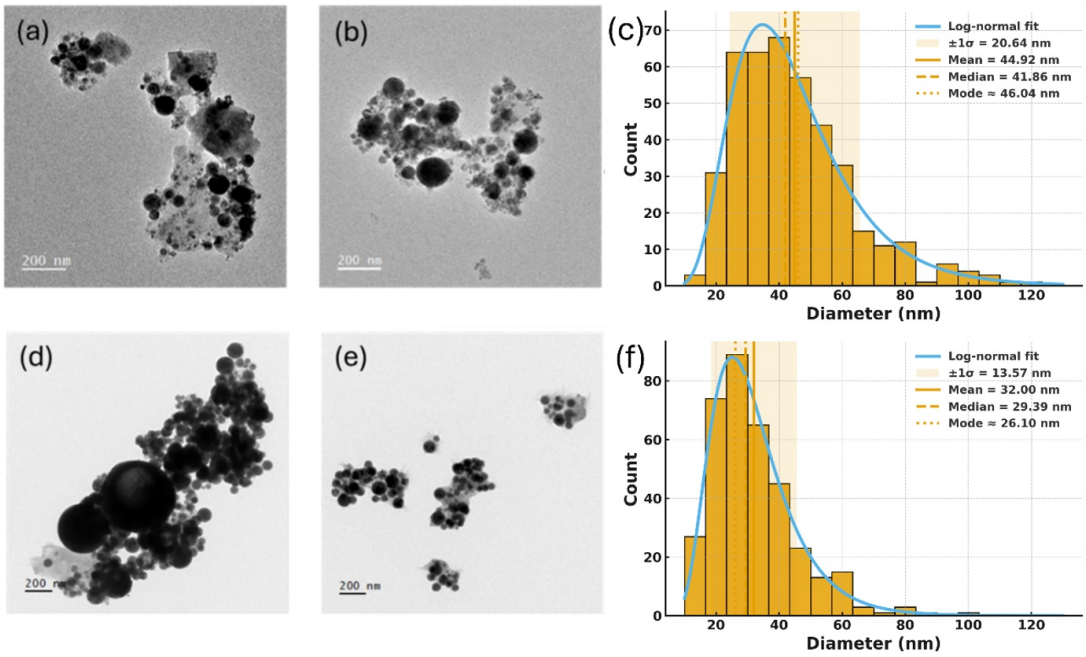


Figure 3.4: Particle size distributions and low-magnification TEM images of nanoparticles produced by femtosecond laser ablation. (a–c) Nanoparticles ablated in ethanol: (a,b) TEM images, (c) size distribution. (d–f) Nanoparticles ablated in liquid nitrogen: (d,e) TEM images, (f) size distribution.

In contrast, the sample ablated in ethanol demonstrates a much narrower and more left-skewed particle-size distribution. The mean particle radius in this case is measured to be 32.36 nm, with a lower standard deviation of 13.06 nm, highlighting improved size uniformity. The histogram reveals a dense concentration of particles within the 10–50 nm range, with far fewer particles observed above this range, suggesting a more confined growth regime. The TEM images associated with

this sample, shown in Figure 3.4d, depict a mixture of particle sizes, including a number of larger particles embedded within tightly packed agglomerates. The ethanol environment appears to promote coalescence of smaller clusters into denser assemblies, possibly due to lower cooling rates and stronger solvent–particle interactions. This observation contrasts with the more dispersed particle formation in liquid nitrogen and indicates that ethanol ablation leads to the generation of slightly larger but more size-consistent particles. These trends imply notable differences in ablation-plume dynamics, energy dissipation, and condensation behavior between the two liquid media, which ultimately influence nucleation, growth, and aggregation mechanisms during nanoparticle formation [192].

3.4.4 Elemental Composition and Distribution

Table 3.4: Elemental composition (wt%) of fs-ablated nanoparticles compared with theoretical and bulk values.

Element	**Theoretical (wt%)**	**Bulk (wt% ± err.)**	**LN_2 (wt%)**	**Ethanol (wt%)**
Cu	20	24.61 ± 4.13	31.0 ± 3.3	33.29 ± 3.50
Co	20	23.16 ± 3.63	20.2 ± 2.4	21.53 ± 2.57
Mn	35	23.45 ± 3.40	22.8 ± 1.5	18.28 ± 1.28
Ni	20	23.25 ± 3.68	21.4 ± 2.7	21.31 ± 2.74
Fe	5	5.53 ± 4.43	4.7 ± 0.7	5.59 ± 0.79

Table 3.4 presents the elemental compositions of nanoparticles synthesized via femtosecond laser ablation in liquid nitrogen and ethanol, alongside the theoretical and bulk compositions. The bulk material, analyzed using EDS, shows a manganese content of 23.45 ± 3.40 wt%, which is well below the theoretical value of 35 wt%. This discrepancy suggests that Mn is prone to evaporation during the fabrication process. Prior studies have indicated that elements like manganese can evaporate rapidly when exposed to laser irradiation due to their chemical properties, leading to reduced concentrations in the final material [222, 223].

In both liquid-nitrogen and ethanol-ablated nanoparticles, the Mn content is further reduced compared to the bulk composition, with values of 22.8 ± 1.5 wt% and 18.28 ± 1.28 wt%, respectively. This trend indicates that the ablation environment influences the extent of Mn loss, with ethanol leading to a more pronounced reduction. The consistent overestimation of copper in both ablation environments, with measured values exceeding the theoretical 20 wt%, is attributed to the use of copper grids during EDS analysis, which can introduce artifacts in the measured composition.

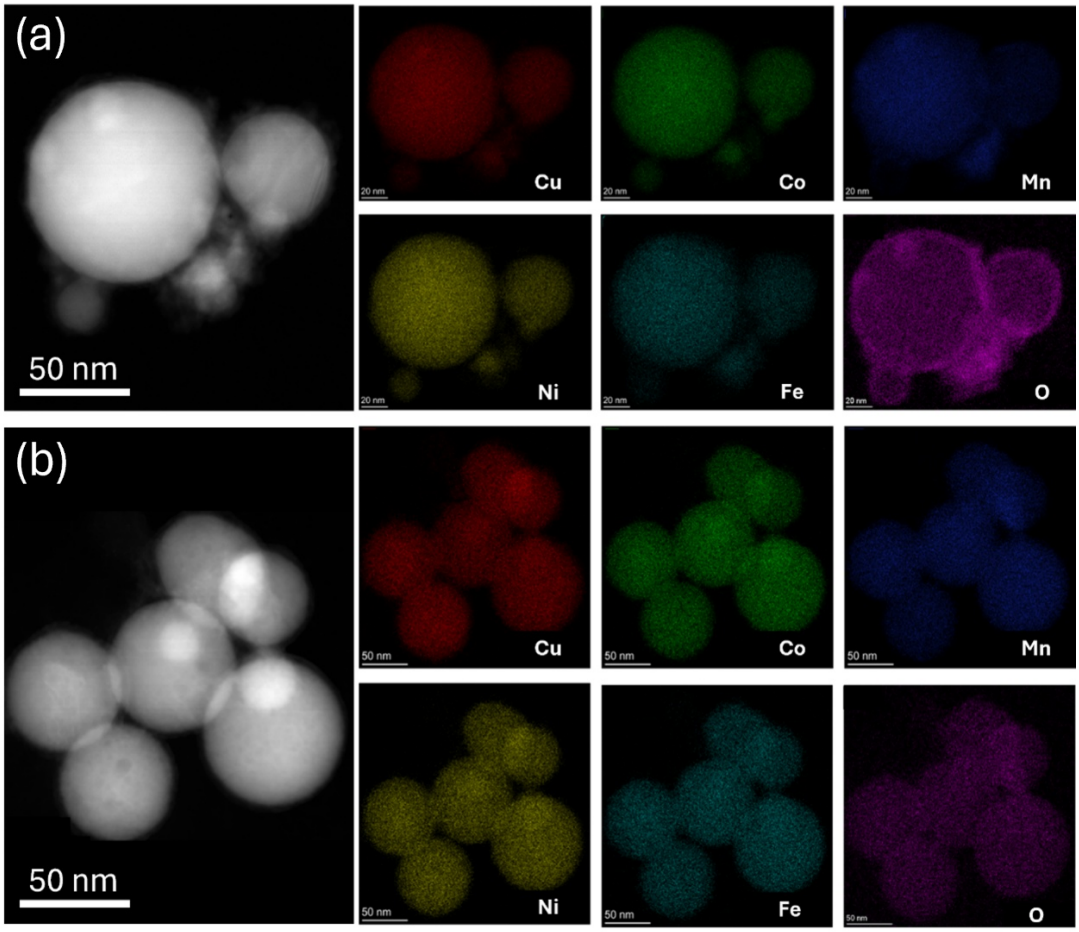


Figure 3.5: EDS mapping on the femtosecond-laser ablated nanoparticles in LN_2 (a) and ethanol (b).

Figure 3.5 shows STEM-EDS mapping of representative nanoparticles synthesized by femtosecond laser ablation in liquid nitrogen and ethanol. In both cases, the HAADF images reveal spherical particles with varying diameters, consistent with the size distributions previously shown. The elemental maps combined with Table 3.4 confirm the presence of all five principal metal components, Cu, Co, Mn, Ni, and Fe, within the particles. In the liquid-nitrogen sample, the EDS signals for all five metals are spatially uniform across the particle volumes, indicating a homogeneous elemental distribution. The oxygen signal is concentrated at the particle surfaces, suggesting the presence of a thin oxide shell formed after synthesis. In the ethanol-ablated sample, the metal elements are also detected throughout the particles, and their distributions appear uniform at this spatial resolution. However, the oxygen signal in this case does not show strong surface localization but is instead more diffusely distributed.

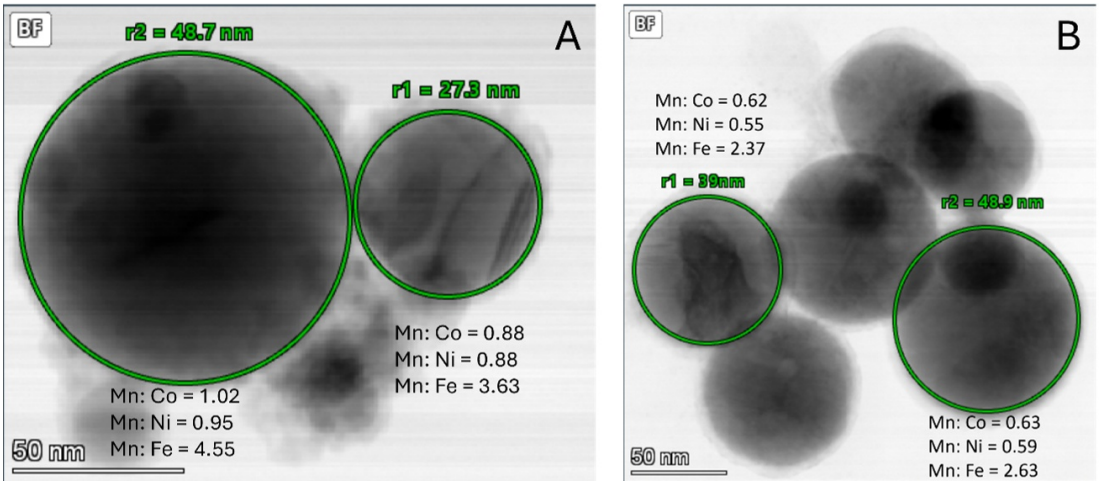


Figure 3.6: STEM bright-field images and corresponding Mn-based elemental ratios for nanoparticles ablated in (A) liquid nitrogen and (B) ethanol.

Figure 3.6 provides specific insights into the chemical uniformity across distinct crystallographic structures formed during femtosecond laser ablation in different liquid media. In liquid nitrogen (Figure 3.6A), the elemental ratios of manganese relative to cobalt, nickel, and iron (Mn:Co:Ni:Fe $\approx$ 4:4:4:1) are nearly identical for single-crystalline and polycrystalline nanoparticles. This indicates that the internal chemical distribution remains uniform irrespective of crystallographic differences

within the LN_2 medium, suggesting negligible crystallinity-dependent elemental segregation. In ethanol-ablated nanoparticles (Figure 3.6B), however, a consistent yet distinct elemental ratio emerges (Mn:Co:Ni:Fe $\approx$ 2.5:4:4:1), specifically identified in polycrystalline structures. Unlike the LN_2-ablated samples, this distinct ratio highlights a notable, crystallinity-dependent compositional difference exclusive to ethanol synthesis.

Table 3.5: Atomic composition from XPS (at%).

Element	**Ethanol (at%)**	**LN_2 (at%)**
Cu	22.75 ± 1.1	24.52 ± 1.2
Ni	19.47 ± 1.0	18.46 ± 0.9
Co	16.16 ± 0.8	23.19 ± 1.2
Fe	9.89 ± 0.5	23.42 ± 1.2
Mn	31.73 ± 1.6	10.40 ± 0.5

Table 3.5 lists the atomic percentages of Cu, Ni, Co, Fe and Mn derived from XPS. A complete breakdown by orbital, including fitted binding energies, FWHM values, and individual peak contributions for each element, is provided in Table 3.6. Corresponding core-level spectra for all five metals, the O 1s region, and the full survey scan are shown in Figure 3.8. Manganese's apparent atomic percentage falls from 31.7 at% in ethanol-ablated particles to 10.4 at% in LN_2, whereas iron and cobalt percentages roughly double. Such shifts arise likely from surface oxide layering. High-resolution Mn 2p spectra (Figure 3.7a) reveal broad multiplet splitting of the Mn $2p_{3/2}$ and Mn $2p_{1/2}$ transitions. Figure 3.7b shows the O 1s region deconvoluted into two components at ~530 eV and ~531–532 eV, which correspond to lattice oxygen and oxygen-deficient species (vacancies or hydroxyls), respectively [224]. The relative oxygen-vacancy (OV) content can be estimated by a simple area ratio,

$$\text{OV ratio} = \frac{A_{\text{def}}}{A_{\text{lat}} + A_{\text{def}}} \times 100\%, \tag{3.7}$$

where A_{lat} and A_{def} are the fitted areas of the lattice-oxygen and defective-oxygen peaks [224]. Applying this formula to our data yields OV $\approx$ 33.4% for the ethanol-ablated sample and $\approx$ 55.1% for the LN_2-ablated sample, indicating that cryogenic quenching produces a more oxygen-deficient oxide shell. Because XPS probes only the top few nanometers of a material [225], the atomic percentages we report reflect the outermost surface rather than the entire material composition.

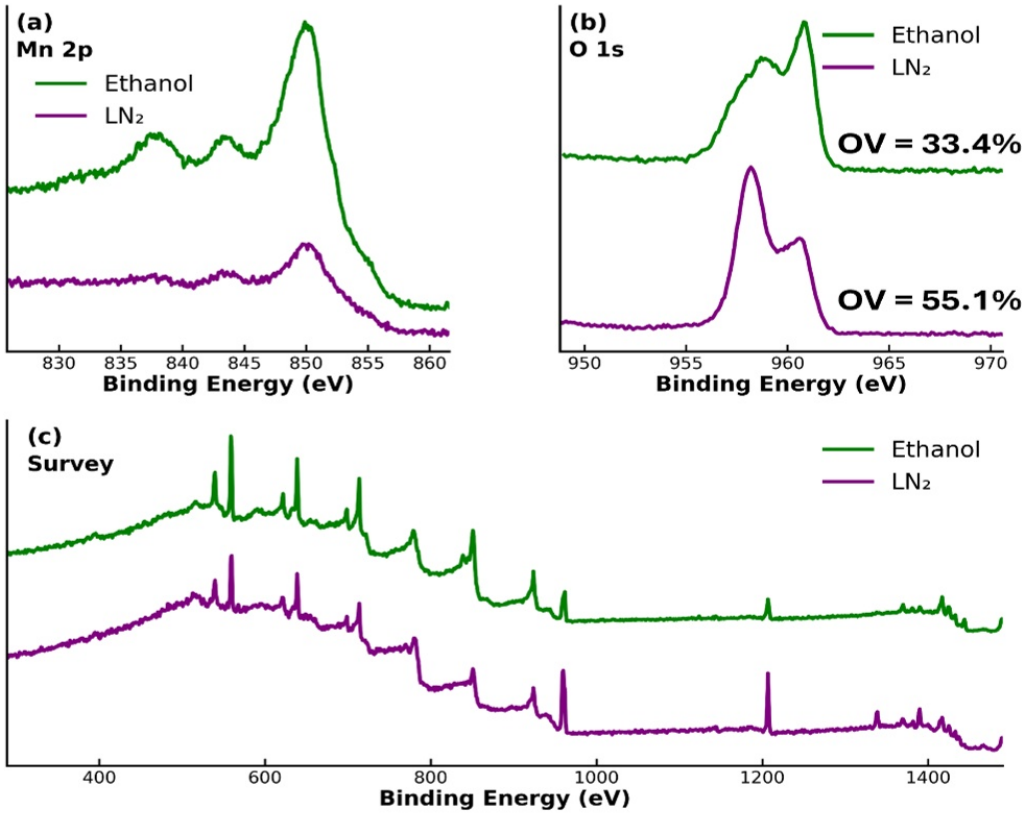


Figure 3.7: XPS scans showing (a) Mn 2p orbital, (b) O 1s orbital, (c) Survey scans.

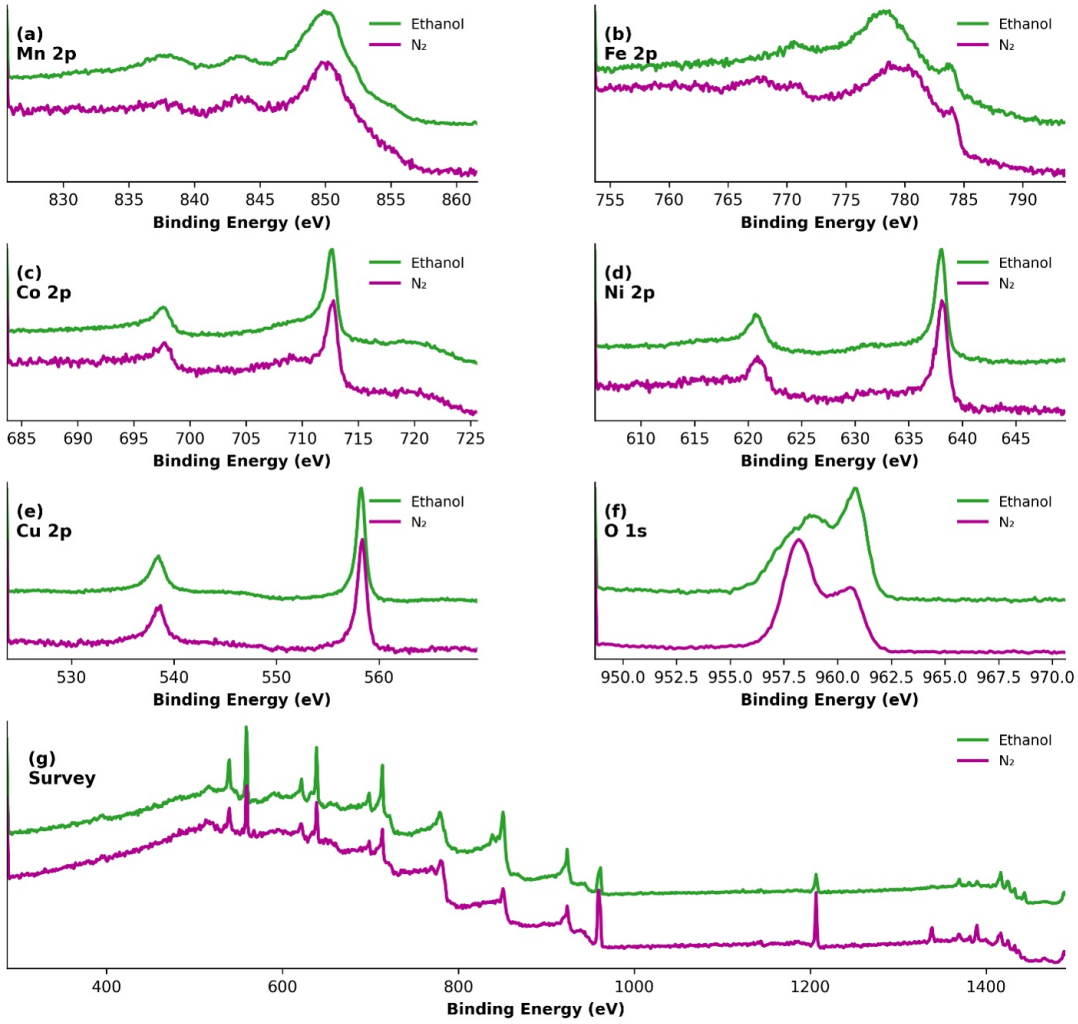


Figure 3.8: Full XPS core-level spectra of $CuCoMn_{1.75}NiFe_{0.25}$ nanoparticles ablated in ethanol and LN_2: (a) Mn 2p, (b) Fe 2p, (c) Co 2p, (d) Ni 2p, (e) Cu 2p, (f) O 1s, (g) survey. All binding energies are calibrated to the adventitious C 1s peak at 284.8 eV. The spectra supplement Table 3.6 by displaying each fitted multiplet component for direct visual comparison between the two ablation environments.

Table 3.6: Complete XPS fitting results. Binding energy and FWHM are given for each fitted peak component, and atomic percentages sum to the element totals in Table 3.5.

Particles in ethanol				Particles in LN_2			
Element	BE (eV)	FWHM (eV)	At.%	Element	BE (eV)	FWHM (eV)	At.%
Cu 2p	932.3	0.97	5.56	Cu 2p	932.2	1.05	3.60
	952.1	1.45	2.79		952.0	1.57	1.81
	946.5	6.58	2.06		946.9	6.58	1.26
	954.5	6.00	1.37		954.5	6.00	0.90
Cu 2p Total	–	–	22.75	Cu 2p Total	–	–	24.52
Ni 2p	852.6	1.10	4.61	Ni 2p	852.5	1.15	2.62
	869.8	1.65	2.31		869.7	1.73	1.31
	856.8	7.05	2.14		856.7	5.80	0.77
	874.0	4.71	1.02		874.4	5.66	1.00
Ni 2p Total	–	–	19.47	Ni 2p Total	–	–	18.46
Co 2p	778.0	0.96	3.12	Co 2p	777.9	1.01	1.74
	793.1	1.69	1.56		793.0	1.77	0.87
	780.8	5.94	2.84		781.7	6.88	3.01
	795.9	10.39	0.85		796.8	12.03	1.54
Co 2p Total	–	–	16.16	Co 2p Total	–	–	23.19
Fe 2p	706.6	1.70	1.05	Fe 2p	706.5	1.70	1.21
	720.2	1.70	0.53		720.1	1.70	0.61
	709.2	3.75	2.36		709.3	3.75	3.60
	722.8	3.75	1.18		722.9	3.75	1.81
Fe 2p Total	–	–	9.89	Fe 2p Total	–	–	23.42
Mn 2p	640.8	3.88	10.95	Mn 2p	640.8	2.85	2.14
	652.5	5.82	5.48		652.5	4.28	1.07
Mn 2p Total	–	–	31.73	Mn 2p Total	–	–	10.40

3.4.5 Thermodynamic Stability

Table 3.7 provides calculated thermodynamic parameters based on measured compositions of the theoretical alloy, the bulk material, and nanoparticles. The ablated samples show significant changes in the mixing enthalpy (ΔH_{mix}), entropy of mixing, and the thermodynamic parameter, Ω, all of which are sensitive to deviations

Table 3.7: Thermodynamic quantitative parameters for experimental materials.

Sample	Alloy composition	Atomic radius difference [%]	VEC	Solvus temp. [°C]	Entropy of mixing [J mol^{-1} K^{-1}]	Enthalpy of mixing (ΔH_{mix}) [kJ/mol]
Theoretical	Co 20 Cu 20 Fe 5 Mn 35 Ni 20	3.65	8.85	1319.3	12.347	2.7772
Bulk	Co 23.09 Cu 22.75 Fe 5.82 Mn 25.07 Ni 23.27	3.30	9.13	1332.4	12.69	4.0447
LN_2 #1	Co 21.7 Cu 30.1 Fe 5.6 Mn 20.7 Ni 21.8	3.07	9.35	1313.4	12.574	6.5047
LN_2 #2	Co 20.2 Cu 31.0 Fe 4.7 Mn 22.8 Ni 21.4	3.13	9.33	1304.6	12.437	6.4894
LN_2 #3	Co 21.1 Cu 28.3 Fe 5.0 Mn 23.1 Ni 22.7	3.18	9.28	1314.7	12.545	5.7041
Ethanol #1	Co 20.9 Cu 35.5 Fe 5.8 Mn 14.0 Ni 23.7	2.70	9.61	1307.2	12.275	7.7712
Ethanol #2	Co 22.4 Cu 32.7 Fe 5.7 Mn 15.2 Ni 24.1	2.78	9.53	1315.9	12.406	7.2506
Ethanol #3	Co 21.53 Cu 33.29 Fe 5.59 Mn 18.28 Ni 21.31	2.93	9.46	1306.7	12.451	7.4461
Ethanol #4	Co 21.9 Cu 32.3 Fe 5.8 Mn 18.1 Ni 21.9	2.94	9.44	1311.1	12.506	7.2078
Ethanol #5	Co 16.5 Cu 34.9 Fe 4.1 Mn 22.5 Ni 21.9	3.09	9.43	1288.5	12.17	6.8858
Ethanol #6	Co 14.8 Cu 36.2 Fe 3.3 Mn 24.5 Ni 21.3	3.13	9.41	1278.5	11.941	6.9388

in elemental composition, particularly the reduction of manganese and the enrichment of copper [223, 161]. Because these descriptors are calculated from compositions measured by EDS, they should be viewed as model-based estimates rather than exact values, and a modest systematic uncertainty from the EDS quantification, especially in the Mn and Cu contents, should be acknowledged.

Compared to the theoretical and bulk compositions, the ethanol-ablated samples consistently yield lower Ω values, in some cases dropping below 2.5. This reduction is driven by a combination of the increased Cu and decreased Mn content, both of which influence the enthalpy of mixing. Ethanol-ablated particles exhibit the highest ΔH_{mix} values, exceeding 7.7 kJ mol^{-1} in some cases, compared to 2.8 kJ mol^{-1} for the theoretical alloy and approximately 6.5 kJ mol^{-1} for the most Cu-rich LN_2 particles. These elevated mixing enthalpies suggest a greater driving force toward phase separation, which aligns with the structural disorder observed in nanocrystalline particles formed in ethanol.

While the theoretical alloy has a Ω value above 7, many ethanol-ablated samples fall below 3, well beneath the empirical threshold ($\Omega \sim 1.1$) often cited for multicomponent solid-solution stability. These values suggest that the nanoparticles formed in ethanol are thermodynamically less stable and more likely to exhibit local chemical fluctuations consistent with the particle-to-particle compositional variation shown in EDS and the nanocrystalline substructure shown in Figure 3.2. Samples ablated in liquid nitrogen show intermediate behavior, with Ω values ranging from 3.0

to 3.5 and ΔH_{mix} values near 5.7 to 6.5 kJ mol^{-1}. While these values are still elevated compared to the bulk, they suggest relatively greater thermodynamic stability than the ethanol-synthesized particles. Particles produced in LN_2 tend to be more compositionally uniform and structurally continuous, forming fewer nanocrystalline aggregates and display more homogeneous lattice fringes in high-resolution TEM. To visualize these trends and the uncertainty from composition, Figure 3.9 plots Ω versus ΔH_{mix} for the theoretical alloy, bulk, and all nanoparticle compositions, with LN_2 and ethanol data shown as point clouds and mean $\pm 1\sigma$ error crosses derived from the EDS-based thermodynamic calculations.

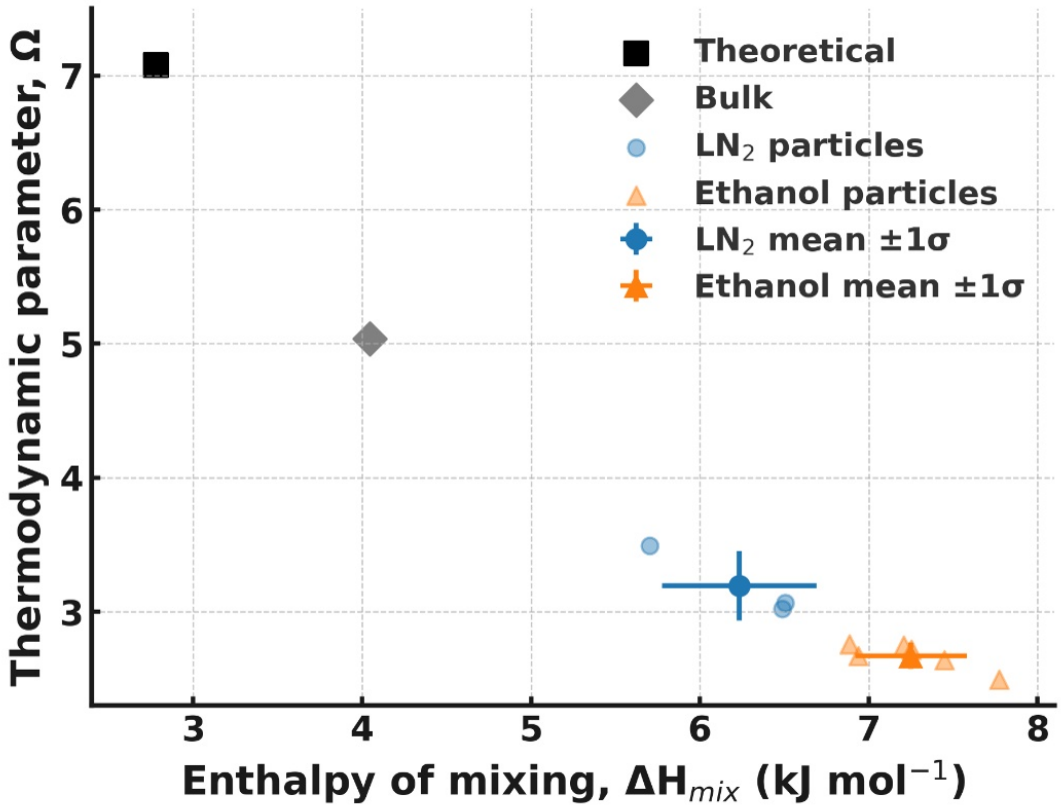


Figure 3.9: Thermodynamic map in Ω–ΔH_{mix} space.

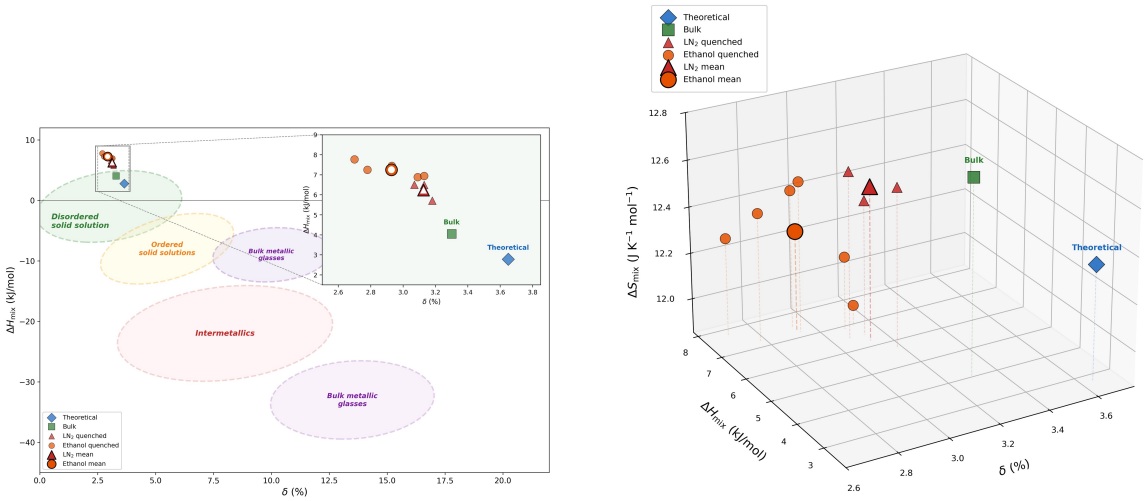
Copper from EDS analysis appears artificially high because of signal bleed from the lacey carbon-coated copper TEM grids. Because the over-reporting is systematic rather than random, the elevated Cu shifts all ΔH_{mix} and Ω calculations by a

constant offset without changing their relative ordering or qualitative conclusions. Consequently, our comparison of ethanol versus LN_2 remains valid: although absolute Cu and Mn values deviate, the relative increase in mixing enthalpy and collapse in Ω under ethanol ablation still reflects genuine shifts in thermodynamic driving forces.

These composition shifts have a pronounced effect on phase stability. In the ideal equiatomic mixture, mixing enthalpy ΔH_{mix} is +2.8 kJ mol^{-1} and the empirical stability parameter Ω ($T\Delta S_{\mathrm{mix}}/|\Delta H_{\mathrm{mix}}|$) sits near 7, indicating strong entropy-dominated stabilization of a single solid solution. Ethanol-derived nanoparticles exhibit ΔH_{mix} of +6.9 to +7.8 kJ mol^{-1}, driven by loss of exothermic Mn–metal interactions and an increased fraction of endothermic Cu–metal pairs. Correspondingly, Ω collapses to $\sim$2.5, just above the empirical single-phase threshold of $\sim$1.1. Although formally in the single-phase regime, this low Ω signals a greatly diminished entropic buffer against local chemical fluctuations or short-range ordering.

Nanoparticles formed in liquid nitrogen occupy an intermediate regime. Their ΔH_{mix} values of +5.7 to +6.5 kJ mol^{-1} remain elevated relative to the bulk alloy but lower than in ethanol, and Ω values of 3.0–3.5 reflect a favorable entropy-enthalpy balance. Under these conditions, rapid quench locks in a homogeneous solid solution before significant demixing can occur, consistent with uniform EDS maps and single- or few-domain crystalline interiors observed by HRTEM. Although ΔH_{mix} still favors some degree of local ordering, the high Ω and ultrafast cooling kinetics inhibit long-range phase separation. In practical terms, these findings indicate that solvent choice tunes the thermodynamic stability of the metastable solid solution. Ethanol ablation pushes the alloy toward a high-enthalpy, low-Ω state prone to nanometer-scale chemical heterogeneity. Liquid nitrogen ablation preserves the original alloy's thermodynamic stability and yields chemically uniform, single-phase nanoparticles. This difference provides a design criterion: ethanol processing for catalytic or magnetic applications that benefit from local compositional gradients, and cryogenic processing when maximal phase fidelity and structural continuity are required.

To place these results in the context of established phase formation boundaries, fig. 3.10 maps all compositions in δ–ΔH_{mix} space alongside the empirical regions from Zhang et al. [211] for disordered solid solutions, ordered solid solutions, intermetallics, and bulk metallic glasses. All data points, including the theoretical, bulk, and laser-ablated compositions, fall within the disordered solid-solution region (fig. 3.10a), consistent with the single-phase FCC structure confirmed by XRD and electron diffraction. The inset magnifies the nanoparticle cluster and shows that ethanol-ablated particles, despite their elevated ΔH_{mix}, remain within the solid-solution boundary. fig. 3.10b extends this view into three dimensions by adding the ΔS_{mix} axis, showing the simultaneous decrease in configurational entropy and increase in mixing enthalpy for the ablated samples relative to the theoretical and bulk compositions.



(a) **(b)**

Figure 3.10: Thermodynamic stability maps for theoretical, bulk, and laser-ablated $CuCoMn_{1.75}NiFe_{0.25}$ compositions. (a) δ–ΔH_{mix} phase formation map with labeled phase regions. Inset magnifies the nanoparticle compositions. (b) Three-dimensional δ–ΔH_{mix}–ΔS_{mix} view of the same data.

Note. Phase formation boundaries adapted from [211].

3.4.6 Solvent-Controlled Cooling Dynamics and Defect Evolution

The choice of solvent alters the balance between nucleation and growth through its impact on heat removal. In ethanol, with its low thermal conductivity and heat capacity, the plasma plume cools relatively slowly. This slower quench produces a lower supersaturation of ablated vapor and molten clusters, leading to a reduced nucleation rate but allowing each nucleus more time to grow before the temperature falls below the solidification threshold. As a result, molten fragments coalesce into smaller particles with a broader size distribution, since growth dominates over nucleation [226, 227]. In liquid nitrogen, the 77 K bath temperature extracts heat almost instantaneously, driving the plume into extreme undercooling that sharply raises supersaturation and triggers a burst of nucleation. Classical nucleation theory predicts that higher supersaturation yields more nuclei per unit volume, but the ultrafast quench also limits the time available for each nucleus to grow [228]. At the same time, the low viscosity of cryogenic nitrogen promotes strong plume dispersion and rapid cavitation bubble collapse, fragmenting the nascent particles and preventing extensive coalescence. These effects produce a larger mean radius near 47 nm yet with a narrower distribution, reflecting a regime where nucleation and mechanical dispersion outweigh growth kinetics [229].

High-resolution TEM analysis (Figure 3.2) confirms that both sets of nanoparticles include single- and polycrystalline structures. However, ethanol ablation distinctly produces particles composed of multiple 2 to 4 nanometer crystallites, giving rise to a nanocrystalline internal structure. These fine crystallites are the product of a high nucleation rate and arrested growth, conditions characteristic of far-from-equilibrium solidification. Stacking faults and nanotwins are frequently observed in both sample sets, especially near particle edges and grain boundaries. These planar defects are common in cases of rapid solidification in face-centered cubic metals, where high undercooling and limited atomic mobility trap metastable stacking sequences and

twinned domains. The formation of these features is promoted under both ethanol and LN_2 ablation due to the ultrafast cooling rates inherent to femtosecond-pulsed laser processes, which can exceed 10^{12} K s^{-1} [230, 231, 117].

To quantitatively connect these structural observations to the thermal environment during ablation, we modeled the cooling of $CuCoMn_{1.75}NiFe_{0.25}$ droplets in ethanol and liquid nitrogen. The model simulates a 3D nanoparticle submerged in liquid nitrogen. A point probe was taken from the surface to represent the surface temperature of the material. The COMSOL simulation in Figure 3.11a, initialized at 1200 °C, which is near the liquidus of $CuCoMn_{1.75}NiFe_{0.25}$ [147] ($\approx 1.47 \times 10^3$ K) for a 40 nm droplet, shows that in ethanol the surface temperature falls to ∼200 °C ($\approx 4.7 \times 10^2$ K) over the first microsecond. Such behavior corresponds to cooling rates on the order of 10^9–10^{10} K s^{-1}, in agreement with theoretical estimates for laser ablation in liquids and two orders of magnitude slower than the 10^{12} K s^{-1} cooling rate of the ablated metal nanoparticle/condensate under femtosecond excitation [231, 232]. Under this moderate quench, the plume remains supersaturated for a longer time, enabling molten fragments to coalesce and crystallites to grow. This is in direct agreement of our TEM and chemical measurements and explains why ethanol-derived particles consist of 2–4 nm crystallites aggregated into larger nanocrystalline grains. In contrast, the liquid-nitrogen case implemented as a 40 nm particle surrounded by a 10 nm N_2 gas shell and embedded in an LN_2 bath (Figure 3.11b) extracts heat almost instantaneously: the droplet temperature plunges from $\sim 1.47 \times 10^3$ K to near the bath temperature (∼77 K) within ∼0.1 μs. Cooling rates in this regime approach the 10^{12} K s^{-1} expected for condensates formed in ultrafast laser ablation [116], driving extreme undercooling and a burst of nucleation while severely limiting subsequent growth. The low viscosity of liquid nitrogen also leads to rapid cavitation-bubble collapse and dispersal of the plume [11], suppressing coalescence and producing single-crystal nanoparticles with narrow size distributions which again, is in direct agreement with our tests. Comparable cryogenic quenching has been shown to kinetically freeze dislocations in Pt nanoparticles [233], which demonstrates the ability of liquid

nitrogen to lock in metastable structures. Taken together, the simulation results and these literature benchmarks confirm that solvent-dependent cooling rates govern the competition between nucleation and growth and thereby determine the distinct morphologies of the ethanol- and LN_2-derived nanoparticles. Further modeling with molecular dynamics is needed to resolve these dynamics in greater detail.

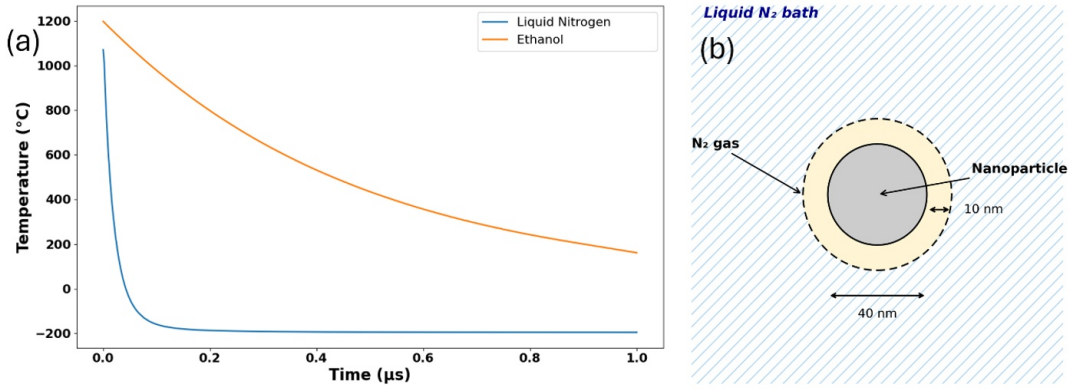


Figure 3.11: (a) COMSOL simulation of nanoparticle surface cooling in liquid media. (b) Geometry of LN_2 nanoparticle showing gas shell.

Unlike ultrafast femtosecond pulses, nanosecond laser pulses deposit energy over a duration much longer than the electron–phonon relaxation time of metals. Thus, a significant portion of the nanosecond pulse energy is converted into heat that diffuses into the target and surrounding fluid, creating a larger heat-affected zone and yielding comparatively slow cooling of the ablated material [234]. Femtosecond pulses, by contrast, deliver energy faster than thermal diffusion can occur. This confines the energy to a shallow surface layer and produces extremely high cooling rates on the order of 10^{12} K s^{-1} [235]. Such ultrarapid quenching promotes the nucleation of numerous small crystallites (and can even trap metastable amorphous or highly twinned structures) rather than allowing significant grain growth [236]. Consequently, experiments have shown that femtosecond laser ablation tends to generate nanoparticles with smaller average sizes and higher defect content compared to nanosecond-pulse ablation, which, due to its prolonged thermal input, often yields

larger, more crystalline particles via enhanced coalescence and slower solidification [237, 236].

These values are consistent with published measurements for ultrafast laser ablation. For example, in femtosecond laser ablation experiments on Au-coated Ni targets, cooling rates on the order of 10^{12} K s^{-1} were reported, which are two orders of magnitude faster than cooling in the nanosecond regime. Time-resolved studies of laser ablation in liquids also indicate cooling rates around 10^{10} K s^{-1} during the first 100 ns of plume expansion [232, 238]. We have compared the simulated cooling rates with experimental proxies: (i) the absence of long-range phase separation and the retention of homogeneous FCC structures are consistent with quench rates above 10^{9} K s^{-1}, and (ii) the simulation-predicted trends agree with the narrower size distributions and higher supersaturation observed experimentally.

3.4.7 Oxide Shell Analysis and Optical Behavior

For the LN_2 case, oxidation can proceed rapidly after the ablation step, when the nanoparticle suspension is warmed to room temperature and exposed to air. Although particle formation and quenching occur in an oxygen-free cryogenic environment, the very high surface area and multicomponent nature of the HEA cores could make them highly reactive toward O_2 and H_2O once the LN_2 has boiled off. The thin, compositionally complex oxide shell inferred from XPS is therefore likely to arise predominantly during this post-synthesis air exposure, rather than during the ultrafast ablation process itself, and should be viewed as a self-limiting passivation layer that naturally forms on the LN_2-ablated particles.

Surface composition also reflects the coupling between solvent chemistry and cooling rate. XPS and EDS mapping (Figures 3.4 and 3.5) show that LN_2-ablated particles develop a distinct oxide-rich shell. Ethanol-derived particles, on the other hand, exhibit weaker oxygen signals and often contain a partially organic shell, likely originating from decomposition products of the solvent. These surface

characteristics are broadly consistent with solvent-dependent reactivity: polar protic solvents like ethanol generate reactive species that can passivate or modify the nanoparticle surface, while LN_2 provides an inert oxygen-free environment during ablation, followed by oxidation only upon ambient exposure [226, 229, 230, 117].

Attenuation modeling of the XPS signals can explain inconsistencies within XPS measurements between samples that the low manganese intensity in the LN_2-ablated particles could arise not from true Mn loss but from a thin surface overlayer. The one-nanometer-scale overlayer extracted by this simple attenuation model confirms that the large Mn deficit in our LN_2-ablated particles is not a true loss of manganese but rather an XPS artifact caused by an oxide-rich film preferentially suppressing low-kinetic-energy photoelectrons. In practice we applied

$$I_{\mathrm{LN_2}} = I_{\mathrm{true}} \exp\left(-\frac{d}{\lambda \sin\theta}\right) \tag{3.8}$$

to the Mn 2p and Ni 2p intensities (with $\lambda \approx 1.5$ nm and $\theta = 45°$) [239, 240, 241]. The measured Mn signal ratio (10.4% vs 31.7%) yields

$$d = -\lambda \sin\theta \ln\left(\frac{I_{\mathrm{LN_2}}}{I_{\mathrm{ethanol}}}\right) \tag{3.9}$$

whereas Ni (18.5% vs 19.5%) gives $d_{\mathrm{Ni}} \approx 0.06$ nm. Co and Fe appear stronger in LN_2, so no attenuation is needed there. Because this film is uniform, it acts as a systematic offset rather than a random error: once you correct the Mn intensity by $\exp[d/(\lambda \sin\theta)]$, the apparent manganese content in the LN_2 particles returns close to the bulk value. These thicknesses are consistent with the rough, high-surface-area morphologies we observe by TEM and explain why only the lighter, lower-energy Mn photoelectrons are strongly attenuated while the heavier ones pass through almost unimpeded.

The UV–Vis spectra in Figure 3.12a show that both samples absorb strongly below 350 nm. The LN_2 sample rises more steeply in this region, which is typical of

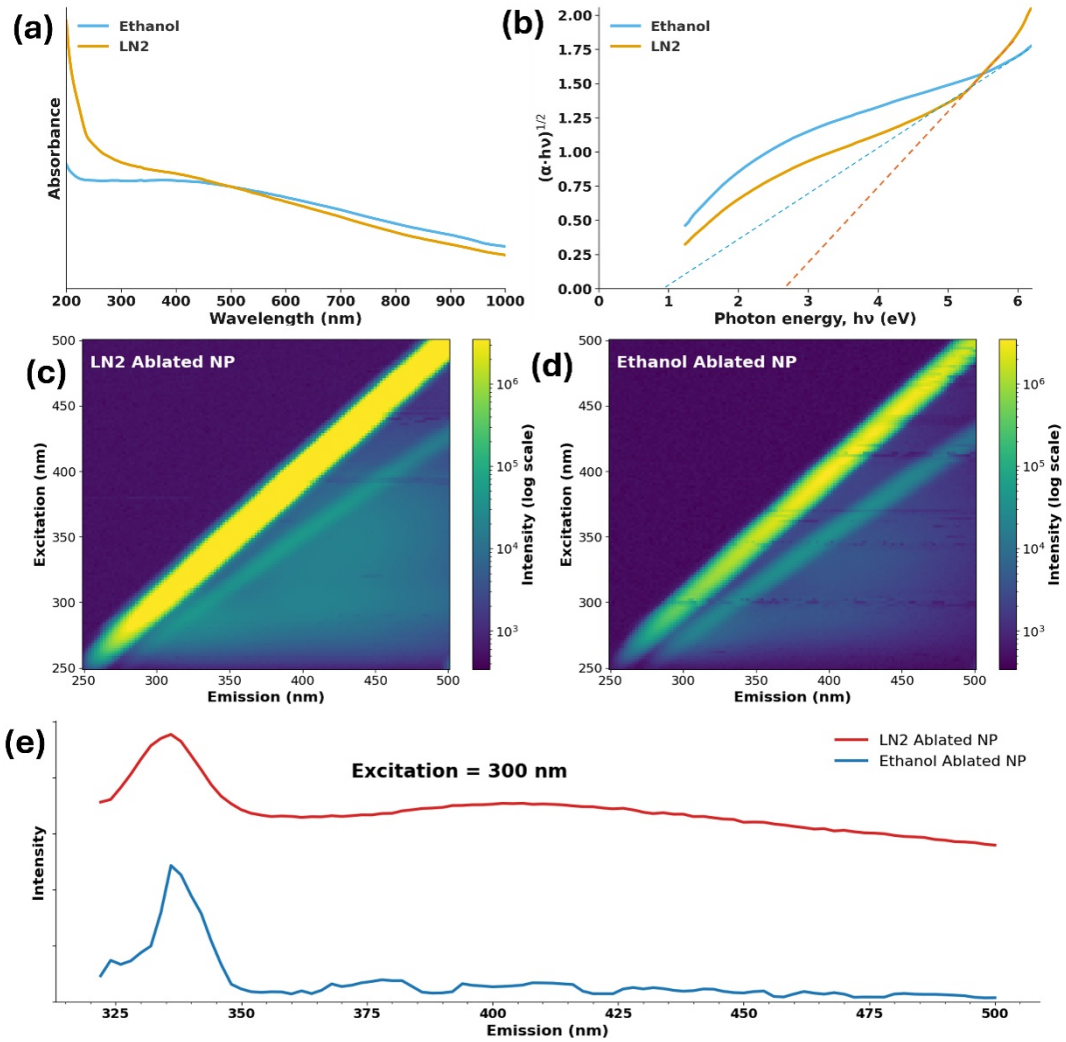


Figure 3.12: UV–Vis absorbance (a), Tauc plots (b), PL excitation–emission maps for LN_2 (c) and ethanol (d), and emission spectra at 300 nm excitation (e) of LN_2- and ethanol-ablated nanoparticles. Dashed lines show the linear fit regions whose intercepts give the optical band gap.

ligand-to-metal charge-transfer transitions in transition-metal oxides that dominate the ultraviolet response [242]. Taken together with the thickness extracted from the attenuation model, these spectral signatures support a thin oxide shell on the particles. The thicker oxide shell identified by TEM likely enhances this contribution, while the partially organic shell on the ethanol particles weakens it. Above 350 nm both spectra decrease in intensity, but the ethanol curve develops a broad plateau near 450 nm. This plateau could result from localized surface plasmon resonances of metallic domains confined beneath an oxide shell [243]. Prior studies show that oxide coatings can red-shift and broaden plasmonic absorption bands [244]. The Tauc plots in Figure 3.12b suggest that both samples behave as direct-gap semiconductors. Extrapolation of the linear regions to zero absorption yields optical band gaps of about 2.6 eV for the LN_2-ablated sample and 0.9 eV for the ethanol-ablated sample, indicating a semiconducting shell in the former while a metallic behavior for the latter.

The excitation–emission matrices shown in Figures 3.12c and 3.12d further show the strong influence of the shell composition on photoluminescence. The LN_2-ablated particles display intense emission centered near 350 nm across a broad range of excitations, while the ethanol-ablated particles show much weaker emission. Oxygen vacancies and interstitial defects in oxide shells introduce deep-level states within the gap. Electrons trapped in these states can recombine radiatively with holes in the valence band, leading to visible or near-UV luminescence. The much higher vacancy fraction measured by XPS for the LN_2 sample ($\sim$55%) therefore provides a plausible origin for its strong emission, whereas the organic overlayer on the ethanol sample likely passivates surface states and suppresses radiative recombination. At a fixed 300 nm excitation (Figure 3.12e), the LN_2 spectrum shows a broad band from 330–475 nm with a maximum near 350 nm, consistent with deep-level emission [245]. The ethanol spectrum exhibits only weak, narrow features. Collectively, these optical data support the conclusion that cryogenic ablation produces a thicker, more defective oxide shell with abundant oxygen vacancies that dominate both absorbance

and photoluminescence, whereas ablation in ethanol yields a thinner, partially organic shell that attenuates defect-mediated emission and modifies the apparent band gap.

The nanometer-scale oxide shell inferred from the XPS attenuation model is also relevant for catalytic applications. The thin oxide layer hosts oxygen-vacancy sites, which are frequently identified as active sites in high-entropy alloy nanoparticle catalysts for reactions such as oxygen reduction, oxygen evolution, and alcohol- or CO-based oxidations [246, 247]. The solvent-dependent shell structure identified in this work, oxide-rich and vacancy-rich after cryogenic ablation and partially organic and thinner after ethanol ablation, provides experimentally accessible variables for tailoring active-site density, stability, and selectivity in future electrochemical or thermocatalytic studies [248, 227]. Although direct catalytic testing is beyond the scope of the present work, the combination of a compositionally complex metallic core with a self-limiting multicomponent oxide shell makes these laser-generated HEA nanoparticles candidates for further functional optimization.

Pulsed laser ablation in liquids is not a chemically inert process. The solvent participates in reactions with the ablation plume. The plasma generated by the laser pulse dissociates solvent molecules, producing radicals and ions that interact with the nascent nanoparticles. Depending on the medium, this can lead to surface oxidation, carbonaceous coatings, or nitrogen incorporation. For instance, ablation in water typically yields oxygen radicals that oxidize particle surfaces [249], while ablation in organic solvents introduces carbon-based layers or carbide phases [250]. Pliatsikas et al. reported that TiN nanoparticles formed in acetone became covered by titanium carbides and graphitic carbon, whereas water led to extensive surface oxidation [249]. Similarly, ablation in liquid nitrogen or nitrogen-rich solutions can drive nitridation, directly producing nitride nanoparticles of transition metals [251]. Beyond unintentional modifications, reactive ablation has been used deliberately: Chemin et al. showed that dissolving $EuCl_3$ in water enabled europium doping of Gd_2O_3 nanoparticles during ablation, achieving incorporation levels that would be inaccessible under equilibrium conditions [252]. These examples confirm that the

liquid medium controls not only heat transfer but also surface chemistry, morphology, and potential doping of nanoparticles synthesized by ultrafast laser ablation.

3.4.8 Conclusions

The central hypothesis of this dissertation states that predictable and transferable material outcomes are achieved by jointly controlling laser energy delivery, environmental conditions, and spatial constraints, and that these coupled controls can be tuned to intentionally tailor distinct microstructures, surface states, and functional properties. The results of this chapter provide direct and systematic evidence for the environmental control dimension of that hypothesis by demonstrating that the choice of ablation medium, with laser energy delivery held constant, determines the internal defect structure, surface chemistry, thermodynamic stability, and optical response of $CuCoMn_{1.75}NiFe_{0.25}$ nanoparticles.

The clearest evidence for environmental control of microstructure comes from the solvent-dependent crystallographic character of the nanoparticles. Liquid nitrogen yields particles with single- or few-domain crystalline interiors and composition closer to the bulk target, whereas ethanol produces smaller particles built from 2–4 nm nanocrystalline domains with greater manganese depletion in polycrystalline structures. HRTEM reveals stacking faults and nanotwins at grain boundaries and particle edges in both media, confirming that the far-from-equilibrium solidification conditions inherent to femtosecond ablation imprint defect populations regardless of solvent, but 4D-STEM shows that the solvent governs whether those defects organize into nanocrystalline aggregates (ethanol) or remain isolated within structurally continuous interiors (liquid nitrogen). EDS maps are broadly uniform in both cases, though ethanol samples show local compositional fluctuations that track the nanocrystalline texture, providing direct microstructural evidence that the environmental input shapes elemental partitioning at the nanometer scale.

Surface state, the second key attribute targeted by the hypothesis, is equally solvent-dependent. XPS reveals that cryogenic ablation produces a thicker, more oxygen-vacancy-rich oxide shell with an estimated oxygen-vacancy fraction of approximately 55%, while ethanol ablation yields a thinner, partially organic surface layer with an oxygen-vacancy fraction of approximately 33%. An XPS attenuation model confirms that the anomalously low manganese signal in the liquid-nitrogen sample arises from a $\sim$1 nm oxide overlayer that preferentially attenuates low-kinetic-energy photoelectrons, rather than from true manganese loss, reconciling apparent discrepancies between XPS and EDS. These solvent-controlled surface states dictate the optical and photoluminescent response: cryogenic particles exhibit intense deep-level emission consistent with vacancy-mediated radiative recombination, while ethanol-derived particles show suppressed emission due to organic passivation of surface states. The fact that two chemically identical cores develop distinct surface chemistries and optical signatures solely through a change in the ablation medium is a direct demonstration that the processing environment is a controllable input that sets surface state, not a passive boundary condition.

Thermodynamic analysis reinforces the predictability component of the hypothesis. Composition-based calculations place liquid-nitrogen particles closer to the bulk alloy in Ω–ΔH_{mix} space, with Ω values of 3.0–3.5 and mixing enthalpies of 5.7–6.5 kJ mol^{-1}, indicating a strong entropic buffer against decomposition. Ethanol-ablated particles shift to lower Ω ($\sim$2.5) and higher ΔH_{mix} (6.9–7.8 kJ mol^{-1}), approaching the empirical boundary for single-phase stability and signaling greater susceptibility to local chemical ordering. COMSOL cooling simulations connect these thermodynamic outcomes to the physical mechanism: ethanol surfaces cool from the melt to a few hundred degrees Celsius within approximately 1 μs, allowing coalescence and compositional redistribution, while liquid nitrogen drives the particle to near bath temperature within approximately 0.1 μs, kinetically freezing a homogeneous solid solution before significant demixing can occur.

These results complete a two-chapter nanoscale validation of the dissertation hypothesis. Chapter 2 showed that the environmental control axis determines *whether* a single-phase HEA nanoparticle forms. This chapter shows that, within the single-phase regime, the same axis predictably tunes *how* that nanoparticle is internally structured, what surface state it develops, and what thermodynamic regime it occupies. The solvent therefore functions as a design variable that connects process input to material outcome through a quantifiable chain of cooling kinetics, nucleation and growth competition, defect evolution, and surface chemistry. Ethanol processing yields nanocrystalline particles with mild compositional modulation suited to catalytic applications that benefit from local compositional gradients, while cryogenic processing preserves compositional fidelity and crystalline continuity for applications demanding maximal phase stability and structural uniformity. This difference provides an experimentally accessible design variable for future targeted property optimization across the process–structure–property framework at the nanoscale.

Chapter 4

Process Optimization in LPBF of Al-Ce-Ni-Mn-Zr

4.1 Disclosure

Source disclosure. The content of this chapter draws from a manuscript authored by David Fieser, Michael Lawton, Sumit Bahl, Amirkoushyar Ziabari, Tomas Grejtak, Janet M. Meier, Mason Smith, Alex Plotkowski, Elaine McDonald, and Anming Hu: *Optimization of Processing, Microstructure, and Hardness of an Al-Ce-Ni-Mn-Zr Alloy With Laser Additive Manufacturing* [253].

Support and contributions disclosure. This work was supported by the DOE Energy Efficiency & Renewable Energy (EERE) project (DE-EE0010222). D.F. discloses support from the EERE scholarship supported by UT-ORII and the 100 PhD Scholarship from UTK. The authors would like to thank Dr. Sudarsanam Babu at the University of Maryland for his guidance and mentorship through this project.

4.2 Motivation and Background

Chapter 1 established the central hypothesis of this dissertation: that predictable and transferable material outcomes are achieved by jointly controlling laser energy delivery, environmental conditions, and spatial constraints, and that these coupled controls can be tuned to intentionally tailor distinct microstructures, surface states, and functional properties. The macroscale portion of Chapter 1 developed the physical framework underlying this hypothesis for laser powder bed fusion, articulating how laser power, scan speed, hatch spacing, and scan strategy jointly set melt pool regime, thermal history, and rapid solidification conditions, and how those conditions govern porosity formation, microstructural scale selection, and mechanical response through the normalized process maps and melt pool scaling reviewed there. Chapters 2 and 3 tested the hypothesis at the nanoscale, demonstrating that environmental control during femtosecond laser ablation in liquid can be tuned to deliver single-phase, compositionally faithful high-entropy alloy nanoparticles with tailored surface chemistry and thermodynamic stability. This chapter applies the same coupled-control framework at the macroscale, using LPBF of an Al–Ce–Ni–Mn–Zr (ACNMZ) alloy as a testbed for the proposition that deliberate, systematic variation of energy delivery and spatial processing parameters produces predictable and transferable outcomes in microstructure, porosity, and mechanical properties.

The ACNMZ alloy is a well-suited test case for this macroscale examination because its alloy design is itself guided by process–structure–property logic. The addition of cerium and nickel promotes eutectic solidification, narrowing the solidification range and suppressing the persistent semi-solid films that drive solidification cracking in conventional wrought aluminum alloys under the rapid thermal cycling of LPBF [254, 129, 126, 127, 122]. This compositional strategy is analogous in principle to the eutectic design that governs the printability of Al–Si systems [255, 78], but it is extended to a chemistry that simultaneously produces a refined intermetallic network with spacings often below 100 nm. The rapid

solidification inherent to LPBF refines this eutectic network further, consistent with classical eutectic scaling theory, enhancing both strength and creep resistance through mechanisms that impede dislocation motion and stabilize grain boundaries [256, 257, 258]. Mn further improves phase selection during solidification, and the combination of cerium and nickel in the aluminum matrix provides low diffusivity and solubility that limits coarsening and preserves the fine microstructure under sustained thermal exposure [257, 128, 259]. The resulting microstructure is thermally stable to approximately 300 °C, a regime within which conventional aluminum alloys suffer significant strength loss [260], positioning ACNMZ as a strong candidate for aerospace, automotive, and energy applications demanding both geometric complexity and high-temperature reliability [127].

A key implication of the dissertation framework is that achieving the alloy's potential requires moving beyond identifying a single usable parameter set and instead characterizing how the full space of energy delivery and spatial constraints maps to the competing defect mechanisms that Chapter 1 identified: keyhole-mode porosity at high energy density and lack-of-fusion porosity at low energy density. When process parameters are optimized within the window between these regimes, LPBF can achieve porosity consistently below 0.1 vol%, a benchmark critical for structural reliability, while simultaneously producing the fine, well-bonded cellular microstructure that generates high hardness [256, 261, 262, 122]. The laser power, scan speed, and hatch spacing that jointly define this window interact through the melt pool energy they impose, so their individual effects on porosity and hardness cannot be characterized in isolation [263, 264, 265, 266, 267].

Despite ACNMZ's demonstrated processing advantages, a systematic quantitative characterization of how those three parameters translate into microstructure, porosity, and hardness across a broad industrial parameter space remains a gap in the literature [122]. The functional form of the parameter–property relationships, which parameter combinations simultaneously minimize porosity and maximize hardness, and whether a single physically grounded metric can capture the dominant trends

across the coupled response surface, have not been established for this system. This chapter addresses that gap by applying response surface methodology over a designed experiment spanning laser power, scan speed, and hatch spacing, and by connecting the resulting statistical models to the underlying solidification physics through a Rosenthal-based instantaneous cooling rate framework. The central question is whether coupled control of energy delivery and spatial constraints alone is sufficient to predict and bound the viable processing window for ACNMZ, and in doing so to demonstrate the transferability of the macroscale process–structure–property logic developed in Chapter 1.

4.3 Materials and Methods

4.3.1 Materials

Gas-atomized Al–8.2Ce–4.5Ni–0.5Mn–0.7Zr (wt%) ACNMZ powder was supplied by Kymera International®. The following particle characterization and chemistry were provided by Kymera International®. Particle morphology was spherical as observed by scanning electron microscopy. The powder exhibited an apparent density of $1.35\,\mathrm{g/cm^3}$ and a Hall flow rate of 15.0 s through a 5.0 mm orifice, measured in accordance with ISO 3923/1 and ISO 4490 standards, respectively. Sieve analysis showed that 98.0% of particles were between 20 and 63 μm, with 0.1% exceeding 63 μm and 1.9% below 20 μm. Laser diffraction analysis determined the D10, D50, and D90 values to be 25.9 μm, 41.5 μm, and 65.7 μm, respectively, with 2.5% of particles smaller than 20 μm. The powder's oxygen content was measured at 0.09%, with hydrogen and moisture contents both below 0.01%. Inductively coupled plasma analysis confirmed the elemental composition as 8.2% cerium, 4.5% nickel, 0.5% manganese, 0.7% zirconium, 0.06% silicon, and 0.11% iron (in wt.%), with aluminum comprising the balance. Unless otherwise noted, material parameters such as moisture content were provided by the supplier based on their internal measurement and quality-control procedures, and the reported values are guaranteed by the supplier.

4.3.2 Laser Powder Bed Fusion

The ACNMZ alloy was fabricated using an EOS M290 laser powder bed fusion system at Beehive Industries. Previous work identified a usable parameter set, which was employed as the center point of a design varying laser power, scan speed, and hatch spacing to evaluate the influence of processing conditions on defect formation and microstructural evolution [122]. Test specimens were designed with a cylindrical base approximately 15 mm in diameter and incorporated a series of geometric features on the top surface to impose localized variations in thermal history. These features

included thin vertical walls (0.5–1.5 mm thick), inclined struts at multiple orientations (15°, 30° and 45°), and freestanding columns of varying diameters (1 mm, 2 mm and 3 mm). Each sample was contained within an overall 15 × 15 × 15 mm^3 volume. This geometry was selected to represent a range of build conditions such as overhangs, unsupported features, and sharp transitions commonly encountered in complex additive manufacturing components, and to enable localized assessment of porosity, microstructure, and dimensional fidelity across a single build. The coordinate system used throughout this study defines the X and Y axes as the horizontal directions parallel to the build plate, while the positive Z axis is oriented vertically, normal to the build surface. During fabrication, the laser scan vectors were rotated by 67° between successive layers to promote microstructural uniformity and minimize the development of anisotropy.

4.3.3 Experimental Design and Statistical Methods

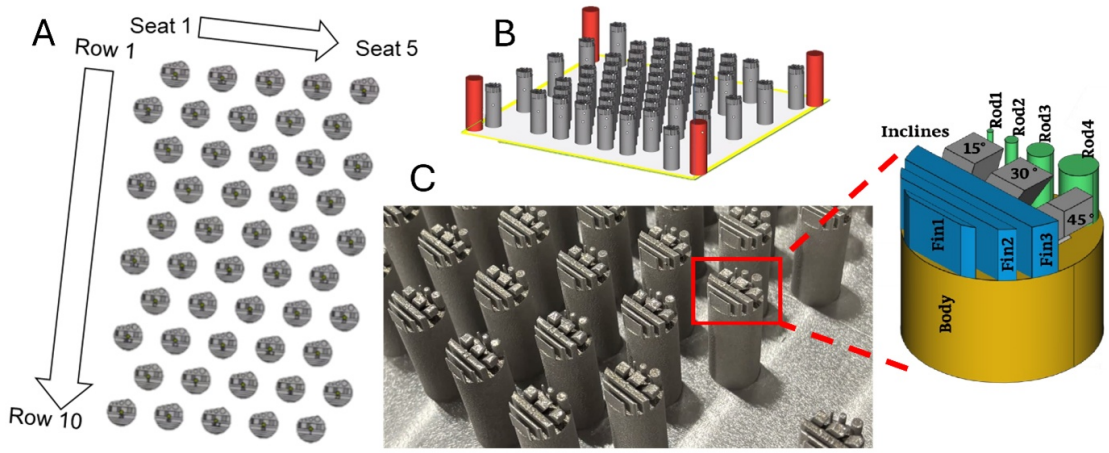


Figure 4.1: Build geometry. (A) Build locations. (B) Rendering of build plate. (C) Detail of completed builds with a zoomed version of a color-separated version of the computer-aided design model. Each region is identified in this model. The design of the sample and geometric features along with high-throughput characterization allows for study of geometric dependence of process parameter design.

Note. See [268] for details on high-throughput characterization methods.

In total, 60 test articles were produced. The parameter sets were designed in JMP®, Version 18 (SAS Institute Inc., Cary, NC, 1989–2024), with 40 unique parameter sets designed to explore variations in deposition conditions, alongside 10 duplicates of the central parameter set (370 W power, 1300 mm/s speed, 0.19 mm hatch) to study data variance. Ten random duplicates of the 40 unique parameters were also fabricated for redundancy. Laser power varied between 330–370 W, scan speeds from 1000–2000 mm/s, and the hatch spacing ranged from 0.13 to 0.21 mm. The 40 unique processing conditions were generated in JMP using a custom design of experiments (DOE) for three continuous factors to achieve space-filling coverage of the selected parameter ranges with low factor correlation, and the conditions were randomized across the build. Replicates were included, including 10 center point repeats and 10 randomly selected repeats of unique conditions, to quantify repeatability and variance. The parameter ranges used in this study are listed in Table 4.1. A full list of processing parameters, as well as row and seat locations, are listed in Appendix A.1. The layer thickness was kept constant at 30 μm throughout. An argon atmosphere was maintained to prevent oxidation during the build process. Sample parameter sets were randomly distributed throughout the build array (Figure 4.1A). Ten of the unique parameter combinations were chosen for additional metallographic characterization by constructing a D-optimal experimental design using the initial 40 unique parameters as candidate treatments [269]. These samples are marked with * in Appendix A.1. Build plate geometry and an image of the finished build are shown in Figure 4.1A, B, and C.

Figure 4.2 shows the full experimental design projected into the three-dimensional parameter space of laser power (330–370 W), scan speed (1000–2000 mm/s), and hatch spacing (0.13–0.21 mm). The 40 unique parameter sets achieve broad, space-filling coverage of this volume, with the cluster of center-point replicates at (370 W, 1300 mm/s, 0.19 mm) providing a direct estimate of pure experimental error. This distribution is not the result of a standard factorial or central composite grid. Instead, the conditions were generated to maximize coverage with low

Table 4.1: Key processing parameters for LPBF.

Parameter	**Range**
Laser Power	330–370 W
Scanning Speed	1000–2000 mm/s
Hatch Distance	0.13–0.21 mm
Layer Thickness	30 μm
Atmosphere	Argon
Powder Particle Size	20–63 μm

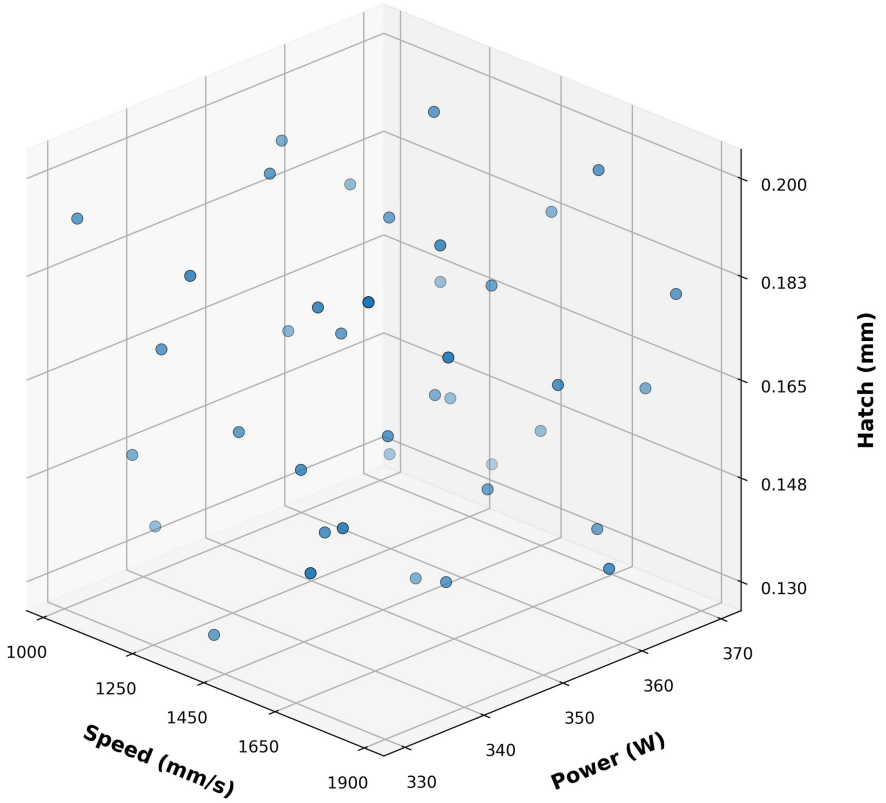


Figure 4.2: Distribution of the 60 LPBF build parameter sets in the laser power–scan speed–hatch spacing design space.

correlation between factors, which is a prerequisite for fitting a second-order response surface [270].

Response surface models were developed and performed in R [271] to describe the relationship between processing parameters and porosity and hardness responses within the domain defined by the experimental design shown above. The response surface methodology employed a second-order polynomial regression approach [270] and was used to develop predictive models incorporating main effects, quadratic terms and two-way interactions between laser power, scanning speed and hatch distance. A systematic analysis was conducted to determine the influence of these parameters on the resulting defects and hardness performance. Model coefficients were estimated via least squares fitting, with stepwise variable selection applied to retain only statistically significant terms. Model accuracy was evaluated through residual analysis and goodness-of-fit metrics including R^2 and adjusted R^2 values.

Porosity was modeled using a logarithmic transformation to normalize the distribution and reduce heteroscedasticity. The resulting model equation is:

$$\log(\varphi) = \beta_0 + \beta_1 P + \beta_2 S + \beta_3 H + \beta_4 P^2 + \beta_5 S^2 + \beta_6 H^2 + \beta_7 PS + \beta_8 PH + \beta_9 SH + \varepsilon \quad (4.1)$$

where φ represents the porosity fraction, P, S, and H denote laser power, scanning speed, and hatch distance, respectively, β_i are the model coefficients, and ε represents the residual error. Hardness was modeled using a second-order polynomial of the same form:

$$HV = \alpha_0 + \alpha_1 P + \alpha_2 S + \alpha_3 H + \alpha_4 P^2 + \alpha_5 S^2 + \alpha_6 H^2 + \alpha_7 PS + \alpha_8 PH + \alpha_9 SH + \varepsilon \quad (4.2)$$

where HV represents the microhardness value, α_i are the model coefficients, and the terms retain the same definitions as in the porosity model.

The second-order response surface model for three factors contains 10 coefficients including the intercept. Classical three-factor response surface designs typically use

about 15 runs for a Box–Behnken design or about 20 runs for a central composite design to support estimation of a quadratic model. In this work, 40 unique parameter sets were used to provide broad coverage of the design space, and 20 replicate builds were included to estimate experimental variance and evaluate model adequacy. To limit overfitting, the final model terms were selected using Akaike information criterion (AIC)-guided stepwise selection consistent with information-theoretic model selection criteria [272, 273, 270] and were verified using residual diagnostics, lack-of-fit testing, and goodness-of-fit metrics. Confidence intervals were computed for predicted responses across the explored processing space.

4.3.4 Hardness and Characterization

Sections of the 60 test coupons were cut into 5 mm segments and embedded in epoxy and polished to 0.5 μm. Vickers hardness measurements were taken on the XY build plane. Five hardness measurements were taken using a 500 g load applied for a 5 s dwell time and averaged. Vickers hardness was measured on the XY plane for all samples to provide a consistent basis for comparing processing conditions. Hardness measurements along the build direction were not performed in this study, so potential build-direction anisotropy is not quantified here and could be addressed in future work if required.

X-ray computed tomography (XCT) was used to quantitatively assess internal porosity within all 60 test coupons. Scans were performed using a ZEISS Metrotom 800 system at the Manufacturing Demonstration Facility at Oak Ridge National Laboratory. Using recent deep learning-based advancement for high-throughput characterization of large numbers of additively manufactured components [268], fast scans were designed and used to characterize all 60 components. Each sample was scanned for 10 min at a voxel size of 17.3 μm with the following scan parameters: 180 kV, 113 μA, 290 projections (in a short-scan setting [274, 275]), 1 s exposure time, 2 image averaging per projection, and using 2 mm Al filter for beam hardening

mitigation. The Simurgh AI-powered reconstruction framework was used to produce high-quality reconstruction from these fast and sparse scans [268, 276, 277, 278]. To segment the flaws in 3D XCT volumes, a 2.5D U-Net based segmentation approach [279, 280] was used allowing for fast and accurate detection of defects, voids, and anomalies. The detected flaws were analyzed in 3D to extract total porosity volume fraction, flaw size distribution, and flaw morphology metrics such as sphericity and aspect ratio. The reconstruction and segmentation of each part was individually registered to the computer-aided design models of the parts, allowing for region-based quantitative analysis, and mapping porosity spatially across different geometries (e.g., thin walls, rods, overhangs seen in Figure 4.1C) and correlation with processing parameters [268]. Small pores can be detected in XCT through partial volume contrast. Total porosity volume fraction and pore count are reliable outputs of the segmentation, while individual pore size and shape metrics have reduced accuracy near the voxel scale and are interpreted with caution for the smallest pores.

SEM was performed on a Tescan Mira 3 using backscatter electron (BSE) imaging. Ten selected coupons were polished for high-resolution imaging down to $1\,\mu$m. SEM was used to study the distribution of intermetallic phases and microstructural uniformity. All SEM images provided are XZ planes.

Surface roughness measurements were performed using a Keyence VK-X3000 laser confocal microscope to characterize the as-built surface quality of the LPBF-fabricated samples. Roughness scans were conducted on three distinct regions along the Z-direction of the cylindrical specimens, with measurements taken from the lower, middle, and upper sections of the build height. These scans were oriented along the build direction to capture any variation in roughness associated with layer-by-layer deposition. The measurements were taken using a $10\times$ objective, with a scan size of $2920 \times 2630\,\mu$m. The surface roughness parameter, S_a, was computed from the 3D topography data according to

$$S_a = \frac{1}{A} \iint_A |z(x, y)| \, \mathrm{d}x \, \mathrm{d}y \tag{4.3}$$

where $z(x, y)$ is the surface height relative to the mean plane over the measurement area A. To correct for specimen curvature, a best-fit second-order polynomial was subtracted from the raw topography before calculation. Representative optical and 3D surface topography images were then acquired to qualitatively assess features such as partially fused particles, melt-pool ridges, and unmelted satellites typical of LPBF.

4.4 Results

4.4.1 Pore Defects

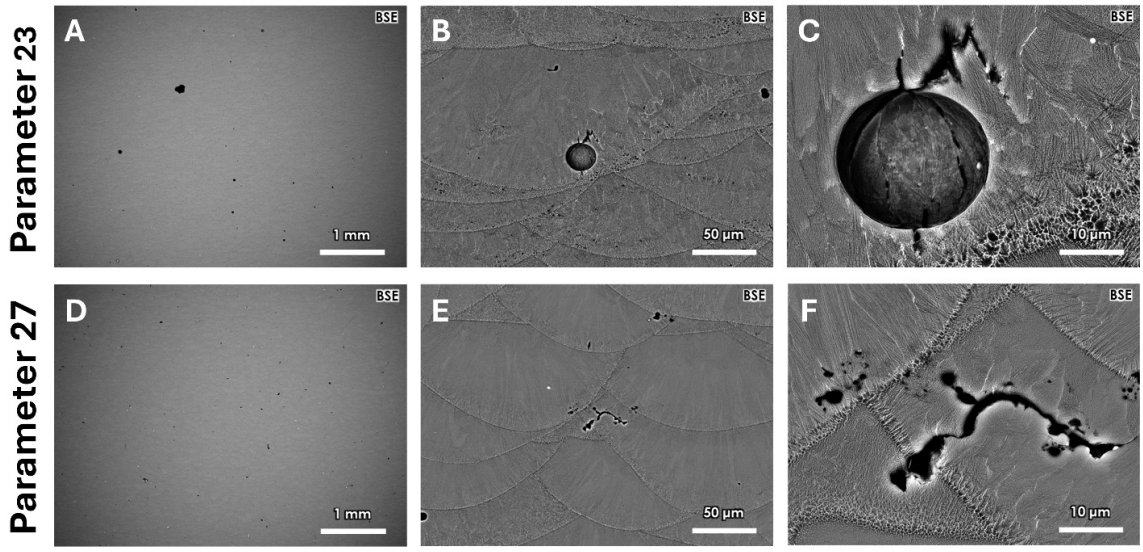


Figure 4.3: SEM images of defects observed in ACNMZ samples. (A–C) Spherical gas pores from parameter set 23 at increasing magnifications. (D–F) Irregular lack-of-fusion defects from parameter set 27 at increasing magnifications.

Microscopy of the ACNMZ samples revealed a microstructure with multiple types of defects depending on process conditions. Although not present in every sample, selected defects are illustrated in Figure 4.3. SEM images captured at varying magnifications of the XZ sample planes show the distribution of intermetallic phases and the absence of structural discontinuities. In the first set of images (Figure 4.3A–C), spherical pores are evident from parameter set 23, which has a relatively high power, low scan speed, and small hatch spacing, and therefore relatively high energy density. The sample exhibits spherical pores roughly 1–25 μm in diameter, with little evidence of interconnected porosity or cracks. Figure 4.3B highlights the presence of these isolated pores near the melt pool boundaries. At higher magnifications, the morphology of the gas pores is shown in detail, with smooth, spherical features. The size and shape of these pores are consistent with gas pores resulting from residual

atmospheric gases or keyholing during fabrication [281]. While uniformly distributed, the presence of such pores can act as stress concentrators that reduce the mechanical performance of the alloy [261].

The second set of images (Figure 4.3D–F) show irregular shaped defects from parameter set 27, which had a comparatively high laser velocity and large hatch spacing (low energy density). The irregular and elongated morphology of the pores are characteristic of lack-of-fusion defects, often located at interlayer boundaries. At high magnifications (Figure 4.3F), these defects are observed to be irregularly shaped and associated with insufficient melt pool overlap. This incomplete fusion between layers not only compromises the structural integrity of the material but also creates potential crack initiation sites under mechanical loading [282].

4.4.2 X-ray Computed Tomography

Given that different porosity mechanisms were observed for specific parameter sets at high and low energy densities, XCT analysis was conducted to evaluate the full dataset and identify the range of safe processing conditions for which porosity was minimized. Figure 4.4 presents representative XCT reconstruction data with associated SEM-BSE images that illustrate the defect distributions across processing conditions.

The sample processed with parameter set 2 exhibited one of the highest relative densities. This specimen reveals minimal porosity within the bulk of the part, with isolated pores observed primarily near regions of detailed features. In contrast, the sample fabricated under parameter set 23 (also highlighted in Figure 4.3) displays slightly more porosity distribution throughout the body. The specimen produced with parameter set 10 demonstrates extensive lack-of-fusion porosity throughout the entire build.

Figure 4.5 illustrates the relationship between LPBF processing conditions and porosity formation in the ACNMZ alloy, highlighting distinct defect mechanisms tied to specific ranges of process conditions. At low scan speeds, excessive energy density

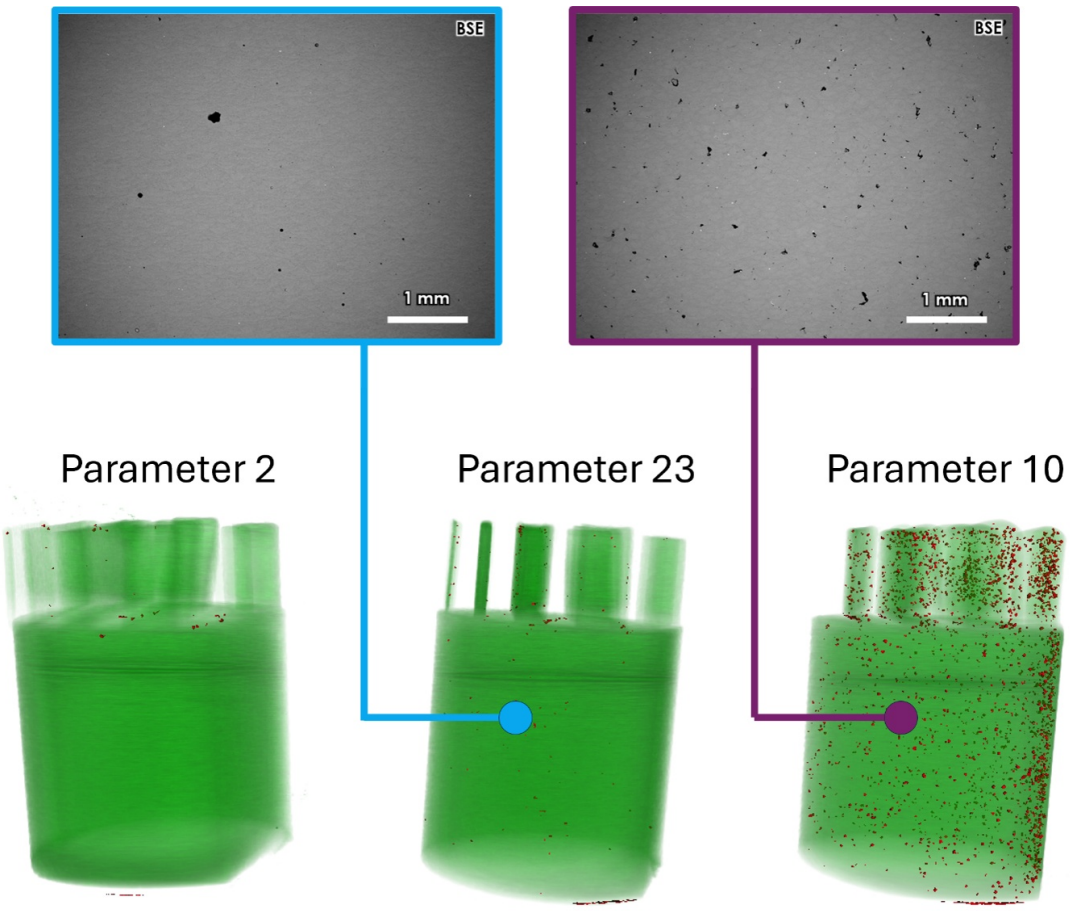


Figure 4.4: Representative XCT reconstruction data with associated SEM-BSE images illustrating defect distributions across processing conditions. Results for XCT and hardness are summarized for all parameter sets in Appendix A.1.

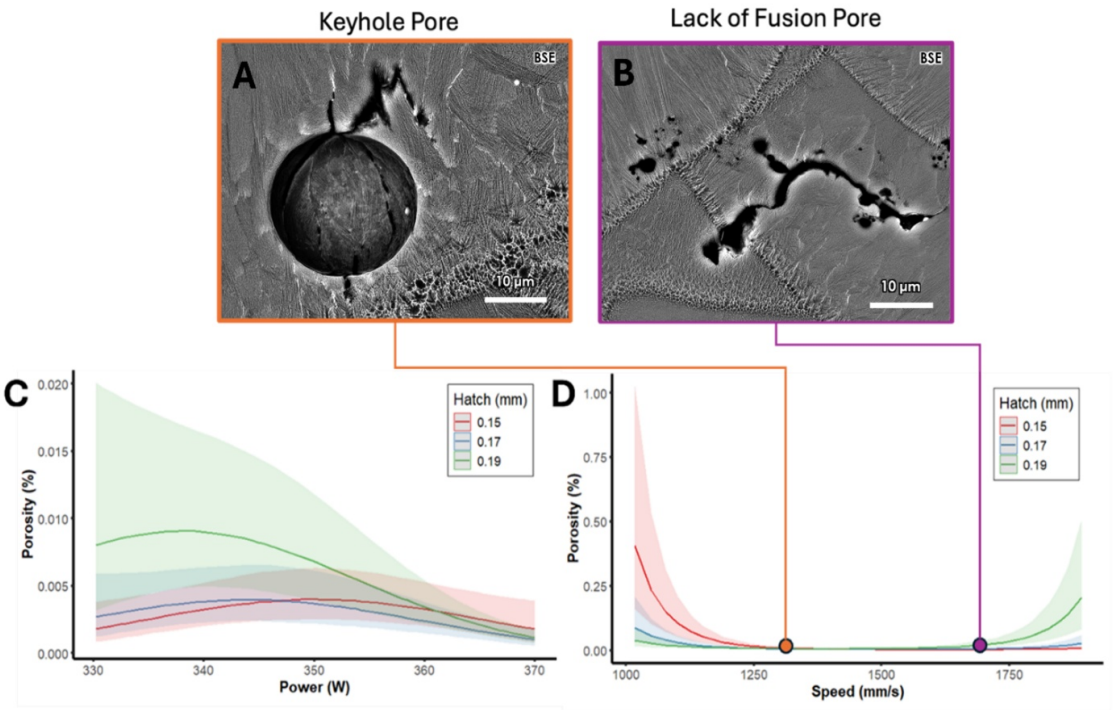


Figure 4.5: Relationship between LPBF processing conditions and porosity formation. (A) BSE image showing keyhole gas pore at low scan speed. (B) BSE image showing lack-of-fusion porosity at high scan speed. (C) Porosity as a function of laser power at three hatch distances. (D) Porosity as a function of scan speed at three hatch distances.

leads to keyhole mode melting, which is characterized by deep, rounded gas pores, as shown in Figure 4.5A, and previously discussed in Section 4.4.1. The BSE image in Figure 4.5A clearly shows the presence of a nearly spherical pore, suggesting turbulent melt dynamics and keyhole collapse [281]. This phenomenon occurs in various alloy additive processes when energy input exceeds the material's ability to conduct heat away, resulting in vaporization-driven pore entrapment [283, 99].

In contrast, Figure 4.5B shows lack-of-fusion porosity formed at high scan speeds and low energy input. Here, elongated and irregularly shaped voids are evident, often located along the boundaries of adjacent melt tracks.

Quantitative porosity trends across a broad process window are shown in Figures 4.5C and 4.5D. In Figure 4.5C, porosity is plotted as a function of laser power at three hatch distances. At lower powers, porosity levels are elevated across all hatch distances, particularly when the hatch spacing is large, indicating that insufficient energy density combined with reduced overlap is a primary driver of defect formation. As power increases, porosity generally decreases due to more complete melting and improved fusion, with the difference between hatch distances narrowing. This convergence at higher power suggests that the increased thermal input compensates for gaps in scan coverage. Figure 4.5D presents porosity as a function of scan speed across the same hatch distances. A strong inverse correlation is evident: porosity is highest at the extremes of the scan speed range [284]. At low speeds, keyhole porosity dominates due to excessive energy input, while at high speeds, lack-of-fusion porosity becomes prevalent due to insufficient energy coupling. The lowest porosity values are observed at intermediate scan speeds, where energy input is balanced and melting behavior is optimized. Additionally, the influence of hatch distance is most pronounced at high and low scan speeds, where reduced overlap worsens defect formation.

Figure 4.6 shows how pore size and shape vary across all the XCT-analyzed samples. In panel A, the histogram of volume equivalent diameters measured from XCT is skewed toward the left. The volume equivalent diameter of a large amount of

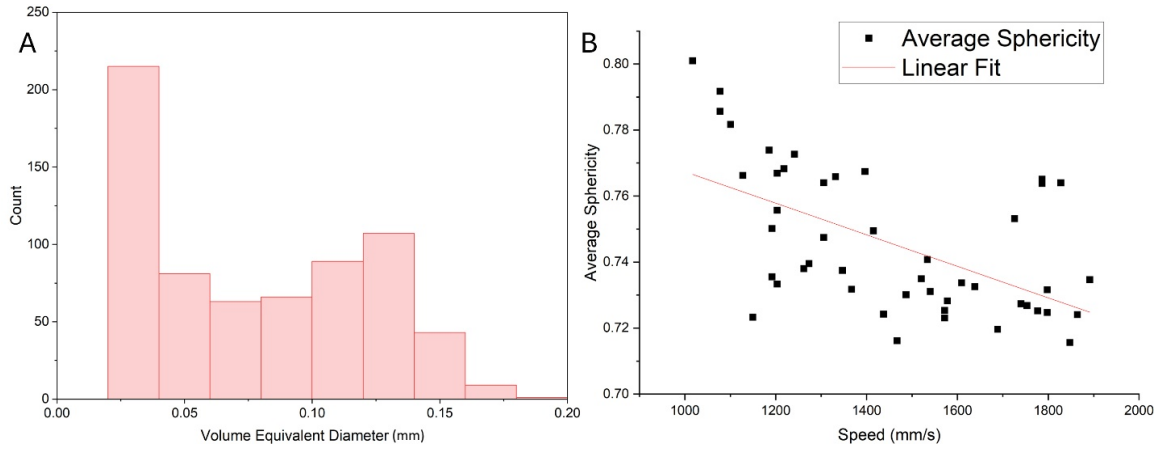


Figure 4.6: Pore size and shape characteristics. (A) Histogram of volume-equivalent diameters measured from XCT. (B) Average sphericity plotted against scan speed for all XCT-analyzed samples.

the pores falls below $\sim$0.05 μm, with frequency dropping off for larger defects. This indicates that small voids dominate the porosity population. In panel B, each sample's average sphericity measured from XCT is plotted against its scan speed, and the negative slope of a loose linear fitting reveals that lower scan speeds produce rounder pores (higher sphericity), whereas higher speeds yield more irregular, elongated voids.

The trends in porosity presented in the previous section were quantitatively derived using a multiple regression model constructed from the full XCT dataset (Eq. 4.1) [285]. The full model fit statistics and coefficient estimates are summarized in Table 4.2. The regression analysis provided a statistical fitting for the porosity trends shown in Figures 4.4 and 4.5 and confirmed the dominant role of scanning speed in determining porosity levels. Specifically, the linear effect of scanning speed was highly significant, with a t statistic of -9.86 and a p-value < 0.0001, indicating that increasing speed reduces porosity until lack of fusion becomes the prevailing defect mechanism. The speed-squared term was also strongly significant ($t = 6.87$, $p < 0.0001$), reflecting the U-shaped relationship where both low and high speeds contribute to elevated porosity.

Laser power was also found to be a statistically meaningful factor as the linear term yielded a t statistic of 2.88 with a p-value of 0.0058, indicating that porosity

tends to increase at lower power levels. However, the power-squared term ($t = -2.48$, $p = 0.0163$) revealed that this trend reverses at higher powers, consistent with the decrease in porosity seen in Figure 4.5C as energy input becomes sufficient to achieve full melting.

While hatch distance alone did not have a significant main effect ($t = -0.52$, $p = 0.6080$), its interaction with other parameters was substantial ($\beta_8 PH + \beta_9 SH$ in Eq. 4.1). The interaction between scanning speed and hatch distance ($t = 8.41$, $p < 0.0001$), as well as between power and hatch distance ($t = -3.03$, $p = 0.0039$), confirmed that hatch spacing plays a more critical role in combination with other factors.

Table 4.2: Response surface model coefficients for log-porosity [$\log(\varphi)$], Eq. 4.1, listed in order of ascending p-value. $F(df_1, df_2)$ is the overall F-statistic on df_1 and df_2 degrees of freedom; p_F is the corresponding overall model p-value; $\hat{\sigma}$ is the residual standard error.

Term	**Estimate**	**Std. Error**	t	p
Speed (S)	-0.0715	0.00726	-9.86	< 0.0001
$S \times H$	0.165	0.0197	8.41	< 0.0001
S^2	1.45×10^{-5}	2.10×10^{-6}	6.87	< 0.0001
$P \times H$	-1.21	0.401	-3.03	0.0039
H^2	859	289	2.97	0.0045
Power (P)	1.59	0.552	2.88	0.0058
P^2	-0.00201	0.000809	-2.48	0.016
Intercept	-221	95.8	-2.30	0.025
Hatch (H)	-89.4	173	-0.52	0.608
$R^2 = 0.8215$	$R^2_{\text{adj}} = 0.7935$	$n = 60$		$\hat{\sigma} = 0.8004$
$F(8, 51) = 29.34$				$p_F < 0.0001$

4.4.3 Microstructure Characterization

Figure 4.7 presents backscatter electron micrographs of three representative coupons produced with Parameter Sets 10, 16, and 40, corresponding to low, intermediate, and high energy inputs, respectively. While all three conditions exhibit cellular

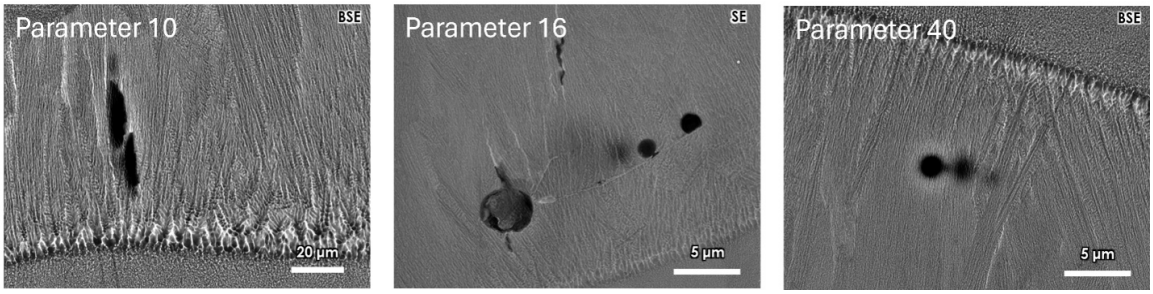


Figure 4.7: Backscatter electron micrographs of three representative coupons produced with Parameter Sets 10, 16, and 40, corresponding to low, intermediate, and high energy inputs, respectively.

microstructures, notable differences emerge in their morphology, refinement, and uniformity. Parameter Set 10, produced at lower energy input, shows a relatively coarse but well-ordered cellular structure composed of elongated features with clear boundaries and gradual variation in spacing and shape. In contrast, Parameter Set 16 displays a more uniform and tightly packed array of cellular features, with sharp boundaries and minimal variation in size or alignment. Compared to Set 10, the structure is finer and more regular. Parameter Set 40, generated under the highest energy input, shows the finest cellular scale of the three conditions. The intermetallic-rich boundary network appears as thinner and more closely spaced lines, giving a higher boundary density within the field of view than observed for Sets 10 and 16.

4.4.4 Hardness

Figure 4.8A illustrates the relationship between laser power and hardness, showing a slight inverse correlation. As power increases from 330 W to 370 W, hardness decreases, with the trend suggesting a gradual reduction rather than an abrupt change. The shaded region represents the 95% confidence interval in the measurements, indicating some degree of dispersion around the trend line. The effect of scanning speed on hardness is shown in Figure 4.8B, where a strong positive correlation is observed. Hardness increases consistently with increasing scanning speed, ranging from approximately 130 HV at lower speeds ($\sim$1000 mm/s) to over

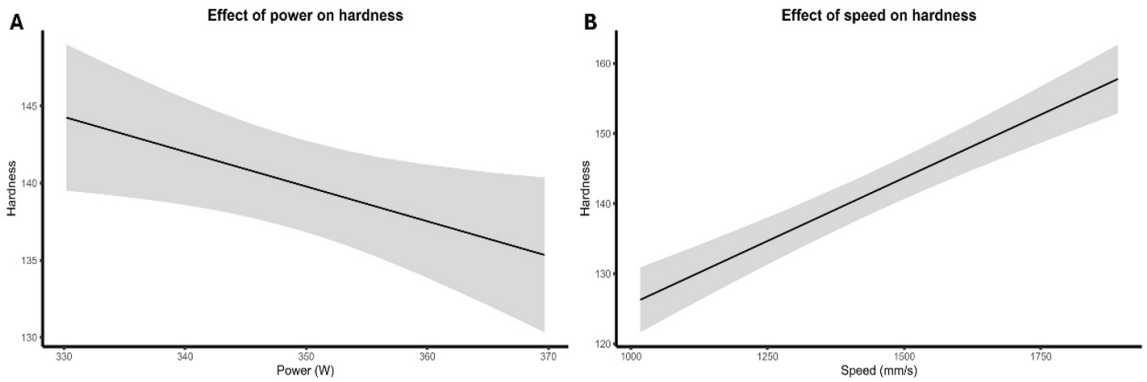


Figure 4.8: Influence of processing parameters on Vickers hardness. (A) Hardness as a function of laser power. (B) Hardness as a function of scanning speed. Shaded regions represent 95% confidence intervals.

160 HV at higher speeds (∼1800 mm/s). The confidence interval remains relatively stable across this range. These findings indicate that while higher scanning speeds promote an increase in hardness, increasing laser power has a modest softening effect on the material. For comparison, the hardness values of 120 to 160 HV measured here are well above the typical hardness of approximately 70 HV observed in friction stir processed Al6061 [286].

Similar to the XCT results, the hardness trends shown in Figure 4.8 were used to fit a multiple regression model. The full model fit statistics and coefficient estimates are summarized in Table 4.3. The model achieved an adjusted R^2 value of 0.7915, indicating that approximately seventy-nine percent of the variation in hardness could be attributed to the selected processing parameters.

Scanning speed was identified as the most statistically significant factor influencing hardness. The linear coefficient for scanning speed was positive, with a t statistic of 2.18 and a p-value of 0.0428, confirming that higher scan speeds generally produce harder material. This trend is consistent with the data shown in Figure 4.8B, where hardness increases steadily with scanning speed. A significant quadratic term for speed ($t = 2.23$, $p = 0.0302$) also indicated a nonlinear relationship beyond our measured parameter set.

Laser power exhibited a small but statistically meaningful inverse relationship with hardness. The model yielded a negative coefficient with a t statistic of -2.41 and a p-value of 0.0268, suggesting that higher energy input results in slight reductions in hardness.

Hatch distance had a marginal effect on hardness, with a t statistic of 1.98 and a p-value of 0.0634, falling just outside conventional significance thresholds. While not definitively influential on its own, this parameter displayed relatively high variability, suggesting that its effect may be geometry-dependent or sensitive to localized thermal history. Interaction terms, such as the speed–hatch distance interaction, were not statistically significant ($t = -1.42$, $p = 0.1723$), indicating that hardness is primarily governed by the independent contributions of scanning speed and, to a lesser extent, laser power.

Table 4.3: Response surface model coefficients for Vickers hardness (HV), Eq. 4.2, listed in order of ascending p-value. $F(df_1, df_2)$ is the overall F-statistic on df_1 and df_2 degrees of freedom; p_F is the corresponding overall model p-value; $\hat{\sigma}$ is the residual standard error.

Term	**Estimate**	**Std. Error**	t	p
Power (P)	-0.225	0.0935	-2.41	0.027
Speed (S)	0.0982	0.0451	2.18	0.043
Hatch (H)	1760	891	1.98	0.063
$S \times H$	-0.352	0.248	-1.42	0.172
H^2	-3700	2720	-1.36	0.190
Intercept	-28.0	83.6	-0.34	0.741
$R^2 = 0.8368$	$R^2_{\text{adj}} = 0.7915$	$n = 24$	$\hat{\sigma} = 4.929\,\text{HV}$	
$F(5,\, 18) = 18.46$			$p_F = 1.6 \times 10^{-6}$	

4.4.5 Roughness

Surface roughness measurements were conducted on eleven representative samples selected to span a broad range of processing parameters, bulk densities, and hardness values. Figure 4.9A and B show a selected optical image and corresponding surface

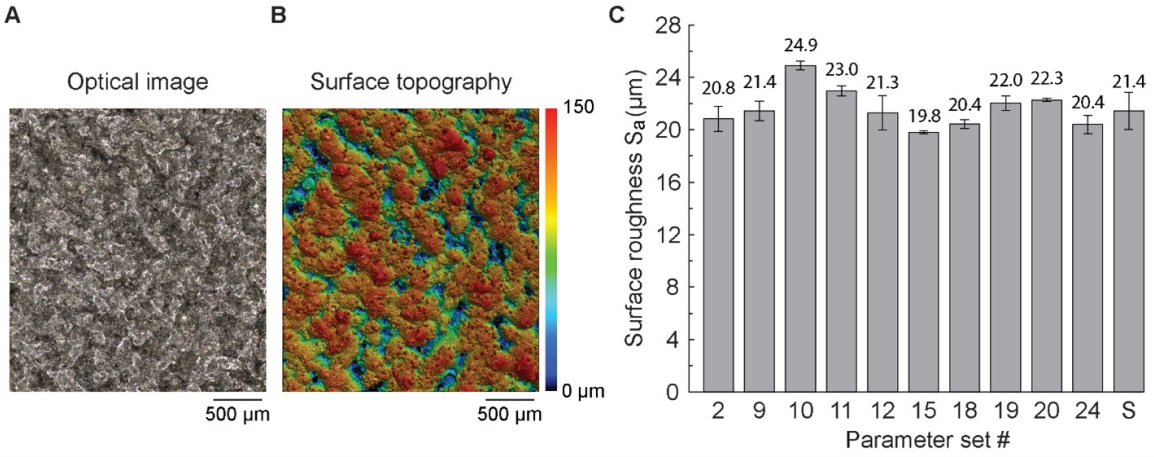


Figure 4.9: Surface roughness characterization. (A) Optical image of a representative sample (parameter set 10). (B) Corresponding 3D surface topography. (C) Areal arithmetic mean height (S_a) for selected samples.

topography of a sample prepared with parameter set 10. Surface roughness results of selected samples are represented as the areal arithmetic mean height (S_a) and are shown in Figure 4.9C. The S_a values varied from 19.8 μm to 24.9 μm across the tested samples. This variation reflects the influence of different LPBF processing conditions on the as-built surface texture. The highest surface roughness was observed in the sample prepared with parameter set 10 ($S_a = 24.9\,\mu$m), while the lowest was measured in the sample prepared with parameter set 15 ($S_a = 19.8\,\mu$m). Most samples fell within a relatively narrow band between approximately 20.0 μm and 23.0 μm, with error bars indicating the standard deviation of three regions per sample. The inclusion of samples with differing porosity and hardness characteristics allows for future analysis to correlate surface condition to internal part quality. Representative optical and 3D surface topography images have been investigated to understand the characteristic morphology of the as-built surface, which includes partially fused particles, melt pool ridges, and unmelted satellite features typical of LPBF [287].

4.5 Discussion

Scan speed has a strong influence on cooling rates during LPBF, which in turn affects microstructure and hardness. High energy input produces larger melt pools and greater superheat, which generally reduces the thermal gradient at the solidification front and lowers the cooling rate, leading to coarser grains and lower hardness [288]. As the areal energy density is reduced, for example by increasing scan speed or decreasing laser power, the estimated cooling rate at the solidification front increases within our process window. Here we use cooling rate in the standard sense as the product of the liquid–solid interface velocity and the temperature gradient at the interface, and we treat it as an effective metric that captures their combined dependence on processing conditions [257, 289, 290, 291, 292].

Building on these observations, plotting Vickers hardness against the combined energy input metric $E_a = P/(vh)$, where E_a is areal energy density (J/mm^2), P is laser power, v is scan speed, and h is hatch spacing, reveals a clear, approximately linear decline in hardness as energy density increases, as shown in Figure 4.10. Areal energy density was used as the quantitative metric to account for variations in scan area and melt-pool overlap. This simple representation confirms that lower energy density (high scan speed or lower power) promotes finer microstructures and higher hardness, whereas higher energy density leads to slower cooling, coarser intermetallics, and a modest hardness drop. Parameter sets 10, 16, and 40 are shown again in Figure 4.10, which directly correlate with the linear energy density. The linear regression of hardness against E_a yields an R^2 of 0.543 and an adjusted R^2 of 0.533, meaning that just over half of the variability in hardness across our parameter sets is captured by areal energy density alone. For porosity, the second-order fit returns an R^2 of 0.670 and an adjusted R^2 of 0.655, so roughly two-thirds of the porosity variation can be explained by E_a. These moderate-to-strong correlations confirm that areal energy density is a primary driver of both microstructural hardening and void formation in our builds.

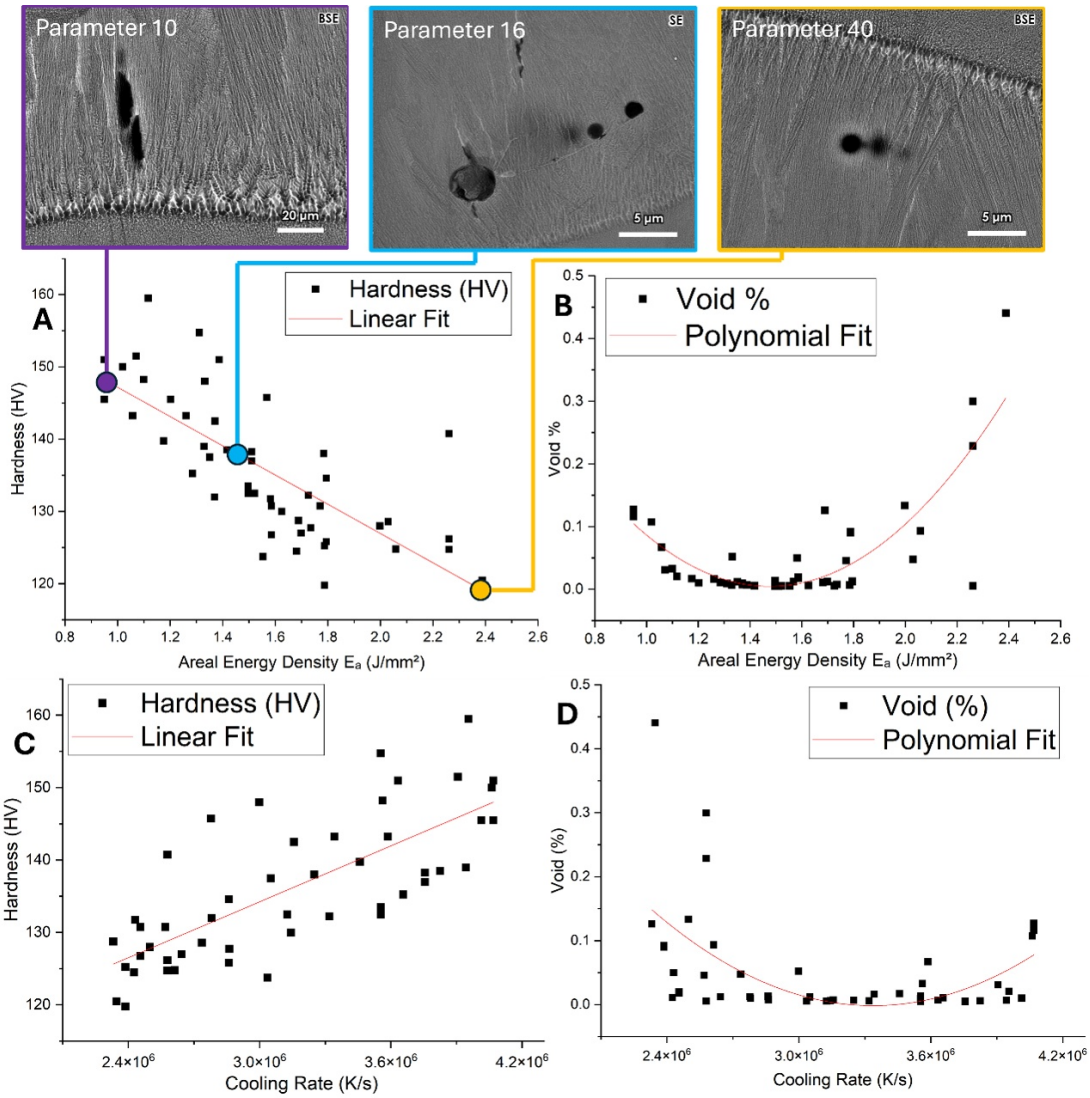


Figure 4.10: Relationships between areal energy density, cooling rate, hardness, and porosity. (A) Hardness versus areal energy density. (B) Porosity versus areal energy density. (C) Hardness versus cooling rate. (D) Porosity versus cooling rate. Parameter sets 10, 16, and 40 are highlighted.

Areal energy density also exhibits a U-shaped relationship with porosity, shown in Figure 4.10B. Both very low and very high scan speeds lead to higher porosity, with optimal parameters near the center. As previously shown in Figure 4.5, higher energy density (lower scan speed and higher power) leads to keyholing porosity while lower energy density (faster scan speed and lower power) leads to lack of fusion. Both trends are seen in Figure 4.10B.

To better understand how process parameters affect microstructure, hardness, and porosity, a more physical metric is the maximum instantaneous cooling rate at the solidification front, based on Rosenthal's solution for a moving heat source [293, 294]:

$$\dot{T} = \left.\frac{dT}{dt}\right|_{T=T_l} \tag{4.4}$$

$$\dot{T} = \frac{2\pi k \left(T_l - T_0\right)^2 v}{\eta P} = C/E_L \tag{4.5}$$

where $\dot{T}$ denotes the maximum cooling rate evaluated at the liquidus temperature. The alloy's thermal conductivity k was taken as $130\,\mathrm{W{\cdot}m^{-1}{\cdot}K^{-1}}$ [295], its liquidus temperature T_l as $873\,\mathrm{K}$ [257], and the base or powder-bed temperature T_0 was initially set to $303\,\mathrm{K}$. The effective laser absorptivity η was set to 0.35 [296]. P and v represent the laser power and the scan speed, respectively, and are taken directly from each build condition. The cooling rate reduces to energy density divided by a constant. Mathematically, the areal energy input that controls melt-pool size and temperature gradient enters directly into the cooling-rate equation, so that any change in laser power, scan speed or track spacing is reflected in a single cooling-rate parameter. This unified formulation captures both how rapidly heat is removed once the melt front passes and how the thermal gradient evolves, providing a direct link between process settings and solidification kinetics. In Figure 4.10C and D we replace the broad energy-density descriptors with the instantaneous cooling rate at solidification, as given by Eq. 4.5.

Figure 4.10C shows a linear increase in hardness with increasing cooling rate, demonstrating that faster solidification uniformly hardens the alloy. Figure 4.10D presents the corresponding porosity behavior as a polynomial curve with a minimum at intermediate cooling rates. Together, these plots identify a narrow processing window in the range of 3.0–3.6 $\times$ 10^6 K/s in which cooling is neither too slow nor too fast, yielding both maximum hardness and minimum porosity.

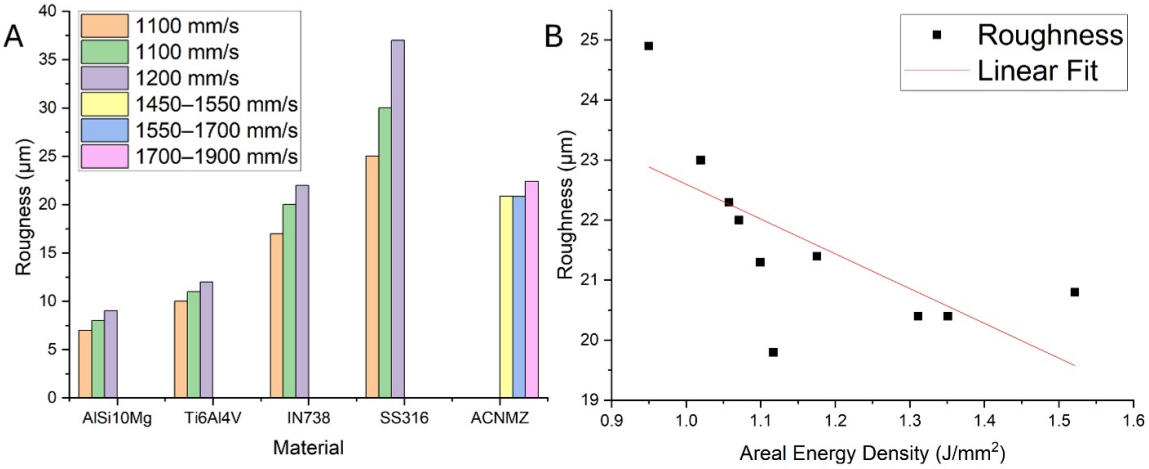


Figure 4.11: Surface roughness comparison. (A) Roughness values for ACNMZ compared with other metal systems across a range of scan speeds. (B) Surface roughness as a function of areal energy density.

The surface roughness behavior of the ACNMZ alloy observed in this study is consistent with broader trends identified through high-throughput surface roughness screening methods. As shown in Figure 4.11, roughness values for ACNMZ fall between 19 and 25 μm across a range of scan speeds, comparable to roughness levels in other metal systems such as AlSi10Mg, Ti6Al4V, and IN738 under similar conditions [297, 298, 299, 300, 301, 302, 303, 304, 305, 306, 307, 308, 309].

The analysis presented in Figure 4.11B reveals a clear correlation between surface roughness and areal energy density. As shown in panel B, surface roughness decreases with energy density, which itself reflects changes in thermal gradients and solidification dynamics. Since areal energy density is the key governing parameter, we can directly relate surface roughness to our physical metrics of hardness and

porosity. More details on this type of trend can be found in previous work [297]. This trend is physically meaningful: lower areal energy density corresponds to reduced heat input, which limits melt pool size and stability, promoting the formation of partially fused particles and increasing surface roughness. Conversely, higher areal energy densities promote more complete melting and smoother consolidation, reducing surface roughness. The observed dependence of surface roughness on laser energy input is consistent with prior observations across multiple alloy systems, where alloys processed at lower scan speeds consistently exhibited higher surface smoothness [297, 298, 299, 300, 301, 302, 303, 304, 305, 306, 307, 308, 309]. This relationship reinforces the importance of carefully balancing process parameters to avoid under-melting, which can result in high surface roughness [310, 311].

These findings offer a template for broader adoption of laser powder bed fusion across a range of high-performance metal systems. This study shows that adjusting scan speed, laser power, and hatch spacing can reduce porosity, improve microstructure, and increase hardness. This approach of precise control over melt pool energetics and thermal gradients is directly applicable to other alloy classes, including titanium, nickel superalloys and novel aluminum formulations.

4.6 Conclusions

This chapter provides macroscale evidence for the central hypothesis of this dissertation: that predictable and transferable material outcomes in laser manufacturing are achieved by jointly controlling energy delivery and spatial constraints. The response surface models constructed from 60 LPBF builds demonstrate that laser power, scan speed, and hatch spacing do not govern porosity and hardness independently. Their effects are fundamentally coupled through the melt pool energy they collectively impose, and this coupling produces the characteristic response surface signatures observed here: a U-shaped porosity dependence centered on intermediate energy inputs, where keyhole-mode collapse and lack-of-fusion voids bracket a narrow stable window, and a monotonically increasing hardness response tied to finer intermetallic spacing at higher cooling rates. These are not incidental trends. They follow directly from the melt pool regime transitions that Chapter 1 identified as the governing failure modes of track-based manufacturing, confirming that the general physical framework extends quantitatively to this specific alloy system.

The practical outcome of this coupled-control analysis is a well-defined processing window. Selecting laser powers between 350 W and 370 W, scan speeds from 1,400 mm/s to 1,800 mm/s, and hatch spacings of 0.14 mm to 0.18 mm with a layer thickness of 30 μm places ACNMZ builds within an instantaneous cooling rate of 3.0–3.6 $\times 10^6$ K/s. Within this window, the melt pool fully consolidates without entering keyhole instability, the eutectic spacing is refined to its finest achievable state, and the resulting components exhibit porosity below 0.01 vol% and as-built hardness up to 160 HV. The Rosenthal cooling rate metric, which captures more than half of the variation in both hardness and porosity responses from process settings alone, provides a physically grounded, transferable design handle: rather than re-searching the parameter space for related alloys or different machines, the processing window

can be re-targeted by mapping power and speed to the same cooling rate range, using the same material physics.

The approach demonstrated here, systematic statistical mapping grounded in a physics-based scaling argument, applies the same strategy that proved effective at the nanoscale in Chapters 2 and 3, now translated to the macroscale. At the nanoscale, identifying which process axis dominates the outcome (the ablation environment for phase constitution) and characterizing its functional form provided the leverage needed to bound the viable design space. Here, scan speed and its effect on cooling rate serve the same role. This consistency across nine orders of magnitude in processing scale, from sub-100 nm nanoparticles to centimeter-scale structural components, reinforces the dissertation's position that laser precision manufacturing is most reliably practiced through the deliberate coupling of energy delivery and spatial constraints, where each axis governs a distinct aspect of the thermal history and each combination of axes determines a distinct material outcome.

Chapter 5

Laser Processing of Tungsten: A Computationally Efficient Hybrid Two-Temperature Model for Multi-Pulse Femtosecond Laser Heat Accumulation

5.1 Disclosure

Source disclosure. The content of this chapter is based on a manuscript authored by David Fieser, Unmanaa Nileen Dewanjee, and Anming Hu: *A Computationally Efficient Hybrid Two-Temperature Model for Multi-Pulse Femtosecond Laser Heat Accumulation in Metals: Application to Tungsten.*

Support and contributions disclosure. This work was supported by the National Science Foundation under Award No. CMMI-2412544, "Collaborative Research: Additive Manufacturing of Crack-Free Tungsten Using Ultrashort Pulsed Lasers" (PI: Dr. Anming Hu, Division of Civil, Mechanical, & Manufacturing Innovation, NSF Program: AM-Advanced Manufacturing). The authors gratefully acknowledge Drs. Yanfei Gao, Wenda Tan, and Seungha Shin for their contributions and collaboration on this project.

5.2 Motivation and Background

Chapter 1 established the central hypothesis of this dissertation: that predictable and transferable material outcomes are achieved by jointly controlling laser energy delivery, environmental conditions, and spatial constraints. It also introduced the TTM as the governing framework for ultrafast laser–metal interaction and reviewed the thermophysical constraints that make tungsten one of the most challenging metals to process by any thermal method. Chapters 2 and 3 tested the environmental control dimension of the hypothesis at the nanoscale, demonstrating that the liquid ablation medium determines the phase constitution, surface chemistry, and thermodynamic stability of high-entropy alloy nanoparticles synthesized by femtosecond laser ablation. Chapter 4 moved to the macroscale, applying response surface methodology to characterize how coupled energy delivery and spatial constraints govern porosity, microstructure, and hardness in laser powder bed fusion of an aluminum alloy.

This chapter returns to the ultrafast physics introduced in Chapter 1 and develops the TTM from a conceptual framework into a quantitative computational method capable of predicting the thermal state of a metal surface under sustained multi-pulse femtosecond laser irradiation. Where Chapter 1 used the TTM to explain the timescale separation between electron excitation and lattice heating, and to motivate the precision advantages of ultrashort pulses, this chapter solves the coupled equations numerically for hundreds to thousands of sequential pulses under conditions relevant to industrial megahertz-rate processing. The material system is tungsten, whose extreme thermophysical properties, high melting point, high thermal conductivity, and the brittleness below its DBTT reviewed in Section 1.5.4, make it both a critical application target and a stringent test of the modeling framework.

Modern ytterbium-doped fiber and thin-disk laser architectures deliver average powers of tens to hundreds of watts at repetition rates from hundreds of kilohertz to tens of megahertz [312, 313], enabling high-throughput industrial processing of metals, semiconductors, and dielectrics [314, 315, 316, 317, 135, 318]. At megahertz

repetition rates, the inter-pulse interval becomes shorter than the thermal diffusion time, and a progressive baseline temperature rise develops near the irradiated surface [319, 320, 321, 322]. This cumulative thermal loading controls damage thresholds, melt onset, recast layer formation, and surface finish, as documented experimentally for steel, copper, aluminum, and titanium alloys [320, 323, 324, 325]. Weber et al. [319] established analytical scaling laws relating the accumulated temperature rise to average power, repetition rate, and spot size, and Bauer et al. [321] extended this framework to scanning ablation geometries, identifying critical scanning speeds below which thermal damage cannot be avoided. These models provide useful scaling relations but rely on lumped-capacitance or Green's function approaches that treat the material as a homogeneous thermal reservoir and do not resolve the nonequilibrium electron–lattice dynamics that govern energy deposition and redistribution during the first picoseconds after each pulse.

Applying the TTM to multi-pulse scenarios at megahertz repetition rates is computationally expensive. The coupled equations are stiff: the small electron heat capacity and large coupling coefficient produce relaxation timescales on the order of picoseconds, requiring sub-picosecond temporal resolution during and immediately after the pulse. At 10 to 20 MHz, the inter-pulse period is 50 to 100 ns, four to five orders of magnitude longer than the equilibration time. Continuing the stiff integration through this gap is wasteful because the electron and lattice temperatures equilibrate long before the next pulse arrives and the system evolves by simple thermal diffusion. For a single pulse the cost is modest, but simulating hundreds or thousands of sequential pulses grows impractical [326, 327]. Most published TTM studies have therefore been limited to single-pulse or few-pulse analyses, leaving the cumulative thermal state uncharacterized from first principles.

Several approaches have attempted to reduce this cost. Zero-dimensional lumped-capacitance models, including those of Weber et al. [319] and later extensions [321, 328], track only a single temperature as a function of pulse number. These are fast and produce useful scaling laws, but they cannot resolve depth-dependent

temperature gradients that determine the HAZ extent, subsurface microstructural changes, or spatially localized phenomena such as the surface temperature inversion in which the lattice temperature transiently exceeds the electron temperature after equilibration. Multi-dimensional TTM simulations have been demonstrated for burst-mode processing with a small number of sub-pulses [329, 330] but have not been extended to the hundreds or thousands of pulses that characterize MHz-rate processing. No existing method preserves the spatially resolved nonequilibrium physics of the TTM during each pulse while avoiding the cost of stiff integration through the inter-pulse gap.

Tungsten is a key application for such a model. As reviewed in Chapter 1, it is the primary plasma-facing material for the divertor and first wall of the ITER fusion reactor and next-generation fusion power plants [331, 332, 333, 334]. Ultrashort-pulsed laser processing at megahertz repetition rates has attracted interest for precision machining, surface texturing, and crack-free additive manufacturing of tungsten, because the femtosecond interaction minimizes the HAZ that would otherwise trigger brittle fracture [335, 336, 337]. Designing such processes requires quantitative prediction of the accumulated surface temperature, the HAZ depth, and the proximity to melt or recrystallization thresholds under multi-pulse irradiation.

This chapter introduces a hybrid two-phase numerical method that exploits the timescale separation inherent to multi-pulse femtosecond laser processing. During each pulse and the subsequent relaxation period, the full one-dimensional coupled TTM is solved on a fine spatial grid with a stiff implicit integrator. Once the electron and lattice temperatures equilibrate, the resulting profile is mapped onto a coarser, deeper grid and advanced through the remaining inter-pulse interval by Crank–Nicolson diffusion with temperature-dependent conductivity from tabulated experimental data. This two-phase handoff reduces the per-pulse cost by roughly two orders of magnitude relative to monolithic TTM integration while retaining the spatial resolution needed to capture depth-dependent phenomena. The method is

applied to tungsten with Sommerfeld and Drude constitutive models, and multi-pulse simulations demonstrate the progressive inter-pulse temperature buildup and a surface temperature inversion in which the lattice temperature exceeds the electron temperature after each pulse, an effect that grows with cumulative heating and has not previously been reported for tungsten. Validation against scanning femtosecond laser experiments on tungsten confirms that the predicted melt zone diameter matches the experimentally measured central zone.

5.3 Methods

5.3.1 Femtosecond Laser Irradiation

Bulk polycrystalline tungsten substrates were irradiated in air using a femtosecond fiber laser (Amplitude Tangor 100, Amplitude Laser Inc., Milpitas, CA, USA) delivering 500 fs pulses at a wavelength of 1030 nm with up to 100 W average power. For all experiments reported here, the repetition rate was set to 40 MHz. The beam was focused to a $1/e^2$ spot radius of approximately 100 µm and scanned across the surface using a three-axis motorized stage. Ten samples, S1–S10, were processed: a power series (S1–S5) at 20 to 100 W with a fixed scanning speed of 60 mm/min, and a speed series (S6–S10) at 80 W with scanning speeds from 120 to 900 mm/min.

5.3.2 Surface Characterization

Processed surfaces were characterized using a confocal Raman microscope (WITec alpha300 RAS) equipped with optical microscope objectives and a 532 nm excitation laser. Optical micrographs were acquired to identify the HAZ and central damage zone boundaries. Raman spectra were collected at room temperature at 0.5 mW power, 5 s integration time, and 10 accumulations per spectrum.

5.3.3 Governing Equations

The one-dimensional TTM describes the coupled evolution of the electron temperature $T_e(z,t)$ and lattice temperature $T_l(z,t)$ along the depth coordinate z, measured into the bulk from the irradiated surface. Originally proposed by Kaganov, Lifshitz, and Tanatarov [7] for electron–phonon relaxation in metals, and later extended to ultrashort-pulse laser heating by Anisimov, Kapeliovich, and

Perel'man [9], the governing equations are

$$C_e(T_e)\,\frac{\partial T_e}{\partial t} = \frac{\partial}{\partial z}\left[k_e(T_e, T_l)\,\frac{\partial T_e}{\partial z}\right] - G\,(T_e - T_l) + S(z,t), \tag{5.1}$$

$$C_l\,\frac{\partial T_l}{\partial t} = \frac{\partial}{\partial z}\left[k_l\,\frac{\partial T_l}{\partial z}\right] + G\,(T_e - T_l), \tag{5.2}$$

where C_e and C_l are the volumetric heat capacities, k_e and k_l are the thermal conductivities, G is the electron–phonon coupling coefficient [338], and $S(z,t)$ is the laser source term. The electronic heat capacity follows the Sommerfeld model [339, 340],

$$C_e = \gamma\,T_e, \tag{5.3}$$

where γ is the Sommerfeld coefficient. In the implementation, T_e is clamped to a minimum of 1 K to prevent division by zero at initialization. The electron thermal conductivity uses the simplified Drude expression [341, 27],

$$k_e = k_{e0}(T_l)\,\frac{T_e}{T_l}, \tag{5.4}$$

where the base conductivity k_{e0} is not a constant but is derived from a tabulated total equilibrium conductivity $k_{\mathrm{hyb}}(T)$ for tungsten [342, 343, 334] via

$$k_{e0}(T_l) = k_{\mathrm{hyb}}(T_l) - k_l. \tag{5.5}$$

At thermal equilibrium ($T_e = T_l = T$), this construction guarantees that the total conductivity $k_e + k_l = k_{\mathrm{hyb}}(T)$ recovers the experimentally measured value. During nonequilibrium ($T_e \neq T_l$), the Drude ratio T_e/T_l redistributes the electron conductivity in proportion to the temperature imbalance while anchoring the equilibrium limit to measured data.

The laser source term assumes Beer–Lambert absorption [344],

$$S(z,t) = A\,F\,g(t)\,\alpha_{\mathrm{opt}}\,\exp(-\alpha_{\mathrm{opt}}\,z), \tag{5.6}$$

where A is the surface absorptance, F is the peak on-axis fluence, $g(t)$ is the normalized temporal pulse profile ($\int g\,\mathrm{d}t = 1$), and α_{opt} is the optical absorption coefficient. The temporal profile is a normalized Gaussian with FWHM τ_p,

$$g(t) = \sqrt{\frac{4\ln 2}{\pi\,\tau_p^2}}\,\exp\left[-4\ln 2\left(\frac{t-t_c}{\tau_p}\right)^2\right], \tag{5.7}$$

where t_c is the pulse center time. For a multi-pulse simulation the source function is evaluated as a sum over all pulse centers, but only contributions from the nearest one or two pulses (within $\pm 10\,\tau_p$) are retained at each evaluation, making the computation independent of the total pulse count.

5.3.4 Material Properties

Table 5.1 lists the TTM parameters for tungsten.

Table 5.1: Material properties for tungsten.

Property	Symbol	Value
Sommerfeld coefficient	γ [J m^{-3} K^{-2}]	137.3 [338, 340]
Lattice heat capacity	C_l [J m^{-3} K^{-1}]	2.54×10^6 [334]
Electron–phonon coupling	G [W m^{-3} K^{-1}]	1.65×10^{17} [345, 346]
Base electron conductivity[a]	k_{e0} [W m^{-1} K^{-1}]	150 [342]
Lattice conductivity	k_l [W m^{-1} K^{-1}]	24 [347, 348]
Optical absorption coeff.	α_{opt} [m^{-1}]	5.88×10^7 [349]

[a] Room-temperature value. In the implementation, $k_{e0}(T_l) = k_{\mathrm{hyb}}(T_l) - k_l$ varies with lattice temperature (see eq. (5.5)).

The equilibrium total thermal conductivity $k_{\mathrm{hyb}}(T)$ is represented by piecewise-linear interpolation of tabulated values at ten reference temperatures from 293 K to 2500 K, as listed in table 5.2 [334, 343]. For temperatures below 293 K or above 2500 K the nearest tabulated value is used via flat extrapolation.

Table 5.2: Tabulated total thermal conductivity $k_{\mathrm{hyb}}(T)$ for tungsten, used for both Drude k_{e0} modulation and Phase 2 diffusion.

T [K]	k_{hyb} [$\mathrm{W\,m^{-1}\,K^{-1}}$]
293	174.9
300	174.0
400	159.0
600	137.0
800	125.0
1000	118.0
1200	113.0
1500	107.0
2000	100.0
2500	95.0

5.3.5 Boundary and Initial Conditions

At the irradiated surface $z = 0$, an adiabatic zero-flux condition is imposed on both electron and lattice temperatures, $\partial T_e/\partial z = \partial T_l/\partial z = 0$, representing a metal-vacuum interface with negligible radiative and convective losses on femtosecond-to-nanosecond timescales. On the fine TTM grid the back face $z = L_z$ is also adiabatic. On the coarse diffusion grid the deep boundary $z = L_{\mathrm{diff}}$ is held at the initial temperature T_0 as a Dirichlet condition, which is valid because L_{diff} is chosen large enough that the thermal front does not reach it within the total simulation time. The initial condition for the first pulse is $T_e(z, 0) = T_l(z, 0) = T_0$ throughout both grids. For each subsequent pulse, the spatial temperature profile is inherited from the end of the preceding inter-pulse diffusion step, with $T_e = T_l$ at thermal equilibrium at the start of each new Phase 1.

5.3.6 Hybrid Two-Phase Solution Strategy

The electron–lattice nonequilibrium produced by each femtosecond pulse resolves within roughly 1 to 50 ps, whereas the inter-pulse period at 10 MHz to 20 MHz repetition rates is 50 to 100 ns. Continuing the coupled TTM integration through

the full inter-pulse gap is unnecessary because T_e and T_l reach local equilibrium long before the next pulse arrives. The hybrid method takes advantage of this timescale separation by dividing each pulse cycle into two phases.

Phase 1 solves the full coupled system (eqs. (5.1) and (5.2)) on a fine spatial grid using a stiff implicit ordinary differential equation (ODE) integrator. This phase begins $5\,\tau_p$ before the pulse center and ends at

$$t_{\mathrm{P1,end}} = t_c + \min\bigl(0.9\,T_{\mathrm{rep}},\ \max(200\,\tau_p,\ 500\,\mathrm{ps})\bigr), \tag{5.8}$$

where $T_{\mathrm{rep}} = 1/f_{\mathrm{rep}}$ is the pulse period. The lower bound of $\max(200\,\tau_p, 500\,\mathrm{ps})$ ensures that even for extremely short pulses the electron and lattice subsystems have sufficient time to equilibrate, while the upper bound of $0.9\,T_{\mathrm{rep}}$ prevents Phase 1 from consuming the entire inter-pulse interval.

Phase 2 maps the equilibrated temperature profile onto a coarser grid that extends to greater depth in the bulk and advances it through the remaining inter-pulse interval using Crank–Nicolson diffusion with temperature-dependent conductivity $k_{\mathrm{hyb}}(T)$. The surface temperature at the end of Phase 2 becomes the initial condition for the next Phase 1, and the cycle repeats for all N pulses.

5.3.7 Phase 1: Stiff ODE Integration on the Fine Grid

Spatial Discretization

The depth domain $[0, L_z]$ is discretized on a uniform grid of N_z nodes with spacing $\Delta z = L_z/(N_z - 1)$. The default parameters are $N_z = 200$ and $L_z = 1\,\mu\mathrm{m}$, giving $\Delta z \approx 5\,\mathrm{nm}$. This approximately satisfies the resolution guideline $\Delta z \leq \alpha_{\mathrm{opt}}^{-1}/4 \approx 4.3\,\mathrm{nm}$ for tungsten. The grid convergence study in section 5.4.1 confirms that this spacing is adequate. The state vector is

$$\mathbf{y} = \bigl[T_e^{(1)}, \ldots, T_e^{(N_z)},\, T_l^{(1)}, \ldots, T_l^{(N_z)}\bigr]^{\top}, \tag{5.9}$$

containing $2N_z$ unknowns.

Finite-Difference Discretization of Diffusion

The electron diffusion term $\partial/\partial z\,[k_e\,\partial T_e/\partial z]$ is discretized using second-order central differences with half-node conductivity averaging. Half-node conductivities are computed as arithmetic means of adjacent nodal values,

$$k_{e,j+\frac{1}{2}} = \tfrac{1}{2}\big(k_{e,j} + k_{e,j+1}\big), \tag{5.10}$$

so that the heat flux at each half-node is $q_{j+1/2} = k_{e,j+1/2}\,(T_{e,j+1} - T_{e,j})/\Delta z$. The divergence at interior node j is then

$$\left[\frac{\partial}{\partial z}\left(k_e \frac{\partial T_e}{\partial z}\right)\right]_j = \frac{q_{j+1/2} - q_{j-1/2}}{\Delta z}. \tag{5.11}$$

At the surface ($j = 1$), $q_{-1/2} = 0$ (adiabatic), so the divergence reduces to $q_{1/2}/\Delta z$. At the back face ($j = N_z$), $q_{N_z+1/2} = 0$, giving $-q_{N_z-1/2}/\Delta z$. Half-node averaging is important here because k_e varies by orders of magnitude across just a few nodes during the pulse, and nodal-center evaluations introduce significant discretization error.

The lattice diffusion term uses the same stencil but with a constant conductivity k_l, collapsing to the standard second-order Laplacian $k_l\,(T_{l,j-1} - 2T_{l,j} + T_{l,j+1})/\Delta z^2$ at interior nodes, with the same adiabatic ghost-node treatment at both boundaries.

ODE Integration

The semi-discrete system is integrated with the MATLAB stiff solver `ode15s`, which uses variable-order backward differentiation formulas. To accelerate the implicit solves, the Jacobian sparsity pattern is supplied explicitly. Because each node's equations depend on at most three adjacent nodes in each subsystem (tridiagonal from diffusion) and on the corresponding node of the other subsystem through coupling and the k_e dependence on T_l, the sparsity pattern has a 2×2 block structure with

tridiagonal blocks:

$$\mathbf{J}_{\text{pattern}} = \begin{bmatrix} \mathbf{J}_{\text{tri}} & \mathbf{J}_{\text{tri}} \\ \mathbf{J}_{\text{tri}} & \mathbf{J}_{\text{tri}} \end{bmatrix}, \tag{5.12}$$

where $\mathbf{J}_{\text{tri}}$ is an $N_z \times N_z$ tridiagonal matrix. Supplying this pattern reduces the cost of each numerical Jacobian evaluation from $\mathcal{O}(N_z^2)$ to $\mathcal{O}(N_z)$.

The maximum time step is limited to τ_p (the pulse FWHM) to prevent the integrator from stepping over the femtosecond pulse. Relative and absolute tolerances are set to 10^{-6} and 0.1 K, respectively. Output times are sampled densely (150 points for the first pulse, 40 for subsequent pulses) in a window from $-5\,\tau_p$ to $+20\,\tau_p$ around the pulse center. Beyond $+20\,\tau_p$, output times are distributed logarithmically through the remainder of Phase 1 (200 points for the first pulse, 50 for subsequent pulses), capturing the relaxation dynamics without unnecessary dense sampling.

5.3.8 Phase 2: Crank–Nicolson Inter-Pulse Diffusion

Coarse Diffusion Grid

Phase 2 operates on a coarse uniform grid of $N_{z,\text{diff}}$ nodes spanning $[0, L_{\text{diff}}]$, with a default spacing of $\Delta z_{\text{diff}} = 500\,\text{nm}$. The total depth L_{diff} is set to $\max\!\left(5\sqrt{\alpha_{\text{diff}}\, t_{\text{sim}}},\ 50\,\mu\text{m}\right)$, where $\alpha_{\text{diff}} = k_{\text{hyb}}(T_0)/C_l$ is the equilibrium thermal diffusivity at the initial temperature and t_{sim} is the total simulation duration. This ensures that the thermal front does not reach the deep Dirichlet boundary during the simulation.

Equilibrium Conductivity and the Crank–Nicolson Scheme

At the end of Phase 1, $T_e \approx T_l$ throughout the fine grid. The equilibrated profile $T_{\text{equil}}(z)$ is obtained by averaging T_e and T_l at each node, $T_{\text{equil}} = (T_e + T_l)/2$. This profile is then interpolated onto the coarse grid (see section 5.3.9), and the remaining

inter-pulse time is advanced by solving

$$C_l \frac{\partial T}{\partial t} = \frac{\partial}{\partial z}\left[k_{\mathrm{hyb}}(T)\,\frac{\partial T}{\partial z}\right] \tag{5.13}$$

with $N_{\mathrm{diff}} = 100$ equally spaced time steps. The Crank–Nicolson scheme is used, which is unconditionally stable, second-order accurate in both space and time, and requires only a tridiagonal solve per step. Temperature-dependent conductivity is handled by lagging k_{hyb} at the current time level, evaluated explicitly at T^n, then applying the implicit-explicit Crank–Nicolson weighting.

Half-node conductivities are again computed as arithmetic means:

$$k_{j+1/2} = \tfrac{1}{2}\big[k_{\mathrm{hyb}}(T_j^n) + k_{\mathrm{hyb}}(T_{j+1}^n)\big], \tag{5.14}$$

and the local Fourier numbers at each half-node are

$$r_{j+1/2} = \frac{k_{j+1/2}\,\Delta t}{2\,C_l\,\Delta z_{\mathrm{diff}}^2}. \tag{5.15}$$

The factor of 2 in the denominator arises from the Crank–Nicolson time averaging. For each interior node j, the tridiagonal system takes the form

$$\begin{aligned} -r_{j-1/2}\,T_j^{n+1} + (1 + r_{j-1/2} + r_{j+1/2})\,T_j^{n+1} - r_{j+1/2}\,T_{j+1}^{n+1} \\ = r_{j-1/2}\,T_{j-1}^{n} + (1 - r_{j-1/2} - r_{j+1/2})\,T_j^{n} \\ + r_{j+1/2}\,T_{j+1}^{n}. \end{aligned} \tag{5.16}$$

At the surface ($j = 1$), the adiabatic condition is enforced by setting a ghost node $T_0^n = T_1^n$, which doubles the effective surface Fourier number. At the deepest active node ($j = N_{z,\mathrm{diff}} - 1$), the Dirichlet condition $T_{N_{z,\mathrm{diff}}} = T_0$ enters the right-hand side as a known term. The system is solved at each step by the Thomas (tridiagonal) algorithm, which requires $\mathcal{O}(N_{z,\mathrm{diff}})$ operations.

5.3.9 Grid Mapping Between Phase 1 and Phase 2

The fine grid, spanning 0 to $L_z \approx 1\,\mu\text{m}$, occupies the shallowest portion of the coarse grid, which extends from 0 to L_{diff}, typically $50\,\mu\text{m}$ or more. At the end of Phase 1, the equilibrated fine-grid profile $T_{\text{equil}}(z)$ is linearly interpolated onto the coarse-grid nodes that fall within the overlap region $z \leq L_z$. The coarse-grid nodes deeper than L_z retain their accumulated temperature values from prior pulse cycles. At the first coarse-grid node beyond the overlap boundary, the temperature is replaced by the average of the deepest interpolated value and the existing coarse-grid value, providing a smooth transition that prevents interpolation discontinuities from generating spurious thermal gradients.

At the start of each new Phase 1, the coarse-grid profile is interpolated back onto the fine grid using the same linear interpolation. Because the fine grid is entirely contained within the coarse grid, this mapping is always well defined. The resulting profile is assigned to both T_e and T_l as the initial condition, reflecting the assumption of thermal equilibrium at the start of each pulse.

5.3.10 Fluence and Radial Profile Reconstruction

The Gaussian spatial profile with $1/e^2$ spot radius w_0 gives the peak on-axis fluence

$$F = \frac{2\,E_p}{\pi\,w_0^2}, \tag{5.17}$$

where $E_p = P_{\text{avg}}/f_{\text{rep}}$ is the single-pulse energy. The full three-dimensional temperature field is reconstructed from the on-axis one-dimensional solution using the scaling relation

$$T(r, z, N) = T_0 + \big[T(0, z, N) - T_0\big]\,\exp\!\left(\frac{-2\,r^2}{w_0^2}\right), \tag{5.18}$$

which is valid when the lateral thermal diffusion length $L_{\mathrm{lat}} = \sqrt{\alpha_{\mathrm{diff}}\, t_{\mathrm{sim}}}$ is small compared with w_0. For the conditions studied here, L_{lat} is on the order of 1 to 5 µm while w_0 ranges from 50 to 300 µm, so the condition $L_{\mathrm{lat}}/w_0 \ll 1$ is satisfied and no additional ODE integrations are needed. The radial profile is sampled at $N_r = 20$ uniformly spaced points from $r = 0$ to $r = 3\, w_0$.

5.3.11 Computational Cost

Each Phase 1 integration involves $2N_z = 400$ coupled ODEs. The block-tridiagonal Jacobian pattern reduces the number of finite-difference perturbations needed for Jacobian evaluation to six (three per block), making the implicit solve cost linear in N_z. The integrator typically takes 200 to 500 adaptive time steps per pulse. Each Phase 2 Crank–Nicolson solve involves a single Thomas algorithm pass with $\mathcal{O}(N_{z,\mathrm{diff}})$ operations, repeated 100 times per inter-pulse interval. The total computational cost per pulse is therefore $\mathcal{O}(N_z) + \mathcal{O}(N_{z,\mathrm{diff}})$, and the overall simulation cost scales linearly with the number of pulses N. By contrast, a monolithic TTM integration that continues the coupled ODE system through the full inter-pulse gap would require the stiff solver to take on the order of 10^4 additional time steps per pulse to traverse the 50 to 100 ns gap at adaptive step sizes constrained by the stiff coupling terms, increasing the per-pulse cost by roughly two orders of magnitude.

5.4 Results and Discussion

The results are organized to follow the model from first principles through to experimental validation. Numerical verification establishes convergence of the solver. Single-pulse simulations reveal the fundamental electron–lattice dynamics, including a surface temperature inversion. Multi-pulse simulations then show how these per-pulse dynamics compound into cumulative heat accumulation. Radial profile reconstruction extends the one-dimensional depth solution into three dimensions. The computational performance of the hybrid solver is then characterized. Finally, the model predictions are validated against scanning laser experiments on tungsten.

All simulations were performed on a single workstation using MATLAB with the `ode15s` stiff integrator for Phase 1 and a custom Crank–Nicolson solver for Phase 2. Unless stated otherwise, the default simulation parameters listed in table 5.3 are used throughout.

Table 5.3: Default simulation parameters.

Parameter	Symbol	Value
Target material		Tungsten
Average power	P_{avg}	40 W
Repetition rate	f_{rep}	18 MHz
Spot radius ($1/e^2$)	w_0	100 µm
Pulse width (FWHM)	τ_p	500 fs
Absorptance	A	0.55
Initial temperature	T_0	25 °C
Pulse energy	E_p	2.22 µJ
Peak on-axis fluence	F	0.014 J/cm^2

5.4.1 Verification and Convergence

Spatial Grid Convergence

To verify that the fine-grid discretization is adequate, a single-pulse simulation was run at three grid resolutions, $N_z = 100$, 200, and 400, corresponding to $\Delta z \approx 10\,\text{nm}$, 5 nm, and 2.5 nm, all on a 1 µm domain. The peak surface electron temperature converged from 4401 °C at $N_z = 100$ to 4074 °C at $N_z = 200$ and 3908 °C at $N_z = 400$. The relative change between the two finest grids is 4.1 %, compared with 8.0 % between the two coarsest, which confirms second-order spatial convergence. The peak lattice temperature shows similar convergence, decreasing from 463 °C to 413 °C and 390 °C. The default $N_z = 200$ balances accuracy and computational cost, with a grid spacing that satisfies $\Delta z \leq \alpha_{\text{opt}}^{-1}/4 \approx 4.3\,\text{nm}$ for tungsten.

Crank–Nicolson Temporal Convergence

The number of Crank–Nicolson time steps per inter-pulse period was varied over $N_{\text{diff}} = 50$, 100, and 200 for a 100-pulse simulation. All three cases produced identical residual temperatures of $T_{\text{resid}} = 232.2\,°\text{C}$ after 100 pulses, identical peak electron temperatures of 4472 °C, and identical wall times within 0.1 s. The Phase 2 diffusion is therefore fully converged at $N_{\text{diff}} = 100$, which is used for all subsequent simulations.

Phase 1 Duration Sensitivity

Two 100-pulse simulations were run with pulse widths of 500 fs and 10 fs, the latter exercising the 500 ps minimum Phase 1 duration enforced by eq. (5.8). Despite the very different electron dynamics during the pulse (the 10 fs case produces a peak surface T_e of 7327 °C compared with 4472 °C for the 500 fs case), both simulations yield the same residual temperature of $T_{\text{resid}} = 232\,°\text{C}$ after 100 pulses. Both cases confirm that the Phase 1-to-Phase 2 handoff occurs after complete electron–lattice

equilibration regardless of pulse width, and that the accumulated thermal state is insensitive to the Phase 1 cutoff.

5.4.2 Single-Pulse Electron–Lattice Dynamics

With numerical convergence established, the solver is applied to examine the fundamental physics of a single femtosecond pulse interaction with tungsten.

Depth-Resolved Temperature Profiles

Figure 5.1 presents the depth-resolved electron and lattice temperature profiles in tungsten at six selected delays after the pulse center. At $t = 1\,\text{ps}$, the electron temperature peaks sharply at the irradiated surface, reaching approximately 4000 °C, while the lattice temperature remains near ambient throughout the depth. The Beer–Lambert absorption profile confines the energy deposition to the top ∼20 nm, corresponding to the optical skin depth of 17 nm. By $t = 2\,\text{ps}$, electron thermal diffusion has already begun to redistribute energy deeper into the bulk: the surface T_e has decreased while a thermal front extends to approximately 50 nm. The lattice temperature begins to rise at the surface through electron–phonon coupling, but remains far below T_e.

Between 4 and 8 ps, the electron and lattice temperatures approach each other as the coupling term $G(T_e - T_l)$ drives energy transfer from the hot electron gas to the cooler lattice. A temperature inversion ($T_l > T_e$) develops at the surface during this equilibration phase, visible as the crossing of the T_e and T_l curves. By $t = 50\,\text{ps}$, the two subsystems have nearly equilibrated throughout the depth, with a residual temperature elevation confined to the top ∼200 nm.

Surface Temperature Dynamics and Inversion

Figure 5.2 shows the surface temperature evolution for a single pulse in tungsten and compares the dynamics across three metals. In tungsten (fig. 5.2a), the electron

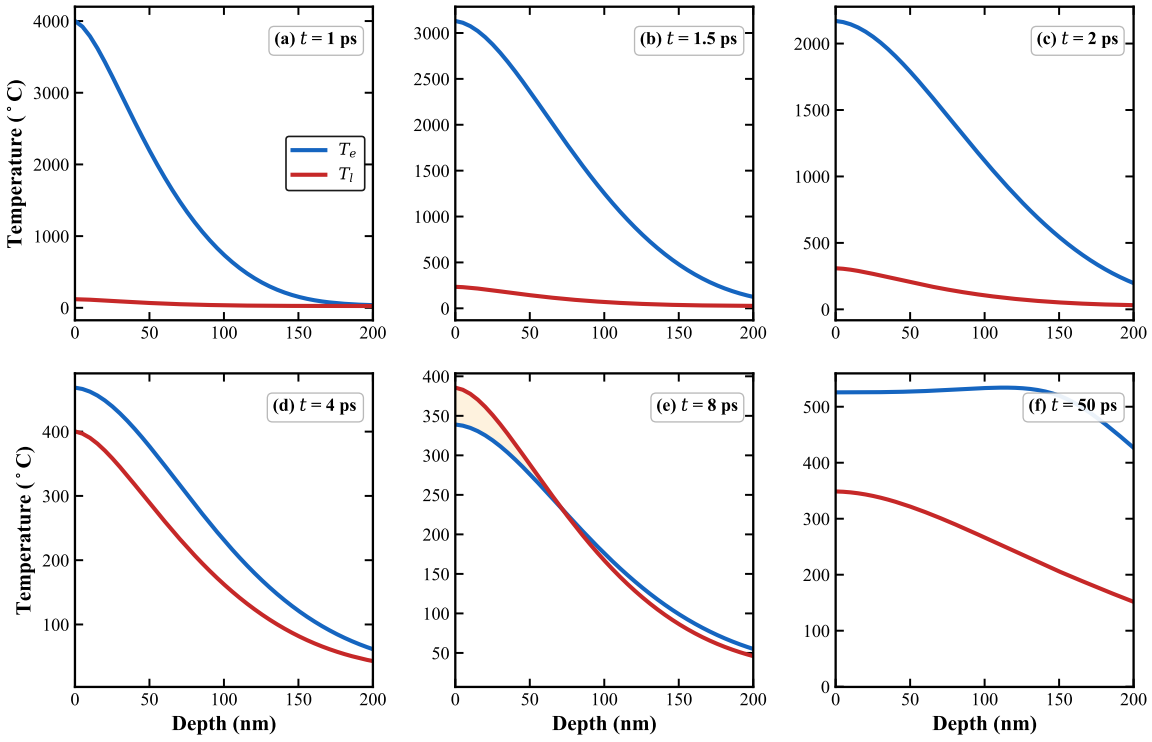


Figure 5.1: Depth-resolved electron temperature $T_e(z)$ (red) and lattice temperature $T_l(z)$ (blue) profiles in tungsten at selected delays after the pulse center. The shaded amber region indicates where $T_l > T_e$ (temperature inversion). Laser conditions: $\tau_p = 500\,\text{fs}$, $F = 0.014\,\text{J/cm}^2$, $A = 0.55$.

temperature rises to a peak of 4023 °C within approximately 1 ps of the pulse center and then decays rapidly as electron–phonon coupling transfers energy to the lattice. The lattice temperature rises more gradually, reaching a peak of 399 °C at approximately 5 ps.

This cooling timescale can be compared with the earliest time-resolved measurement of nonequilibrium heating in tungsten. Fujimoto et al. [8] used 75 fs optical pulses and measured an electron–phonon energy relaxation time of several hundred femtoseconds. Because the relaxation time $\tau_{ep} = \gamma T_e / G$ scales linearly with T_e, it depends on excitation level. At the simulated peak electron temperature of approximately 4273 K, the model predicts $\tau_{ep} \approx 3.6$ ps. The Fujimoto et al. experiment used lower fluences on thin films, producing much lower peak electron temperatures near 500 K, for which the same expression gives $\tau_{ep} \approx 0.4$ ps, consistent with their measured value.

A surface temperature inversion $T_l > T_e$ develops after approximately 3 ps, as shown in fig. 5.2b. The high electron thermal conductivity k_e diffuses energy away from the surface faster than electron–phonon coupling replenishes it, causing T_e to fall below the slowly rising T_l. The inversion persists for several hundred picoseconds before the two temperatures re-equilibrate. Zero-dimensional lumped-capacitance models cannot capture this spatially resolved effect.

The cross-material comparison in fig. 5.2c shows that aluminum reaches the highest peak lattice temperature of 517 °C and equilibrates most rapidly because of its large electron–phonon coupling coefficient, whereas copper shows the lowest peak lattice temperature of 175 °C due to its weaker coupling and high electron conductivity. Tungsten lies between the two. Peak electron temperatures are similar across all three metals, ranging from 3805 °C to 4405 °C, consistent with comparable absorbed fluences and Sommerfeld coefficients.

When the initial temperature is raised to 500 °C (case B4), simulating a pulse after heat accumulation, the peak electron temperature increases to 5113 °C and the peak lattice temperature rises to 1017 °C. The elevated baseline increases the electronic

heat capacity, and the same pulse energy deposited into an already warm lattice produces a larger absolute temperature excursion.

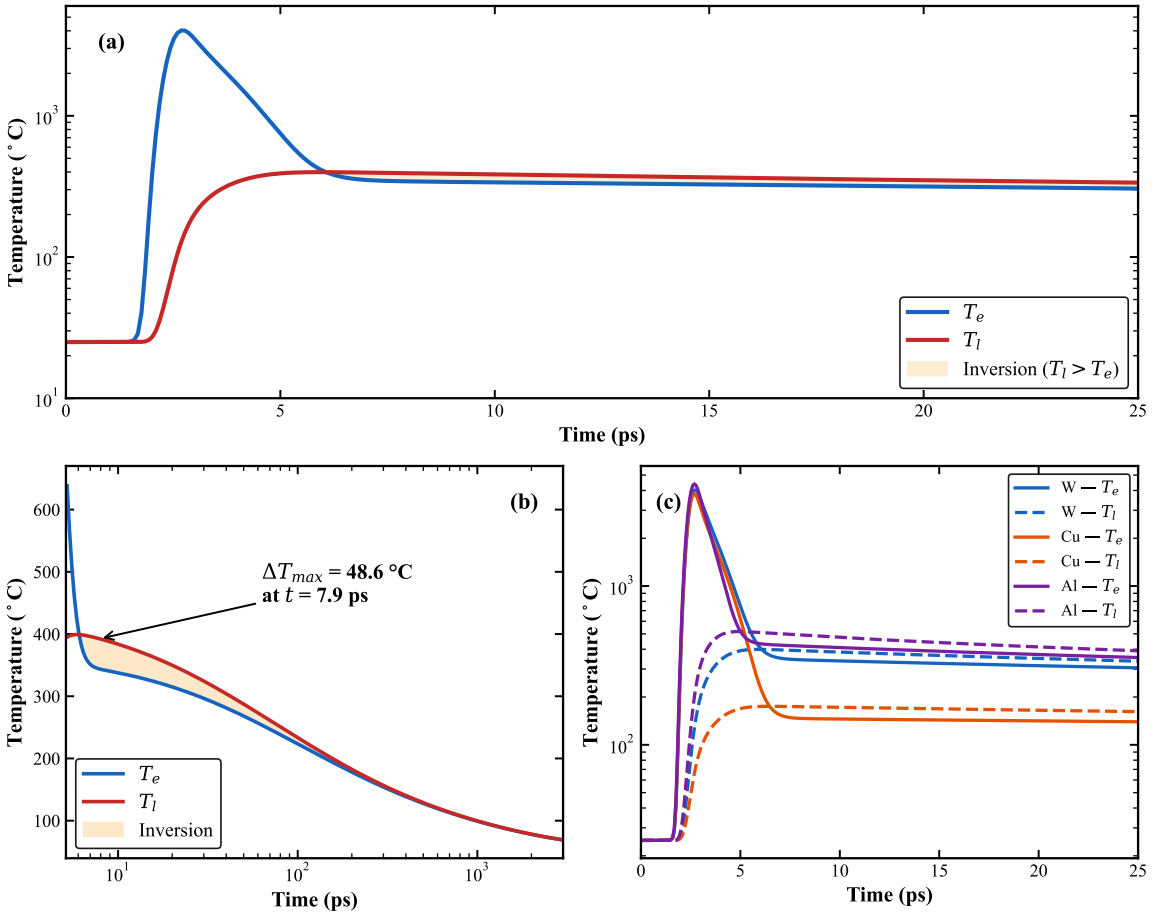


Figure 5.2: (a) Surface electron and lattice temperature evolution for a single 500 fs pulse in tungsten (log-scale ordinate). (b) Zoomed view of the inversion region where $T_l > T_e$, with the peak inversion magnitude annotated. (c) Comparison of surface dynamics across tungsten, copper, and aluminum under identical irradiation conditions (solid lines: T_e, dashed lines: T_l).

5.4.3 Multi-Pulse Heat Accumulation

The single-pulse results show that each femtosecond pulse deposits energy into a shallow surface layer that equilibrates within tens of picoseconds. At megahertz repetition rates, the next pulse arrives before this residual heat fully dissipates,

so successive pulses compound into a progressive temperature rise. The following subsections characterize this accumulation process.

Pulse-by-Pulse Temperature Buildup

Figure 5.3 shows the pulse-by-pulse evolution of the post-equilibration temperature T_{eq}, defined as the peak temperature after electron–lattice equilibration within each pulse cycle, and the pre-pulse residual temperature T_{resid}, the surface temperature immediately before the next pulse arrives, for the reference case C1 at 40 W, 18 MHz, $w_0 = 100\,\mu\mathrm{m}$, over 1800 pulses. The residual temperature rises rapidly over the first $\sim$100 pulses and then approaches a quasi-equilibrium, reaching $T_{\mathrm{resid}} = 1091\,^{\circ}\mathrm{C}$ after 1800 pulses. The equilibration temperature follows a parallel trajectory offset above T_{resid} by the per-pulse temperature increment $T_{\mathrm{eq}} - T_{\mathrm{resid}} \approx 50\,^{\circ}\mathrm{C}$ to $60\,^{\circ}\mathrm{C}$ per pulse at late times. The peak electron and lattice temperatures at 1800 pulses are $5682\,^{\circ}\mathrm{C}$ and $1672\,^{\circ}\mathrm{C}$, respectively.

This behavior reflects the balance between per-pulse energy deposition and inter-pulse thermal diffusion. In the early pulses, the thermal penetration depth is shallow and most of the deposited energy remains near the surface, so the temperature rises rapidly. Figure 5.4 shows the surface T_e and T_l over the first six pulses, where each pulse produces a sharp T_e spike that equilibrates with the lattice within picoseconds while the baseline T_l rises progressively between pulses. As the thermal front propagates deeper, the effective thermal mass increases, the per-pulse increment diminishes, and the system approaches a dynamic equilibrium.

At the lower repetition rate of 10 MHz, case C2, the pulse energy is 4 µJ compared with 2.22 µJ at 18 MHz, and the longer 100 ns inter-pulse interval allows more cooling per cycle. Despite the longer cooling time, the higher fluence drives T_{resid} to $1552\,^{\circ}\mathrm{C}$ after 2000 pulses, with peak electron and lattice temperatures of $8218\,^{\circ}\mathrm{C}$ and $2577\,^{\circ}\mathrm{C}$, respectively. The higher peak temperatures at 10 MHz confirm that the single-pulse fluence, rather than the repetition rate alone, is the dominant factor controlling the thermal response.

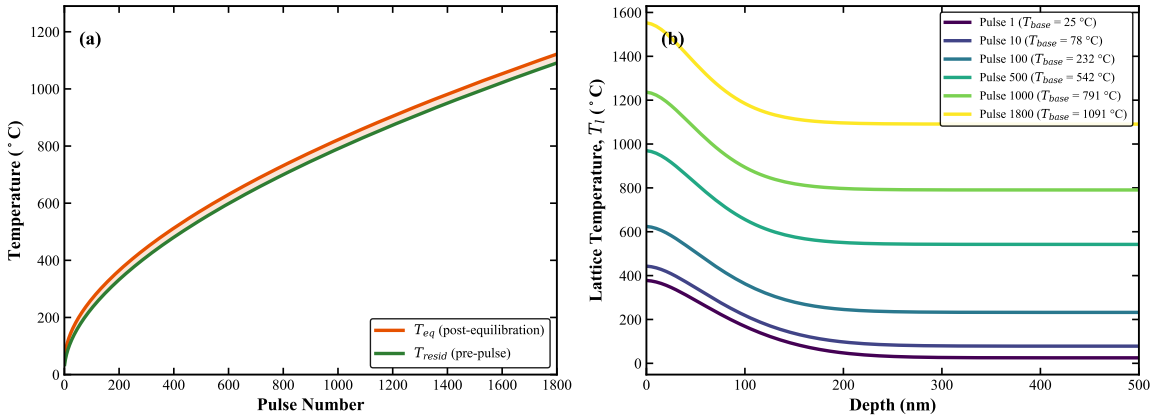


Figure 5.3: Heat accumulation for case C1 (W, 40 W, 18 MHz, $w_0 = 100\,\mu\text{m}$). (a) Per-pulse post-equilibration temperature T_{eq} and pre-pulse residual temperature T_{resid} versus pulse number. The shaded region represents the per-pulse temperature excursion. (b) Lattice temperature profiles $T_l(z)$ at selected pulse counts (1, 10, 100, 500, 1000, and 1800), showing progressive thermal penetration into the bulk.

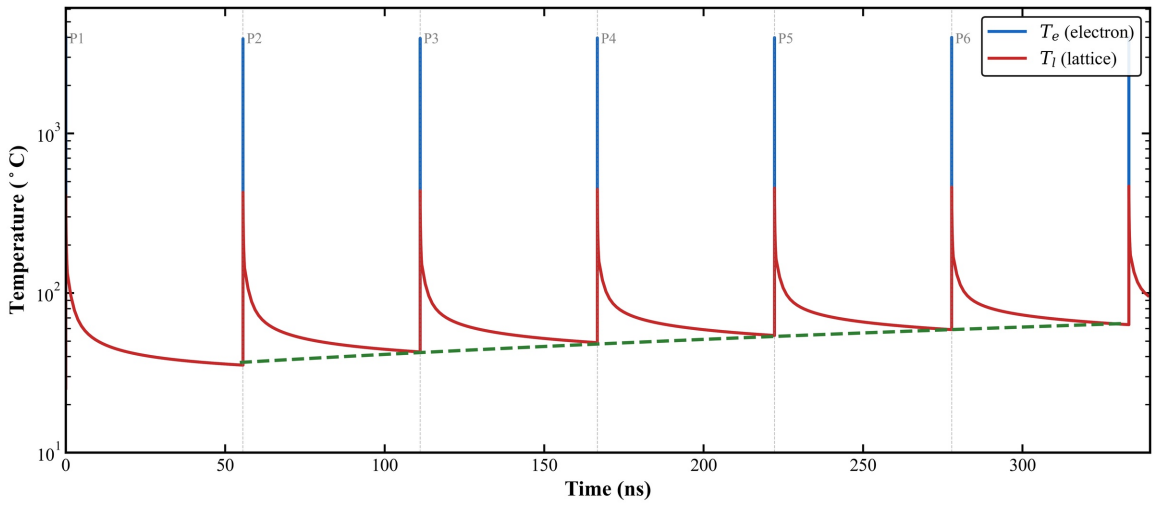


Figure 5.4: Surface electron temperature T_e (blue) and lattice temperature T_l (red) during the first six pulses (P1 through P6) for case C1. Each pulse produces a sub-picosecond T_e spike followed by rapid electron–lattice equilibration. The dashed green line traces the rising inter-pulse baseline temperature.

Depth-Profile Evolution

Figure 5.3b presents lattice temperature versus depth at logarithmically spaced pulse counts (1, 10, 100, 500, 1000, and 1800) for the reference case C1. After the first pulse, the temperature elevation is confined to the top ∼100 nm. As pulses accumulate, the thermal front diffuses deeper into the bulk. By pulse 100 it extends to approximately 300 nm, and by pulse 1800 the elevated-temperature region spans several micrometers into the bulk on the coarse diffusion grid. The surface temperature rises with pulse count, as shown in fig. 5.3a, while the subsurface gradient becomes shallower as the thermal front penetrates deeper.

Evolution of the Temperature Inversion Under Accumulation

Figure 5.5 shows the peak inversion magnitude, $T_l - T_e$ at the instant of maximum inversion, as a function of pulse number over 1800 pulses. The inversion grows from approximately 60 K at early pulses to approximately 84 K at pulse 1800, with a 50-pulse moving average slope of approximately 0.011 K/pulse. The growth arises because the Drude electron conductivity (eq. (5.4)) decreases at elevated baseline temperatures: as the lattice temperature increases with accumulation, k_e decreases for a given T_e, which reduces the electron diffusion rate at the surface and deepens the inversion. The inversion is small in absolute terms, less than 100 K, compared with the peak electron temperatures of thousands of degrees, but it departs from the assumption of monotonic electron-to-lattice energy flow and could affect near-surface defect formation and phase stability.

Ultrafast electron diffuse scattering measurements by Mo et al. [350] on femtosecond-excited tungsten support this picture. They observed that electron–phonon coupling populates zone-boundary phonon modes within ∼1 ps, and that the subsequent phonon–phonon equilibration proceeds over ∼8 ps, during which the lattice retains the deposited energy. This two-stage process (fast electron-to-lattice coupling followed by slow phonon redistribution) is the same sequence that drives the

surface inversion in the model: once the pulse ends, the high electron conductivity k_e carries electron energy into the bulk, while the lattice at the surface cools far more slowly because $k_l \ll k_e$.

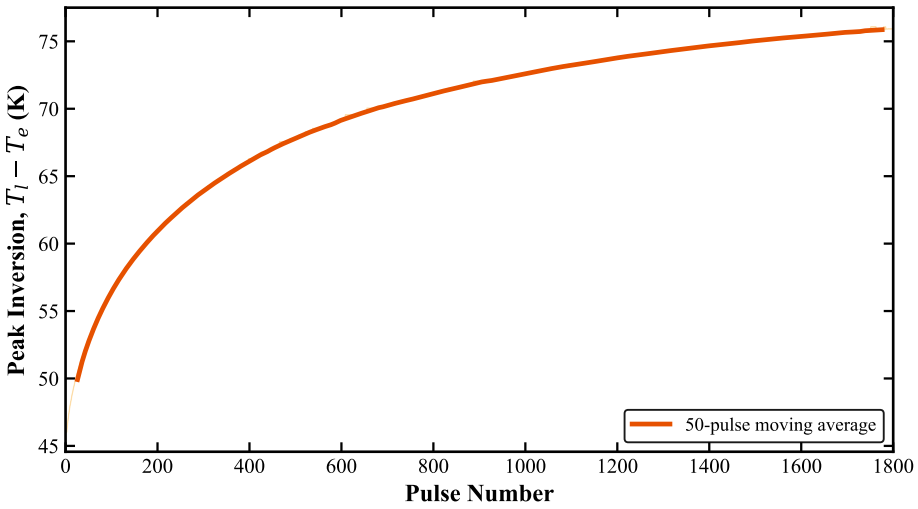


Figure 5.5: Peak surface temperature inversion ($T_l - T_e$) versus pulse number over 1800 pulses (case C1). The thin line shows pulse-by-pulse data and the thick line is a 50-pulse moving average.

5.4.4 Radial and Cross-Sectional Temperature Fields

The preceding analysis resolves heat accumulation along the depth coordinate only. To predict experimentally observable quantities such as the HAZ width, the on-axis solution must be extended radially.

The three-dimensional temperature field is reconstructed from the on-axis depth solution using the Gaussian radial scaling of eq. (5.18). Figure 5.6a shows the radial surface temperature profiles after 1800 pulses for the reference case C1, plotted at several depths below the surface. The on-axis residual temperature is 1091 °C at the surface and decreases with depth because of the finite thermal penetration. At one spot radius ($r = w_0$), the surface temperature has decayed to approximately 169 °C, as expected from the Gaussian spatial profile.

Figure 5.7 presents the two-dimensional cross-sectional temperature map $T(r, z)$ for case C1. The highest temperatures are concentrated at the surface center, $r = 0$ and $z = 0$, with isotherms that curve outward following the Gaussian beam profile radially and the diffusion front axially. The thermal penetration depth at the beam center is approximately 10 µm to 20 µm, consistent with a thermal diffusion length of approximately 3 µm accumulated over 100 µs.

Figure 5.6b shows the residual temperature buildup at five radial positions from $r = 0$ to 200 µm. The on-axis position accumulates heat most rapidly, while off-axis positions show lower temperatures and delayed onset of accumulation. At twice the spot radius, the Gaussian beam profile reduces the residual temperature rise to only a few degrees above ambient.

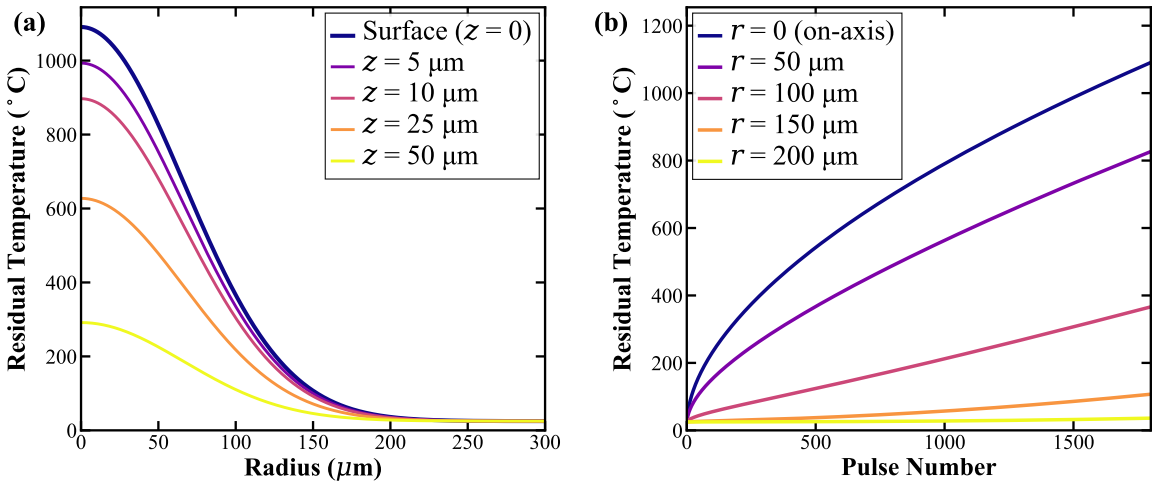


Figure 5.6: (a) Radial residual temperature profiles after 1800 pulses (case C1) at several depths below the irradiated surface. The beam $1/e^2$ radius is $w_0 = 100$ µm. (b) Residual surface temperature versus pulse number at five radial positions for case C1. The on-axis position $r = 0$ accumulates heat most rapidly.

5.4.5 Computational Performance

The hybrid Phase 1/Phase 2 architecture is designed to make multi-pulse TTM simulations tractable. Its computational cost is characterized below.

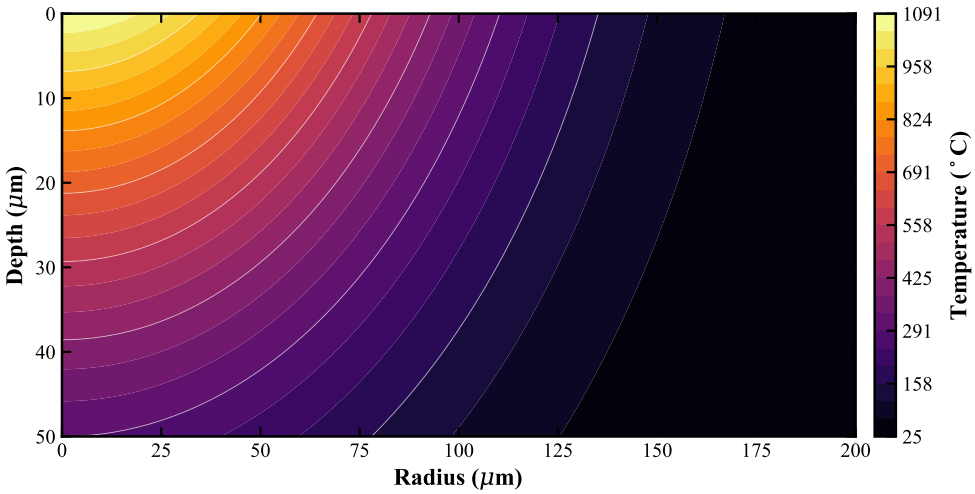


Figure 5.7: Two-dimensional cross-sectional temperature map $T(r, z)$ after 1800 pulses for case C1. The vertical axis is depth, increasing downward, and the horizontal axis is radial distance from the beam center.

Table 5.4 summarizes the wall-clock times for simulations of 100 to 10 000 pulses at the default conditions. The computational cost scales linearly with pulse count: a linear fit yields a marginal cost of approximately 85 ms per pulse. The 10 000-pulse simulation, 856 s or approximately 14.3 min, shows that the hybrid solver can handle the pulse counts encountered in practical MHz-rate laser processing on a single workstation without parallelization.

Table 5.4: Wall-clock times for multi-pulse simulations at default conditions (W, 40 W, 18 MHz, $w_0 = 100\,\mu\text{m}$, $\tau_p = 500\,\text{fs}$).

Pulses	Wall time (s)	Time per pulse (ms)	T_{resid} [°C]
100	11.0	110	232
1 000	93.7	94	791
5 000	471.6	94	1918
10 000	855.7	86	2779

The slight decrease in per-pulse cost from 110 ms at 100 pulses to 86 ms at 10 000 pulses results from amortization of startup overhead, including grid construction, precomputation of the Jacobian sparsity pattern, and first-pulse ODE integration which requires more adaptive steps. By contrast, a monolithic TTM integration

that continues the stiff coupled ODE system through the full 55.6 ns inter-pulse gap at 18 MHz would require on the order of 10^4 additional adaptive time steps per pulse, increasing the per-pulse cost by roughly two orders of magnitude. The hybrid approach therefore allows multi-pulse simulations that would be impractical with a monolithic solver.

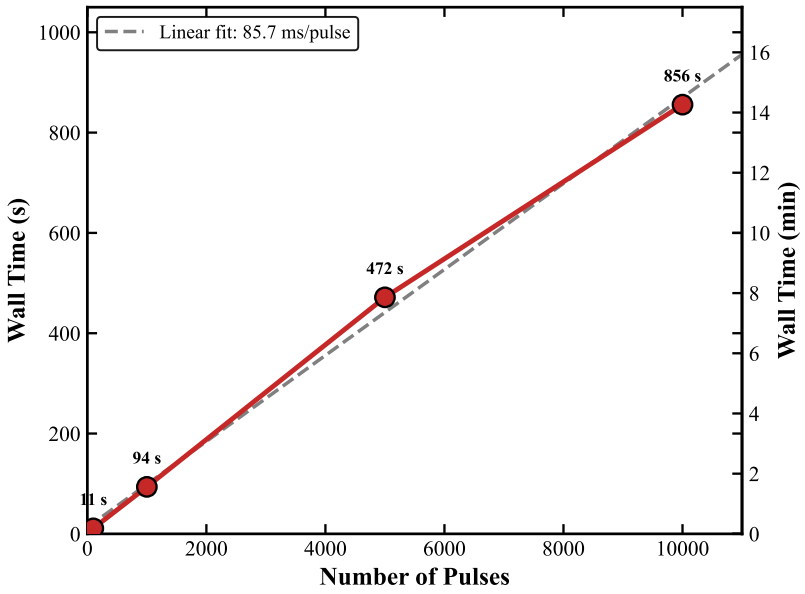


Figure 5.8: Wall-clock time versus number of pulses, demonstrating linear computational scaling. The dashed line shows a linear fit with a slope of 85 ms/pulse.

5.4.6 Experimental Validation

The computational results presented above demonstrate the model's ability to resolve multi-pulse thermal dynamics, but their practical value depends on agreement with experiment. This section compares the model predictions against scanning femtosecond laser experiments on bulk polycrystalline tungsten at 40 MHz.

Experimental Conditions

Ten tungsten samples, S1–S10, were processed using the femtosecond laser system described in section 5.3.1. Optical microscopy reveals three morphological regimes

with increasing power or decreasing scan speed: light oxidation only (S1), ablation with a central damage zone surrounded by a HAZ (S2–S7), and surface melting (S8–S10). Table 5.5 summarizes the experimental parameters and measured zone widths, and Figure 5.9 shows representative micrographs.

Table 5.5: Experimental conditions and measured damage zone widths for tungsten samples processed at $f_{\text{rep}} = 40\,\text{MHz}$, $\tau_p = 500\,\text{fs}$, $w_0 \approx 100\,\mu\text{m}$.

Sample	P (W)	v (mm/min)	N_{eff}	E_p (µJ)	Morphology	HAZ (µm)	Central zone (µm)
S1	20	60	8.0×10^6	0.50	Oxidation	10	—
S2	40	60	8.0×10^6	1.00	Ablation	75	20
S3	60	60	8.0×10^6	1.50	Ablation	100	25
S4	80	60	8.0×10^6	2.00	Ablation	120	25
S5	100	60	8.0×10^6	2.50	Ablation	200	35
S6	80	120	4.0×10^6	2.00	Ablation	100	25
S7	80	180	2.7×10^6	2.00	Ablation	85	25
S8	80	300	1.6×10^6	2.00	Melting	80	25
S9	80	600	8.0×10^5	2.00	Melting	75	25
S10	80	900	5.3×10^5	2.00	Melting	70	20

To confirm that the discolored zones surrounding the ablation tracks are thermal in origin, Raman spectroscopy was performed. Figure 5.10 shows spectra acquired from two regions of sample S4: the dark debris zone and the surrounding light oxidation zone. Both spectra exhibit the characteristic peaks of monoclinic γ-WO_3, with O–W–O bending modes near 273 and 327 cm^{-1} and W–O stretching modes at 715 and 808 cm^{-1} [351]. The debris zone produces stronger and sharper peaks, indicating a thicker or more crystalline oxide layer, while the light oxidation zone shows the same peak positions at reduced intensity. The HAZ widths reported in table 5.5 are therefore measured as the full extent of spectroscopically verified WO_3 formation.

Melt-Zone Prediction for Sample S8

Of the ten samples, S8 (80 W, 300 mm/min) was selected for direct simulation comparison because it exhibits clear melting morphology with a well-defined central

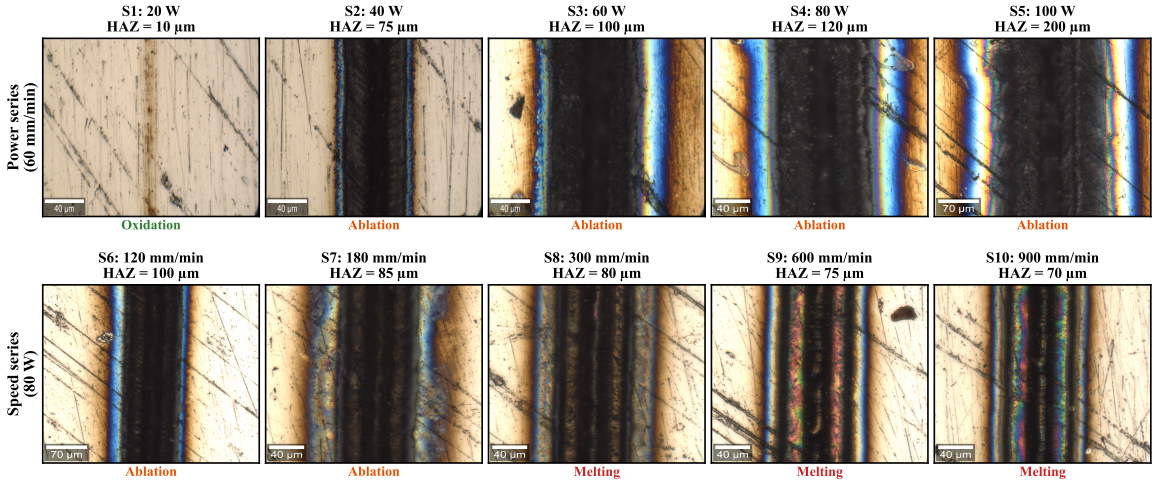


Figure 5.9: Optical micrographs of all ten tungsten samples. Top row: power series S1–S5 at 60 mm/min. Bottom row: speed series S6–S10 at 80 W. Annotations show measured HAZ widths and morphological classification.

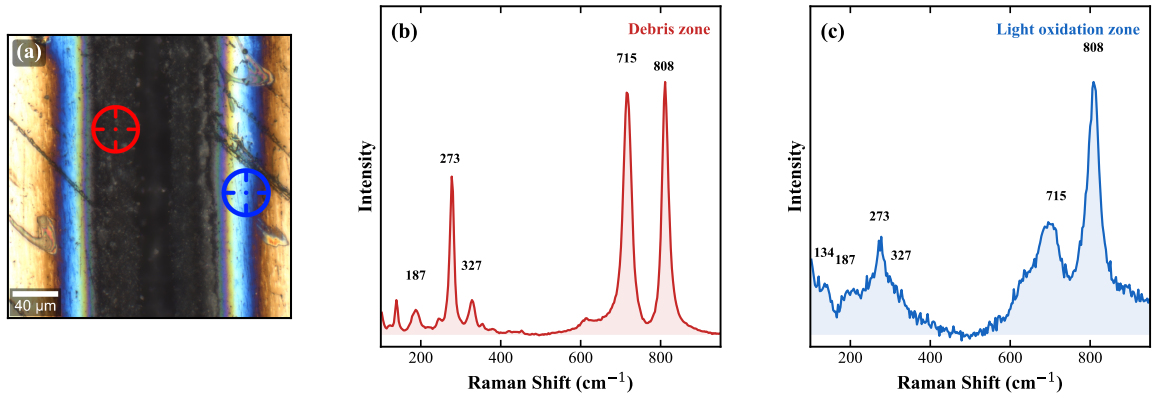


Figure 5.10: Raman spectroscopy of sample S4 (80 W, 60 mm/min). (a) Optical micrograph with Raman measurement locations indicated by crosshairs. (b) Spectrum from the debris zone showing strong monoclinic γ-WO_3 peaks. (c) Spectrum from the light oxidation zone with the same WO_3 peak positions at reduced intensity. Labeled peaks correspond to δ(O–W–O) bending modes at 134, 273, and 327 cm^{-1}, ν(W–W) at 187 cm^{-1}, ν(O–W–O) at 715 cm^{-1}, and ν(W–O) at 808 cm^{-1}.

zone diameter of 25 µm measured by optical microscopy, and its high scanning speed minimizes plume-shielding effects that complicate interpretation of the lower-speed samples.

The simulation was run for 2832 pulses at 80 W, 40 MHz, 500 fs, with $w_0 = 100\,\mu\text{m}$ and $A = 0.55$, completing in 20.2 s. The on-axis residual temperature first exceeded the melting point $T_{\text{melt}} = 3422\,^{\circ}\text{C}$ at pulse 2649, and reached $T_{\text{resid}} = 3530\,^{\circ}\text{C}$ after the full 2832 pulses. The radial temperature profile, reconstructed via the Gaussian beam scaling of eq. (5.18), crosses T_{melt} at a radius of 12.5 µm, yielding a predicted melt zone diameter of 25.0 µm. This matches the experimentally measured central zone of 25 µm for S8.

Figure 5.11 presents the radial profile mirrored about $r = 0$ alongside the corresponding two-dimensional surface temperature field obtained by revolving the profile. The predicted melt boundary and the measured central zone boundary are overlaid on both views. The model uses no fitted parameters: the absorptance $A = 0.55$ and beam radius $w_0 = 100\,\mu\text{m}$ are fixed by independent measurement.

The model does not account for ablation-driven material removal or plume shielding, both of which reduce the effective delivered fluence at lower scanning speeds and higher overlap counts. These effects explain why the ablation-regime samples (S2–S7) cannot be directly compared without coupling the thermal model to ablation and plume dynamics, which is a natural direction for future work.

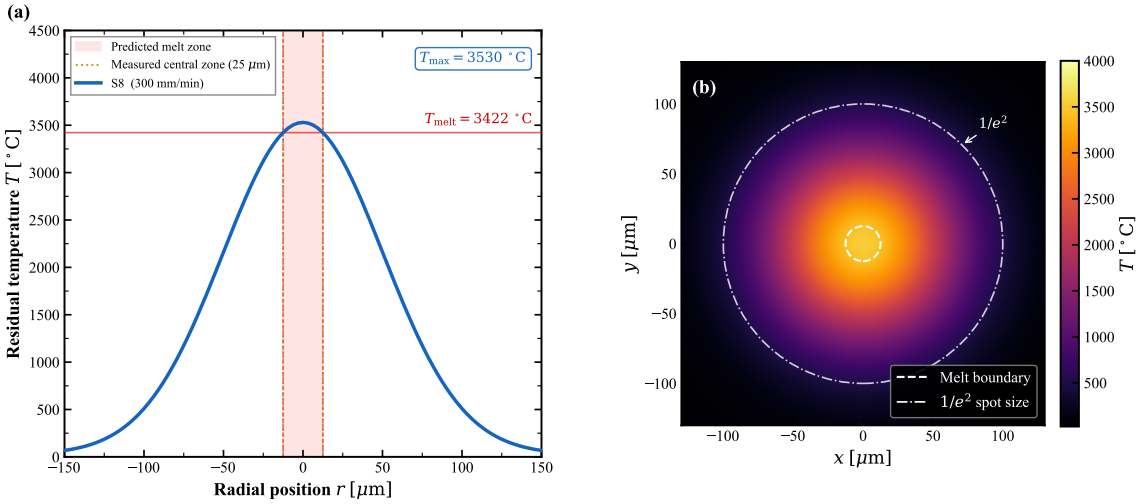


Figure 5.11: Simulation results for sample S8 (80 W, 300 mm/min, 40 MHz) after 2832 pulses. (a) Reconstructed radial surface temperature profile. The shaded region marks the predicted melt zone ($T > T_{\mathrm{melt}}$, diameter 25.0 µm). Dashed lines indicate the experimentally measured central zone boundary (Ø25 µm). (b) Two-dimensional surface temperature field obtained by revolving the radial profile. The dashed circle marks the predicted melt boundary.

5.5 Conclusions

This chapter addressed the computational bottleneck that has prevented spatially resolved two-temperature modeling of multi-pulse femtosecond laser processing. The hybrid two-phase method introduced here solves the full coupled TTM during each pulse on a fine grid, then hands off the equilibrated profile to Crank–Nicolson diffusion on a coarser grid through the inter-pulse gap. The resulting solver is roughly two orders of magnitude faster than monolithic TTM integration, scaling linearly at approximately 85 ms per pulse, so that a 10 000-pulse simulation completes in under 15 min on a single workstation.

Applied to tungsten, the model captures the full depth-resolved electron–lattice dynamics of each pulse, the progressive inter-pulse temperature buildup, and a surface temperature inversion ($T_l > T_e$) that grows with cumulative heating, a spatially resolved effect that zero-dimensional models cannot capture.

Validation against a scanning femtosecond laser experiment on tungsten at 40 MHz demonstrates that the predicted melt zone diameter of 25.0 µm matches the experimentally measured central zone of sample S8 (80 W, 300 mm/min) exactly, using only literature values for absorptance and the nominal beam radius with no fitted parameters. The omission of ablation, plume dynamics, and lateral thermal diffusion defines the natural direction for future work: two-dimensional axisymmetric geometries, ablation-driven material removal, temperature-dependent absorptance, and plume-beam interaction models for scanning geometries.

Chapter 6

Conclusions and Outlook

6.1 Summary of Contributions

This dissertation investigated the hypothesis that predictable and transferable material outcomes are achieved by jointly controlling laser energy delivery, environmental conditions, and spatial constraints, and that these coupled controls can be tuned to intentionally tailor distinct microstructures, surface states, and functional properties. Four experimental and computational studies, spanning nanoparticle synthesis, nanostructure characterization, powder bed fusion process optimization, and multi-pulse thermal modeling, tested this hypothesis across nine orders of magnitude in processing length scale. The principal contributions of each study are summarized below.

Chapter 2 established that the ablation medium is an independent and controllable determinant of phase constitution in femtosecond laser ablation of a $CuCoMn_{1.75}NiFe_{0.25}$ HEA target. By holding laser parameters fixed and varying only the liquid environment among water, liquid nitrogen, ethanol, and hydrocarbons, four distinct nanoparticle populations were produced: oxide-shell core-shell particles, phase-separated metal-nitride particles, carbide-contaminated amorphous-residue particles, and single-phase FCC metallic nanoparticles. XPS analysis confirmed that the ethanol-synthesized nanoparticles retained the designed stoichiometry (measured ratio 1:0.89:1.97:0.93:0.37 against a target of 1:1:1.75:1:0.25) despite extreme thermal gradients and rapid quenching. At elevated pulse energies above 250 mJ, a

nonthermal surface melting regime fused individual nanoparticles into micron-length chains through laser-induced nanojoining, demonstrating that laser energy delivery provides a second independent control axis. The single-phase nanoparticles exhibited electrocatalytic activity toward ORR, OER, and HER, and when deployed as a cathode catalyst in an aluminum-air battery, they increased limiting current density from under 250 mA/cm^2 to approximately 325 mA/cm^2 and raised peak power density from 70 mW/cm^2 to 90 mW/cm^2.

Chapter 3 extended the environmental control framework by resolving how the ablation medium governs internal defect structure, surface chemistry, thermodynamic stability, and optical response within the single-phase regime. Liquid nitrogen produced particles with single- or few-domain crystalline interiors and composition closer to the bulk target, while ethanol produced smaller particles built from 2–4 nm nanocrystalline domains with greater manganese depletion. XPS revealed that cryogenic ablation formed a thicker, oxygen-vacancy-rich oxide shell (estimated vacancy fraction of approximately 55%), whereas ethanol ablation yielded a thinner, partially organic surface layer (vacancy fraction of approximately 33%). COMSOL cooling simulations linked these outcomes to a physical mechanism: liquid nitrogen drives particles from the melt to near bath temperature within approximately 0.1 μs, kinetically freezing a homogeneous solid solution, while ethanol surfaces cool within approximately 1 μs, allowing coalescence and compositional redistribution. These results established that the solvent functions as a quantitative design variable connecting process input to material outcome through a chain of cooling kinetics, nucleation and growth competition, defect structure, and surface chemistry.

Chapter 4 translated the coupled-control framework to the macroscale by constructing quantitative process maps for LPBF of an Al–Ce–Ni–Mn–Zr alloy across 60 builds. Response surface models showed that laser power, scan speed, and hatch spacing govern porosity and hardness not independently but through the melt pool energy they collectively impose. A U-shaped porosity response centered on intermediate energy inputs, with keyhole collapse and lack-of-fusion voids bracketing

a narrow stable window, and a monotonically increasing hardness response tied to finer intermetallic spacing at higher cooling rates confirmed the melt pool regime transitions that Chapter 1 identified as the governing failure modes of track-based manufacturing. The resulting processing window (350–370 W, 1400–1800 mm/s, hatch spacing 0.14–0.18 mm, layer thickness 30 μm) placed builds within a cooling rate of 3.0–3.6 $\times$ 10^6 K/s, producing porosity below 0.01 vol% and as-built hardness up to 160 HV. The Rosenthal cooling rate metric captured more than half of the variation in both hardness and porosity, providing a transferable design handle for reuse across alloys and machines.

Chapter 5 addressed the computational bottleneck that has prevented spatially resolved two-temperature modeling of multi-pulse femtosecond laser processing. A hybrid two-phase method was developed that solves the full coupled TTM on a fine grid during each pulse, then hands the equilibrated profile to Crank–Nicolson diffusion on a coarser grid through the inter-pulse gap. Applied to tungsten at 40 MHz repetition rate, the solver achieved roughly two orders of magnitude speedup over monolithic TTM integration, scaling linearly at approximately 85 ms per pulse and completing a 10 000-pulse simulation in under 15 min on a single workstation. The model captured progressive inter-pulse temperature buildup and a surface temperature inversion ($T_l > T_e$) that grows with cumulative heating, a spatially resolved effect invisible to zero-dimensional models. Validation against a scanning femtosecond laser experiment on tungsten showed that the predicted melt zone diameter of 25.0 μm matched the measured central zone of sample S8 (80 W, 300 mm/min) exactly, using only literature values for absorptance and the nominal beam radius with no fitted parameters.

6.2 Conclusions

The four studies presented in this dissertation provide converging evidence for the central hypothesis from complementary directions.

At the nanoscale, Chapters 2 and 3 demonstrated that the processing environment is not a passive boundary condition but a controllable input that determines microstructure and surface state. With laser parameters held constant, the choice of ablation medium alone was sufficient to switch between oxide-shell, nitride, carbide-contaminated, and single-phase FCC nanoparticle populations. Within the single-phase regime, the same environmental axis predictably tuned internal crystallographic texture, surface oxide thickness and vacancy concentration, thermodynamic stability, and optical response. When laser energy delivery was varied as a second independent axis, the process shifted from isolated nanoparticle synthesis to directed chain assembly without any change in target material or liquid medium. These results confirm the hypothesis that laser energy delivery and environmental conditions act as independent, tunable control axes that jointly determine material outcomes.

At the macroscale, Chapter 4 confirmed that the same coupled-control logic governs track-based additive manufacturing. The processing window for LPBF was defined not by any single parameter but by the melt pool regime that laser power, scan speed, and hatch spacing collectively impose. Porosity and hardness varied systematically with cooling rate in a manner consistent with the physical framework established in Chapter 1, and the Rosenthal cooling rate metric provided a single transferable variable for targeting comparable outcomes on different machines or in related alloys. The consistency of this physics-based scaling argument across nine orders of magnitude in feature size, from sub-100 nm nanoparticles to centimeter-scale structural components, reinforces the position that laser precision manufacturing is practiced most reliably through deliberate coupling of energy delivery and spatial constraints.

At the modeling scale, Chapter 5 demonstrated that the thermal history governing multi-pulse femtosecond laser processing of a refractory metal can be predicted quantitatively from first principles without fitted parameters. The hybrid two-phase solver produced depth-resolved temperature fields that captured inter-pulse heat accumulation, lattice-electron temperature inversion, and melt zone geometry,

reproducing the experimentally measured melt zone within the measurement uncertainty. This computational capability closes a gap in the control framework by providing a predictive tool for process design in regimes where direct measurement of sub-surface thermal fields is not possible.

Taken together, these results establish that the governing principle across all four studies is the same: the material outcome is set by the thermal history, and the thermal history is set by the combination of energy delivery parameters and boundary conditions. When these inputs are characterized and controlled deliberately, the process produces repeatable and predictable outcomes. When they are not, the variability in the material response cannot be attributed to any single parameter in isolation. The dissertation therefore supports the conclusion that laser precision manufacturing across scales is best practiced as a coupled-control problem in which energy delivery, environmental conditions, and spatial constraints are treated as co-equal design variables.

6.3 Future Work and Outlook

Several directions follow naturally from the results of this dissertation.

At the nanoscale, the ablation medium control axis demonstrated in Chapters 2 and 3 should be extended to include mixed-solvent systems and gas-saturated liquids, which would allow continuous interpolation between the discrete environments studied here. Quantitative process maps relating pulse number, repetition rate, target rotation speed, and solvent composition to particle size distribution and chain architecture would convert the current qualitative environmental control framework into a predictive design tool. In situ diagnostics, including time-resolved scattering and emission spectroscopy of the ablation plume, would provide direct measurement of the nucleation and growth kinetics that currently must be inferred from post-mortem characterization.

At the macroscale, the LPBF processing window identified in Chapter 4 for the Al–Ce–Ni–Mn–Zr alloy should be validated on additional machines to test whether the Rosenthal cooling rate metric transfers across platforms as the physical argument predicts. Extending the design-of-experiments methodology to include build height, support structure geometry, and gas flow conditions would capture the spatial constraint and environmental axes that were held fixed in the present study. Fatigue testing and elevated-temperature mechanical characterization of the optimized builds would complete the process–structure–property–performance chain for this alloy system.

At the computational scale, the hybrid two-phase TTM solver developed in Chapter 5 should be extended to two-dimensional axisymmetric geometries that capture lateral thermal diffusion and radial melt pool shape. Incorporating ablation-driven material removal, temperature-dependent absorptance, and plume-beam interaction models would allow the solver to handle the high-fluence scanning conditions where the current one-dimensional model reaches its physical limits. Coupling the thermal solver to a phase-field or cellular automaton solidification model would enable direct prediction of the grain structure and defect populations that determine the mechanical response of laser-processed tungsten.

A longer-term direction is the integration of these three scales into a unified computational and experimental workflow. The nanoscale thermal histories predicted by TTM-class models, the macroscale process maps constructed from statistical response surface methods, and the environmental control relationships established through systematic solvent variation all operate on the same underlying principle: the material outcome follows from the thermal history. A multi-scale simulation framework that connects femtosecond pulse absorption to melt pool dynamics to part-level thermal accumulation, validated at each scale by the experimental methods developed in this dissertation, would provide a single design environment for laser precision manufacturing across the full range of length scales addressed here.

Bibliography

[1] William M. Steen and Jyotirmoy Mazumder. *Laser Material Processing*. Springer Science & Business Media, 4th edition, 2010. 2

[2] J Dutta Majumdar and Indranil Manna. Laser processing of materials. *Sadhana*, 28(3):495–562, 2003. 2

[3] Tarasankar DebRoy, Huiliang L Wei, James S Zuback, Tuhin Mukherjee, John W Elmer, John O Milewski, Allison Michelle Beese, A de Wilson-Heid, Amitava De, and Wei Zhang. Additive manufacturing of metallic components–process, structure and properties. *Progress in materials science*, 92:112–224, 2018. 2, 4, 5, 28, 29, 30, 31, 33, 34, 35, 36, 37

[4] David Bergström. *The absorptance of metallic alloys to Nd: YAG and Nd: YLF laser light*. PhD thesis, Luleå tekniska universitet, 2005. 3

[5] Cang Zhao, Bo Shi, Shuailei Chen, Dong Du, Tao Sun, Brian J Simonds, Kamel Fezzaa, and Anthony D Rollett. Laser melting modes in metal powder bed fusion additive manufacturing. *Reviews of Modern Physics*, 94(4):045002, 2022. 4

[6] SA David and JM Vitek. Correlation between solidification parameters and weld microstructures. *International materials reviews*, 34(1):213–245, 1989. 4

[7] MI Kaganov. Relaxation between electrons and the crystalline lattice. *Sov. Phys. JETP*, 4:173–178, 1957. 4, 157

[8] J. G. Fujimoto, J. M. Liu, E. P. Ippen, and N. Bloembergen. Femtosecond laser interaction with metallic tungsten and nonequilibrium electron and lattice temperatures. *Physical Review Letters*, 53(19):1837, 1984. 4, 171

[9] SI Anisimov, BL Kapeliovich, TL Perelman, et al. Electron emission from metal surfaces exposed to ultrashort laser pulses. *Zh. Eksp. Teor. Fiz*, 66(2):375–377, 1974. 4, 158

[10] Ian Robinson, Jesse Clark, and Ross Harder. Materials science in the time domain using bragg coherent diffraction imaging. *Journal of Optics*, 18(5): 054007, 2016. 5

[11] Enza Fazio, Bilal Gökce, Alessandro De Giacomo, Moreno Meneghetti, Giuseppe Compagnini, Matteo Tommasini, Friedrich Waag, Andrea Lucotti, Chiara Giuseppina Zanchi, Paolo Maria Ossi, et al. Nanoparticles engineering by pulsed laser ablation in liquids: concepts and applications. *Nanomaterials*, 10(11):2317, 2020. 4, 40, 41, 110

[12] Kavil Mehta and Prahlad K Baruah. A comprehensive review and outlook on the experimental techniques to investigate the complex dynamics of pulsed laser ablation in liquid for nanoparticle synthesis. *Review of Scientific Instruments*, 93(9), 2022. 4

[13] Shuai Yan, Zhiyong Li, Linling Song, Yingqiao Zhang, and Shouzheng Wei. Research and development status of laser micro-welding of aluminum-copper dissimilar metals: A review. *Optics and Lasers in Engineering*, 161:107312, 2023. 5

[14] Jian Cheng, Yunhao Xing, Enjie Dong, Linjie Zhao, Henan Liu, Tingyu Chang, Mingjun Chen, Jinghe Wang, Junwen Lu, and Jun Wan. An overview of laser metal deposition for cladding: Defect formation mechanisms, defect suppression

methods and performance improvements of laser-cladded layers. *Materials*, 15 (16):5522, 2022. 5

[15] Emil Roduner. Size matters: why nanomaterials are different. *Chemical society reviews*, 35(7):583–592, 2006. 6, 7, 8

[16] Ming Xiao, Shuo Zheng, Daozhi Shen, Walter W Duley, and Y Norman Zhou. Laser-induced joining of nanoscale materials: processing, properties, and applications. *Nano Today*, 35:100959, 2020. 6, 14, 15, 16, 17, 18

[17] Shuowei Dai, Qiang Li, Guoping Liu, Hangbo Yang, Yuanqing Yang, Ding Zhao, Wei Wang, and Min Qiu. Laser-induced single point nanowelding of silver nanowires. *Applied Physics Letters*, 108(12), 2016. 6, 18

[18] Nadeem Baig, Irshad Kammakakam, and Wail Falath. Nanomaterials: A review of synthesis methods, properties, recent progress, and challenges. *Materials advances*, 2(6):1821–1871, 2021. 6

[19] Ph Buffat and Jean Pierre Borel. Size effect on the melting temperature of gold particles. *Physical review A*, 13(6):2287, 1976. 7

[20] G Kaptay. On the size and shape dependence of the solubility of nano-particles in solutions. *International Journal of Pharmaceutics*, 430(1-2):253–257, 2012. 7

[21] K Lance Kelly, Eduardo Coronado, Lin Lin Zhao, and George C Schatz. The optical properties of metal nanoparticles: the influence of size, shape, and dielectric environment. *The Journal of Physical Chemistry B*, 107(3):668–677, 2003. 8

[22] Susie Eustis and Mostafa A El-Sayed. Why gold nanoparticles are more precious than pretty gold: noble metal surface plasmon resonance and its enhancement of the radiative and nonradiative properties of nanocrystals of different shapes. *Chemical society reviews*, 35(3):209–217, 2006. 8

[23] Gabor A Somorjai, Anthony M Contreras, Max Montano, and Robert M Rioux. Clusters, surfaces, and catalysis. *Proceedings of the National Academy of Sciences*, 103(28):10577–10583, 2006. 8

[24] Denis Gentili and Guido Ori. Reversible assembly of nanoparticles: theory, strategies and computational simulations. *Nanoscale*, 14(39):14385–14432, 2022. 8

[25] John Turkevich, Peter Cooper Stevenson, and James Hillier. A study of the nucleation and growth processes in the synthesis of colloidal gold. *Discussions of the faraday society*, 11:55–75, 1951. 9

[26] Baerbel Rethfeld, Dmitriy S Ivanov, Martin E Garcia, and Sergei I Anisimov. Modelling ultrafast laser ablation. *Journal of Physics D: Applied Physics*, 50 (19):193001, 2017. 9, 10, 11

[27] S-S Wellershoff, J Hohlfeld, J Güdde, and E Matthias. The role of electron–phonon coupling in femtosecond laser damage of metals. *Applied Physics A*, 69 (Suppl 1):S99–S107, 1999. 9, 158

[28] Xinxin Li and Yingchun Guan. Theoretical fundamentals of short pulse laser–metal interaction: A review. *Nanotechnology and Precision Engineering*, 3(3): 105–125, 2020. 10

[29] Jeppe Byskov-Nielsen, Juha-Matti Savolainen, Martin Snogdahl Christensen, and Peter Balling. Ultra-short pulse laser ablation of copper, silver and tungsten: experimental data and two-temperature model simulations. *Applied Physics A*, 103(2):447–453, 2011. 11

[30] Antonio Miotello and Roger Kelly. Laser-induced phase explosion: new physical problems when a condensed phase approaches the thermodynamic critical temperature. *Applied Physics A*, 69(Suppl 1):S67–S73, 1999. 10

[31] Xianfan Xu. Phase explosion and its time lag in nanosecond laser ablation. *Applied surface science*, 197:61–66, 2002. 10, 12

[32] Leonid V Zhigilei, Zhibin Lin, and Dmitriy S Ivanov. Atomistic modeling of short pulse laser ablation of metals: connections between melting, spallation, and phase explosion. *The Journal of Physical Chemistry C*, 113(27):11892–11906, 2009. 10

[33] Rie Tanabe, Thao TP Nguyen, Takahiro Sugiura, and Yoshiro Ito. Bubble dynamics in metal nanoparticle formation by laser ablation in liquid studied through high-speed laser stroboscopic videography. *Applied Surface Science*, 351:327–331, 2015. 12

[34] Shyjumon Ibrahimkutty, Philipp Wagener, Andreas Menzel, Anton Plech, and Stephan Barcikowski. Nanoparticle formation in a cavitation bubble after pulsed laser ablation in liquid studied with high time resolution small angle x-ray scattering. *Applied Physics Letters*, 101(10), 2012. 12

[35] Philipp Wagener, Shyjumon Ibrahimkutty, Andreas Menzel, Anton Plech, and Stephan Barcikowski. Dynamics of silver nanoparticle formation and agglomeration inside the cavitation bubble after pulsed laser ablation in liquid. *Physical Chemistry Chemical Physics*, 15(9):3068–3074, 2013. 12

[36] B. C. Stuart, M. D. Feit, S. Herman, A. M. Rubenchik, B. W. Shore, and M. D. Perry. Nanosecond-to-femtosecond laser-induced breakdown in dielectrics. *Physical review B*, 53(4):1749, 1996. 12, 13, 14

[37] Eugene G Gamaly, Andrei V Rode, Barry Luther-Davies, and Vladimir T Tikhonchuk. Ablation of solids by femtosecond lasers: Ablation mechanism and ablation thresholds for metals and dielectrics. *Physics of plasmas*, 9(3): 949–957, 2002. 12, 14

[38] Masaki Hashida, Shin Namba, Kiminori Okamuro, Shigeki Tokita, and Shuji Sakabe. Ion emission from a metal surface through a multiphoton process and optical field ionization. *Physical Review B—Condensed Matter and Materials Physics*, 81(11):115442, 2010. 12, 13, 14

[39] R Stoian, A Rosenfeld, D Ashkenasi, IV Hertel, NM Bulgakova, and EEB Campbell. Surface charging and impulsive ion ejection during ultrashort pulsed laser ablation. *Physical review letters*, 88(9):097603, 2002. 13, 14

[40] NM Bulgakova, R Stoian, A Rosenfeld, EEB Campbell, and IV Hertel. Model description of surface charging during ultra-fast pulsed laser ablation of materials. *Applied Physics A*, 79(4):1153–1155, 2004. 13, 14

[41] Inam Mirza, Nadezhda M Bulgakova, Jan Tomáštík, Václav Michálek, Ondřej Haderka, Ladislav Fekete, and Tomáš Mocek. Ultrashort pulse laser ablation of dielectrics: Thresholds, mechanisms, role of breakdown. *Scientific reports*, 6 (1):39133, 2016. 13

[42] M Lebugle, N Sanner, O Utéza, and M Sentis. Guidelines for efficient direct ablation of dielectrics with single femtosecond pulses. *Applied Physics A*, 114 (1):129–142, 2014. 13

[43] Ming Li, Saipriya Menon, John P Nibarger, and George N Gibson. Ultrafast electron dynamics in femtosecond optical breakdown of dielectrics. *Physical review letters*, 82(11):2394, 1999. 13

[44] Matthias Lenzner, Ferenc Krausz, J Krüger, and W Kautek. Photoablation with sub-10 fs laser pulses. *Applied Surface Science*, 154:11–16, 2000. 13

[45] Sha Tao and Benxin Wu. The effect of emitted electrons during femtosecond laser–metal interactions: A physical explanation for coulomb explosion in metals. *Applied surface science*, 298:90–94, 2014. 14

[46] Y Zhou, Anming Hu, et al. From microjoining to nanojoining. *Open Surface Science Journal*, 3:32–41, 2011. 14

[47] Jeonghong Ha, Bong Jae Lee, David J Hwang, and Dongsik Kim. Femtosecond laser nanowelding of silver nanowires for transparent conductive electrodes. *Rsc Advances*, 6(89):86232–86239, 2016. 15, 17, 18

[48] W_ D_ Kingery and Morris Berg. Study of the initial stages of sintering solids by viscous flow, evaporation-condensation, and self-diffusion. *Journal of Applied Physics*, 26(10):1205–1212, 1955. 16

[49] Randall M. German. *Sintering Theory and Practice*. Wiley-Interscience, 1996. ISBN 9780471057864. 16

[50] Nanhua Wu, Xiaohua Lu, Rong An, and Xiaoyan Ji. Thermodynamic analysis and modification of gibbs–thomson equation for melting point depression of metal nanoparticles. *Chinese Journal of Chemical Engineering*, 31:198–205, 2021. 16

[51] Luchan Lin, Lei Liu, Peng Peng, Guisheng Zou, Walt W Duley, and Y Norman Zhou. In situ nanojoining of y-and t-shaped silver nanowires structures using femtosecond laser radiation. *Nanotechnology*, 27(12):125201, 2016. 17

[52] Shuo Zheng, Walter W Duley, Peng Peng, and Y Norman Zhou. Formation of metal–semiconductor nanowire heterojunctions by nanosecond laser irradiation. *AIP Advances*, 11(9), 2021. 17

[53] Qiong Nian, Mojib Saei, Yang Xu, Ganguli Sabyasachi, Biwei Deng, Yong P Chen, and Gary J Cheng. Crystalline nanojoining silver nanowire percolated networks on flexible substrate. *ACS nano*, 9(10):10018–10031, 2015. 18

[54] Qiang Li, Guoping Liu, Hangbo Yang, Wei Wang, Si Luo, Shuowei Dai, and Min Qiu. Optically controlled local nanosoldering of metal nanowires. *Applied Physics Letters*, 108(19), 2016. 18

[55] Yaasin A Mayi, Morgan Dal, Patrice Peyre, Michel Bellet, and Remy Fabbro. Physical mechanisms of conduction-to-keyhole transition in laser welding and additive manufacturing processes. *Optics & Laser Technology*, 158:108811, 2023. 19

[56] Khalid M Hafez. The influence of shielding gases on keyhole-induced porosity and nitrogen absorption in ss 304 stainless steel fiber laser welds. *The International Journal of Advanced Manufacturing Technology*, 127(3):1887–1894, 2023. 19

[57] HL Wei, John W Elmer, and T DebRoy. Crystal growth during keyhole mode laser welding. *Acta Materialia*, 133:10–20, 2017. 19

[58] Jingjing Yang, Yun Wang, Tongbo Wei, and Zemin Wang. A comparable study on laser welding behaviors of selective laser melted 304 stainless steel, inconel 718 superalloy and ti-6al-4v alloy. *3D Printing and Additive Manufacturing*, 11 (3):1310–1323, 2024. 19, 21

[59] Pavaret Preedawiphat, Numpon Mahayotsanun, Keerati Sa-Ngoen, Mai Noipitak, Pongsak Tuengsook, Sedthawatt Sucharitpwatskul, and Kuniaki Dohda. Mechanical investigations of astm a36 welded steels with stainless steel cladding. *Coatings*, 10(9):844, 2020. 20

[60] Manfred Stadler, Ronald Schnitzer, Martin Gruber, Katharina Steineder, and Christina Hofer. Microstructure and local mechanical properties of the heat-affected zone of a resistance spot welded medium-mn steel. *Materials*, 14(12): 3362, 2021. 20

[61] Ramachandran Oyyaravelu, Palaniyandi Kuppan, and Natarajan Arivazhagan. Metallurgical and mechanical properties of laser welded high strength low alloy steel. *Journal of advanced research*, 7(3):463–472, 2016. 20

[62] Paulo Henrique de Oliveira Monteiro Alves, Milton Sérgio Fernandes Lima, Dierk Raabe, and Hugo Ricardo Zschommler Sandim. Laser beam welding of dual-phase dp1000 steel. *Journal of Materials Processing Technology*, 252: 498–510, 2018. 20

[63] Jiwen Cheng, Gang Song, Xiaosheng Zhang, Chunbai Liu, and Liming Liu. Review of techniques for improvement of softening behavior of age-hardening aluminum alloy welded joints. *Materials*, 14(19):5804, 2021. 20, 25

[64] Szymon Tofil, Hubert Danielewski, Grzegorz Witkowski, Krystian Mulczyk, and Bogdan Antoszewski. Technology and properties of peripheral laser-welded micro-joints. *Materials*, 14(12):3213, 2021. 21

[65] Joris Hochanadel, Boyd Panton, Carolin Fink, and John Lippold. Solidification behavior and microstructure evolution in dissimilar electron beam welds between commercially pure iron and nickel. *Metallurgical and Materials Transactions A*, 55(6):2004–2018, 2024. 21

[66] Sergey Kuryntsev. A review: laser welding of dissimilar materials (al/fe, al/ti, al/cu)—methods and techniques, microstructure and properties. *Materials*, 15 (1):122, 2021. 21

[67] Yongchao Su, Xueming Hua, Yixiong Wu, Yong Zhang, and Yazhou Guo. Characterization of intermetallic compound layer thickness at aluminum–steel interface during overlaying. *Materials & Design*, 78:1–4, 2015. 21

[68] Xiaoquan Yu, Jiankang Huang, Tao Yang, and Ding Fan. The growth behavior for intermetallic compounds at the interface of aluminum-steel weld joint. *Materials*, 15(10):3563, 2022. 21, 26

[69] Daniel Wallerstein, Antti Salminen, Fernando Lusquinos, Rafael Comesana, Jesús del Val García, Antonio Riveiro Rodríguez, Aida Badaoui, and Juan Pou.

Recent developments in laser welding of aluminum alloys to steel. *Metals*, 11 (4):622, 2021. 21

[70] John Stavridis, Alexios Papacharalampopoulos, and Panagiotis Stavropoulos. Quality assessment in laser welding: a critical review. *The International Journal of Advanced Manufacturing Technology*, 94(5):1825–1847, 2018. 22

[71] RD Seidgazov and F Kh Mirzade. Keyhole-induced porosity in laser manufacturing processes: Formation mechanism and dependence on scan speed. *Chinese Journal of Mechanical Engineering: Additive Manufacturing Frontiers*, 1(3):100044, 2022. 22

[72] Nicole Trometer, Buwei Chen, Michael Moodispaw, Wayne Cai, Teresa Rinker, Shardul Kamat, Zachary Velasco, and Alan A Luo. Modeling and validation of hydrogen porosity formation in aluminum laser welding. *Journal of Manufacturing Processes*, 124:877–890, 2024. 22

[73] Sindo Kou. Predicting susceptibility to solidification cracking and liquation cracking by calphad. *Metals*, 11(9):1442, 2021. 22, 23

[74] Andrzej Klimpel. Review and analysis of modern laser beam welding processes. *Materials*, 17(18):4657, 2024. 22, 23

[75] Mingjun Zhang, Zheng Zhang, Kun Tang, Cong Mao, Yongle Hu, and Genyu Chen. Analysis of mechanisms of underfill in full penetration laser welding of thick stainless steel with a 10 kw fiber laser. *Optics & Laser Technology*, 98: 97–105, 2018. 22

[76] Sindo Kou. A criterion for cracking during solidification. *Acta Materialia*, 88: 366–374, 2015. 23, 24, 25

[77] Zhuoxin Li, Lingshan Ou, Yipeng Wang, Hong Li, Mariusz Bober, Jacek Senkara, and Yu Zhang. Solidification cracking restraining mechanism of al-cu-mg-zn alloy welds using cold metal transfer technique. *Materials*, 16(2):721, 2023. 24

[78] Holden Hyer, Le Zhou, Abhishek Mehta, Sungho Park, Thinh Huynh, Shutao Song, Yuanli Bai, Kyu Cho, Brandon McWilliams, and Yongho Sohn. Composition-dependent solidification cracking of aluminum-silicon alloys during laser powder bed fusion. *Acta Materialia*, 208:116698, 2021. 25, 122

[79] Ramy A Fouad, Mohamed IA Habba, Yousef GY Elshaghoul, Mohamed M El-Sayed Seleman, Khalid M Hafez, FS Hamid, and Waheed S Barakat. The influence of various welding wires on microstructure, and mechanical characteristics of aa7075 al-alloy welded by tig process. *Scientific Reports*, 14 (1):19023, 2024. 25

[80] Junliang Xue, Peng Peng, Wei Guo, Mingsheng Xia, Caiwang Tan, Zhandong Wan, Hongqiang Zhang, and Yongqiang Li. Haz characterization and mechanical properties of qp980-dp980 laser welded joints. *Chinese Journal of Mechanical Engineering*, 34(1):80, 2021. 25

[81] Timon Suckow, Stephan Völkers, Ezgi Bütev Öcal, Markus Grass, Stefan Böhm, and Peter Groche. Effect of shortened post weld heat treatment on the laser welded aa7075 alloy. *Metals*, 12(3):393, 2022. 25

[82] Pei-quan Xu, Leijun Li, and Chunbo Sam Zhang. Microstructure characterization of laser welded ti-6al-4v fusion zones. *Materials Characterization*, 87: 179–185, 2014. 26

[83] Vinicius Machado Mansur, Raquel Alvim de Figueiredo Mansur, Sheila Medeiros de Carvalho, Rafael Humberto Mota de Siqueira, and Milton Sergio Fernandes de Lima. Effect of laser welding on microstructure

and mechanical behaviour of dual phase 600 steel sheets. *Heliyon*, 7(12), 2021. 26, 27

[84] Jonathan D Madison, Larry K Aagesen, Victor WL Chan, and Katsuyo Thornton. Advancing quantitative description of porosity in autogenous laser-welds of 304l stainless steel. *Integrating Materials and Manufacturing Innovation*, 3(1):141–157, 2014. 27, 36

[85] Bolong Li, Jiayi Zhou, Rongxun Hu, Hua Pan, Tianhai Wu, and Yulai Gao. Microstructure evolution and fracture mode of laser welding–brazing dp780 steel-5754 aluminum alloy joints with various laser spot positions. *Materials*, 18(12):2676, 2025. 27

[86] Wayne E King, Andrew T Anderson, Robert M Ferencz, Neil E Hodge, Chandrika Kamath, Saad A Khairallah, and Alexander M Rubenchik. Laser powder bed fusion additive manufacturing of metals; physics, computational, and materials challenges. *Applied Physics Reviews*, 2(4), 2015. 28, 29, 30, 31, 33, 34

[87] Dmitry S Bulgarevich, Sukeharu Nomoto, Makoto Watanabe, and Masahiko Demura. Crystal plasticity simulations with representative volume element of as-build laser powder bed fusion materials. *Scientific Reports*, 13(1):20372, 2023. 29

[88] Saad A Khairallah, Andrew T Anderson, Alexander Rubenchik, and Wayne E King. Laser powder-bed fusion additive manufacturing: Physics of complex melt flow and formation mechanisms of pores, spatter, and denudation zones. *Acta Materialia*, 108:36–45, 2016. 30, 33, 36

[89] Wayne E King, Holly D Barth, Victor M Castillo, Gilbert F Gallegos, John W Gibbs, Douglas E Hahn, Chandrika Kamath, and Alexander M Rubenchik. Observation of keyhole-mode laser melting in laser powder-bed fusion additive

manufacturing. *Journal of Materials Processing Technology*, 214(12):2915–2925, 2014. 30

[90] Junaid Dar, Andre Georges Ponsot, Caden Jacob Jolma, and Dong Lin. A review on scan strategies in laser-based metal additive manufacturing. *Journal of Materials Research and Technology*, 36:5425–5467, 2025. 31

[91] Umberto Scipioni Bertoli, Alexander J Wolfer, Manyalibo J Matthews, Jean-Pierre R Delplanque, and Julie M Schoenung. On the limitations of volumetric energy density as a design parameter for selective laser melting. *Materials & Design*, 113:331–340, 2017. 32

[92] Meurig Thomas, Gavin J Baxter, and Iain Todd. Normalised model-based processing diagrams for additive layer manufacture of engineering alloys. *Acta Materialia*, 108:26–35, 2016. 32, 34

[93] Minh Anh Luan Phan, Oliver Dew, and Iain Todd. Predictive process diagram for parameters selection in laser powder bed fusion to achieve high-density and low-cracking built parts. *Additive Manufacturing*, 85:104145, 2024. 32

[94] Jerard V Gordon, Sneha P Narra, Ross W Cunningham, He Liu, Hangman Chen, Robert M Suter, Jack L Beuth, and Anthony D Rollett. Defect structure process maps for laser powder bed fusion additive manufacturing. *Additive Manufacturing*, 36:101552, 2020. 32

[95] Manyalibo J Matthews, Gabe Guss, Saad A Khairallah, Alexander M Rubenchik, Philip J Depond, and Wayne E King. Denudation of metal powder layers in laser powder-bed fusion processes. In *Additive manufacturing handbook*, pages 677–692. CRC Press, 2017. 33

[96] Ross Cunningham, Cang Zhao, Niranjan Parab, Christopher Kantzos, Joseph Pauza, Kamel Fezzaa, Tao Sun, and Anthony D Rollett. Keyhole threshold and

morphology in laser melting revealed by ultrahigh-speed x-ray imaging. *Science*, 363(6429):849–852, 2019. 33, 36

[97] Sindo Kou. *Welding Metallurgy*. John Wiley & Sons, Hoboken, NJ, 2nd edition, 2003. 35

[98] Bey Vrancken, Lore Thijs, Jean-Pierre Kruth, and Jan Van Humbeeck. Heat treatment of ti6al4v produced by selective laser melting: Microstructure and mechanical properties. *Journal of alloys and compounds*, 541:177–185, 2012. 35, 36

[99] Aiden A Martin, Nicholas P Calta, Saad A Khairallah, Jenny Wang, Phillip J Depond, Anthony Y Fong, Vivek Thampy, Gabe M Guss, Andrew M Kiss, Kevin H Stone, et al. Dynamics of pore formation during laser powder bed fusion additive manufacturing. *Nature communications*, 10(1):1987, 2019. 35, 137

[100] Lore Thijs, Frederik Verhaeghe, Tom Craeghs, Jan Van Humbeeck, and Jean-Pierre Kruth. A study of the microstructural evolution during selective laser melting of ti–6al–4v. *Acta materialia*, 58(9):3303–3312, 2010. 36

[101] Christian Weingarten, Damien Buchbinder, Norbert Pirch, Wilhelm Meiners, Konrad Wissenbach, and Reinhart Poprawe. Formation and reduction of hydrogen porosity during selective laser melting of alsi10mg. *Journal of Materials Processing Technology*, 221:112–120, 2015. 37

[102] J-W Yeh, S-K Chen, S-J Lin, J-Y Gan, T-S Chin, T-T Shun, C-H Tsau, and S-Y Chang. Nanostructured high-entropy alloys with multiple principal elements: novel alloy design concepts and outcomes. *Advanced engineering materials*, 6 (5):299–303, 2004. 38, 79

[103] Brain Cantor, Isaac TH Chang, Peter Knight, and AJB Vincent. Microstructural development in equiatomic multicomponent alloys. *Materials Science and Engineering: A*, 375:213–218, 2004. 38, 79

[104] Easo P George, Dierk Raabe, and Robert O Ritchie. High-entropy alloys. *Nature reviews materials*, 4(8):515–534, 2019. 38, 39, 40

[105] Denzel Bridges, David Fieser, Jannira J Santiago, and Anming Hu. Novel frontiers in high-entropy alloys. *Metals*, 13(7):1193, 2023. 39, 55, 73, 82, 245

[106] Ming-Hung Tsai and Jien-Wei Yeh. High-entropy alloys: a critical review. *Materials Research Letters*, 2(3):107–123, 2014. 39

[107] Daniel B Miracle and Oleg N Senkov. A critical review of high entropy alloys and related concepts. *Acta materialia*, 122:448–511, 2017. 39, 40, 42

[108] Yong Zhang, Ting Ting Zuo, Zhi Tang, Michael C Gao, Karin A Dahmen, Peter K Liaw, and Zhao Ping Lu. Microstructures and properties of high-entropy alloys. *Progress in materials science*, 61:1–93, 2014. 39, 40

[109] Xiao Yang and Yong Zhang. Prediction of high-entropy stabilized solid-solution in multi-component alloys. *Materials Chemistry and Physics*, 132(2-3):233–238, 2012. 40, 80

[110] Sheng Guo, Chun Ng, Jian Lu, and CT Liu. Effect of valence electron concentration on stability of fcc or bcc phase in high entropy alloys. *Journal of applied physics*, 109(10), 2011. 40

[111] Céline Varvenne, Aitor Luque, and William A Curtin. Theory of strengthening in fcc high entropy alloys. *Acta Materialia*, 118:164–176, 2016. 40

[112] Bernd Gludovatz, Anton Hohenwarter, Dhiraj Catoor, Edwin H Chang, Easo P George, and Robert O Ritchie. A fracture-resistant high-entropy alloy for cryogenic applications. *Science*, 345(6201):1153–1158, 2014. 40

[113] Vincenzo Amendola and Moreno Meneghetti. Laser ablation synthesis in solution and size manipulation of noble metal nanoparticles. *Physical chemistry chemical physics*, 11(20):3805–3821, 2009. 40, 82

[114] Vincenzo Amendola and Moreno Meneghetti. What controls the composition and the structure of nanomaterials generated by laser ablation in liquid solution? *Physical Chemistry Chemical Physics*, 15(9):3027–3046, 2013. 40, 41, 42

[115] Fumitaka Mafuné, Jun-ya Kohno, Yoshihiro Takeda, Tamotsu Kondow, and Hisahiro Sawabe. Formation of gold nanoparticles by laser ablation in aqueous solution of surfactant. *The Journal of Physical Chemistry B*, 105(22):5114–5120, 2001. 40

[116] Friedrich Waag, Yao Li, Anna Rosa Ziefuß, Erwan Bertin, Marius Kamp, Viola Duppel, Galina Marzun, Lorenz Kienle, Stephan Barcikowski, and Bilal Gökce. Kinetically-controlled laser-synthesis of colloidal high-entropy alloy nanoparticles. *RSC advances*, 9(32):18547–18558, 2019. 41, 42, 56, 82, 110

[117] Hadi Jahangiri, Yağız Morova, Armin Asghari Alamdari, Zafer Eroğlu, Alphan Sennaroğlu, Sheng Guo, Onder Metin, and Amir Motallebzadeh. Femtosecond laser-mediated preparation of hfnbtatizr refractory high-entropy alloy nanoparticles for photothermal therapy applications: Influence of solvent and fluence. *Intermetallics*, 156:107834, 2023. 41, 42, 56, 81, 110, 113

[118] Shabbir Tahir, Natalia Shkodich, Benedikt Eggert, Johanna Lill, Oleksandr Gatsa, Miroslava Flimelová, Esmaeil Adabifiroozjaei, Nadezhda M Bulgakova, Leopoldo Molina-Luna, Heiko Wende, et al. Synthesis of high entropy alloy nanoparticles by pulsed laser ablation in liquids: influence of target preparation on stoichiometry and productivity. *ChemNanoMat*, 10(5):e202400064, 2024. 41, 42, 81

[119] Bibek Kumar Singh, Rajesh Rawat, Archana Tiwari, Venugopal Rao Soma, and Ajay Tripathi. Recent advances in the laser-based fabrication and applications of high-entropy alloy nanoparticles. *MetalMat*, page e70036, 2026. 42, 56, 83

[120] Dongshi Zhang, Bilal Gokce, and Stephan Barcikowski. Laser synthesis and processing of colloids: fundamentals and applications. *Chemical reviews*, 117 (5):3990–4103, 2017. 42

[121] Richard A Michi, Alex Plotkowski, Amit Shyam, Ryan R Dehoff, and Sudarsanam Suresh Babu. Towards high-temperature applications of aluminium alloys enabled by additive manufacturing. *International Materials Reviews*, 67(3):298–345, 2022. 42

[122] Sumit Bahl, Tiffany Wu, Richard A Michi, Ke An, Dunji Yu, Lawrence F Allard, Jovid U Rakhmonov, Jonathan D Poplawsky, Chris M Fancher, David C Dunand, et al. An additively manufactured near-eutectic al-ce-ni-mn-zr alloy with high creep resistance. *Acta Materialia*, 268:119787, 2024. 42, 44, 46, 47, 122, 123, 125

[123] Zachary C Sims, David Weiss, SK McCall, Michael A McGuire, Ryan T Ott, Tom Geer, Orlando Rios, and PAE Turchi. Cerium-based, intermetallic-strengthened aluminum casting alloy: high-volume co-product development. *Jom*, 68(7):1940–1947, 2016. 43

[124] Zachary C Sims, Orlando R Rios, David Weiss, Patrice EA Turchi, Aurelien Perron, Jonathan RI Lee, Tian T Li, Joshua A Hammons, Michael Bagge-Hansen, Trevor M Willey, et al. High performance aluminum–cerium alloys for high-temperature applications. *Materials Horizons*, 4(6):1070–1078, 2017. 43

[125] Eric T Stromme, Hunter B Henderson, Zachary C Sims, Michael S Kesler, David Weiss, Ryan T Ott, Fanqiang Meng, Sam Kassoumeh, James Evangelista,

Gerald Begley, et al. Ageless aluminum-cerium-based alloys in high-volume die casting for improved energy efficiency. *Jom*, 70(6):866–871, 2018. 43

[126] Alex Plotkowski, Kevin Sisco, Sumit Bahl, Amit Shyam, Ying Yang, L Allard, Peeyush Nandwana, A Marquez Rossy, and RR Dehoff. Microstructure and properties of a high temperature al–ce–mn alloy produced by additive manufacturing. *Acta Materialia*, 196:595–608, 2020. 43, 122

[127] Richard A Michi, Kevin Sisco, Sumit Bahl, Ying Yang, Jonathan D Poplawsky, Lawrence F Allard, Ryan R Dehoff, Alex Plotkowski, and Amit Shyam. A creep-resistant additively manufactured al-ce-ni-mn alloy. *Acta Materialia*, 227: 117699, 2022. 44, 46, 122, 123

[128] Alice E Perrin, Richard A Michi, Donovan N Leonard, Kevin D Sisco, Alex J Plotkowski, Amit Shyam, Jonathan D Poplawsky, Lawrence F Allard Jr, and Ying Yang. Effect of mn on eutectic phase equilibria in al-rich al-ce-ni alloys. *Journal of Alloys and Compounds*, 965:171455, 2023. 45, 123

[129] Richard A Michi, Joseph J Simpson, Sumit Bahl, Quinn Campbell, Paul Brackman, Alex Plotkowski, Ryan R Dehoff, James A Haynes, Qigui Wang, and Amit Shyam. Additively manufactured al-ce-ni-mn alloy with improved elevated-temperature fatigue resistance. *Additive Manufacturing*, 66:103477, 2023. 46, 122

[130] Jovid Rakhmonov, Obaidullah Rahman, Sumit Bahl, Amir Koushyar Ziabari, Alex Plotkowski, and Amit Shyam. Creep ductility limiting mechanisms in an additively manufactured al-ce-ni-mn-zr alloy. *Additive Manufacturing*, page 104983, 2025. 46

[131] Bey Vrancken, Rishi K Ganeriwala, and Manyalibo J Matthews. Analysis of laser-induced microcracking in tungsten under additive manufacturing

conditions: Experiment and simulation. *Acta Materialia*, 194:464–472, 2020. 48

[132] Aljaž Iveković, Neda Omidvari, Bey Vrancken, Karel Lietaert, Lore Thijs, Kim Vanmeensel, Jef Vleugels, and Jean-Pierre Kruth. Selective laser melting of tungsten and tungsten alloys. *International Journal of Refractory Metals and Hard Materials*, 72:27–32, 2018. 48

[133] Jiayao Zhang, Dongdong Gu, Ying Yang, Hongmei Zhang, Hongyu Chen, Donghuai Dai, and Kaijie Lin. Influence of particle size on laser absorption and scanning track formation mechanisms of pure tungsten powder during selective laser melting. *Engineering*, 5(4):736–745, 2019. 48

[134] Meng Guo, Dongdong Gu, Lixia Xi, Hongmei Zhang, Jiayao Zhang, Jiankai Yang, and Rui Wang. Selective laser melting additive manufacturing of pure tungsten: Role of volumetric energy density on densification, microstructure and mechanical properties. *International Journal of Refractory Metals and Hard Materials*, 84:105025, 2019. 49

[135] Boris N Chichkov, Carsten Momma, Stefan Nolte, Ferdinand Von Alvensleben, and Andreas Tünnermann. Femtosecond, picosecond and nanosecond laser ablation of solids. *Applied physics A*, 63(2):109–115, 1996. 49, 153

[136] Stefan Nolte, Cl Momma, H Jacobs, A Tünnermann, Boris N Chichkov, Bernd Wellegehausen, and Herbert Welling. Ablation of metals by ultrashort laser pulses. *Journal of the Optical Society of America B*, 14(10):2716–2722, 1997. 49

[137] A Ya Vorobyev and Chunlei Guo. Colorizing metals with femtosecond laser pulses. *Applied physics letters*, 92(4), 2008. 49

[138] PT Mannion, J Magee, E Coyne, GM O'connor, and TJ Glynn. The effect of damage accumulation behaviour on ablation thresholds and damage

morphology in ultrafast laser micro-machining of common metals in air. *Applied surface science*, 233(1-4):275–287, 2004. 49

[139] Jianchi Huang, Ming Li, Jyhwen Wang, Zhijian Pei, Peter Mclntyre, and Chao Ma. Selective laser melting of tungsten: Effects of hatch distance and point distance on pore formation. *Journal of Manufacturing Processes*, 61:296–302, 2021. 50

[140] Zhangping Hu, Yanan Zhao, Kai Guan, Zumin Wang, and Zongqing Ma. Pure tungsten and oxide dispersion strengthened tungsten manufactured by selective laser melting: Microstructure and cracking mechanism. *Additive Manufacturing*, 36:101579, 2020. 50

[141] Xin Zhou, Xihe Liu, Dandan Zhang, Zhijian Shen, and Wei Liu. Balling phenomena in selective laser melted tungsten. *Journal of Materials Processing Technology*, 222:33–42, 2015. 50

[142] A v Müller, G Schlick, R Neu, C Anstätt, T Klimkait, J Lee, B Pascher, M Schmitt, and C Seidel. Additive manufacturing of pure tungsten by means of selective laser beam melting with substrate preheating temperatures up to 1000° c. *Nuclear Materials and Energy*, 19:184–188, 2019. 50

[143] AY Vorobyev and Chunlei Guo. Femtosecond laser-induced periodic surface structure formation on tungsten. *Journal of Applied Physics*, 104(6), 2008. 51

[144] David Fieser, Yucheng Lan, Antonino Gulino, Giuseppe Compagnini, Doug Aaron, Matthew Mench, Denzel Bridges, Hugh Shortt, Peter Liaw, and Anming Hu. Synthesis and unique behaviors of high-purity hea nanoparticles using femtosecond laser ablation. *Nanomaterials*, 14(6):554, 2024. 53, 81, 82, 84, 85, 244

[145] Lingyue Zhang, David Fieser, Bapi Bera, Douglas Aaron, Matthew M Mench, Anming Hu, Yuan Li, Jian Chen, Zhili Feng, Antonino Gulino, et al. High

performance aluminum-air flow batteries through double-face architecture and laser-modified and friction-stir processed 3d anode. *Journal of Power Sources*, 589:233752, 2024. 54, 60, 245

[146] Chunlian Wang, Yongchao Yu, Jiajia Niu, Yaxuan Liu, Denzel Bridges, Xianqiang Liu, Joshi Pooran, Yuefei Zhang, and Anming Hu. Recent progress of metal–air batteries—a mini review. *Applied Sciences*, 9(14):2787, 2019. 54

[147] Michael C. Gao. Development of new high entropy alloys for brazing of ni-base superalloys. Master's thesis, Colorado School of Mines, 2017. 54, 55, 110

[148] Hailong Peng, Yangcenzi Xie, Zicheng Xie, Yunfeng Wu, Wenkun Zhu, Shuquan Liang, and Liangbing Wang. Large-scale and facile synthesis of a porous high-entropy alloy crmnfeconi as an efficient catalyst. *Journal of Materials Chemistry A*, 8(35):18318–18326, 2020. 54

[149] Denzel Bridges. *Nanobrazing of Inconel 718 and Ti-6Al-4V*. PhD thesis, University of Tennessee, Knoxville, 2019. 54, 55

[150] Rui-Qi Yao, Yi-Tong Zhou, Hang Shi, Wu-Bin Wan, Qing-Hua Zhang, Lin Gu, Yong-Fu Zhu, Zi Wen, Xing-You Lang, and Qing Jiang. Nanoporous surface high-entropy alloys as highly efficient multisite electrocatalysts for nonacidic hydrogen evolution reaction. *Advanced Functional Materials*, 31(10):2009613, 2021. 54

[151] Guoliang Zhang, Kaisheng Ming, Jianli Kang, Qin Huang, Zhijia Zhang, Xuerong Zheng, and Xiaofang Bi. High entropy alloy as a highly active and stable electrocatalyst for hydrogen evolution reaction. *Electrochimica Acta*, 279: 19–23, 2018. 54

[152] Minrui Gao, Benjamin Schneiderman, Sarah M Gilbert, and Zhenzhen Yu. Microstructural evolution and mechanical properties of nickel-base superalloy

brazed joints using a mpca filler. *Metallurgical and Materials Transactions A*, 50(11):5117–5127, 2019. 54

[153] Ji-Yoon Song, Chansol Kim, Minki Kim, Kyeong Min Cho, Issam Gereige, Woo-Bin Jung, Hyeonsu Jeong, and Hee-Tae Jung. Generation of high-density nanoparticles in the carbothermal shock method. *Science Advances*, 7(48): eabk2984, 2021. 55

[154] Wei Ji, Zhengyi Fu, Weimin Wang, Hao Wang, Jinyong Zhang, Yucheng Wang, and Fan Zhang. Mechanical alloying synthesis and spark plasma sintering consolidation of cocrfenial high-entropy alloy. *Journal of Alloys and Compounds*, 589:61–66, 2014. 55

[155] Viktor Chikan and Emily J McLaurin. Rapid nanoparticle synthesis by magnetic and microwave heating. *Nanomaterials*, 6(5):85, 2016. 55

[156] Linlin Xu and Jun Yang. Size and shape-controlled synthesis of ru nanocrystals. *Physical Sciences Reviews*, 3(12):20170080, 2018. 55

[157] Paolo Veronesi, Roberto Rosa, Elena Colombini, and Cristina Leonelli. Microwave-assisted preparation of high entropy alloys. *Technologies*, 3(4):182–197, 2015. 55

[158] Gracita M Tomboc, Taehyun Kwon, Jinwhan Joo, and Kwangyeol Lee. High entropy alloy electrocatalysts: a critical assessment of fabrication and performance. *Journal of materials chemistry A*, 8(30):14844–14862, 2020. 55, 81

[159] Dada Modupeola and Patricia Popoola. High entropy nanomaterials for energy storage and catalysis applications. *Frontiers in Energy Research*, 11:1149446, 2023. 55

[160] David Redka, Christian Gadelmeier, Jan Winter, Maximilian Spellauge, Constanze Eulenkamp, Pavel Calta, Uwe Glatzel, Ján Minár, and Heinz P

Huber. Sub-picosecond single-pulse laser ablation of the crmnfeconi high entropy alloy and comparison to stainless steel aisi 304. *Applied Surface Science*, 544:148839, 2021. 56, 82

[161] Rajesh Rawat, Bibek Kumar Singh, Archana Tiwari, Nimmala Arun, Anand P Pathak, Yagnesh Shadangi, NK Mukhopadhyay, Srinivasa Rao Nelamarri, S Venugopal Rao, and Ajay Tripathi. Formation of cu-ni enriched phases during laser processing of non-equiatomic alsicrmnfenicu high entropy alloy nanoparticles. *Journal of Alloys and Compounds*, 927:166905, 2022. 56, 105

[162] A Hu, P Peng, H Alarifi, XY Zhang, JY Guo, Y Zhou, and WW Duley. Femtosecond laser welded nanostructures and plasmonic devices. *Journal of Laser Applications*, 24(4), 2012. 57

[163] Yongchao Yu, Ming Xiao, David Fieser, Wei Zhou, and Anming Hu. Nanoscale memristor devices: materials, fabrication, and artificial intelligence. *Journal of Materials Chemistry C*, 12(11):3770–3810, 2024. 57, 244

[164] Qiuyue Su, Shi Bai, Jitai Han, Ying Ma, Yongchao Yu, Yangbao Deng, Meiping Wu, Chong Zheng, and Anming Hu. Precise laser trimming of alloy strip resistor: A comparative study with femtosecond laser and nanosecond laser. *Journal of Laser Applications*, 32(2), 2020. 61

[165] Lei Wang, Bin-Bin Xu, Xiao-Wen Cao, Qian-Kun Li, Wen-Jing Tian, Qi-Dai Chen, Saulius Juodkazis, and Hong-Bo Sun. Competition between subwavelength and deep-subwavelength structures ablated by ultrashort laser pulses. *Optica*, 4(6):637–642, 2017. 61

[166] Bin-Bin Xu, Dan-Dan Zhang, Xue-Qing Liu, Lei Wang, Wei-Wei Xu, Masanobu Haraguchi, and Ai-Wu Li. Fabrication of microelectrodes based on precursor doped with metal seeds by femtosecond laser direct writing. *Optics letters*, 39 (3):434–437, 2014. 61

[167] Ranjana Verma and SK Samdarshi. Correlating oxygen vacancies and phase ratio/interface with efficient photocatalytic activity in mixed phase tio2. *Journal of Alloys and Compounds*, 629:105–112, 2015. 62

[168] Noemi Bosio, Andreas Schaefer, and Henrik Grönbeck. Can oxygen vacancies in ceria surfaces be measured by o1s photoemission spectroscopy? *Journal of Physics: Condensed Matter*, 34(17):174004, 2022. 62

[169] D Montalvo, V Gómez, W de la Cruz, S Camacho-López, I Rivero, K Carrera, V Orozco, C Santillán, J Matutes, and M Herrera-Zaldívar. Influence of single-ionized oxygen vacancies on the generation of ferromagnetism in sno2 and sno2: Cr nanowires. *Applied Physics A*, 129(8):537, 2023. 62

[170] Jiali Zhao, Chen Liu, Jinmei Li, Rui Wu, Jiaou Wang, Haijie Qian, Haizhong Guo, Jiankun Li, and Kurash Ibrahim. Oxygen vacancy induced electronic structure variation in the la0. 2sr0. 8mno3 thin film. *AIP Advances*, 9(5), 2019. 62

[171] Claudio Cazorla. Lattice effects on the formation of oxygen vacancies in perovskite thin films. *Physical Review Applied*, 7(4):044025, 2017. 62

[172] Zheling Li, Libo Deng, Ian A Kinloch, and Robert J Young. Raman spectroscopy of carbon materials and their composites: Graphene, nanotubes and fibres. *Progress in Materials Science*, 135:101089, 2023. 65

[173] A Hu, Q-B Lu, WW Duley, and Maksym Rybachuk. Spectroscopic characterization of carbon chains in nanostructured tetrahedral carbon films synthesized by femtosecond pulsed laser deposition. *The Journal of chemical physics*, 126(15), 2007. 65

[174] Anming Hu and Walt W Duley. Synthesis of nanocrystalline hexagonal diamond films in organic solvents by femtosecond laser irradiation. *MRS Online Proceedings Library (OPL)*, 1039:1039–P15, 2007. 65

[175] Omar Martinez-Mora, Kristof Tirez, Filip Beutels, Wilfried Brusten, Luis F Leon-Fernandez, Jan Fransaer, Xochitl Dominguez-Benetton, and Milica Velimirovic. Exploring pt-pd alloy nanoparticle cluster formation through conventional sizing techniques and single-particle inductively coupled plasma—sector field mass spectrometry. *Nanomaterials*, 13(18):2610, 2023. 68

[176] Yongchao Yu, Yangbao Deng, Md Abdullah Al Hasan, Yanfeng Bai, Ruo-Zhou Li, Shuguang Deng, Pooran Joshi, Seungha Shin, and Anming Hu. Femtosecond laser-induced non-thermal welding for a single cu nanowire glucose sensor. *Nanoscale Advances*, 2(3):1195–1205, 2020. 70

[177] A Hu, Maksym Rybachuk, Q-B Lu, and WW Duley. Direct synthesis of sp-bonded carbon chains on graphite surface by femtosecond laser irradiation. *Applied Physics Letters*, 91(13), 2007. 70

[178] Shutong Wang, Junjie Yang, Guoliang Deng, and Shouhuan Zhou. Femtosecond laser direct writing of flexible electronic devices: A mini review. *Materials*, 17 (3):557, 2024. 70, 71

[179] XiaoHui Lin, HaiQuan Chen, ShuYun Jiang, and ChiBin Zhang. A coulomb explosion theoretical model of femtosecond laser ablation materials. *Science China Technological Sciences*, 55(3):694–701, 2012. 70, 82

[180] Shane M Eaton, Haibin Zhang, Peter R Herman, Fumiyo Yoshino, Lawrence Shah, James Bovatsek, and Alan Y Arai. Heat accumulation effects in femtosecond laser-written waveguides with variable repetition rate. *Optics express*, 13(12):4708–4716, 2005. 73

[181] Lauren L Taylor, Ryan E Scott, and Jie Qiao. Integrating two-temperature and classical heat accumulation models to predict femtosecond laser processing of silicon. *Optical Materials Express*, 8(3):648–658, 2018. 73

[182] Hongdong Li, Yi Han, Huan Zhao, Wenjing Qi, Dan Zhang, Yaodong Yu, Wenwen Cai, Shaoxiang Li, Jianping Lai, Bolong Huang, et al. Fast site-to-site electron transfer of high-entropy alloy nanocatalyst driving redox electrocatalysis. *Nature communications*, 11(1):5437, 2020. 73

[183] David Fieser, Kaijun Yin, Hugh Shortt, Unmanaa Dewanjee, Baldur Steingrimsson, Ilia N Ivanov, James Burns, Peter K Liaw, Jian-Min Zuo, and Anming Hu. Surface nanostructure control and thermodynamic stability analysis of femtosecond laser-ablated cucomn1. 75nife0. 25 nanoparticles. *Langmuir*, 41(50):34173–34188, 2025. 78, 244

[184] EJ Pickering and NG Jones. High-entropy alloys: a critical assessment of their founding principles and future prospects. *International Materials Reviews*, 61 (3):183–202, 2016. 79

[185] Jien-Wei Yeh. Alloy design strategies and future trends in high-entropy alloys. *Jom*, 65(12):1759–1771, 2013. 79

[186] Rui Feng, Peter K Liaw, Michael C Gao, and Michael Widom. First-principles prediction of high-entropy-alloy stability. *npj Computational Materials*, 3(1): 50, 2017. 79

[187] M Claudia Troparevsky, James R Morris, Paul RC Kent, Andrew R Lupini, and G Malcolm Stocks. Criteria for predicting the formation of single-phase high-entropy alloys. *Physical Review X*, 5(1):011041, 2015. 79

[188] Hedayat Hamdi, Hamid Reza Abedi, and Yong Zhang. A review study on thermal stability of high entropy alloys: Normal/abnormal resistance of grain growth. *Journal of Alloys and Compounds*, 960:170826, 2023. 79

[189] Yu Zou, Huan Ma, and Ralph Spolenak. Ultrastrong ductile and stable high-entropy alloys at small scales. *Nature communications*, 6(1):7748, 2015. 79

[190] Jack K Pedersen, Thomas AA Batchelor, Alexander Bagger, and Jan Rossmeisl. High-entropy alloys as catalysts for the co2 and co reduction reactions. *ACS catalysis*, 10(3):2169–2176, 2020. 81

[191] Yong Yang, Boao Song, Xiang Ke, Feiyu Xu, Krassimir N Bozhilov, Liangbing Hu, Reza Shahbazian-Yassar, and Michael R Zachariah. Aerosol synthesis of high entropy alloy nanoparticles. *Langmuir*, 36(8):1985–1992, 2020. 81

[192] Yonggang Yao, Qi Dong, Alexandra Brozena, Jian Luo, Jianwei Miao, Miaofang Chi, Chao Wang, Ioannis G Kevrekidis, Zhiyong Jason Ren, Jeffrey Greeley, et al. High-entropy nanoparticles: Synthesis-structure-property relationships and data-driven discovery. *Science*, 376(6589):eabn3103, 2022. 81, 82, 98

[193] Mahmoud Tamadoni Saray, Vitaliy R Yurkiv, and Reza Shahbazian-Yassar. In situ tem studies on the formation of high-entropy alloy nanoparticles from mixed metal-salt precursors. *Langmuir*, 41(23):14727–14742, 2025. 81

[194] Rintaro Ninomiya, Dasom Kim, Naoki Takata, Stephen M Lyth, Kazuhiro Ishikawa, and Yoji Miyajima. Production of sub-micron-sized high-entropy alloy particles and nanoparticles via pulsed laser ablation of crmnfeconi targets in water. *Applied Physics Letters*, 124(20), 2024. 81

[195] David Fieser, Lingyue Zhang, Matthew Yao, Hugh Shortt, Peter Liaw, and Anming Hu. Femtosecond laser joining of stellite and stainless steel. *Manufacturing Letters*, 41:332–338, 2024. 82, 244

[196] Yongchao Yu, Pooran Joshi, Denzel Bridges, David Fieser, and Anming Hu. Femtosecond laser-induced nano-joining of volatile tellurium nanotube memristor. *Nanomaterials*, 13(5):789, 2023. 82, 245

[197] Lin Zhang, Han Wu, Jincheng Wen, Meng Li, Xinyu Shao, and Xiuquan Ma. Glass to aluminum joining by forming a mechanical pin structure using

femtosecond laser. *Journal of Materials Processing Technology*, 302:117504, 2022. 82

[198] Taihe Li, Rongjingxi Tang, Lurun Xu, Jingchao Tao, Guo He, Zhuguo Li, and Dongshi Zhang. Femtosecond laser ablation of high-entropy ceramics re2 (ce0. 2zr0. 2hf0. 2sn0. 2ti0. 2) 2o7 (re= sm, eu, er) in liquid for colloid synthesis. *The Journal of Physical Chemistry C*, 129(7):3707–3720, 2025. 82

[199] Rajesh Rawat, Nicholas P Blanchard, Yagnesh Shadangi, Ajay Tripathi, and David Amans. Laser generation of alcrcufeni high-entropy alloy nanocolloids. *The Journal of Physical Chemistry C*, 128(46):19815–19828, 2024. 82, 90

[200] Jovan Maksimovic, Haoran Mu, Molong Han, Daniel Smith, Tomas Katkus, Vijayakumar Anand, Yoshiaki Nishijima, Soon Hock Ng, and Saulius Juodkazis. Si-cr nano-alloys fabricated by direct femtosecond laser writing. *Materials*, 16 (5):1917, 2023. 82

[201] David Redka, Maximilian Spellauge, Christian Sandner, Ján Minár, and Heinz P Huber. Mechanisms of ultrashort laser ablation in crmnfeconi high-entropy alloy and stainless steel. *Applied Surface Science*, 686:162190, 2025. 82

[202] Yuxiang Liu, Jianghuai Yuan, Jiantao Zhou, Kewen Pan, Ran Zhang, Rongxia Zhao, Lin Li, Yihe Huang, and Zhu Liu. Laser solid-phase synthesis of graphene shell-encapsulated high-entropy alloy nanoparticles. *Light: Science & Applications*, 13(1):270, 2024. 83

[203] Litian Zhang, Hao Wang, Wei Cheng, Lingchao Kong, Xiubing Liang, and Lingfei Ji. Femtosecond laser sintering of irregular nbmotawzr powders to fabricate fine grain, single-phase body-centered cubic solid solution refractory high-entropy alloys. *Journal of Alloys and Compounds*, 944:169208, 2023. 83

[204] COMSOL AB. COMSOL Multiphysics® v. 6.4, 2025. URL https://www.comsol.com. Version 6.4.0.343. 87

[205] JA Schroeder, SG Penoncello, and JS Schroeder. A fundamental equation of state for ethanol. *Journal of Physical and Chemical Reference Data*, 43(4), 2014. 87, 89, 90

[206] Young-Kyun Kim, Sangsun Yang, and Kee-Ahn Lee. Superior temperature-dependent mechanical properties and deformation behavior of equiatomic cocrfemnni high-entropy alloy additively manufactured by selective laser melting. *Scientific reports*, 10(1):8045, 2020. 87

[207] Sila Ece Atabay, Sheida Sarafan, Aminul Islam, Fabrice Bernier, Javad Gholipour, Robert Amos, Prakash Patnaik, Priti Wanjara, and Mathieu Brochu. Laser powder bed fusion printing of cocrfemnni high entropy alloy: processing, microstructure, and mechanical properties. *High Entropy Alloys & Materials*, 2(1):129–173, 2024. 87

[208] Samy Merabia, Sergei Shenogin, Laurent Joly, Pawel Keblinski, and Jean-Louis Barrat. Heat transfer from nanoparticles: A corresponding state analysis. *Proceedings of the National Academy of Sciences*, 106(36):15113–15118, 2009. 88

[209] Juan D Olarte-Plata and Fernando Bresme. Thermal conductance of the water–gold interface: The impact of the treatment of surface polarization in non-equilibrium molecular simulations. *The Journal of chemical physics*, 156(20), 2022. 88

[210] Blake A Wilson, Steven O Nielsen, Jaona H Randrianalisoa, and Zhenpeng Qin. Curvature and temperature-dependent thermal interface conductance between nanoscale gold and water. *The Journal of Chemical Physics*, 157(5), 2022. 88

[211] Yong Zhang, Yun Jun Zhou, Jun Pin Lin, Guo Liang Chen, and Peter K Liaw. Solid-solution phase formation rules for multi-component alloys. *Advanced engineering materials*, 10(6):534–538, 2008. 90, 91, 108

[212] Zibing An, Tao Yang, Caijuan Shi, Shengcheng Mao, Lihua Wang, Ang Li, Wei Li, Xianmeng Xue, Ming Sun, Yifan Bai, et al. Negative enthalpy alloys and local chemical ordering: a concept and route leading to synergy of strength and ductility. *National Science Review*, 11(4):nwae026, 2024. 90

[213] AR Miedema, PF De Chatel, and FR De Boer. Cohesion in alloys—fundamentals of a semi-empirical model. *Physica B+ c*, 100(1):1–28, 1980. 90

[214] Michael Widom. Modeling the structure and thermodynamics of high-entropy alloys. *Journal of Materials Research*, 33(19):2881–2898, 2018. 91

[215] A. Miedema and A. Niessen. The enthalpy of solution for solid binary alloys of two 4d-transition metals. *Calphad*, 7(1):27–36, 1983. 91

[216] AP Goncalves and M Almeida. Extended miedema model: Predicting the formation enthalpies of intermetallic phases with more than two elements. *Physica B: Condensed Matter*, 228(3-4):289–294, 1996. 91

[217] Mahbubeh Sadat Mousavi, Roozbeh Abbasi, and Seyed Farshid Kashani-Bozorg. A thermodynamic approach to predict formation enthalpies of ternary systems based on miedema's model. *Metallurgical and Materials Transactions A*, 47(7):3761–3770, 2016. 91

[218] M Widom. Frequency estimate for multicomponent crystalline compounds. *Journal of Statistical Physics*, 167(3):726–734, 2017. 91

[219] Michael Nastasi, James W Mayer, and James K Hirvonen. *Ion-solid interactions: fundamentals and applications*. Cambridge University Press, 1996. 91

[220] Toshihiro Tanaka, Nev A Gokcen, C Kumar Kumar, Shigeta Hara, and Zenichiro Morita. Thermodynamic relationship between enthalpy of mixing and excess entropy in solid solutions of binary alloys. *Zeitschrift für Metallkunde*, 87(10):779–783, 1996. 91

[221] Scott Kirklin, James E Saal, Bryce Meredig, Alex Thompson, Jeff W Doak, Muratahan Aykol, Stephan Rühl, and Chris Wolverton. The open quantum materials database (oqmd): assessing the accuracy of dft formation energies. *npj Computational Materials*, 1(1):1–15, 2015. 91

[222] Črtomir Donik, Jakob Kraner, Aleksandra Kocijan, Irena Paulin, and Matjaž Godec. Evolution of the ε and γ phases in biodegradable fe–mn alloys produced using laser powder-bed fusion. *Scientific Reports*, 11(1):19506, 2021. 98

[223] Zhang Peng, Jiaheng Yin, Yaowen Cui, Yongzhi Cao, Lihua Lu, Yongda Yan, and Zhengjiang Hu. Numerical and experimental investigation on pulsed nanosecond laser ablation processing of aluminum alloy. *Journal of Materials Research and Technology*, 19:4708–4720, 2022. 98, 105

[224] Zhidong Zhang, Bin Yang, Longyu Chen, Zaoli Zhang, and Jinming Guo. Oxygen vacancy-induced strengthening and toughening in (k, na) nbo3-based piezoceramics revealed via nanoindentation. *Nature Communications*, 16(1): 7015, 2025. 101, 102

[225] Donald R Baer, Kateryna Artyushkova, Christopher Richard Brundle, James E Castle, Mark H Engelhard, Karen J Gaskell, John T Grant, Richard T Haasch, Matthew R Linford, Cedric J Powell, et al. Practical guides for x-ray photoelectron spectroscopy: First steps in planning, conducting, and reporting xps measurements. *Journal of Vacuum Science & Technology A*, 37(3), 2019. 102

[226] R Intartaglia, G Das, K Bagga, A Gopalakrishnan, A Genovese, M Povia, E Di Fabrizio, R Cingolani, A Diaspro, and F Brandi. Laser synthesis of ligand-free bimetallic nanoparticles for plasmonic applications. *Physical Chemistry Chemical Physics*, 15(9):3075–3082, 2013. 109, 113

[227] Theo Fromme, Sven Reichenberger, Katharine M Tibbetts, and Stephan Barcikowski. Laser synthesis of nanoparticles in organic solvents–products, reactions, and perspectives. *Beilstein Journal of Nanotechnology*, 15(1):638–663, 2024. 109, 116

[228] Kenneth F Kelton. Crystal nucleation in liquids and glasses. In *Solid state physics*, volume 45, pages 75–177. Elsevier, 1991. 109

[229] PV Kazakevich, PS Yares' ko, VS Kazakevich, and DA Kamynina. Gold nanoparticle production by laser ablation in liquid nitrogen medium followed by cryogenic medium substitution with ethanol. *Bulletin of the Lebedev Physics Institute*, 41(9):269–274, 2014. 109, 113

[230] NG Semaltianos, E Hendry, H Chang, and ML Wears. Laser ablation of a bulk cr target in liquids for nanoparticle synthesis. *RSC Advances*, 4(92):50406–50411, 2014. 110, 113

[231] Niusha Lasemi, Christian Rentenberger, Gerhard Liedl, and Dominik Eder. The influence of the fluid nature on femtosecond laser ablation properties of a sio 2/si target and synthesis of ultrafine-grained si nanoparticles. *Nanoscale Advances*, 2(9):3991–4002, 2020. 110

[232] Niusha Lasemi, Günther Rupprechter, Gerhard Liedl, and Dominik Eder. Near-infrared femtosecond laser ablation of au-coated ni: effect of organic fluids and water on crater morphology, ablation efficiency and hydrodynamic properties of niau nanoparticles. *Materials*, 14(19):5544, 2021. 110, 112

[233] Xiaoya Cui, Yanchang Liu, and Yanan Chen. Ultrafast micro/nano-manufacturing of metastable materials for energy. *National Science Review*, 11(4):nwae033, 2024. 110

[234] B Rethfeld, K Sokolowski-Tinten, D Von Der Linde, and S Ivanovich Anisimov. Timescales in the response of materials to femtosecond laser excitation. *Applied Physics A*, 79(4):767–769, 2004. 111

[235] Frans Spaepen. Thermodynamics and kinetics of metallic alloy formation by picosecond pulsed laser irradiation. In *Laser Surface Treatment of Metals*, pages 79–92. Springer, 1986. 111

[236] Takeshi Tsuji, Yasuyuki Tsuboi, Noboru Kitamura, and Masaharu Tsuji. Microsecond-resolved imaging of laser ablation at solid–liquid interface: investigation of formation process of nano-size metal colloids. *Applied surface science*, 229(1-4):365–371, 2004. 111, 112

[237] Takeshi Tsuji, Toshihiko Kakita, and Masaharu Tsuji. Preparation of nano-size particles of silver with femtosecond laser ablation in water. *Applied Surface Science*, 206(1-4):314–320, 2003. 112

[238] Vito Coviello, Catherine Reffatto, Mehdi W Fawaz, Benoit Mahler, Arnaud Sollier, Bratislav Lukic, Alexander Rack, David Amans, and Vincenzo Amendola. Time-resolved dynamics of laser ablation in liquid with gas-evolving additives: toward molding the atomic structure of nonequilibrium nanoalloys. *Advanced Science*, 12(21):2416035, 2025. 112

[239] M Pl Seah and WA Dench. Quantitative electron spectroscopy of surfaces: A standard data base for electron inelastic mean free paths in solids. *Surface and interface analysis*, 1(1):2–11, 1979. 113

[240] Charles S Fadley. Angle-resolved x-ray photoelectron spectroscopy. *Progress in Surface Science*, 16(3):275–388, 1984. 113

[241] Cedric J Powell. Practical guide for inelastic mean free paths, effective attenuation lengths, mean escape depths, and information depths in x-ray photoelectron spectroscopy. *Journal of Vacuum Science & Technology A*, 38 (2), 2020. 113

[242] Bibek Kumar Singh, Yagnesh Shadangi, Harsh Jain, R Sai Prasad Goud, NK Mukhopadhyay, AP Pathak, Venugopal Rao Soma, Archana Tiwari, and A Tripathi. Phase evolution and morphological transformation of high-entropy alloy femnnialsic nanoparticles via sequential picosecond laser ablation and nanosecond laser annealing. *RSC advances*, 15(35):28395–28412, 2025. 115

[243] Jiangtian Li, Scott K Cushing, Joeseph Bright, Fanke Meng, Tess R Senty, Peng Zheng, Alan D Bristow, and Nianqiang Wu. Ag@ cu2o core-shell nanoparticles as visible-light plasmonic photocatalysts. *Acs Catalysis*, 3(1):47–51, 2013. 115

[244] Stephen F Bartolucci, Asher C Leff, and Joshua A Maurer. Gold–copper oxide core–shell plasmonic nanoparticles: The effect of ph on shell stability and mechanistic insights into shell formation. *Nanoscale Advances*, 6(9):2499–2507, 2024. 115

[245] Ashish Chhaganlal Gandhi and Sheng Yun Wu. Strong deep-level-emission photoluminescence in nio nanoparticles. *Nanomaterials*, 7(8):231, 2017. 115

[246] Chenglong Luan, Daniel Escalera-Lopez, Ulrich Hagemann, Aleksander Kostka, Guillaume Laplanche, Dongshuang Wu, Serhiy Cherevko, and Tong Li. Revealing dynamic surface and subsurface reconstruction of high-entropy alloy electrocatalysts during the oxygen evolution reaction at the atomic scale. *ACS Catalysis*, 14(17):12704–12716, 2024. 116

[247] Ruonan Liu, Yaotian Yan, Liang Dun, Taili Yang, Bin Qin, Peijia Wang, Wei Cai, Shude Liu, and Xiaohang Zheng. Oxygen vacancy-mediated high-entropy

oxide electrocatalysts for efficient oxygen evolution reaction. *Materials Today Catalysis*, 8:100086, 2025. 116

[248] Seung Heon Lee, Hyeon Jin Jung, Seung Jun Lee, Jayaraman Theerthagiri, Tae Ho Kim, and Myong Yong Choi. Selective synthesis of au and graphitic carbon-encapsulated au (au@ gc) nanoparticles by pulsed laser ablation in solvents: Catalytic au and acid-resistant au@ gc nanoparticles. *Applied Surface Science*, 506:145006, 2020. 116

[249] Nikolaos Pliatsikas, Stavros Panos, Tamara Odutola, Spyridon Kassavetis, Chrysanthi Papoulia, Ilias Fekas, John Arvanitidis, Dimitris Christofilos, Eleni Pavlidou, Maria Gioti, et al. Colloidal titanium nitride nanoparticles by laser ablation in solvents for plasmonic applications. *Nanomaterials*, 14(14):1214, 2024. 116

[250] Dongshi Zhang, Chao Zhang, Jun Liu, Qi Chen, Xiaoguang Zhu, and Changhao Liang. Carbon-encapsulated metal/metal carbide/metal oxide core–shell nanostructures generated by laser ablation of metals in organic solvents. *ACS Applied Nano Materials*, 2(1):28–39, 2018. 116

[251] Greici Gubert, E Ribeiro, J Varalda, AG Bezerra Jr, WH Schreiner, and DH Mosca. Laser irradiation of iron, cobalt, and nickel targets in liquid nitrogen: A facile approach for nitride nanoparticle fabrication of ferromagnetic transition metals. *Journal of Alloys and Compounds*, 725:519–525, 2017. 116

[252] Arsène Chemin, Julien Lam, Gaétan Laurens, Florian Trichard, Vincent Motto-Ros, Gilles Ledoux, Vítězslav Jarỳ, Valentyn Laguta, Martin Nikl, Christophe Dujardin, et al. Doping nanoparticles using pulsed laser ablation in a liquid containing the doping agent. *Nanoscale Advances*, 1(10):3963–3972, 2019. 116

[253] David Fieser, Michael Lawton, Sumit Bahl, Amirkoushyar Ziabari, Tomas Grejtak, Janet M. Meier, Mason Smith, Alex Plotkowski, Elaine McDonald,

and Anming Hu. Optimization of processing, microstructure, and hardness of an Al–Ce–Ni–Mn–Zr alloy with laser additive manufacturing. *Advanced Engineering Materials*, page e202502615, 2026. doi: 10.1002/adem.202502615. URL https://advanced.onlinelibrary.wiley.com/doi/abs/10.1002/adem.202502615. 121, 244

[254] Alex Plotkowski, Ryan Dehoff, and Reginald Cochran. High strength aluminum additive manufacturing. Technical report, Oak Ridge National Laboratory (ORNL), Oak Ridge, TN (United States); Boeing Research and Technology, 2024. 122

[255] Fan Zhang, Lyle E. Levine, Andrew J. Allen, Carelyn E. Campbell, Eric A. Lass, Sudha Cheruvathur, Mark H. Nero, Jan Ilavsky, and Greta Lindwall. Prediction of cracking susceptibility of commercial aluminum alloys during solidification. *Metals*, 11(9):1479, 2021. 122

[256] Le Zhou, Thinh Huynh, Sharon Park, Holden Hyer, Abhishek Mehta, Shutao Song, Yuanli Bai, Brandon McWilliams, Kyu Cho, and Yongho Sohn. Laser powder bed fusion of al–10 wt% ce alloys: microstructure and tensile property. *Journal of Materials Science*, 55(29):14611–14625, 2020. 123

[257] Tiffany Wu, Alex Plotkowski, Amit Shyam, and David C Dunand. Microstructure and creep properties of cast near-eutectic al–ce–ni alloys. *Materials Science and Engineering: A*, 833:142551, 2022. 123, 144, 146

[258] KA Jackson and JD Hunt. Lamellar and rod eutectic growth. In *Dynamics of curved fronts*, pages 363–376. Elsevier, 1988. 123

[259] D Weiss. Development and casting of high cerium content aluminum alloys. *Transactions of the American Foundry Society*, pages 17–013, 2017. 123

[260] Vladyslav Turlo and Timothy J Rupert. Grain boundary complexions and the strength of nanocrystalline metals: Dislocation emission and propagation. *Acta Materialia*, 151:100–111, 2018. 123

[261] Yuanfan Liu, Yang Li, Mingliang Wang, and Zhe Chen. Review of laser powder bed fusion's microstructure and mechanical characteristics for al-ce alloys. *Materials*, 17(20):5085, 2024. 123, 134

[262] Feng Li, Taomei Zhang, Yiyou Wu, Chao Chen, and Kechao Zhou. Microstructure, mechanical properties, and crack formation of aluminum alloy 6063 produced via laser powder bed fusion. *Journal of materials Science*, 57 (21):9631–9645, 2022. 123

[263] Haixiang Wang, Xiyuan Wang, Jinliang Zou, Huan Zhou, Qiuli Zheng, Jiang Bi, Mikhail Dmitrievich Starostenkov, Guojiang Dong, and Caiwang Tan. Recent progress on the control strategies of microstructure and mechanical properties of lpbf-printed aluminum alloys. *The International Journal of Advanced Manufacturing Technology*, 134(9):4015–4039, 2024. 123

[264] Yang Liu, Richard A Michi, and David C Dunand. Cast near-eutectic al-12.5 wt.% ce alloy with high coarsening and creep resistance. *Materials Science and Engineering: A*, 767:138440, 2019. 123

[265] SV Chernyshikhin, EL Dzidziguri, LV Fedorenko, AA Gromov, KB Larionov, MV Lyange, NA Kharitonova, EA Naumova, D Yu Ozherelkov, IA Pelevin, et al. Structure and mechanical properties of al–ce–fe alloy synthesized by lpbf method. *Metals and Materials International*, 30(11):3184–3201, 2024. 123

[266] Sébastien Vaudreuil, Salah-Eddine Bencaid, Hamid Reza Vanaei, and Anouar El Magri. Effects of power and laser speed on the mechanical properties of alsi7mg0. 6 manufactured by laser powder bed fusion. *Materials*, 15(23):8640, 2022. 123

[267] Clement N Ekaputra, Jovid U Rakhmonov, Ekin Senvardarli, David Weiss, Jon-Erik Mogonye, and David C Dunand. Design and characterization of hierarchically-strengthened, cast al-ce-ni-mn-sc-zr alloys for high-temperature applications. In *TMS Annual Meeting & Exhibition*, pages 255–262. Springer, 2024. 123

[268] Amirkoushyar Ziabari, Singanallur V Venkatakrishnan, Zackary Snow, Aleksander Lisovich, Michael Sprayberry, Paul Brackman, Curtis Frederick, Pradeep Bhattad, Sarah Graham, Philip Bingham, et al. Enabling rapid x-ray ct characterisation for additive manufacturing using cad models and deep learning-based reconstruction. *npj Computational Materials*, 9(1):91, 2023. 126, 130, 131

[269] P Fernandes de Aguiar, B Bourguignon, MS Khots, DL Massart, and R Phan-Than-Luu. D-optimal designs. *Chemometrics and intelligent laboratory systems*, 30(2):199–210, 1995. 127

[270] Raymond H Myers, Douglas C Montgomery, and Christine M Anderson-Cook. *Response surface methodology: process and product optimization using designed experiments*. John Wiley & Sons, 2016. 129, 130

[271] R Core Team. R: A language and environment for statistical computing, 2013. 129

[272] Hirotugu Akaike. A new look at the statistical model identification. *IEEE Transactions on Automatic Control*, 19(6):716–723, 1974. 130

[273] K. P. Burnham and D. R. Anderson. *Model Selection and Multimodel Inference: A Practical Information-Theoretic Approach*. Springer, 2nd edition, 2002. 130

[274] Amirkoushyar Ziabari, Dong Hye Ye, Somesh Srivastava, Ken D. Sauer, Jean-Baptiste Thibault, and Charles A. Bouman. Model based iterative

reconstruction with spatially adaptive sinogram weights for wide-cone cardiac CT. *arXiv preprint arXiv:1812.08364*, 2018. 130

[275] Dennis L Parker. Optimal short scan convolution reconstruction for fan beam ct. *Medical physics*, 9(2):254–257, 1982. 130

[276] Amirkoushyar Ziabari, Singanallur Venkatakrishnan, Abhishek Dubey, Alex Lisovich, Paul Brackman, Curtis Frederick, Pradeep Bhattad, Philip Bingham, Alex Plotkowski, Ryan Dehoff, et al. Simurgh: A framework for cad-driven deep learning based x-ray ct reconstruction. In *2022 IEEE international conference on image processing (ICIP)*, pages 3836–3867. IEEE, 2022. 131

[277] Amir Ziabari, Singanallur Venkatakrishnan, Philip R Bingham, Michael M Kirka, Vincent C Paquit, Ryan R Dehoff, and Abhishek Dubey. System and method for artifact reduction of computed tomography reconstruction leveraging artificial intelligence and a priori known model for the object of interest, September 2 2025. US Patent 12,406,104. 131

[278] Amirkoushyar Ziabari et al. Simurgh. Oak Ridge National Laboratory, U.S. Copyright Office, 2022. Software copyright registration. 131

[279] Amani Cheniour, Amir Koushyar Ziabari, and Yann Le Pape. A mesoscale 3d model of irradiated concrete informed via a 2.5 u-net semantic segmentation. *Construction and Building Materials*, 412:134392, 2024. 131

[280] Amir Ziabari, Obaid Rahman, Michael Sprayberry, Rahul Franklin, Amra Peles, Holden Hyer, Chase Joslin, Sarah Graham, Elizabeth Schmitt, Peeyush Nandwana, et al. High-throughput characterization tools/algorithms to outline porosity variability in am samples as a function of processing conditions. Technical report, Oak Ridge National Laboratory (ORNL), Oak Ridge, TN (United States), 2025. 131

[281] Yuze Huang, Tristan G Fleming, Samuel J Clark, Sebastian Marussi, Kamel Fezzaa, Jeyan Thiyagalingam, Chu Lun Alex Leung, and Peter D Lee. Keyhole fluctuation and pore formation mechanisms during laser powder bed fusion additive manufacturing. *Nature communications*, 13(1):1170, 2022. 134, 137

[282] Minxiang Zeng, Yipu Du, Qiang Jiang, Nicholas Kempf, Chen Wei, Miles V Bimrose, ANM Tanvir, Hengrui Xu, Jiahao Chen, Dylan J Kirsch, et al. High-throughput printing of combinatorial materials from aerosols. *Nature*, 617 (7960):292–298, 2023. 134

[283] Lu Wang, Yanming Zhang, Hou Yi Chia, and Wentao Yan. Mechanism of keyhole pore formation in metal additive manufacturing. *NPJ Computational Materials*, 8(1):22, 2022. 137

[284] Ming Tang, P Chris Pistorius, and Jack L Beuth. Prediction of lack-of-fusion porosity for powder bed fusion. *Additive Manufacturing*, 14:39–48, 2017. 137

[285] Ken Kelley and Jocelyn H. Bolin. Multiple regression. In *Handbook of Quantitative Methods for Educational Research*, pages 71–101. Sense Publishers, 2013. 138

[286] Suhong Zhang, Alan Frederick, Yiyu Wang, Mike Eller, Paul McGinn, Anming Hu, and Zhili Feng. Microstructure evolution and mechanical property characterization of 6063 aluminum alloy tubes processed with friction stir back extrusion. *JOM*, 71(12):4436–4444, 2019. 141

[287] Min Zheng, Lei Wei, Jing Chen, Qiang Zhang, Jiaqiang Li, Shang Sui, Geng Wang, and Weidong Huang. Surface morphology evolution during pulsed selective laser melting: Numerical and experimental investigations. *Applied Surface Science*, 496:143649, 2019. 143

[288] Zhen Chen, Yongxin Lu, Fan Luo, Shuzhe Zhang, Pei Wei, Sen Yao, and Yongxin Wang. Effect of laser scanning speed on the microstructure

and mechanical properties of laser-powder-bed-fused k418 nickel-based alloy. *Materials*, 15(9):3045, 2022. 144

[289] Takashi Maeshima, Keiichiro Oh-Ishi, and Hiroaki Kadoura. Microstructural evolution and hardening phenomenon caused by aging of alsi10mg alloy by laser powder bed fusion. *Heliyon*, 10(6), 2024. 144

[290] Artur Leis, David Traunecker, Rudolf Weber, and Thomas Graf. Tuning the hardness of produced parts by adjusting the cooling rate during laser-based powder bed fusion of alsi10mg by adapting the process parameters. *Metals*, 12 (12):2000, 2022. 144

[291] Jiankai Yang, Luhao Yuan, and Hongmei Zhang. Hall-petch relationship in multiscale cellular structures of al-si alloy fabricated by laser powder bed fusion. *Materials Today Communications*, 40:109518, 2024. 144

[292] Yangyang Fan, Kai Huang, and Makhlouf M Makhlouf. Precipitation strengthening in al-ni-mn alloys. *Metallurgical and Materials Transactions A*, 46(12):5830–5841, 2015. 144

[293] Daniel Rosenthal. The theory of moving sources of heat and its application to metal treatments. *Transactions of the American Society of Mechanical Engineers*, 68(8):849–865, 1946. 146

[294] TW Eagar, NS Tsai, et al. Temperature fields produced by traveling distributed heat sources. *Welding journal*, 62(12):346–355, 1983. 146

[295] Ailing Zhang and Yanxiang Li. Thermal conductivity of aluminum alloys—a review. *Materials*, 16(8):2972, 2023. 146

[296] Johannes Trapp, Alexander M Rubenchik, Gabe Guss, and Manyalibo J Matthews. In situ absorptivity measurements of metallic powders during laser powder-bed fusion additive manufacturing. *Applied Materials Today*, 9:341–349, 2017. 146

[297] Y Du, T Mukherjee, N Finch, A De, and T DebRoy. High-throughput screening of surface roughness during additive manufacturing. *Journal of Manufacturing Processes*, 81:65–77, 2022. 147, 148

[298] Chunlei Qiu, Chinnapat Panwisawas, Mark Ward, Hector C Basoalto, Jeffery W Brooks, and Moataz M Attallah. On the role of melt flow into the surface structure and porosity development during selective laser melting. *Acta Materialia*, 96:72–79, 2015. 147, 148

[299] A. M. Khorasani, Ian Gibson, Moshe Goldberg, and Guy Littlefair. Modelling of laser powder bed fusion process and analysing the effective parameters on surface characteristics of Ti-6Al-4V. *International Journal of Mechanical Sciences*, 168:105299, 2020. 147, 148

[300] M. Oyesola, K. Mpofu, N. Mathe, and M. Muchindu. Optimization of selective laser melting process parameters for surface quality performance of the fabricated Ti6Al4V. *The International Journal of Advanced Manufacturing Technology*, 114:1585–1599, 2021. 147, 148

[301] Z. Li, I. Kucukkoc, D. Z. Zhang, and F. Liu. Optimising the process parameters of selective laser melting for the fabrication of Ti6Al4V alloy. *Rapid Prototyping Journal*, 24(1):150–159, 2018. 147, 148

[302] Ali Fatemi, Reza Molaei, Shahriar Sharifimehr, Nam Phan, and Nima Shamsaei. Multiaxial fatigue behavior of wrought and additive manufactured Ti-6Al-4V including surface finish effect. *International Journal of Fatigue*, 100:347–366, 2017. 147, 148

[303] Flaviana Calignano, Diego Manfredi, Elisa Paola Ambrosio, Luca Iuliano, and Paolo Fino. Influence of process parameters on surface roughness of aluminum parts produced by dmls. *The International Journal of Advanced Manufacturing Technology*, 67(9):2743–2751, 2013. 147, 148

[304] Ahmed H Maamoun, Yi F Xue, Mohamed A Elbestawi, and Stephen C Veldhuis. Effect of selective laser melting process parameters on the quality of al alloy parts: Powder characterization, density, surface roughness, and dimensional accuracy. *Materials*, 11(12):2343, 2018. 147, 148

[305] M. Balbaa, S. Mekhiel, M. Elbestawi, and J. McIsaac. Role of powder particle size on laser powder bed fusion processability of AlSi10Mg alloy. *Additive Manufacturing*, 37:101630, 2021. 147, 148

[306] C. Taute, H. Möller, and A. du Plessis. Characterization of additively manufactured AlSi10Mg cubes with different porosities. *Journal of the Southern African Institute of Mining and Metallurgy*, 121(4):143–150, 2021. 147, 148

[307] M. Badrossamay, E. Yasa, J. Van Vaerenbergh, and J.-P. Kruth. Improving productivity rate in SLM of commercial steel powders. *Technical Paper – Society of Manufacturing Engineers*, pages 1–13, 2009. 147, 148

[308] Di Wang, Yang Liu, Yongqiang Yang, and Dongming Xiao. Theoretical and experimental study on surface roughness of 316l stainless steel metal parts obtained through selective laser melting. *Rapid Prototyping Journal*, 22(4): 706–716, 2016. 147, 148

[309] L. Cao, J. Li, J. Hu, H. Liu, Y. Wu, and Q. Zhou. Optimization of surface roughness and dimensional accuracy in LPBF additive manufacturing. *Optics & Laser Technology*, 142:107246, 2021. 147, 148

[310] H. Zhang, C. K. P. Vallabh, and X. Zhao. Influence of spattering on in-process layer surface roughness during laser powder bed fusion. *Journal of Manufacturing Processes*, 104:289–306, 2023. 148

[311] Lu Li, Ji-Qin Li, and Tai-Hsi Fan. Phase-field modeling of wetting and balling dynamics in powder bed fusion process. *Physics of Fluids*, 33(4), 2021. 148

[312] Jan-Philipp Negel, Andreas Voss, Marwan Abdou Ahmed, Dominik Bauer, Dirk Sutter, Alexander Killi, and Thomas Graf. 1.1 kw average output power from a thin-disk multipass amplifier for ultrashort laser pulses. *Optics Letters*, 38(24): 5442–5445, 2013. 153

[313] A Ancona, S Döring, C Jauregui, F Röser, J Limpert, S Nolte, and A Tünnermann. Femtosecond and picosecond laser drilling of metals at high repetition rates and average powers. *Optics Letters*, 34(21):3304–3306, 2009. 153

[314] Mangirdas Malinauskas, Albertas Žukauskas, Satoshi Hasegawa, Yoshio Hayasaki, Vygantas Mizeikis, Ričardas Buividas, and Saulius Juodkazis. Ultrafast laser processing of materials: from science to industry. *Light: Science & Applications*, 5(8):e16133–e16133, 2016. 153

[315] X Liu, D Du, and Gé Mourou. Laser ablation and micromachining with ultrashort laser pulses. *IEEE Journal of Quantum Electronics*, 33(10):1706–1716, 1997. 153

[316] Rafael R Gattass and Eric Mazur. Femtosecond laser micromachining in transparent materials. *Nature Photonics*, 2(4):219–225, 2008. 153

[317] Koji Sugioka and Ya Cheng. Femtosecond laser three-dimensional micro-and nanofabrication. *Applied Physics Reviews*, 1(4), 2014. 153

[318] D Von der Linde, K Sokolowski-Tinten, and J Bialkowski. Laser–solid interaction in the femtosecond time regime. *Applied Surface Science*, 109:1–10, 1997. 153

[319] Rudolf Weber, Thomas Graf, Peter Berger, Volkher Onuseit, Margit Wiedenmann, Christian Freitag, and Anne Feuer. Heat accumulation during pulsed laser materials processing. *Optics Express*, 22(9):11312–11324, 2014. 154

[320] Johannes Finger and Martin Reininghaus. Effect of pulse to pulse interactions on ultra-short pulse laser drilling of steel with repetition rates up to 10 mhz. *Optics Express*, 22(15):18790–18799, 2014. 154

[321] Franziska Bauer, Andreas Michalowski, Thomas Kiedrowski, and Stefan Nolte. Heat accumulation in ultra-short pulsed scanning laser ablation of metals. *Optics Express*, 23(2):1035–1043, 2015. 154

[322] Gediminas Raciukaitis, Marijus Brikas, Paulius Gecys, and Mindaugas Gedvilas. Accumulation effects in laser ablation of metals with high-repetition-rate lasers. In *High-Power Laser Ablation VII*, volume 7005, pages 725–735. SPIE, 2008. 154

[323] Xxx Sedao, Maxim V. Shugaev, Chengping Wu, Thierry Douillard, Claude Esnouf, Claire Maurice, Stéphanie Reynaud, Florent Pigeon, Florence Garrelie, Leonid V. Zhigilei, and Jean-Philippe Colombier. Growth twinning and generation of high-frequency surface nanostructures in ultrafast laser-induced transient melting and resolidification. *ACS Nano*, 10(7):6995–7007, 2016. 154

[324] Daniel J Förster, Rudolf Weber, and Thomas Graf. Residual heat during ultrashort laser drilling of metals. In *Proceedings of LPM2017—the 18th International Symposium on Laser Precision Microfabrication*, 2017. 154

[325] Liliana Cangueiro, José Antonio Ramos-de Campos, and David Bruneel. Prediction of thermal damage upon ultrafast laser ablation of metals. *Molecules*, 26(21):6327, 2021. 154

[326] N Hodgson, S Heming, A Steinkopff, H Haloui, and TS Lee. Ultrafast laser ablation at 1035 nm, 517 nm and 345 nm as a function of pulse duration and fluence. In *Proceedings of the Lasers in Manufacturing Conference*, page 345, 2019. 154

[327] Maxim V Shugaev, Chengping Wu, Oskar Armbruster, Aida Naghilou, Nils Brouwer, Dmitry S Ivanov, Thibault J-Y Derrien, Nadezhda M Bulgakova, Wolfgang Kautek, Baerbel Rethfeld, et al. Fundamentals of ultrafast laser–material interaction. *MRS Bulletin*, 41(12):960–968, 2016. 154

[328] Sungkwon Shin, Jun-Gyu Hur, Jong Kab Park, and Doh-Hoon Kim. Thermal damage free material processing using femtosecond laser pulses for fabricating fine metal masks. *Optics & Laser Technology*, 134:106618, 2021. 154

[329] Luis Omeñaca, Santiago Miguel Olaizola, Ainara Rodríguez, Mikel Gomez-Aranzadi, Isabel Ayerdi, and Enrique Castaño. Optimization of ultrafast laser ablation of stainless steel in burst mode based on experimentally validated simulations and analytical modelling. *Scientific Reports*, 2026. 155

[330] Jinping Zhang, Yuping Chen, Mengning Hu, and Xianfeng Chen. An improved three-dimensional two-temperature model for multi-pulse femtosecond laser ablation of aluminum. *Journal of Applied Physics*, 117(6), 2015. 155

[331] Michael Rieth, Sergei L Dudarev, SM Gonzalez De Vicente, Jürgen Aktaa, T Ahlgren, S Antusch, DEJ Armstrong, M Balden, Nadine Baluc, M-F Barthe, et al. Recent progress in research on tungsten materials for nuclear fusion applications in europe. *Journal of Nuclear Materials*, 432(1-3):482–500, 2013. 155

[332] Richard A Pitts, Xavier Bonnin, Frédéric Escourbiac, Heinke Frerichs, JP Gunn, Takeshi Hirai, AS Kukushkin, Elizaveta Kaveeva, MA Miller, David Moulton, et al. Physics basis for the first iter tungsten divertor. *Nuclear Materials and Energy*, 20:100696, 2019. 155

[333] Y Ueda, JW Coenen, G De Temmerman, RP Doerner, J Linke, V Philipps, and E Tsitrone. Research status and issues of tungsten plasma facing materials for iter and beyond. *Fusion Engineering and Design*, 89(7-8):901–906, 2014. 155

[334] Panagiotis Tolias, EUROfusion MST1 Team, et al. Analytical expressions for thermophysical properties of solid and liquid tungsten relevant for fusion applications. *Nuclear Materials and Energy*, 13:42–57, 2017. 155, 158, 159

[335] Hong-Da Zhang, Han Yu, Jie Ning, Lin-Jie Zhang, Ai-fei Pan, and Wen-Jun Wang. Experimental research on micro-drilling of refractory material tungsten by multi-pulse femtosecond laser ablation. *Optics & Laser Technology*, 168: 109962, 2024. 155

[336] Kendrick Mensink, Elías H Penilla, Pablo Martínez-Torres, Natanael Cuando-Espitia, Suveen Mathaudhu, and Guillermo Aguilar. High repetition rate femtosecond laser heat accumulation and ablation thresholds in cobalt-binder and binderless tungsten carbides. *Journal of Materials Processing Technology*, 266:388–396, 2019. 155

[337] Logan Howard, Gabriel D. Parker, and Xiao-Ying Yu. Progress and challenges of additive manufacturing of tungsten and alloys as plasma-facing materials. *Materials*, 17(9):2104, 2024. 155

[338] Zhibin Lin, Leonid V Zhigilei, and Vittorio Celli. Electron-phonon coupling and electron heat capacity of metals under conditions of strong electron-phonon nonequilibrium. *Physical Review B*, 77(7):075133, 2008. 158, 159

[339] Arnold Sommerfeld. Zur elektronentheorie der metalle auf grund der fermischen statistik. *Zeitschrift für Physik*, 47(1):1–32, 1928. 158

[340] Charles Kittel and Paul McEuen. *Introduction to solid state physics*. John Wiley & Sons, 2018. 158, 159

[341] Sergei I Anisimov and Baerbel Rethfeld. Theory of ultrashort laser pulse interaction with a metal. In *Nonresonant Laser-Matter Interaction (NLMI-9)*, volume 3093, pages 192–203. SPIE, 1997. 158

[342] Jerome G Hust and Alan B Lankford. Thermal conductivity of aluminum, copper, iron, and tungsten for temperatures from 1 k to the melting point. Technical report, National Bureau of Standards, Boulder, CO (USA), 1984. 158, 159

[343] GK White and ML Minges. Thermophysical properties of some key solids: an update. *International Journal of Thermophysics*, 18(5):1269–1327, 1997. 158, 159

[344] Max Born, Emil Wolf, A. B. Bhatia, P. C. Clemmow, D. Gabor, A. R. Stokes, A. M. Taylor, P. A. Wayman, and W. L. Wilcock. *Principles of Optics: Electromagnetic Theory of Propagation, Interference and Diffraction of Light*. Cambridge University Press, Cambridge, 7th edition, 1999. doi: 10.1017/CBO9781139644181. 158

[345] S Khakshouri, D Alfe, and DM Duffy. Development of an electron-temperature-dependent interatomic potential for molecular dynamics simulation of tungsten under electronic excitation. *Physical Review B*, 78(22):224304, 2008. 159

[346] Szymon L Daraszewicz, Yvelin Giret, Hiroshi Tanimura, Dorothy M Duffy, Alexander L Shluger, and Katsumi Tanimura. Determination of the electron–phonon coupling constant in tungsten. *Applied Physics Letters*, 105(2), 2014. 159

[347] Yani Chen, Jinlong Ma, and Wu Li. Understanding the thermal conductivity and lorenz number in tungsten from first principles. *Physical Review B*, 99(2): 020305, 2019. 159

[348] Md Rafiqul Islam, Pravin Karna, Niraj Bhatt, Sandip Thakur, Helge Heinrich, Daniel M Hirt, Saman Zare, Christopher Jezewski, Rinus TP Lee, Kandabara Tapily, et al. Unveiling phonon contributions to thermal conductivity and the

applicability of the wiedemann—franz law in ruthenium and tungsten thin films. *Advanced Functional Materials*, 36(12):e11592, 2026. 159

[349] Edward D Palik. *Handbook of optical constants of solids*, volume 3. Academic Press, 1998. 159

[350] Mianzhen Mo, Artur Tamm, Erki Metsanurk, Zhijiang Chen, Ling Wang, Mungo Frost, Nicholas J Hartley, Fuhao Ji, Silvia Pandolfi, Alexander H Reid, et al. Direct observation of strong momentum-dependent electron-phonon coupling in a metal. *Science advances*, 10(11):eadk9051, 2024. 175

[351] Martine F Daniel, B Desbat, JC Lassegues, B Gerand, and M Figlarz. Infrared and raman study of wo_3 tungsten trioxides and wo_3, xh_2o tungsten trioxide tydrates. *Journal of Solid State Chemistry*, 67(2):235–247, 1987. 180

[352] Unmanaa Dewanjee, Gadde Deepak, Shi Bai, David Fieser, Yang Du, Marco Fronzi, Qiang He, and Anming Hu. Ultra-sensitive SERS analysis for PFOA degradation based on femtosecond laser-processed probes, DFT calculation and machine learning. *Microchemical Journal*, page 117787, 2026. 245

Appendices

Appendix A

Experimental Results

A.1 LPBF Processing Parameters and Results for ACNMZ

Table A.1 lists the complete set of processing parameters and measured responses for the 49 LPBF parameter sets investigated in Chapter 4. Parameter sets marked with * were selected for additional metallographic characterization using a D-optimal experimental design. Rows labeled CP denote center-point replicates (370 W, 1300 mm/s, 0.19 mm hatch), which were included to estimate pure experimental error and assess repeatability.

Table A.1: Complete LPBF processing parameters and results for ACNMZ. Void% and hardness (HV) are averages. E_a is the areal energy density (J/mm^2).

Set	Void%	HV	Power (W)	Speed (mm/s)	Hatch (mm)	Row	Seat	E_a (J/mm^2)
1	0.0025	155.58	350	1600	0.15	8	5	1.458
2*	0.0026	141.34	370	1200	0.15	4	3	2.056
3	0.0043	157.5	330	1600	0.15	3	3	1.375
4	0.0033	149.22	350	1100	0.19	1	3	1.675
5	0.0013	148.68	370	1400	0.17	10	5	1.555
6	0.0217	157.52	330	1700	0.13	2	5	1.494
7	0.005	145.32	350	1300	0.19	1	5	1.420

Continued on next page

Table A.1 – continued from previous page

Set	Void%	HV	Power (W)	Speed (mm/s)	Hatch (mm)	Row	Seat	E_a (J/mm^2)
8	0.0084	140.2	370	1000	0.21	6	1	1.762
9	0.0012	155.3	330	1900	0.15	6	3	1.158
10*	0.0827	157.36	330	2000	0.17	5	2	0.971
11	0.0076	155.14	350	1600	0.19	7	7	1.151
12	0.0024	141.24	370	1200	0.17	4	5	1.814
13	0.0069	150.54	370	1400	0.21	3	1	1.259
14	0.0052	142.78	330	1100	0.21	4	1	1.429
15*	0.0039	136.86	370	1000	0.13	5	4	2.846
16*	0.0015	151.36	350	1400	0.15	9	5	1.667
17	0.0028	149.4	350	1500	0.21	10	3	1.111
18	0.0039	144.16	350	1200	0.13	9	3	2.244
19	0.0028	144.34	370	1100	0.15	3	5	2.242
20	0.0032	153.56	330	1800	0.17	6	5	1.078
21	0.0038	135.62	350	1000	0.17	7	3	2.059
22	0.0044	146.54	330	1400	0.13	5	6	1.813
23*	0.0093	130.08	370	1000	0.15	4	7	2.467
24	0.0054	141.66	350	1100	0.13	7	1	2.448
25	0.0022	148.58	350	1300	0.15	8	3	1.795
26	0.0048	143.72	330	1300	0.21	2	1	1.209
27*	0.0361	160.28	330	1700	0.21	9	7	0.928
28	0.0045	150.42	330	1500	0.19	10	1	1.158
29	0.0024	151.42	370	1600	0.13	8	1	1.779
30	0.0024	153.3	350	1700	0.17	6	7	1.211
31*	0.0012	150.22	370	1500	0.19	8	7	1.298
32	0.0088	149.38	330	1200	0.19	1	1	1.447
33	0.0085	145.92	350	1800	0.13	2	3	1.496
34	0.0019	143.4	370	1300	0.19	5	8	1.498

Continued on next page

Table A.1 – continued from previous page

Set	Void%	HV	Power (W)	Speed (mm/s)	Hatch (mm)	Row	Seat	E_a (J/mm^2)
35	0.0026	155.68	370	1800	0.21	3	7	0.979
36	0.0038	157.76	370	1700	0.15	7	5	1.451
37*	0.0065	148.76	330	1400	0.19	1	7	1.241
38	0.017	153.14	370	1900	0.17	9	1	1.146
39	0.0017	149.98	350	1900	0.19	2	7	0.970
40*	0.0024	137.5	330	1000	0.13	10	7	2.538
CP	0.0048	147.52	370	1300	0.19	10	8	1.498
CP	0.0051	145.68	370	1300	0.19	10	6	1.498
CP	0.0049	144.78	370	1300	0.19	10	4	1.498
CP	0.005	145.36	370	1300	0.19	10	2	1.498
CP	0.0012	147.16	370	1300	0.19	9	8	1.498
CP	0.0038	143.42	370	1300	0.19	9	6	1.498
CP	0.002	146.54	370	1300	0.19	9	4	1.498
CP	0.0014	143.88	370	1300	0.19	9	2	1.498
CP	0.0022	145.3	370	1300	0.19	8	8	1.498

Appendix B

Publications

1. **Fieser, D.**, Lan, Y., Gulino, A., Compagnini, G., Aaron, D., Mench, M., Bridges, D., Shortt, H., Liaw, P., & Hu, A. (2024). Synthesis and unique behaviors of high-purity HEA nanoparticles using femtosecond laser ablation. *Nanomaterials*, *14*(6), 554. [144]

2. **Fieser, D.**, Yin, K., Shortt, H., Dewanjee, U., Steingrimsson, B., Ivanov, I. N., Burns, J., Liaw, P. K., Zuo, J.-M., & Hu, A. (2025). Surface nanostructure control and thermodynamic stability analysis of femtosecond laser-ablated $CuCoMn_{1.75}NiFe_{0.25}$ nanoparticles. *Langmuir*, *41*(50), 34173–34188. [183]

3. **Fieser, D.**, Zhang, L., Yao, M., Shortt, H., Liaw, P., & Hu, A. (2024). Femtosecond laser joining of Stellite and stainless steel. *Manufacturing Letters*, *41*, 332–338. [195]

4. **Fieser, D.**, Lawton, M., Bahl, S., Ziabari, A. K., Grejtak, T., Meier, J. M., Smith, M., Plotkowski, A., McDonald, E., & Hu, A. (2026). Optimization of processing, microstructure, and hardness of an Al–Ce–Ni–Mn–Zr alloy with laser additive manufacturing. *Advanced Engineering Materials*, e202502615. [253]

5. Yu, Y., Xiao, M., **Fieser, D.**, Zhou, W., & Hu, A. (2024). Nanoscale memristor devices: Materials, fabrication, and artificial intelligence. *Journal of Materials Chemistry C*, *12*(11), 3770–3810. [163]

6. Zhang, L., **Fieser, D.**, Bera, B., Aaron, D., Mench, M. M., Hu, A., Li, Y., Chen, J., Feng, Z., Gulino, A., & Compagnini, G. (2024). High performance aluminum–air flow batteries through double-face architecture and laser-modified and friction-stir processed 3D anode. *Journal of Power Sources*, *589*, 233752. [145]

7. Bridges, D., **Fieser, D.**, Santiago, J. J., & Hu, A. (2023). Novel frontiers in high-entropy alloys. *Metals*, *13*(7), 1193. [105]

8. Yu, Y., Joshi, P., Bridges, D., **Fieser, D.**, & Hu, A. (2023). Femtosecond laser-induced nano-joining of volatile tellurium nanotube memristor. *Nanomaterials*, *13*(5), 789. [196]

9. Dewanjee, U. N., Deepak, G., Bai, S., **Fieser, D.**, Du, Y., Fronzi, M., He, Q., & Hu, A. (2026). Ultra-sensitive SERS analysis for PFOA degradation based on femtosecond laser-processed probes, DFT calculation and machine learning. *Microchemical Journal*, 117787. [352]

Vita

David Fieser was born in Martin, Tennessee, on July 5, 2000. He attended the University of Tennessee at Martin, earning his Bachelor of Science in Mechatronics Engineering, magna cum laude, in 2022. Following his graduation, he immediately transitioned to the University of Tennessee, Knoxville, to pursue his PhD in Mechanical Engineering and serve as a Teaching Assistant. Over the course of his four years of doctoral research in ultrafast laser processing, David has published four papers as the primary author and coauthored five additional publications. A complete list of publications is provided in Appendix B.